Development of novel mesoporous silica and carbon materials

Tengyao Jiang

PhD

University of York

Chemistry

September 2015

Abstract

The aim of this project was to develop new route to silica and silica based materials through utilizing green techniques and demonstrate its following applications.

Due to the properties of supercritical fluids including high diffusivity, low dynamic viscosity and low surface tension, supercritical fluid (SCF) is becoming a potential alternative solvent class in materials chemistry. The physical properties of SCF could be tuned to more liquid- or more gas- like thus providing an enhanced selectivity of the solubility performance of SCF. Several conditions such as reaction time, pressure and temperature were have been taken into consideration for the synthesis of a spherical mesoporous silica using supercritical carbon dioxide as solvent.

Bio-oil has successfully been utilized to prepare carbon-silica composites (CSCs) from mesoporous silicas. These CSCs comprise a thin film of carbon dispersed over the silica matrix and exhibit porosity similar to parent silica with BET surface areas ranging from 39 to 636 m^2/g and pore volumes ranging from 0.03 to 0.31 cm^3/g. The surface properties of resulting materials can be simply tuned by the variation of preparation temperatures leading to a continuum of functionalities ranging from polar hydroxyl rich surfaces to carbonaceous aromatic surfaces.

The as-synthesised CSC was subsequently used as solid support for the deposition of palladium nanoparticles to catalyse the Heck reaction. This CSC catalyst exhibited a high catalytic activity and excellent reusability for the Heck reaction using either conventional solvent NMP or propylene carbonate. It should be noted that a side product - methyl 3,3-diphenylacrylate was generated during the reaction using CSC catalyst in propylene carbonate with the yield of up to 15.5%. The CSCs were also used to prepare carbonaceous materials by silica etching process. After silica removal, a mesoporous carbonaceous material with the morphology ranging from rod-like to tubular-like could be synthesised.

Table of contents

List of tables

List of figures

16

18

Acknowledgements

I would like to show my deepest gratitude to my two supervisors, Dr. Duncan Macquarrie and Dr. Andrew Hunt, who guided me about the topic design, operation of the experiment and result discussion. I benefitted a lot from thire scientific methods and academic thinking. Without their enlightening instruction, impressive kindness and patience, I could not have completed my thesis.

I would also like to thank all the staff in Green Chemistry Centre of Excellence who have helped me to develop the fundamental and essential academic competence. Huge thanks to Andy, Duncan and Vitaliy for proof-reading this thesis.

I also owe my sincere gratitude to my dear friends and my fellow classmates and time in listening to me and helping me work out my problems during the difficult course of my PhD study. They are Roy, Cheng, Summer and Tom Attard.

Last but not least, to my family, thank you for all the love and the support that allows me to overcome all the difficulties during my lifetime.

Declaration

I hereby declare that the work presented in this thesis is my own, expect where otherwise acknowledged, and has not previously been submitted for a degree at this or any other university.

Chapter 1   Introduction

1.1 <u>Scope of Thesis</u>

The scope of this project is to synthesise mesoporous silica materials in supercritical fluids and develop new routes for the modification of silica based materials from waste and demonstrate applications in a range of fields.

1.2 <u>Green chemistry</u>

Green chemistry is a relatively new emerging field and it has received great attention in the last few decades since the concept was first formulated at the beginning of the 1990s. It is defined as the "design of chemical products and processes to reduce or eliminate the use and generation of hazardous substances". The 12 principles of green chemistry were subsequently introduced by Paul Anastas and John Warner in 1998,[1] which direct the green chemists to a sustainable and environmental friendly future.

1. *Prevention*

It is better to prevent waste than to treat or clean up waste after it is formed.

2. *Atom Economy*

Synthetic methods should be designed to maximize the incorporation of all materials used in the process into the final product.

3. *Less Hazardous Chemical Syntheses*

Wherever practicable, synthetic methodologies should be designed to use and generate substances that possess little or no toxicity to human health and the environment.

4. *Designing Safer Chemicals*

Chemical products should be designed to preserve efficacy of function while reducing toxicity.

5. *Safer Solvents and Auxiliaries*

The use of auxiliary substances (e.g. solvents, separation agents, etc) should be made unnecessary wherever possible and innocuous when used.

6. Design for Energy Efficiency

Energy requirements should be recognized for their environmental and economic impacts and should be minimized. Synthetic methods should be conducted at ambient temperature and pressure.

7. Use of Renewable Feedstocks

A raw material of feedstock should be renewable rather than depleting wherever technically and economically practicable.

8. Reduce Derivatives

Unnecessary derivatisation (blocking group, protection/deprotection, and temporary modification of physical/chemical processes) should be avoided whenever possible.

9. Catalysis

Catalytic reagents (as selective as possible) are superior to stoichiometric reagents.

10. Design for Degradation

Chemical products should be designed so that at the end of their function they do not persist in the environment and break down into innocuous degradation products.

11. Real-time Analysis for Pollution Prevention

Analytical methodologies need to be further developed to allow for real-time, in-process monitoring and control prior to the formation of hazardous substances.

12. Inherently Safer Chemistry for Accident Prevention

Substances and the form of a substance used in a chemical process should be chosen so as to minimize the potential for chemical accidents.

These principles were taken into consideration throughout the whole thesis. More specifically, the supercritical fluids, which are regarded as an alternative green solvent, have been utilized in the preparation of porous silicas as solvent in Chapter 2. The importance of utilizing green solvent has permeated into most of inorganic or organic chemistry areas. In a chemical reaction, solvents - employed both as reaction media and for purification of final products - occupy the majority of the material input. The impact of solvents on the environment must be first considered. Generally speaking, most of silica and silica based materials were synthesised in aqueous phase. The non-aqueous synthesis of zeolites and silicas using organic solvents have also been paid attention in order to design new molecular sieves either with new architectures or with different chemical properties.[2] It is believed that most organic solvents are included within volatile organic compounds (VOCs).[3] Resulting from a low boiling point, it could cause large numbers of molecules to evaporate from the liquid, thus leading to the associated environmental problems such as atmospheric pollution or ozone level.[3, 4] Where possible, the ideal situation in terms of the green concept is to carry out the reaction without any solvents and auxiliaries. Other than this, supercritical fluids and ionic liquids have been proposed and studied as green alternative solvents in recent years.[5] Bio-oils derived from waste paper with microwave pyrolysis technique have been used as carbon source in silica modification. Besides, NMP, a conventional solvent for conducting the Heck reaction, was substituted by cyclic carbonate based on Principle 5.

1.3 <u>Porous materials</u>

Table 1.1 different types of porous materials[6]

Type of material	Pore size (nm)	Examples	Pore size range (nm)
Macroporous	>50	Porous glasses	>50
mesoporous	2-50	M41S	1.6-10
		SBA-15	8-10
		SBA-16	5
		Mesoporous alumina	2
microporous	<2	Zeolites	<1.4
		Activated carbon	0.6
		ZSM-5	0.4-0.6
		Zeolite A	0.3-0.4

Porous materials have been developed for a wide range of applications, such as insulation, cushioning, impact protection, catalysis, membranes and construction materials. According to the IUPAC definition, inorganic solids that contain pores with diameter (i) > 50 nm are called macroporous, (ii) between 2 - 50 nm are mesoporous and (iii) < 2 nm are microporous (see Table 1.1).

1.3.1 Zeolites

One of the oldest members of the porous materials family are zeolites, which was firstly obtained from mineral in 1756.[7, 8] Zeolites are hydrated crystalline aluminosilicates of the form $M_{2/n}O$-Al_2O_3-$ySiO_2$-wH_2O where M is a cation such as sodium, potassium, magnesium or calcium, n is its charge and y ranges from 2 to infinity. Zeolite means "boiling stone" in Greek word as natural zeolites absorb water and this boils out of the material when heated. They occur naturally but are also produced industrially on a large scale. Due to the structural characteristics and applications in catalysis and molecular sieving chemistry, huge progress has been made in the development of synthetic zeolites and zeolite-like materials. Zeolites are widely used in various catalytic applications. Zeolite X is used as cracking catalyst, zeolite Y as isomerization catalyst and ZSM-5 in fluid catalytic reactions.[9]

1.3.2 Mesoporous silicas

There are several types of mesoporous silicas, including silica aerogels, silica xerogels, Vycor glasses, and surfactant templated mesoporous materials. Unlike the crystalline zeolites, all of these silica materials are amorphous although their pores could be arranged in a regular manner. Due to the uniform pore diameters and the controllable pore structure by utilizing a range of different surfactants, the surfactant template mesoporous materials including the M41S family and SBA series have been of great importance in materials science.[10]

The mesoporous M41S family was first synthesized by Mobil Oil group in 1992 through sol-gel method via S^+I^- route:[11] under basic conditions, silicate anions (I^-) matches with surfactant cations (S^+) through Coulombic forces.[12] A typical synthesis starts with the formation of organic micellar species in an alkaline solution, followed by the condensation of the silica matrix and finally the removal of organic template. MCM-41 possesses two-dimensional (2D) hexagonal mesosphere belonging to the p6m space group, MCM-48 structure is a Ia3d cubic mesosphere, which can be visualized as two interlinked networks of spherical cages separated by continuous silica frameworks. MCM-50 exhibits a lamellar structure. The surfactant to silicon molar ratio is a critical factor in the formation of M41S. As the ratio was increased from 0.5 to 2.0, MCM-41, MCM-48 and MCM-50 were respectively prepared. This could be explained by the well-known liquid-crystal phase transformations.[13]

In 1998, a new family of mesoporous silicas called SBA were synthesized in an acidic aqueous environment.[14] SBA-1, 2, 3 use cationic surfactants to form a cubic phase, a 3D micellar hexagonal phase and a 2D hexagonal phase, respectively, while SBA-15, 16 are 2D hexagonal and Im3m cubic phases, synthesized using non-ionic triblock copolymer surfactants, which is different from other members of this family. These materials prepared from non-ionic surfactant possess thicker pore walls and better thermal stability than the MCM family due to the slower self-assembly of surfactant-silica mesophase. SBA-15 (see Figure 1.1) especially has been the most frequently studied as solid support because of its high surface-to-volume ratio, variable framework composition and high thermal stability.[15]

Micropores on the silica walls
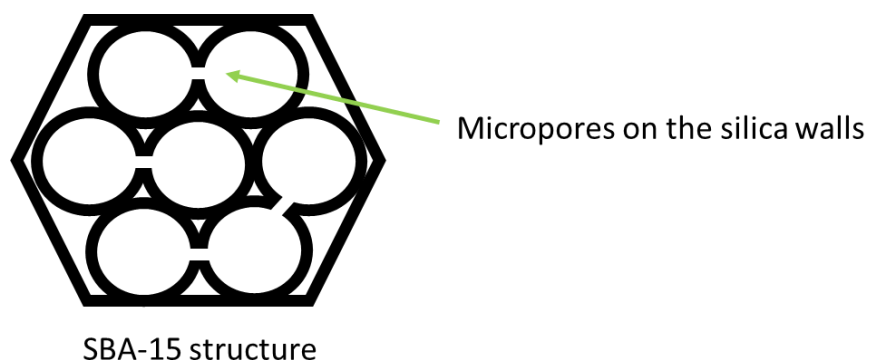
SBA-15 structure

Figure 1.1 Schematic illustration for the pore structure of mesoporous SBA-15

The same research group who developed SBA-15 silica materials then reported that a well-ordered hexagonal SBA-15 material with tuneable pore size and pore wall thickness could be synthesised via a range of reaction conditions.[16] TEM images of the calcined SBA-15 samples clearly showed the pore size of the material was controllable and ranged from 6 nm to 26 nm, and the corresponding pore wall thickness decreased from 5.3 nm to 4 nm. Not only the pore size of SBA-15 material, but also its morphology, is extremely important to expand the range of applications. Thus, mesoporous silica SBA-15 with tuneable morphologies such as fibre-, rope-, doughnut-, sphere-, gyroid- and discoidlike have successfully been synthesised by the incorporation of co-solvent, co-surfactant or inorganic electrolyte. The formation of these different silicas was explained by the surface curvature energy at the interface of inorganic silica and organic block copolymer species.[17] It is well known that SBA-15 is a mesoporous material. If macropores were introduced to SBA-15 materials, they could have a better efficiency in mass transfer, thus leading to a wider application in adsorption and catalysis. In order to achieve a hierarchical combination of different pore sizes into SBA-15, a modified SBA-15 synthesis approach by combining P123 and polystyrene bead as templates was developed.[18, 19] The ordering of macropores could be improved with the increased amount of polystyrene beads.[18] The resultant material possesses high surface areas and well defined interconnecting macro- and mesopore networks with respective narrow size distributions. The catalysis utilizing this macroporous-mesoporous material showed an enhanced reactivity since the material could improve diffusion of bulk molecules.[19]

In consideration of the application of mesoporous silica, it frequently performs a role of support material, which needs to be insoluble in aqueous or polar solutions, be porous

32

and chemically stable but easily derivatived.[20] It is essential to modify functional groups onto the surface of the silica support. If the chemical structure is bonded with the silica surface, the properties might be combined with specific applications. Modified silica could be widely applied as a stationary phase in various kinds of chromatography in low pH range. Other than this, the immobilization of metal complex is well established as a route to heterogeneous catalysts.[21-29] The advantages of this system include high activity and selectivity for the catalysis and easy separation of heterogeneous catalysts.[20] Some examples of modification of SBA-15 with metals are summarised in Table 1.2.

Table 1.2 Examples of metal incorporation into SBA-15 materials

Type of metal incorporated into SBA-15	Remarks	Reference(s)
ZnO	ZnO was deposited by solvent-free method and it was highly dispersed	Zhu[21]
Europium	An easy method for doping of Eu^{3+} inside the pores of the material	Zhao[22]
Titanium	High thermal stability and excellent endurance against Ti leaching	Tatsumi[23]
Tin	A direct synthetic route under milder acidic conditions	Ramaswamy[24]
Cobalt	High catalytic activity due to the ordered structure of SBA-15	Khodakov[25]
Nickel	Rapid diffusion of molecules through the pore system	Yi[26]
Gold	Used for carbon monoxide oxidation at room temperature	Schuth[27]
Palladium	Synthesis of well-dispersed Pd-SBA-15 catalyst by a facile one-step approach	Ji[28]
Palladium	Palladium deposited on SBA-15 in supercritical carbon dioxide	Hunt[29]

1.4   <u>Synthesis of mesoporous materials</u>

The most documented method for the synthesis of silica is the sol-gel route.[20] It is a wet chemical process, involving sol step of hydrolysis of precursor and gel step of condensation of metal alkoxides or inorganic salts, followed by the aging, drying and calcination. A sol is a continuous liquid phase suspension of small solid particles ranging in the size from 1 nm to 1 µm. The further condensation of solid particles into 3-dimensional cross-linked network produces a gel, which behaves like a solid due to the continuous solid phase and discontinuous liquid phase.[30] The hydrolysis and condensation occur simultaneously and the relative rates of both processes determine the sol structure. In order to get a rapid and complete reaction, an acid or a base catalyst may be used during the hydrolysis process.[20]

Aging represents the time between the formation of a gel and the removal of the solvents, which leads to a more cross-linked network because the gel is not static as long as the liquid remains in the matrix.[20, 30]

This method is commonly applied in material processing with the ability of forming pure and homogeneous products at relatively low temperature compared to other methods. However, the inherent disadvantages such as high cost of raw materials, large shrinkage of gel network, long processing time and the hazards of organic solutions may limit the further application of this approach.

1.4.1 Templating method

It is well-known that by introducing the templating-fabrication strategy, a variety of porous networks with a wide range of pore sizes, well-defined morphologies on controllable length scales and various chemical functionalities could be synthesised in order to match the needs of different applications.[31]

1.4.1.1 Hard templating method (nanocasting)

The hard template method is pretty much like the traditional casting but in nano scale. [32-38] Ordered porous materials (activated carbon, silica or anodic aluminium oxide) are

always used as templates, and through the process the pore structure of the template can be replicated into the products. Thus, a porous material with the same pore structure and morphology as the template, but with a different composition, could be synthesised by this method. Compared to the soft template method below, hard template, due to the rigidity of material, generally has a stronger restriction effect on controlling the pore matrix and size of the products. In 2006, Shi and co-workers successfully synthesized mesoporous SiC materials by using mesoporous silica as a hard template.[36] Commercial polycarbosilane (PCS) precursor is filled into the pore channels of the ordered silicate template and converted to SiC by high temperature calcination under nitrogen. These products had a surface area of 720 m^2/g, a pore volume of 0.8 cm^3/g and a narrow pore size distribution at a mean value of 3.5 nm.[36] More recently, a nanosized LiMn$_2$O$_4$ spinel was prepared using silica gel as hard template with sizes between 8 and 20 nm.[38] Mesoporous carbon was also synthesised by this approach using mesoporous SBA-16 silica having a pore size of 7.9 nm as the hard template.[39, 40]

1.4.1.2 Soft templating method

Dating back to 1970s, it is reported that the concept of soft templating was introduced in the synthesis of zeolites.[41] The zeolite framework structure is determined by the type and size of cations. As an extension of the single molecule templating, the aggregates such as micelles was used as template for the synthesis of mesoporous silica materials, which was published in Mobil's report In the early 1990's.[11] Cetyltrimethylammonium bromide (CTAB) was used as templates to prepare highly ordered M41S mesoporous silicate molecular sieves under hydrothermal conditions. After that, this kind of attractive material make the mesoporous materials play an important role in the material science.[12]

The synthesis of mesoporous materials is mainly focused on how to build mesopore channel. In soft template method, the pore arrangement is achieved by the cooperative assembly of amphiphilic surfactant molecules and guest species. The precursor and the soft template have a strong interaction to assemble the target molecules. Thus the constituents and properties of the organic templates are crucial for mesoporous material structures.[42]

Typically the various kinds of surfactants could be considered as templates in the soft template process. Most of the templates are composed of amphiphilic molecules with hydrophilic part (water loving) and hydrophobic part (water hating), which is shown in Figure 1.2.[43] Depending on the nature of the charge of the hydrophilic group, there are electropositive surfactant (quaternary amine salt), electronegative surfactant (long chain sulphate, long chain phosphate) and neutral surfactant (primary amine, non-ionic surfactant). Numerous papers have been published on the preparation of materials by using ionic or non-ionic surfactants. For instance, one of the most popular porous silicas, MCM-41, is synthesised by sol-gel method with ionic surfactant cetyltrimethylammonium bromide (CTAB). CTAB, shown in Figure 1.2, is a cationic surfactant with a positive ammonium group with which the negative silicate group can interact.[6] It transforms to hexagonal phase in the presence of silicate ions in aqueous environment.

nonpolar tail   polar head group
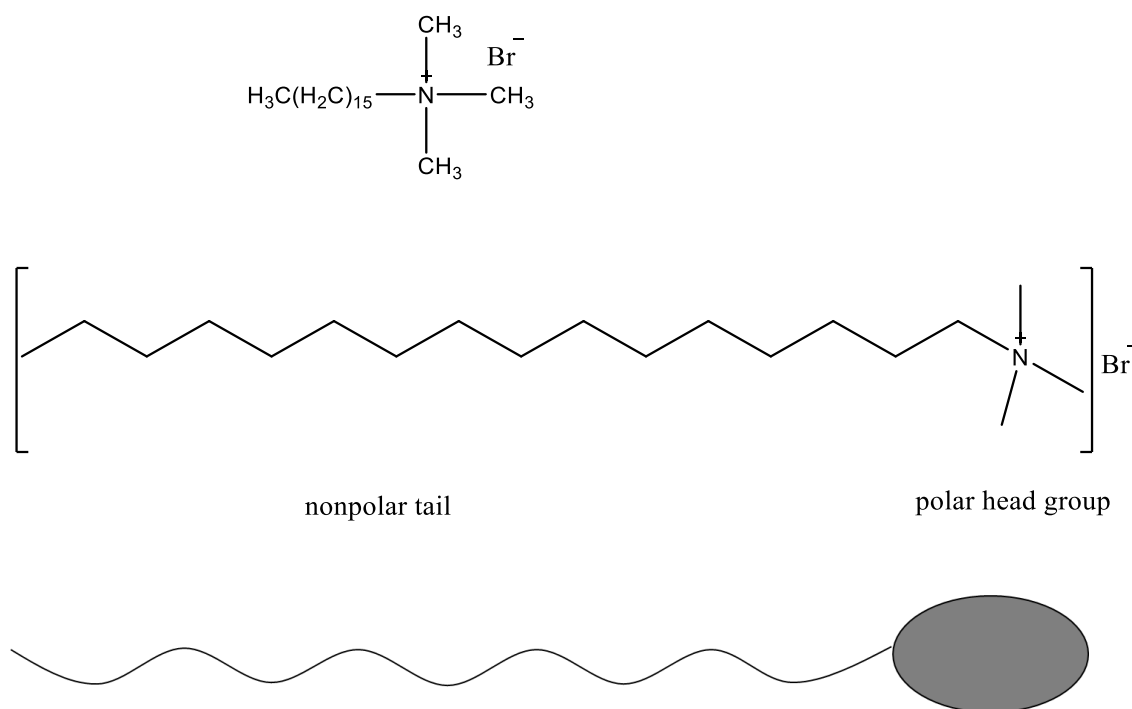
Figure 1.2 Chemical structure of CTAB

Owing to the excellent interfacial stabilization properties, low cost, and their non-toxic and biodegradable nature, non-ionic surfactants, including polyoxyethylene alkyl surfactant and triblock copolymers, have played a very important role in SBA series silica synthesis and other mesoporous metal oxide synthesis. The ordering properties of a

surfactant would affect the mesoporous phase formation dramatically; even change the synthetic route of the reaction. High molecular weight triblock copolymers are regarded as two functional group templates, such as hydrophilic group and hydrophobic group for the synthesis of SBA-15 silica.[14, 16] The characteristics of triblock copolymers are determined by the ratio of hydrophilic group and hydrophobic group, which are always considered as means of controlling the structure of the silica mesophase. Compared to other kinds of templates, hydrogen bond and relatively weak coordination bond are formed between the triblock copolymer and the inorganic oxide instead of strong electrostatic interactions.
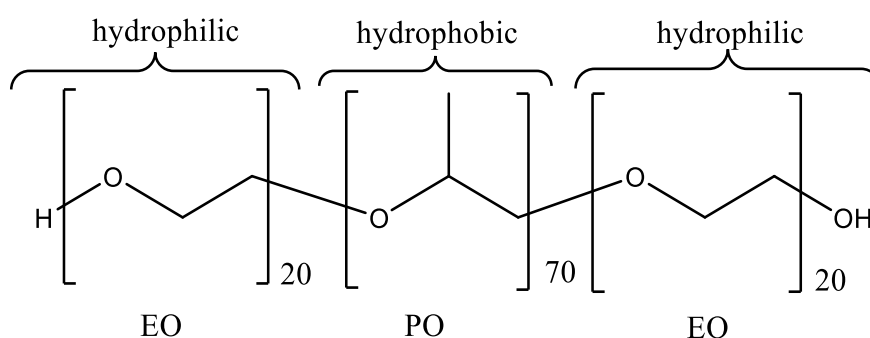
Figure 1.3 Structure of the organic template Pluronic P123

The silica sieve family SBA-15 was synthesized by using the non-ionic triblock copolymer Pluronic 123 (see Figure 1.3) as soft template and TEOS as silica source.[6] The micelles prepared by this triblock copolymer were considered as a hard PO core and soft EO shell (shown in Figure 1.4), which suggest that this kind of micelle has an excellent deformability. When template is dissolved in the solvent, the hydrophilic group may spread in the system and interact with cationic silica species during the synthesis. Thus as indicated, the hydrophilic group mainly affects the mesoporous structure and thickness of silica wall, while the hydrophobic group adjusts the pore size of the material.[44] It is worthwhile to note that the complementary micropores on the wall of SBA-15 are generated from partial occlusion of PO chains of the copolymers into the silica walls, which could be of great importance for catalysis and microreactors (shown in Figure 1.1).[45-47]
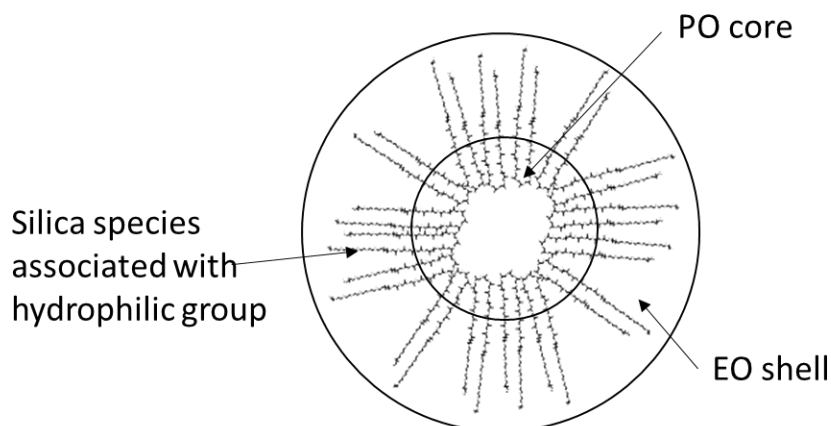
Figure 1.4 Coordinated Pluronic P123 micelles with EO shell and PO core

1.4.1.3 Template removal techniques in silica preparation

In the last few decades, a variety of methods have been investigated for template removal, such as organic solvent removal, [14, 48] calcination,[49-52] plasma treatment,[32-35, 53-55] supercritical fluid extraction,[56-58] and microwave digestion.[59] Washing with the reflux of organic solvents, such as ethanol, ethanol-H_2SO_4, ethanol-NaOH and ethanol-HCl, has been demonstrated. However, few of these methods are impressive in template removal efficiency. Another way is to perform high temperature calcination in air after organic solvent (ethanol) washing several times, which is regarded as the most efficient method for template removal because of the decomposition of organic polymeric template. However, a significant drawback was shown that during the high temperature calcination, the pores and the structures of the mesoporous materials can collapse.[56] Berube and co-workers reported the mechanisms of the organic template oxidation along the calcination process.[60] Under the oxidative atmosphere, the primary mesopores and the larger framework intrawall pores are first emptied with the production of volatile organic compounds by the oxidation of PEO chain below 200 °C, and this is followed by the oxidation of template from the micropores. The removal of template from primary mesopores is much slower under inert atmosphere than for calcination under air condition.

Besides, supercritical fluid, as a green solvent, has been reported to remove the organic template, with and without the co-solvent.[56-58] Although the $SCCO_2$ cannot remove the organic template completely, it is still regarded as a preferred solvent due to the better

solvating power and mild extraction conditions, and thus would not significantly affect mesoporous structures.[56] The researchers also demonstrated that liquid carbon dioxide (92.7%) removed the template better than $SCCO_2$ (50.7%) due to the higher solubility, even higher than traditional organic solvents, in removing hydrophilic parts. After the incorporation of methanol or water in to $SCCO_2$ as co-solvent, it is reported that the template removal efficiency has increased to 86.3% and 93.6%, respectively.[61]

The templates also were removed by various kinds of plasmas. The organic template was degraded in reactive plasmas (H_2 - N_2 plasma), as demonstrated by Pai and co-workers.[53] Some relevant works about hard template removal have been done by researchers in the last decades.[32-35, 54, 55] They removed the hard templates like activated carbon by oxidation in oxygen plasma at around 453 K, and also compared the calcination treatment and plasma treatment. The plasma treatment promoted the crystallization, which yielded the micropores in the sample, while the pore collapse and the rearrangement would appear in the calcined sample, resulting in a smaller BET surface area for the calcined sample.[54]

1.5 <u>Supercritical fluids</u>

A supercritical fluid (SCF) is defined as any substance at a temperature and pressure above its critical point, where a distinct liquid and gas phase does not exist, as shown in Figure 1.5.[62, 63] The critical point represents the highest temperature and pressure the substance can reach as both a liquid and gas. The triple point depicts the temperature and pressure at which three phases can coexist.
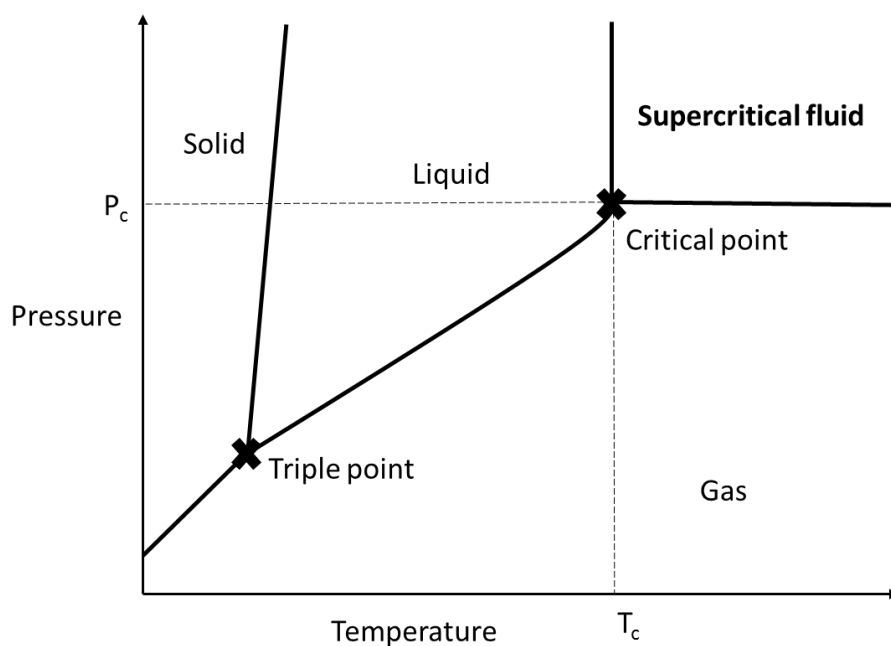
Figure 1.5 Phase diagram of supercritical fluid

The physical properties of SCF are generally between those of gases and liquids. SCFs tend to have much higher density than most gases, but closer to that of liquids, as shown in Table 1.3. In contrast, the viscosity of SCF is quite close to that of gas, leading to very good diffusion ability in the material preparation process. As a result, the SCF has a good solubility of solutes like liquid and excellent diffusion and movement in the process period like gas. Varying the pressure and temperature, the physical properties like density and viscosity could be tuned to more liquid or more gas like thus providing an enhanced selectivity of the solubility and polarity of SCF. Besides, Dobbs *et al.* proposed that solutes could be introduced into the supercritical fluid phase as co-solvents, which is referred to as an entrainer effect. The more solute in the SCF phase, the greater the solubilisation of substrates.[64]

Table 1.3 Comparisons among gas, liquid and supercritical fluid[3]

Parameter	Gas	Supercritical fluid	Liquid
Diffusion coefficient (cm²/s)	10^{-1}	$2*10^{-4}$	$5*10^{-6}$
Viscosity (g/cm³/s)	10^{-4}	$2*10^{-4}$	10^{-2}
Density (g/cm³)	10^{-3}	0.1-0.9 (CO_2 0.4)	1.0

Generally speaking, carbon dioxide is the most common supercritical fluid for extraction and supercritical fluid chromatography.[65] Carbon dioxide is relatively cheap, chemically stable, easily recyclable and widely available compared to other solvents. Avoiding the use of volatile organic compounds (VOCs), it is a safe solvent which is non-toxic and non-flammable. Carbon dioxide can be obtained in large quantities by fermentation and combustion.[3] There is no solvent residue in the extraction and separation process and it is easy to separate from the extracts by pressure release and evaporation instead of the further removal process. Besides, the physical state of carbon dioxide can be easily manipulated. As shown in Table 1.4, the critical temperature of carbon dioxide is 304.1 K and the critical pressure is 72.8 atm., which is facile to achieve, with critical density of 0.448 g/cm^3.[3] The relatively low critical temperature allows the supercritical CO_2 ($SCCO_2$) to be used near room temperature, making it especially suitable for the separation of heat-sensitive and chemically unstable natural products.[3, 66] Besides, in terms of carbon dioxide as a greenhouse gas, it is not generated but utilized corresponding with the purpose of green chemistry.

Table 1.4 Critical properties of various solvents[3]

Substance	Critical temperature (K)	Critical pressure (atm.)	Critical density (g/cm^3)
CHF_3	299.3	46.9	0.528
CH_4	190.5	41.4	0.162
C_2H_4	282.3	50.5	0.215
C_2H_6	305.2	48.2	0.203
CO_2	304.1	72.8	0.469
H_2O	647.1	218.3	0.348
CH_3CH_2OH	513.9	60.6	0.276
Xe	289.7	58	1.110

1.5.1 Mesoporous materials synthetic methods in SCFs

Supercritical fluids, a green and tuneable solvents, have been studied in materials science for many years as possible alternative to traditional organic solvents. A variety of preparation processes have also been proposed, either through physical pathways or chemical pathways.

1.5.1.1 Rapid expansion of supercritical solutions (RESS)

For physical pathways, rapid expansion of supercritical solutions (RESS) is always applied for synthesising fine powders.[67, 68] This process starts with the solutes dissolved in supercritical fluid. Then, the rapid depressurization of the solutions leads to a significant drop in the solubility of the solutes. Through adjusting the RESS parameters, various morphologies and particle sizes can be produced. The most restrictive condition for carrying out the RESS technique is that the target compound has to be soluble in SCF. If the supercritical solution is rapidly expanded into a liquid solution to initiate a chemical reaction rather than air or vacuum in RESS process, a modified process called chemical RESS process would happen. Numerous chemical reactions have a chance to be initiated in the supercritical fluid by this process.[69] For example, polymer-protected metal and semiconductor nanoparticles such as nickel, cobalt, iron and silver have been successfully prepared based on this method.[70-72]

1.5.1.2 Supercritical antisolvent precipitation (SAS)

Another physical technique referred to as supercritical antisolvent precipitation (SAS) takes advantage of the supercritical fluid as an antisolvent. Then a solution composed of a solute and a solvent is injected into the antisolvent. The solvent and the antisolvent are miscible, while the solute is non-soluble since the solution expands and the viscosity is reduced. As a result, the solute becomes supersaturated, leading to precipitation of products.[69]

1.5.1.3 Nanocasting process

In 1999, Fukushima and co-workers demonstrated a process which used activated carbon as hard template and supercritical fluid as solvent to prepare silica materials.[32] The possible mechanism was also proposed:[33] the silica precursor dissolved in SCF was

carried into the micropores of the hard template activated carbon. After the hydrolysis and condensation of silica species, the surface of the pores of activated carbon is covered with silica layers. Silica materials with pores corresponding to the sizes of activated carbon were obtained through the combustion to remove the carbon species.[33] Later in 2006, Fukushima tried to apply this technique to synthesise smaller pore size materials templated by microporous and mesoporous silicas with uniform pore size, FSM-16, and they also emphasised that the products could not be prepared if the liquid solvents were applied instead of SCF.[32-35] Moreover, a titania/silica mesoporous composite has been successfully prepared by nanocasting process using activated carbon as hard template in supercritical fluid.[37]

1.5.1.4 Supercritical microemulsions and micelle formation

Supercritical carbon dioxide is particularly attractive in chemical processes involving small organic and organometallic compounds (including metal alkoxides) because of its suitable solvation properties. Conversely, supercritical carbon dioxide is generally a poor solvent for organic polymers, which are always used as soft templates in preparation of silica materials.[53] Since these substrates exhibit low solubility in supercritical fluids limiting the application of SCF in the catalytic process, one approach to overcome this limitation is to employ amphiphilic surfactants with the formation of micelles in microemulsions. Such a system combines both the benefit of SCF and water.[73] More recently, many researchers studied the microemulsion reaction in supercritical fluids for synthesising hollow spheres. [49, 50, 62, 74]

Wang and co-workers investigated the interactions between particles and oil (CO_2) or water phases in microemulsions.[50] During the formation of emulsions, the contact angle (θ) which the particle makes with the interface is the relevant parameter in determining the emulsion type and stability (Figure 1.6). For hydrophilic particles, θ measured into the water phase is less than 90°, and the majority of the particle resides in the water phase. Consequently, the interface bends around the CO_2 phase resulting in a CO_2-in-water emulsion. While for hydrophobic particles, θ is generally greater than 90° and the particle resides more in CO_2 than in water, resulting in the formation of a water-in-CO_2 emulsion.[74] Based on such a method, they successfully prepared a silica hollow sphere

structure in CO_2-in-water microemulsion with the use of Pluronic 123 as template. In Figure 1.7 left, the triblock copolymers formed lamellar vesicles with the CO_2-philic PPO group (thick lines) shielded from aqueous phase while the hydrophilic (thin lines) PEO group protruded out from the vesicles. At the interface, the precursor is hydrolysed and solidified to form mesopores. However, in the CO_2-in-water system, CO_2 adsorbed into the polymer core of the surfactant micelles might cause the expansion of the pore size. They also proposed that the silica precursor such as TEOS had a high solubility in $SCCO_2$ because the silicone group is CO_2-philic.[49, 50]
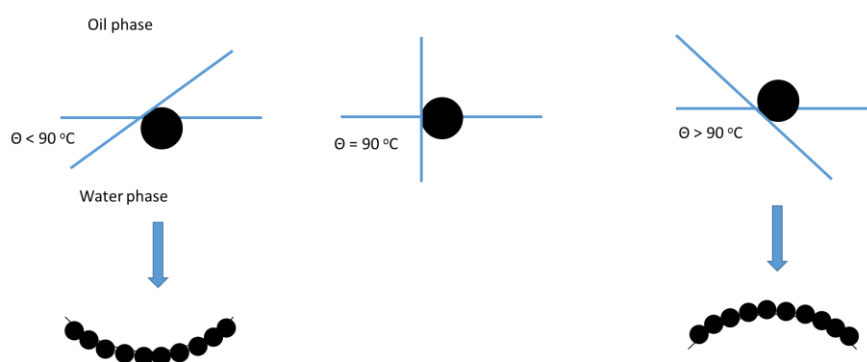
Figure 1.6 Schematic demonstrating the relationship between contact angles and position of a spherical particle at the planar oil/water phase[50]

Besides, a water-in-$SCCO_2$ microemulsion composed of amphiphilic surfactant has also been taken into consideration. As shown in Figure 1.7 right, the water partitions into the hydrophilic core forming thermodynamically stable water pools. This kind of nanoreactor can be used for synthesizing nanomaterials, and the particle size can be manipulated by varying the pressure and temperature.[69] As such, metallic copper nanomaterials were synthesized by the reduction of Cu ions by using sodium bis(2-ethylhexyl sulfosuccinate) (AOT) reverse micelles as template in SCF ethane.[75] Other metals (Ag, Rh and Pd), metal oxides (TiO_2 and TiO_2/SiO_2) and metal sulphides/halides (CdS, AgI, AgBr, AgCl and Ag_2S) have also been successfully synthesized in water-in-SCF microemulsions in a similar way to water-in-oil microemulsions.[62]
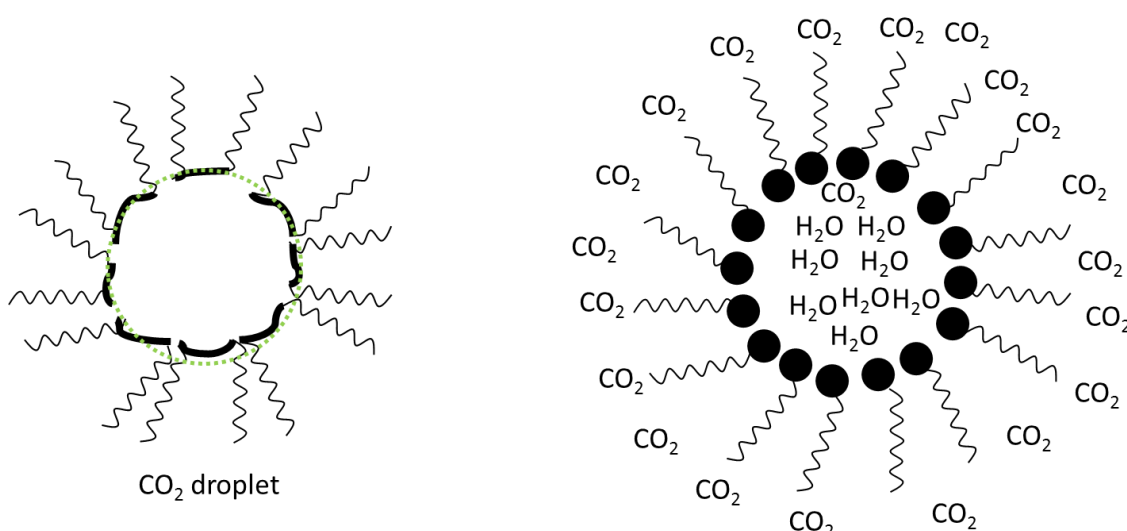
Figure 1.7 (Left) The CO_2 droplet in the CO_2-in-water emulsion[49], (Right) Water-in-SCCO$_2$ microemulsion[69]

In order to improve the solubility for high-molecular-weight or hydrophilic molecules, Han *et al.* proposed a new type of microemulsion with an ionic surfactant *N*-ethyl perfluorooctylsulfonamide (*N*-EtFOSA) as surfactant forming reverse micelles in supercritical CO_2 with ionic liquid, which are organic salts with melting points below 100 °C. Many ionic liquids can be considered as green solvents due to the non-toxic and non-volatile features. Gold spheres were successfully prepared from this method, in which N-EtFOSA acts as surfactant to form reverse micelles in supercritical CO_2 with 1,1,3,3-tetramethylguanidinium acetate (TMGA), 1,1,3,3-tetramethylguanidinium lactate (TMGL), or 1,1,3,3-tetramethylguanidinium trifluoroacetate (TMGT) domains.[76] Later in 2012, liquid polyethylene glycol (PEG) with a small molecular weight was used in the microemulsion for replacing ionic liquid. The phase behaviour of PEG/N-EtFOSA/CO_2 system was first observed at different conditions and gold nanoparticles were obtained by this method. HAuCl$_4$ used as precursor, was solubilized in the nanosized PEG domains and reduced by the surfactant head groups. The SAXS curves showed that the reverse micelles in the system were spherical-shaped. The size and property of the emulsion can be easily tuned by the amount of PEG added, the molecular weight of PEG or even the pressure of CO_2 in the new PEG/N-EtFOSA/CO_2 system. Besides, both the PEG and SCF are environmentally friendly solvents.[77]

In terms of the size and shape control of nanoparticles in microemulsions, the properties of template and the ability to tune the density of supercritical fluid by changes in pressure or temperature are useful and regular routes in influencing intermicellar exchange and maximum size by changing the inter particle attractions. Hollow silica and titanium-containing silica spheres could be fabricated at the interface of $SCCO_2$/CTAB aqueous solution.[78] Carbon dioxide was used here as both the solvent for the precursors and as the source of Brφnsted acid for catalysing the hydrolysis reaction. The diameter and the wall thickness of the hollow silica spheres could be simply tuned by adjusting the pressure of carbon dioxide and the concentration of CTAB. TEM images demonstrated that the hollow silica spheres with the diameter of 50 ±20 nm and the wall thickness of 16 ±4 nm when the pressure was at 9.78 MPa. The diameters were 160 ±70 nm and 400 ±70 nm, and the wall thicknesses were 30 ±15 nm and 65 ±15 nm when the pressure decreased to 8.69 MPa and 6.54 MPa, respectively. Besides, several researchers demonstrated that the addition of chloride ions (HCl) induced the formation of stable diamond shaped assemblies.[14, 62] That is also noteworthy to emphasise that the addition order of all the substances into the system has a significant effect.[62, 79] Eastoe *et al.* proposed in order to make the nanoparticle reactions take place in the same way to the normal liquid microemulsions, growth must be strongly dependent on intermicellar exchange and inter particle attraction. The microemulsions must be formulated in a pressure cell containing water, reactant and surfactant, and then CO_2 is pumped in with the single phase formed by increasing pressure and temperature, followed by the second reactant being injected into the vessel using a high pressure syringe pump.[62]

AOT (Aerosol OT, sodium bis(2-ethylhexyl sulfosuccinate)) is quite popular for building microemulsion with liquid/supercritical alkanes. Microemulsion phases formed in supercritical alkanes were shown to be strongly dependent on pressure.[80, 81] A variety of metal oxide nanoparticles have been synthesized by this route. Submicron spherical $Al(OH)_3$ particles were produced by precipitation of aqueous $Al(OH)_3$ solutions present in the cores of reverse micelles suspended in the supercritical propane continuous phase.[82] In 2000, Cason *et al.* successfully synthesized fine copper particles (<20 nm) by the reduction of copper ions from copper bis(2-ethylhexyl) sulfosuccinate, $Cu(AOT)_2$,

incorporated within AOT reverse micelles dispersed in supercritical ethane with small amounts of isooctane as co-solvent.[75] However, in supercritical carbon dioxide, AOT will not form stable microemulsions alone, thus a new stabilizer is necessary in the system. Fluorinated surfactants, such as perfluoropolyether-phosphate (PFPE-PO$_4$), F-pentanol or ammonium perfluoropolyether (PFPE-NH$_4$) must be employed in the system to stabilize the dispersions.[62] Another route to achieve this goal is to introduce special types of hydrocarbon-based surfactants or polymers, which was proven by Roberts and co-workers.[83] Through SAS-like process, WO$_3$ and MoO$_3$ have been obtained using an alkane mixture as continuous phase with AOT in 2010.[84] The phase behaviour of AOT/water/CO$_2$ system was investigated by Han and co-workers.[85] The viscosity analysis and X-ray scattering results indicated that carbon dioxide could induce a lamellar liquid crystal (L$_\alpha$) to micellar solution (L$_1$) transition by controlling the pressure (see Figure 1.8). L$_\alpha$ is the bilayer formation with hydrocarbon tail composing of inner part, while the ionic heads constitute the outer surface. Carbon dioxide could easily be inserted into the hydrophobic part, which gives rise to the structure change of the bilayer. Through controlling the system pressure, the L$_\alpha$ phase would be disrupted, and a thermodynamically stable L$_1$ phase subsequently forms. It is also reported that in the absence of CO$_2$, this transition could happen with the temperature over than 140 ^oC.
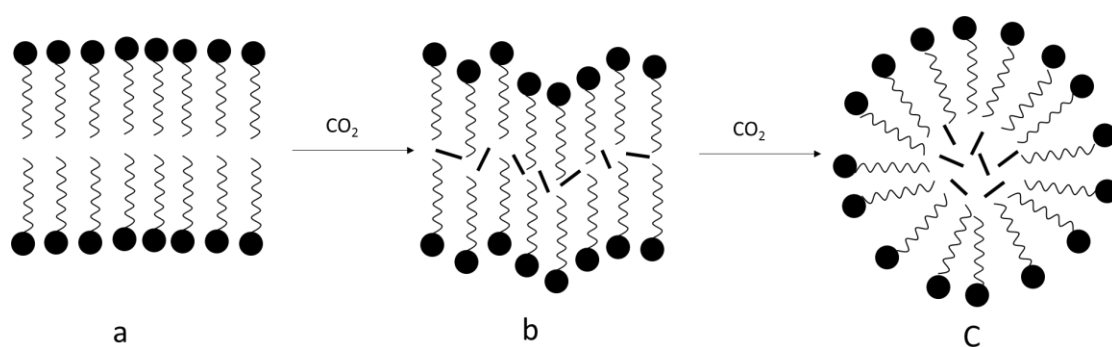
Figure 1.8 The mechanism for the L$_\alpha$ to L$_1$ transition. (a) Without CO$_2$, (b) low pressure, (c) higher pressure[85]

Various kinds of ionic surfactant have also been investigated for forming micelles in supercritical fluid. A homopolymer poly (1,1-dihydroperfluorooctylacrylate) (PFOA) dispersing polymerization in supercritical CO$_2$ was first reported,[86] owing to the low solubility parameters of fluorinated group which is close to that of carbon dioxide,

suggesting the miscibility of both. Besides, fluorinated group and carbon dioxide also exhibit the low (much less than zero) dipolarity/polarizability parameter, indicating both of them may be miscible.[87, 88] Later, diblock copolymers have been synthesized with CO_2-philic and CO_2-phobic portions for use in supercritical fluids to achieve spherical particles in quantitative yields.[86] TiO_2 was successfully synthesized by the controlled hydrolysis of titanium tetraisopropoxide (TTIP) in the presence of reverse micelles formed in carbon dioxide with the surfactants ammonium carboxylate perfluoropolyether ($PFPECOONH_4$) and poly (dimethyl amino ethyl methacrylate-block-1H,1H,2H,2H-perfluorooctyl methacrylate) (PDMAEMA-b-PFOMA). $PFPECOONH_4$ is an anionic type stabilizer for polar substances dispersed in carbon dioxide, while PDMAEMA-b-PFOMA is non-ionic when bulk water is not present. Stable micelles were formed at high molar ratio of water to surfactant headgroup.[79]

Recently polymers have been attractive in the micelle formation in SCF.[89, 90] Xu *et al.* described a simple and efficient route to prepare silica or titanium dioxide hollow spheres using cross-linked polystyrene (PS) microspheres as template through sol-gel process.[89] The cross-linked PS templates with robust properties in SCF were firstly prepared via emulsifier-free polymerization method by using ethylene glycol dimethacrylate or divinylbenzene as cross-linkers. With the assistance of $SCCO_2$, the silica precursor tetraethyl orthosilicate (TEOS) penetrated easily into the PS template.[89] In a recent publication, the hollow silica spheres with a variety of shell thickness ranging from 15 to 60 nm were successfully obtained, which revealed that the shell thicknesses of the hollow silica spheres could be finely tuned not only by adjusting the TEOS/PS ratio, which is the most frequently used method, but also by changing the pressure and aging time of the $SCCO_2$ treatment.[90]

Watkins *et al.* developed a method for producing long-range ordered mesoporous materials by blending templates (pluronic copolymers or brij surfactants) with the homopolymers such as poly (acrylic acid) (PAA) and poly (4-hydroxystyrene) (PHS). The advantages included higher degrees of order compared to the weakly segregated copolymer and the potential to produce smaller domains by inducing phase segregation in lower molecular weight copolymers. Moreover, they can adjust the homopolymer

concentration to control the properties of mesoporous silica films such as long-range order, total porosity and morphology.[53, 91] At the modest conditions, CO_2 sorption can increase the diffusivity of penetration in polymer films by several orders of magnitude, without disrupting the template order.[53]

It is worthwhile to note that one of the primary limitations for the ordered mesoporous silica synthesis in SCF is the micelle formation and formation mechanism in supercritical CO_2. The resultant morphology is profoundly dependent on the formation of micelle. Several researchers have investigated various kinds of templates forming micelles (or reverse micelles) in SCFs. A small angle neutron scattering (SANS) investigation of micelle formation of fluorocarbon-hydrocarbon block copolymers has been reported by Triolo and co-workers.[92] A PVAc-PFOA block copolymer composed of a CO_2-phobic polyvinylacetate (PVAc) and a CO_2-philic fluorinated octyl acrylate (PFOA) has been studied as a function of pressure at constant temperature. At high pressure, the copolymer is in a monomeric state with a random coil structure. However, on lowering the pressure, aggregates are formed with a structure similar to aqueous micelles with the hydrocarbon segments forming the core and the fluorocarbon segments forming the corona of the micelle. Comparison of the related data on the same polymer at different temperatures indicates that the transition is critically related to the density of the solvent.[93] Fremgen et $al.$ reported that high pressure NMR spectroscopy was applied to investigate the microemulsions of water in supercritical fluid with a family of anionic perfluoropolyether ammonium carboxylate ($C_{15}H_4F_{29}NO_6$, $C_{15}AS$) used as surfactant.[73] The NMR imaging technique demonstrated that the surfactants were uniformly dispersed throughout the CO_2 phase, even without mechanical stirring. The micelle formation provided evidence towards the production of thermodynamically stable microemulsions.[73] Salaniwal and co-workers focused on the research of self-assembly of reversed micelles in microemulsions by molecular simulation.[94] They studied the formation of stable, spherical reversed micelles by modelling the surfactant as dichain molecules of perfluoroalkane tail and alkane tail.[94] A much faster reverse micellization process in SCCO$_2$ than in liquid solvents was also proposed.[62, 94]

1.5.1.5 Modification technique in SCFs

Modification on porous materials using SCFs is also a promising additional route to generate porous particles. The deposition of metals, polymers and other functional groups in supercritical fluids has been investigated, offering several advantages of rapid mass transfer, easy separation and the ability of penetrating into even small micropores and mesopores.[95] Poliakoff and co-workers investigated the advantages of modification using the solvent in the supercritical fluid state compared to that in the liquid state. They found that the materials prepared in the supercritical fluid state had higher hydrothermal stability, suggesting the SCF led to better dispersion of the metal and the interactions between metal and silica surface might change.[96]

In the modification process, thin metal films cannot have the mechanical integrity to be freestanding and must be supported in some manner. Therefore, several papers reported that thin palladium films were produced on a porous alumina disk support in supercritical fluid, which is called chemical fluid deposition (CFD) process.[95] The previously mentioned chemical vapor deposition process is another effective route to synthesis nanoscale films that can be carried out in supercritical fluid system. The process route was that the precursor dissolved in a SCF formed an aerosol, and then a chemical reaction was carried out at the heated substrate to form thin film.[69]

A large amount of metal nanoparticles can be incorporated into mesoporous silicas with high surface area and narrow pore size in the supercritical fluid due to the low viscosity and high diffusivity of SCFs for rapid mass transport. Gold nanoparticles have been considered as uniform seeds for the dimensional ordered growth of silicon nanowires from supercritical fluid solution, and the growth orientation of the nanowires could be adjusted by changing the parameters of supercritical fluid.[95] Pd was successfully deposited into mesoporous silica SBA-15 using supercritical carbon dioxide. The support was impregnated with the precursor palladium hexafluoroacetylacetonate ($Pd(hfac)_2$) in $SCCO_2$ at quite mild conditions (40 ^{o}C, 85 bar), followed by the reduction either by a H_2 in CO_2 mixture or after depressurization in pure H_2.[97] Several other types of metals ions such as Al, Ti, V, B, Mn, Sn and Ga have also been modified with different kinds of silica

supports (MCM-41, MCM-48, SBA-15 and etc.) to obtain materials for various potential applications.[6]

1.6 <u>Microwave technique and bio-oil</u>

Microwaves belong to the portion of the electromagnetic spectrum with wavelengths from 1 mm to 1 m with corresponding frequencies between 100 MHz and 300 GHz (shown in Figure 1.9). Within this portion of electromagnetic spectrum there are frequencies that are used for cellular phones, radar, and television satellite communications. For microwave heating in industrial, scientific, and medical fields, two frequencies (0.915 GHz and 2.45 GHz) are reserved and used by the Federal Communications Commission.[98] Typically, the microwave source, which is a vacuum tube allowing for a high power and frequency, generates the electromagnetic radiation. The transmission lines then deliver the electromagnetic energy to the applicator, where this energy is either adsorbed or reflected by the material. As the energy is transferred to the materials by interaction of the electromagnetic fields at the molecular level, the dielectric properties of the materials are of primary importance in microwave heating. Compared to conventional heating, microwave heating could have a superior ability of coupling energy directly to the material, allowing for more rapid, uniform heating, decreased processing time and enhanced material property.[98] As an emerging technique, further developments of microwave heating such as the fundamental data regarding the dielectric properties of materials, the design of microwave heating equipment for industrial scale and the detailed knowledge of microwave processing are still needed.[99]
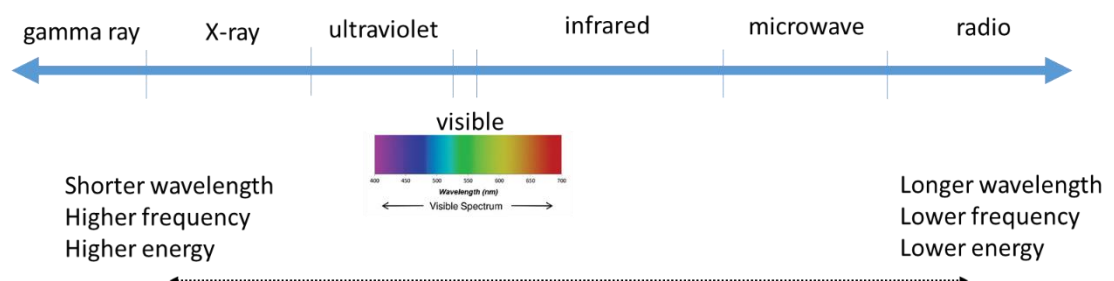
Figure 1.9 Electromagnetic spectrum

1.6.1 Microwave pyrolysis

Pyrolysis is essentially a thermal decomposition process of organic materials in the absence of air or oxygen. The reaction happens at high temperatures and varies depending on the materials. It should be noted that gasification is a different process than pyrolysis as controlled amounts of oxygen are introduced during the gasification. Conventional pyrolysis, also named slow pyrolysis, has developed for thousands of years and is mainly used for the production of charcoal.[100] Keep biorefinery concept in mind, pyrolysis has become an important method for converting biomass into oil as major product. Microwave pyrolysis has a number of advantages compared to the conventional heating methods such as furnaces. This technique is referred to as fast pyrolysis owing to the slower processing time. The energy generated by microwave could penetrate the surface of the materials and come in contact with the core of the material, while the conventional could only heat the surface of the materials prior to conducting heat to inside. Therefore, utilizing microwave technique in pyrolysis processing could obtain a time saving, high efficiency, and controllable process,[101] which generates a series of useful final products, including bio-oil, syngas and bio-char. The solid char could be used as a solid fuel instead of conventional charcoal. The gases have medium to high calorific values and contain sufficient energy to supply the energy requirements of a pyrolysis plant.[102] The bio-oil is formed during the pyrolysis and considered as an important product containing a variety of components.

1.6.2 Bio-oil introduction

Bio-oil is typically a dark brown, highly viscous mixture with acrid and smoky smell, and it can be made from a variety of forest and agricultural biomass wastes, such as rice straw, bagasse, wheat straw and wood.[100] The yield of bio-oil is frequently in the range of 60 – 95 wt. %, depending on the composition of the biomass. There are numerous oxygenated organic compounds, including acids, alcohols, aldehydes, ketones, phenols, ethers, esters, sugars, furans and multifunctional compounds. The results show around 300 organic components were present in bio-oils, but most of the compounds are in low concentrations.[103] Most of oligomeric species are derived from lignin and cellulose, and the molecular weight varies from several hundred to 5000 or more. Due to the high

amounts of volatile acids existing in bio-oil, its pH is relatively low (typically 2 - 3).[104] In Zhu's report, thermogravimetric analysis (TGA) shows two stages of bio-oil mass loss in inert atmospheres: the evaporation of light volatiles and the decomposition of unstable compounds at higher temperature. For the bio-oil combustion in air, there is one more stage of combustion of chars, where the oxygen participates.[103]

Until now, the bio-oil can be used both as an energy source instead of the conventional fossil fuel and a feedstock for chemical production because of the large number of components. It is well documented that bio-oils could be potentially used in engines, turbines and boilers, however, some limitations were also noted due to the high financial costs.[105] A number of techniques including column separation,[106-110] solvent extraction,[111-115], phase separation[116] and molecular distillation[117] have been applied for fractionating and purifying the bio-oil in order to obtain valuable fractions, which are summarised in Table 1.5. The valuable components such as phenols[108] and phthalate esters[110]were successfully identified or separated.

Table 1.5 Examples of bio-oil fractionation methods

Method name	Solvent or chemical used	Mode of separation	Reference(s)
fractionation of vacuum-pyrolyzed softwood bark derived bio-oil	pentane, benzene, dichloromethane, ethyl acetate, methanol	column separation	Roy[106, 107]
fractionation of vacuum-pyrolyzed birchwood-derived bio-oils	pentane, toluene, water, ethyl acetate	column separation	Roy[108]
fractionation of bio-oil derived from rice husk	methanol, ethyl acetate, acetone, cyclohexane	column separation	Sheng[109]
separation of bio-oil from rice husk	ethyl acetate, ethanol	column separation	Jiang[110]
fractionation of biomass-derived flash pyrolysis oils	diethyl ether	solvent extraction	Sipila[111]
fractionation of bio-oil from waste office paper	ethyl acetate	solvent extraction	Matharu[112]
bio-oil fractionation method	hexane, dichloromethane, diethyl ether	solvent extraction	Oasmaa[113-115]
phase separation of bio-oil from rise husk	various inorganic salts, including $LiCl$, $CaCl_2$, $FeCl_3$, $(NH_4)_2SO_4$, K_2CO_3 and $Fe(NO_3)_3$	phase separation	Song[116]
fractionation of bio-oil from sawdust	/	molecular distillation	Wang[117]

1.7 <u>Techniques used in material characterization</u>

A variety of analytical techniques used in this project are briefly described below.

1.7.1 Porosity and porosimetry

Porosity refers to the pore space in a material.[118, 119] An open pore is a cavity or channel that communicates with the surface of the material; these can be of any shape, including the classical models: ink-bottle pore and cylindrical, open ended pore. A closed pore is inside the material without a connection to the exterior of the material. As discussed above, pores can be classified into three groups according to the size: micropores, mesopores and macropores. Pore diameter ranges of 0.3 – 300 nm can be determined by the nitrogen adsorption approach, while mercury porosimetry determines a wider pore diameter range up to 200 μm, depending upon the equipment.[118]

1.7.1.1 N$_2$-adsorption analysis method

Nitrogen at 77 K is considered to be a standard adsorbate for surface area and pore size analysis.[120] Three parameters can be analysed by porosimetry, which are specific surface area, pore size distribution and pore volume. They are sufficient to characterize the physical properties of the silica material. The measured pore diameter typically ranges from 0.3 nm to 300 nm. However, one drawback is that the analysis time for a single sample could be hours.[118]

The most widespread method for determining the specific surface area is the Brunauer-Emmett-Teller (BET) method,[121] which is based on a kinetic model of the adsorption process by Langmuir,[122] assuming that the surface of the solid is an array of uniform adsorption sites. The BET equation is used in the multilayer-adsorption region of the adsorption isotherm:

$$\frac{p}{V(p_o - p)} = \frac{1}{V_m c} + \frac{c-1}{V_m c}\frac{p}{p_o}$$

where V is volume adsorbed, V_m is volume of monolayer, p is sample pressure, p_o is saturation pressure and c constant related to the enthalpy of adsorption (BET

constant).[118] The specific surface area (S_{BET}) is then calculated from V_m by the following equation:

$$S_{BET} = \frac{V_m n_a a_m}{m V_L}$$

Where n_a is Avogadro's number (6.02 * 10^{23} molecules/mol), a_m is the cross sectional area occupied by each nitrogen molecule (0.162 nm^2), m is the weight of the sample and V_L is the molar volume of nitrogen gas (22414 cm^3 at standard temperature and pressure).[118]

According to the BET theory, c value gives an indication of the magnitude of the adsorbent-adsorbate interaction energy. In nitrogen adsorption analysis method, c is the relative magnitude of the interaction energy between nitrogen and the surface compared to the energy of interaction of a nitrogen molecule with liquid nitrogen, meaning that a high value of c indicates a strong preference for monolayer surface adsorption over multilayer. In terms of the isotherm plot, a high value of c indicates a sharp knee, thus making it possible to obtain the uptake at Point B (see Figure 1.10) by visual inspection so that the c at this point satisfies the BET equation. If c is low than 20, Point B could not be identified as a single point, resulting in an unreliable S_{BET} value.[119]

The calculation of pore size distribution of a material is based on the Kelvin equation.[123] The volume pore size distribution could be determined according to the Barrett, Joyner and Halenda (BJH) model,[124] which is based on the calculation methods for cylindrical pores. The modified Kelvin equation

$$\ln \frac{p}{p_o} = -\frac{2\gamma V_L}{rRT} \cos\theta$$

is then used to calculate the relative pressure of nitrogen in equilibrium with a porous solid. In this equation, p is the equilibrium vapour pressure of a liquid in a pore of radius r, p_o is the equilibrium pressure of the same liquid on a surface, γ is the surface tension of the liquid, VL is the molar volume of the liquid, Θ is the contact angle between the liquid and pore wall, R is the gas constant and T is the absolute temperature.[118]

1.7.1.2 Classification of isotherm plots

The sorption isotherm is the amount of adsorbate on the adsorbent as a function of its pressure or concentration at constant temperature. Measurements are made at temperatures at which the adsorbate is in the liquid state.[20] There are six major types (Figure 1.10) of isotherm.

Type I corresponds to a monolayer adsorption and can be explained using the Langmuir adsorption isotherm, which indicates a non-porous or microporous material is formed (e.g. activated carbons, molecular sieve zeolites and certain porous oxides).[119, 125] Starting at relatively low pressure, a rapid increase in adsorption is observed. Adsorption proceeds until all pores are filled with nitrogen, reflecting a constant adsorption. The adsorption and desorption branches are identical, so no hysteresis is observed.[20]

Type II corresponds to the case when first, a monolayer is formed, and then a multimolecular layer predominantly develops, which is formed by a nonporous or macroporous material. Point B is often taken to indicate the stage at which monolayer coverage is complete and the multimolecular layer adsorption starts.[119]

The Type III curve does not happen frequently and there is a continual curve which indicates that Point B could not be identified properly so that the monolayer formation is missing.

Type IV is quite similar to Type II at lower pressure, while the curve increases more sharply at medium pressure. The characteristic feature of this type is the hysteresis loop, which will be discussed in next section. The low pressure part is attributed to monolayer-multilayer adsorption, which is in agreement to that of Type II.[119] The horizontal branch near the saturation pressure ($p/p_0 = 1$) indicates that all pores are filled with liquid adsorbate.[20] Type IV isotherms are exhibited by mesoporous materials.[119]

Type V is not common, showing phenomenon of capillary condensation, which indicates that a hysteresis loop probably appears.[119]

The Type VI isotherm depicts stepwise multilayer adsorption on a uniform non-porous structure. The height of the step represents the monolayer capacity for each adsorbed layer.[119]
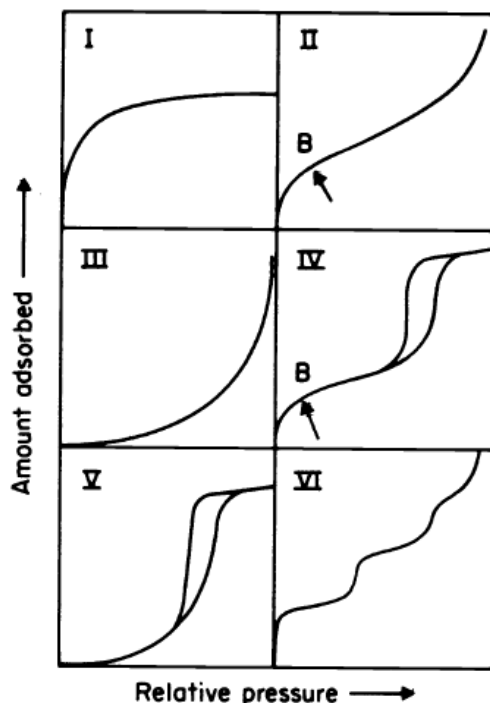
Figure 1.10 Six types of isotherms according to the classification of Brunauer, Emmett and Teller[119]

1.7.1.3 Hysteresis loop

A hysteresis loop is the unique feature for mesoporous materials.[120] The model of nitrogen filling in pores might be spherical, cylindrical or slit type, decided by the materials characteristics. During the analysis of mesoporous material, a multilayer of adsorbate can be formed, with increasing relative pressures. The amount absorbed is always greater along the desorption branch compared to the adsorption branch. As a consequence, desorption branch would not follow the adsorption branch, thus causing the hysteresis loop.[20] This typical pattern for mesoporous solids is explained by capillary condensation of adsorbate in the pores, resulting in an increase of adsorbate during the adsorption run, and a consequent retardation during desorption. Depending on the properties of adsorbate and adsorbent temperature, capillary condensation always takes place above $p/p_0 = 0.40 - 0.50$ for nitrogen adsorption.[20] Capillary condensation often

introduces a considerable complication for pore size analysis, especially for mesopore analysis.[120]
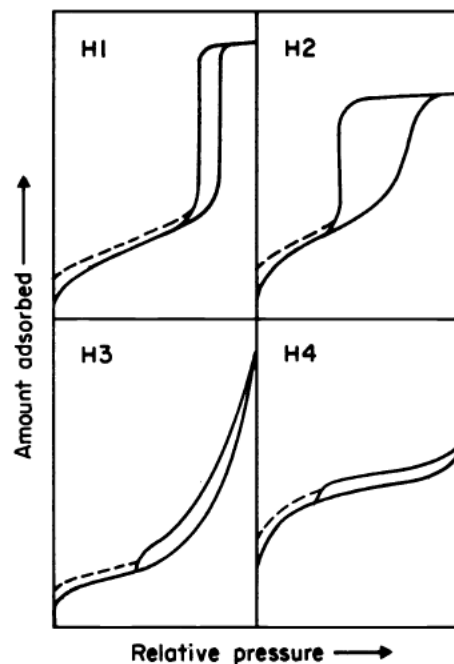
Figure 1.11 Types of hysteresis loops[119]

Correlated with the texture of the adsorbent, such hysteresis hoops may exhibit several types, illustrated in Figure 1.11. Type H1 shows two vertical and parallel branches over an appreciable range of gas uptake, which are often associated with porous materials having uniform size and shape (cylindrical-like pore). Many porous materials tend to give Type H2 loops, which is regarded as ink-bottle model. In such systems, the distribution of pore size and shape is not well-defined. Type H3 and H4 loop doesn't exhibit any limiting adsorption at high p/p_0, which is attributed to the aggregates of plate-like particles giving rise to slit-shaped pores. Besides, the Type I character of the adsorption branch in Type H4 at low p/p_0 is indicative of microporsity.[119]

In some cases, low pressure hysteresis (indicated by the dash lines in Figure 1.11) may be observed especially for those containing micropores. This is possibly associated with the swelling of a non-rigid porous material or with the irreversible uptake of molecules in pores or with an irreversible chemical interaction of the adsorbate with the adsorbent.[119]

1.7.2 X-ray techniques

X-rays are electromagnetic waves with a much shorter wavelength than visible light, typically in the range of 0.01 to 10 nm. They are generally generated by bombarding a metal with high-energy electrons.[126]

1.7.2.1 X-ray diffraction (XRD)

The phenomenon of diffraction is the interference caused by an object in the path of waves and the pattern of varying intensity that is called the diffraction pattern. X-ray diffraction is based on constructive interference of monochromatic X-rays and a crystalline sample. The interaction of the incident rays with the sample produces constructive interference when the conditions satisfy Bragg's Law:

$$n\lambda=2d\sin\theta$$

where n is the order of reflection, λ is the wavelength of the incident X-rays, d is the interplanar spacing of the crystal and θ is the angle of incidence. This law relates the wavelength of electromagnetic radiation to the diffraction angle and the lattice spacing in a crystalline sample. By scanning the sample through a range of angles, all diffraction directions of the lattice should be attained. The characteristic X-ray pattern are produced by detecting these reflections.[127]

XRD is a useful non-destructive technique which could provide information on phase identification of a crystalline material through comparing data with known standards in the JCPDS file. The structural information such as lattice parameter, grain size, d spacing could be obtained from XRD results based on Bragg equation. By combining the results of other techniques like porosimetry, the thickness of the pore wall of porous materials could be possibly calculated.

1.7.2.2 X-ray photoemission spectroscopy (XPS)

XPS is a non-destructive surface analysis technique giving information on the elemental composition of a material's surface, based on one of the fundamental interactions of photons with matter (the photoelectric effect).[20, 128] All the elements from the periodic

table except hydrogen and helium can be detected in XPS spectra. Although the photon emitted from the X-ray tube could penetrate into a relatively large depth from the surface of sample, the analysed photoelectrons come from the topmost layers only due to the inelastic collisions of the photoelectrons from deep layers. Hence, the analysed depth of the solid material is typically ~10 nm for XPS.[20] Generally, the chemical and physical properties of the surface and its bulk material are quite different, because the atom in the bulk of the material is surrounded on all sides by atoms, while the atom on the surface is not surrounded all the sides. This reduces the coordinative stabilisation of the surface atom and make it more active than an atom in the bulk material, which suggests that the surface area is most involved in catalysis.[20]

XPS is also a powerful technique for providing information on molecular environment of the elements on the surface such as oxidation state. The photoelectron kinetic energy depends on the chemical environment of atom. When the atom is bonded with another one, some charge is transferred to a more electronegative or from a more electropositive atom, the electron kinetic energy will be lower or higher, respectively. By monitoring this chemical shift, the molecular environment of the sample could be attained which is especially important in the composite material analysis.[128]

1.7.3 Fourier transform infrared spectroscopy (FTIR)

Infrared spectroscopy has been developed for materials analysis over seventy years. Basically, in infrared spectroscopy, IR radiation is passed through a sample. Some of it is absorbed by the sample whereas some is transmitted through the sample. Thus the resulting infrared spectrum represents a fingerprint of a sample with absorption peaks which correspond to the frequencies of vibrations between the bonds of the atoms making up the material.[20] A molecule could exhibit two distinct types of molecular vibrations: stretching and bending. Since each different material is a unique combination of atoms, therefore their corresponding spectra are never exactly same from one materials to another, even if the overall compositions are similar.

In order to overcome the original slow continuous wave scanning process, an interferometer was employed to measure all the infrared frequencies simultaneously

rather than individually. The interferometer produces a unique type of signal which has all of the infrared frequencies, but cannot be interpreted directly. Thus the Fourier transformation is employed for transforming the signal from intensity vs. time to a frequency spectrum.[20] FTIR now has become a useful technique for qualitatively identifying unknown materials or quantitatively determining the amount of components in a sample.

1.7.3.1 Diffuse reflectance infrared Fourier transform (DRIFT)

As FTIR spectroscopy is not suitable for some solid and opaque samples such as silicas, another technique has developed. An often used technique called DRIFT consists of pressing approximately 2-5 % of the samples with KBr into a self-supporting disk at 10 tons. However, this technique is not only time consuming, tricky to carry out consistently and destructive, also a lot of information could possibly be lost due to the collapse of the surface structure and the interaction of the hygroscopic KBr with the sample.[20]

1.7.4 Electron microscopy techniques

An electron microscope is an optical device for producing high resolution images of samples by a beam of electrons, which is due to the focussing ability and extremely short wavelength of electron beams. Transmission electron microscopy (TEM) is based on transmitted electrons, while scanning electron microscopy (SEM) deals with various signals scattered from the surface of the sample.[129] The image of transmission electron microscopy is formed by transmitted electrons. Since the electron image could not be viewed directly by the eye, the image is projected onto a fluorescent screen. Denser areas of atoms and heavier elements appear darker due to increased scattering of electrons. The sample for TEM should be thin enough to allow electrons to penetrate through the sample because even atoms with a low atomic number scatter electrons significantly. TEM images are two-dimensional and could measure the particle size of the sample, the crystallization and the atomic arrangement from the image. The image of SEM is formed in a cathode ray tube synchronized with an electron probe scanning the surface of sample. The electron interact with atoms of the sample, producing the signals including secondary electrons, backscattered electrons, characteristic X-rays and photons of various energies. SEM images are three-dimensional and are used to

characterize the sample's surface morphology and its composition (when equipped with Energy-dispersive X-ray spectroscopy). In terms of magnification and resolution, the image of SEM could not achieve as high as that of TEM.

1.7.5 Nuclear magnetic resonance spectroscopy (NMR)

NMR is a powerful technique used to obtain physical, chemical, electronic and structural information about molecules due to the chemical shift on the resonant frequencies of the nuclei present in the sample. Not all nuclei can be seen by NMR spectroscopy; this can be predicted from the nuclear spin quantum number I. The atoms such as ^{12}C and ^{16}O have I = 0 and are magnetically inactive, thus could not be analysed by NMR. The most common nuclei studied including ^{1}H, ^{13}C, ^{19}F, ^{29}Si and ^{31}P are I = 1/2, which adopt either of 2I+1 possible orientations during the spinning.[130] In the absence of an external magnetic field, these orientations are of equal energy. When an external magnetic field is applied, the energy levels split, which is referred to as nuclear Zeeman splitting. A variable radiofrequency is then applied to cause the nuclear transitions between different levels. The energy that is given out is detected and can then be interpreted to obtain spectra. The presence of the surrounding electrons and the bonding of the atoms have a significant effect on the resonance frequency, leading to a chemical shift of the resonance frequency.[127] Typically the peak at zero ppm of the NMR spectra is attributed to the hydrogen atoms in tetramethylsilane (TMS) because 12 hydrogen atoms of TMS all presented in the same environment give rise to a strong single peak.

1.7.6 Thermogravimetric analysis (TGA)

TGA studies the variation in weight of a sample as a function of time or temperature during which the sample is subjected to a controlled heat treatment in a controlled atmosphere. TGA is widely used to characterize materials.[131]

Several TGA-based techniques are used to analyse the gas products, which is called evolved gas analysis (EGA). TG-FT-IR, which could be achieved by a thermogravimetric analyser combined with an Infrared Spectrometer, is a common TG-EGA system. When

the samples are heated in TG equipment, the gases released from sample are transferred to an IR cell, where the components could be identified.

1.8 Summary of project objectives

In this project, the main objectives are the following:

Development of a porous silica preparation method by using SCF as solvent

The acid choice of SBA-15 preparation in aqueous phase, and transferring the knowledge to develop a SCF-based route to structured silicas. The resultant silica material possesses comparable BET surface areas, pore volumes and pore sizes with vesicular structure.

Green route to the synthesis of carbon silica composite

Preparation of a novel carbon silica composite by modify a carbonaceous layer on the surface of a variety types of mesoporous silica from bio-oil and optimise the conditions such as bio-oil/silica ratio, carbonization temperature, heating rate and holding time. The resultant CSC materials possess not only considerable specific BET surface area, narrow pore size distribution and ordered meosporous structure, but also tuneable surface properties by adjusting the carbonization temperature.

Catalytic performance of CSC based catalyst in the Heck reaction

Utilize the Pd modified carbon silica composite as catalyst to catalyse coupling reaction such as Heck reaction in alternative solvent - cyclic carbonate. The results demonstrated an excellent catalytic activity and recoverability of the Pd-CSC catalysts.

Preparation of carbon materials through the etching process of CSCs

The synthesis of rod-like carbon and tubular-like carbon materials by the silica removal from CSCs is investigated.

Chapter 2   Mesoporous silica synthesis in supercritical fluid

2.1 <u>Background</u>

As described in Chapter 1, the SBA family silica was firstly synthesised in acidic condition in 1998,[14] and SBA-15 is prepared using the non-ionic triblock copolymer surfactant Pluronic P123, and possesses thick pore walls and excellent thermal stability. Poly block copolymers are also considered to possess mesostructural ordering properties, amphiphilic character, low cost commercial availability and biodegradability. SBA-15 silica possesses hexagonal arrays of pores with uniform pore diameters in a range of 5 - 30 nm, large surface area ranging from 600 to 1000 m^2/g, and high pore volume (0.6 - 1.2 cm^3/g), properties which can be varied *via* tuning the reaction temperature.[16] Owing to the uniform mesopores, high specific surface area, good thermal and chemical stability, SBA-15 could be specifically used as the solid support for heterogeneous catalysts. For instance, SBA-15 silica incorporating Al^{3+}, Ti^{4+} or Zr^{4+} could be used as support for hydrodesulfurization reaction due to the high catalyst acidity and the enhanced active phase dispersion.[15] A gold modified SBA-15 catalyst prepared via a solution technique was used for carbon monoxide oxidation at room temperature.[27] SBA-15 has also been functionalized by the deposition of some other metal cations such as Eu,[22] Zn,[21] and Ni[26] for specific applications. Moreover, it is reported that amine groups could be used for functionalization of SBA-15 and the resultant materials showed a high adsorption capacity for CO_2 capture.[132-134]

$$Si(OEt)_4 \ + \ nH_3O^+ \ \xrightarrow[pH<2]{Hydrolysis} \ Si(OEt)_{4-n}(OH_2^+)_n \ + \ nEtOH \qquad\qquad 1$$

$$REO_m \ + \ yHX \ \xrightarrow{H_2O} \ REO_{m-y}[(EO)H_3O^+]_y...yX^- \qquad\qquad 2$$
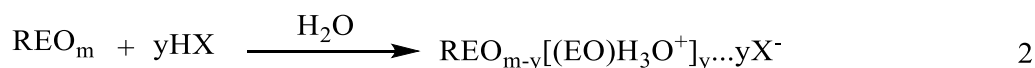
Equation 2.1 Mechanism for synthesis of silica materials

Over the last 30 years, there has been extensive research on the study of mechanism of formation of mesoporous silicas.[12, 14, 135] Stucky has proposed a popular formation mechanism of mesoporous silica in the acidic condition named as cooperative formation mechanism (shown in Figure 2.1).[14] First, alkoxysilane species are hydrolyzed by water (Equation 2.1-1). This is then followed by partial oligomerization of the monomeric Si

species. The EO moieties of the surfactant in strong acid media associate with hydronium ions. The equation was shown in Equation 2.1, where R = poly(propylene oxide) and X stands for the anions of the acid. The EO units and cationic silica are then assembled by a combination of electrostatic, hydrogen bonding and van der Waals interactions, which is mediated by the negatively charged chloride ions in the form of $REO_{m-y}[(EO)H_3O^+]y...yX^-...I^+$. This form is designated as $(S^0H^+)(X^-I^+)$.[16, 136] It is believed that polymerization and cross-link effect of the silica species at the interface changes the charge density of the inorganic layers, thus influencing the 3D arrangement of the surfactants.[12] Thereby, further condensation of the silica species and organization of the surfactant and inorganic species both result in formation of the lowest energy silica - surfactant mesophase structure such as hexagonal, cubic or lamellar. The detailed micelle formation of P123 is described in Chapter 1.
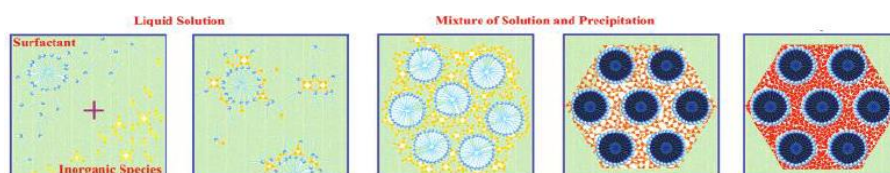
Figure 2.1 Synthetic strategy of SBA-15 materials[12]

It is well-known that the critical micelle concentration (CMC) value of the surfactant is an important criterion to form a well-ordered mesoporous structure. A detailed investigation of the correlation between CMC and the structure of the resultant material was carried out by Zhao.[44] A surfactant with a small CMC value (< 20 mg/L for PEO-type block copolymer) will template ordered silica mesoporous materials with certain structures, such as hexagonal, cubic and vesicle, while a surfactant with a large CMC values (> 300 mg/L) will give rise to disordered mesoporous structures. The surfactant that have middle range CMC value could possibly produce ordered structures by increasing the temperature[16] or addition of inorganic salts[137] to decrease its CMC value.

Generally speaking, SBA-15 can be synthesized over a relatively narrow range of PEO-PPO-PEO copolymer concentrations (2 - 6 wt.%). Higher concentrations of the block copolymer species form only silica gel or yield no precipitation of silica product; at lower concentrations, only amorphous silica is obtained.[14] A reaction temperature of 35 - 80

^{o}C is ideal for SBA-15 synthesis. At room temperature, only amorphous silica or poorly ordered products result, while higher temperatures (>80 ^{o}C) yield silica gel.[16] Tetraethoxysilane (TEOS), tetramethoxysilane (TMOS), and tetrapropoxysilane (TPOS) are typical sources of silica for the preparation of SBA-15. In spite of utilization of TEOS leading to a slower condensation rate than TMOS, [138, 139] Witte *et al.* reported that there are minor differences of the properties between the samples synthesised from TEOS and TMOS.[140]

Dating back to 1997, Morris and Weigel summarised the non-aqueous synthesis of molecular sieves in order to design new molecular sieves either with new architectures or with different chemical properties.[2] SCFs can dissolve solid compound in the same way as a liquid solvent and have low viscosities and high diffusivities like gases. Their physicochemical properties can be tuned continuously between gas-like and liquid-like by adjusting the pressure or the temperature of the system. Owing to these unique properties, SCFs has been attractive in materials chemistry.[69, 95, 141] Hence, the tuneable physical properties of supercritical fluids allow for the preparation of novel mesoporous silica with specific morphology. The properties and the corresponding advantages of utilization of SCFs for material synthesis are listed in Table 2.1.

Table 2.1 The properties and the corresponding advantages of utilization of SCFs for material synthesis

Properties of SCFs	Corresponding advantages of SCFs in materials chemistry
High diffusivity and low viscosity	Allow high uniformity and penetration into small areas
Tunable solvent strength	Rapid separation of solute
CO_2 is environmentally benign	Green alternative solvent
Low boiling point of CO_2	A energy effective drying step
Low surface tensions	A versatile wetting agent

There are several comprehensive reviews existing in the literature on synthesis of materials in the presence of supercritical fluids.[35, 69, 95, 141, 142] It is important to note that

the Mokaya group developed a silica preparation method in SCF by using HCl as acid and PEO-PPO-PEO triblock copolymers as template.[49, 50] The pore size and the morphology of the resultant silica material could be simply tuned by varying the pressure of the reaction system. They proposed that the small silica particles were formed and dispersed in the water phase, followed by the generation of CO_2/water emulsion and eventually the formation of hollow silica spheres.

The aim of this chapter is to investigate the synthesis route of mesoporous silicas in the presence of SCFs, followed by the optimisation of the various conditions in order to obtain a spherical silica material. Prior to this, a study of acid effect including the different types of acid and the concentration of acid on the synthesis of SBA-15 in the aqueous phase was carried out.

2.2   Conventional synthesis for SBA-15 silica

The general synthetic route of SBA-15 was based on the procedure in Stucky's paper.[14] Briefly, the surfactant P123 was completely dissolved in the mixture of water and acid, then the precursor TEOS was added with stirring for 20h. The mixture was aged at 80 $^\circ$C overnight without stirring. Finally the product was obtained by washing, filtration and calcination.

2.2.1 Effect of different acids

The mesoporous silica SBA-15 is typically formed in strong acid media (pH << 1) by using an inorganic acid like HCl, H_2SO_4, and H_3PO_4. If the acid concentration is in the range of 2 - 6, no precipitation of silica is observed. At neutral pH = 7, only disordered or amorphous silica is obtained. Ha pointed out that the synthesis of mesoporous silica under mild condition was extremely important for its commercialization in industry.[143] As such, a new synthetic route of SBA-15 mesoporous silica with well-ordered mesoporous structure at a mild condition (pH = 2 - 5) by using pre-hydrolysed TEOS as silica source was proposed by them.

A comprehensive study of mesoporous silica synthesis under weak acidic environment (pH = 2.5 – 3.0) was reported by Qiao,[144] which indicated the decreased hydronium ion

concentration induced weaker assembly forces under weak acidities as compared to strong acidities so restricting the elongation of the micelle-silica hybrids. The silica material with low hexagonal ordering or even wormhole structure was subsequently synthesised at high pH value (pH = ~3.5). Most papers reported that several of types of acids could be used for hydrolysing the precursor in the synthesis of SBA-15. Zhao *et al.* demonstrated the times required for precipitation to occur strongly depended on the acid anion and hydrogen ion concentration, and the radius or charge of the anion and the strength of acid might most influence the reaction rates.[14] The results obtained in the experiments here are in agreement with this conclusion. In our hands, the precipitation time in the HCl solution was shortest. As soon as precursor was added into the HCl acid and template mixture, a white cloudy precipitate formed immediately.

Due to the relatively high solubility in SCF, the TFA is taken into consideration as hydrolysis reagent,[145] and Vogt proposed that the solid acid p-TSA could be used in place of a typical mineral acid to avoid any ambiguities from homogeneous hydrolysis in the fluid phase.[53, 146] Hence, several kinds of acids were introduced in the preparation processes, including inorganic acid hydrochloric acid: (HCl), sulfuric acid (H_2SO_4), phosphoric acid (H_3PO_4), and organic acid: trifluoroacetic acid (TFA), p-toluenesulphonic acid (p-TSA). The five samples were all prepared based on the conventional method in the same conditions except the different acids used with the same hydrogen ion concentration. As can be seen in Table 2.1, different acids used in the preparation process led to little distinction in the textural properties. That is because the synthesis mechanism did not change very much with different acids in the process. Generally, in SBA family materials, some micropores may exist in the pore wall so that the S_{BET} of these samples could achieve up to 1000 m^2/g due to the partial occlusion of EO chains of the copolymers into the silica wall.[45-47]

Table 2.2 Textural properties of silica materials synthesised by different acids

Sample	BET surface area (m^2/g)	Pore volume (cm^3/g)	Pore size (nm)
SBA-15-HCl	942	0.83	3.51
SBA-15-TFA	768	1.01	5.28
SBA-15-H$_2$SO$_4$	739	0.76	4.13
SBA-15-H$_3$PO$_4$	798	0.73	3.65
SBA-15-p-TSA	955	1.04	4.37

TEM images (Figure 2.2) showed that there was a major difference between the samples prepared with inorganic acids and organic acids. For HCl, H$_2$SO$_4$ and H$_3$PO$_4$ samples, there are clearly linear mesopore channels and ordered hexagonal matrixes. However, due to the weaker acidity of phosphoric acid (pKa$_1$ = 2.12) compared to other two (pKa = -8 for HCl and pKa = -3 for H$_2$SO$_4$),[147] the relatively weak assembly forces restrict the elongation of the micelle and silica, which led to a short pore channel. Surprisingly, the image of sample made from TFA did not show a hexagonal matrix and mesopore channel like others but a vesicle matrix with the estimated diameter of 40 - 60 nm according to the scale in the TEM image. This may because the fluorinated group destroys the micelle formed by the template in the solution so that the different matrix type was prepared. The images of p-TSA samples are also shown, where disordered worm-like silicas appeared, indicating that the templating process using p-TSA as acid did not proceed successfully. This suggests that organic acid and inorganic acid give rise to different morphologies of the solid materials. Thereby, the anion effects of the acid during the preparation may influence the stabilization of the micelle formed by the surfactant, thus resulting in the different morphologies. Figure 2.3 shows the pore size distributions of SBA-15-HCl, SBA-15-TFA, SBA-15-H$_2$SO$_4$, SBA-15-H$_3$PO$_4$ and SBA-15-p-TSA samples, indicating that HCl and H$_2$SO$_4$ sample has narrow pore size distributions and H$_3$PO$_4$ sample also has a distinct peak at ~4 nm accompanying with a small shoulder peak. However, it is observed that when organic acids including p-TSA and TFA are utilized,

there is no significant peak on their pore size distribution curves, supporting the hypothesis that a less uniform silica was synthesised.
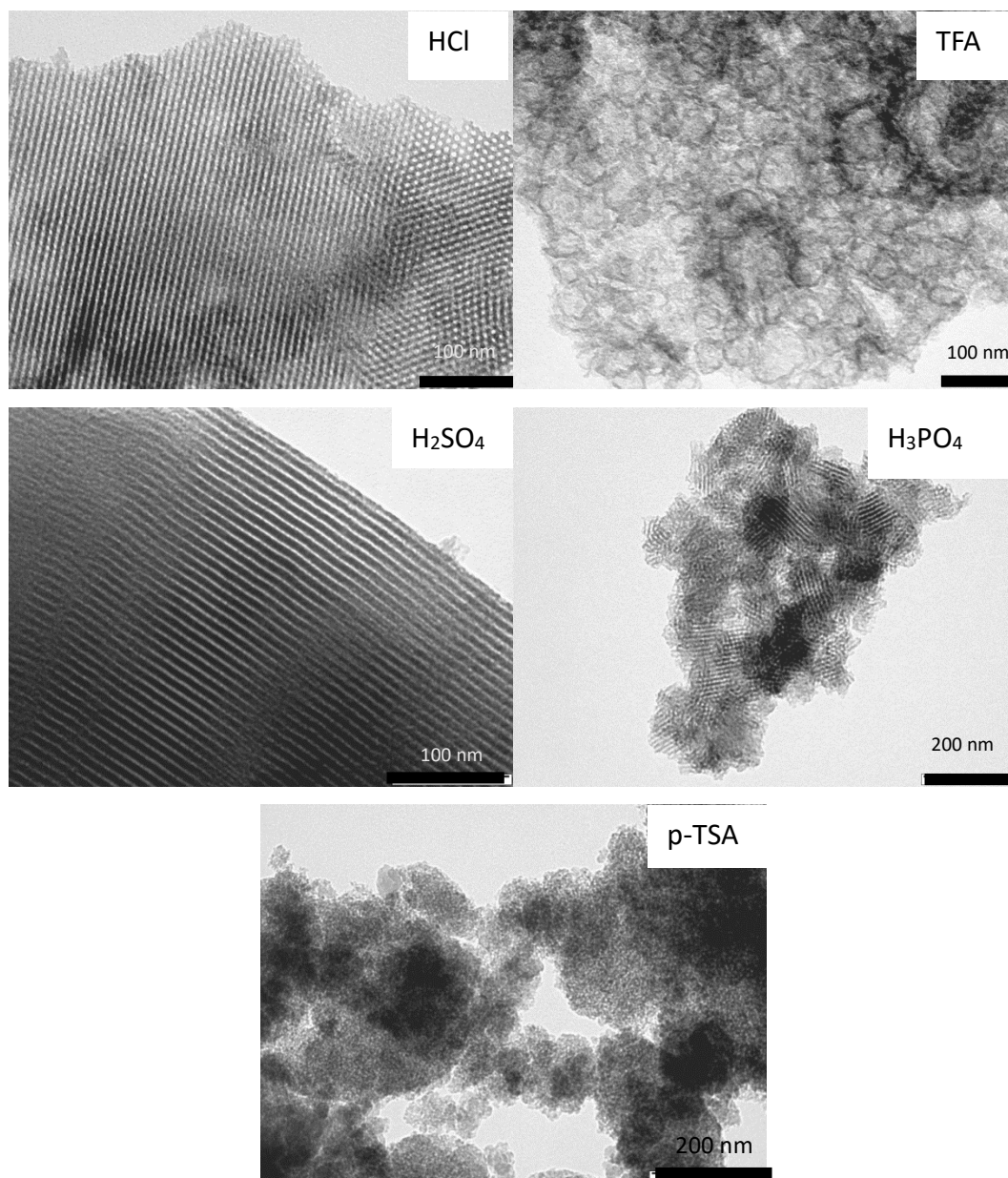
Figure 2.2 TEM images of silica materials synthesised by different acids
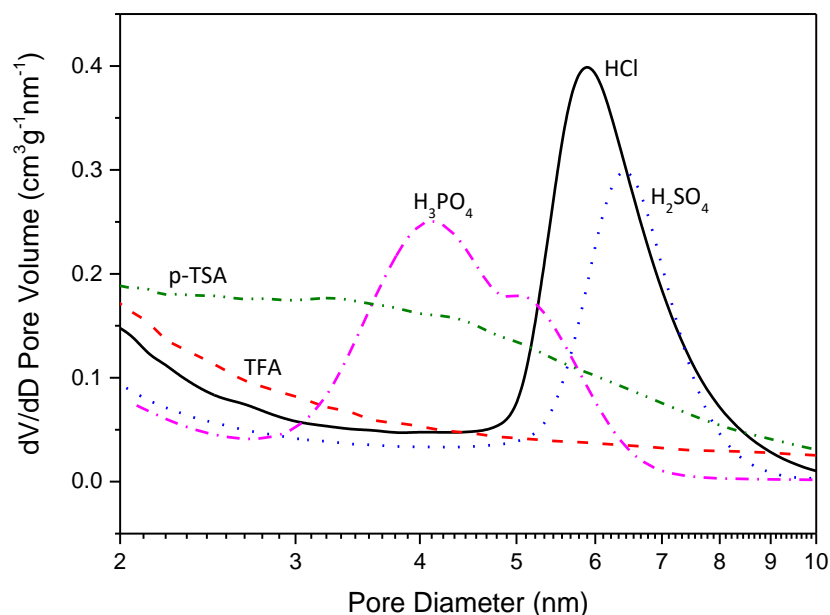
Figure 2.3 Pore size distributions of SBA-15-HCl, SBA-15-TFA, SBA-15-H$_2$SO$_4$, SBA-15-H$_3$PO$_4$ and SBA-15-p-TSA

2.2.2 Variations on acid concentrations (HCl)

The effect on pH environment for the synthesis of mesoporous silica was investigated. In 1998, Stucky and co-workers reported that the hexagonal mesoporous SBA-15 is prepared in acid solutions (pH<1).[14, 16] At pH values from 2 to 6, above the isoelectric point of silica, no precipitation or silica gel occurs. In a neutral solution, the disordered or amorphous silica is obtained.[14, 16]

As can be seen in Table 2.3, low acid concentration (HCl) sample possessed an increased BET surface area (1327 m^2/g), pore volume (1.69 cm^3/g) and pore size (4.80 nm) compared to the conventional SBA-15 sample prepared with middle HCl concentration. The enhancement of hydrophobicity of copolymer micelles under low acid concentration can contribute to the expansion of the mesoporosity of the silica. The result was consistent with the method demonstrated by Hao *et al.* in 2009.[144] The decreased H$^+$ concentration also induced weaker assembly forces during the synthesis, thus restricting the length of pore channel, which leads to the short mesochannel and low hexagonal ordering, which could be observed in Figure 2.4. As indicated above, several papers successfully synthesised SBA-15 with comparable textural properties and pore matrixes under weak acidity range by using pre-hydrolysed silica precursor.[143, 144] Under lower pH

74

values, the resulting sample had higher textural properties than middle concentration sample, and the micrograph showed that well-ordered silica with a longer pore channel was prepared, which is likely to due to the increased charge density on the micelle.

Table 2.3 Textural properties of silica materials synthesised by different concentrations of HCl

Samples (mol/L)	BET surface area (m^2/g)	Pore volume (cm^3/g)	Pore size (nm)
Low Conc.(0.76)	1327	1.69	4.80
Mid Conc.(1.53)	942	0.83	3.51
High Conc.(3.06)	1338	1.70	4.71
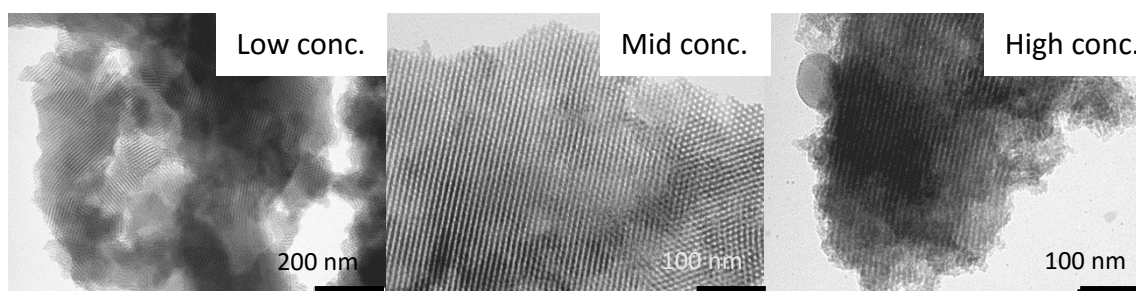
Figure 2.4 TEM images of silica materials synthesised by different concentrations of HCl

2.2.3 Variations on acid concentrations (TFA)

No silica precipitate was formed when conducting the synthesis at high TFA concentrations, therefore, no porosimetry or TEM results could be obtained for this sample. A silica sample with larger pore volume (1.01 cm^3/g) and pore size (5.28 nm) was synthesised under middle acid concentration compared to the low concentration sample, whereas it's BET surface area (768 m^2/g) was slightly lower than the other one.

Table 2.4 Textural properties of silica materials synthesised by different concentrations of TFA

Samples (mol/L)	BET surface area (m²/g)	Pore volume (cm³/g)	Pore size (nm)
Low Conc. (0.76)	877	0.73	3.33
Mid Conc. (1.53)	768	1.01	5.28
High Conc. (3.06)	/	/	/

The TEM images (Figure 2.5) of silica materials synthesised by different concentrations of TFA, demonstrated that the material prepared under low acid concentration possessed well-ordered multi-lamellar vesicular structures, while an intact spiral shape structure of silica was observed in the middle concentrated sample (Figure 2.5). Presumably if a long enough reaction time was taken, more and more complete spirals may form. In terms of the sample prepared in middle TFA concentration, there were complete vesicle-shaped particles with an average diameter of 40 nm, which is quite different to the sample made under low concentration. That also can be concluded from the textural properties shown in Table 2.4. It suggests that by changing the concentration of TFA, the silica structure transited from multi-lamellar vesicle to single-lamellar vesicle. The TEM images for highly concentrated sample were not obtained due to the synthesis providing no product.
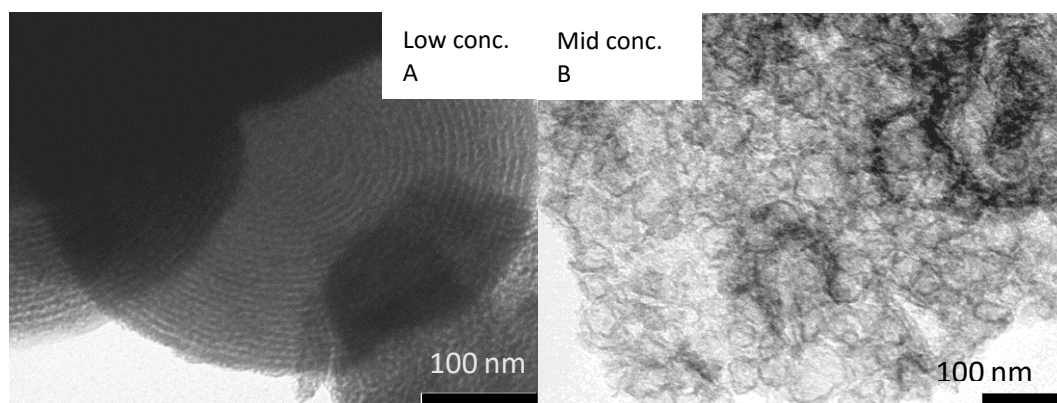
Figure 2.5 TEM images of silica materials synthesised by different concentrations of TFA

Compared to the different acids used in the silica synthesis, mesoporous silica exhibits regular linear pore arrangement when the inorganic acid is utilized in the synthesis, while different silicas with spherical structure were prepared when using TFA. As discussed in 2.1, the function of the acid in the silica synthesis is to hydrolyse the silica precursor and the anions of the acid (X^-), is associated with the hydrophilic EO group (shown in Equation 2.1-2). The fact that utilization of inorganic acid and TFA gave such different morphologies of the materials indicates the anion effects of the acid during the preparation. The stabilization of the micelle formed by the surfactant would be affected by the anions of the acid.

It is reported that spherical silica shells comprising the vesicular mesoporous structure were successfully synthesised *via* a rapid, aerosol-based process.[148] This method relied on the evaporation-induced interfacial self-assembly confined to spherical aerosol droplets. The formation of spheres was profoundly influenced by the curvature of the particle surface. The bulk and film samples were prepared by flat liquid-vapour interfaces, while the liquid-vapour interface serves as a nucleating surface, which will give rise to vesicular mesophases.[148]

Thereby, based on the discussion of curvature effect above, it could be concluded that TFA could stabilize the vesicular mesophases thus resulting in the production of spherical silicas. In other words, the incorporation of TFA induces a different structural form from the ordered SBA-15 structure to vesicle. Compared to the literature, some research groups investigated the formation of such spherical meosporous silicas also using P123 as a structure directing agent, but with the incorporation of hydrophobic additives to transform hexagonal arrays of cylindrical micelles into multilamellar vesicles.[149-151] It is obvious that our synthetic method is superior as no additive was utilized in the process, and moreover, the BET specific surface area and the pore volume of the vesicular silica is up to 877 m^2/g and 1.01 cm^3/g, respectively, which is comparable to previous results (691 m^2/g and 0.8 cm^3/g).[150]

2.2.4 Investigation of organic template removal by calcination

In Chapter 1, it is mentioned that a variety of methods have been used for template removal. High temperature calcination is considered to be the most effective method among these techniques in this work since the organic triblock polymeric template would easily decompose *via* this method.

The infrared spectra of the template, uncalcined silica sample and calcined silica sample was shown in Figure 2.6. In the spectra of the template P123 (Figure 2.6c), the absorption bonds at 2900 and 1373 cm^{-1} were attributed to the C-H stretching and bending vibrations. The highest intensity band in the spectrum of the template at 1096 cm^{-1} was attributed to C-O stretching vibration. The polymer structure of P123 shown in the figure illustrates the C-H bond and C-O bond. In the spectra of the sample before (Figure 2.6a) and after calcination (Figure 2.6b), the absorption bands at 1090 cm^{-1} and 800 cm^{-1} were ascribed to the asymmetric and symmetric stretching vibrations of Si-O-Si bonds.[152] It should be noted that the C-O signal of P123 (1096 cm^{-1}) and Si-O signal of silica (1090 cm^{-1}) are located quite closely, thus it could not be easily differentiated completely. In the absorption spectrum, there is no doubt template is left in the sample before calcinations. From the spectra of the calcined sample, there were only the peaks attributed to the Si-O-Si vibrations, which also suggested that the calcination step was effective for the removal of templates from silicas.
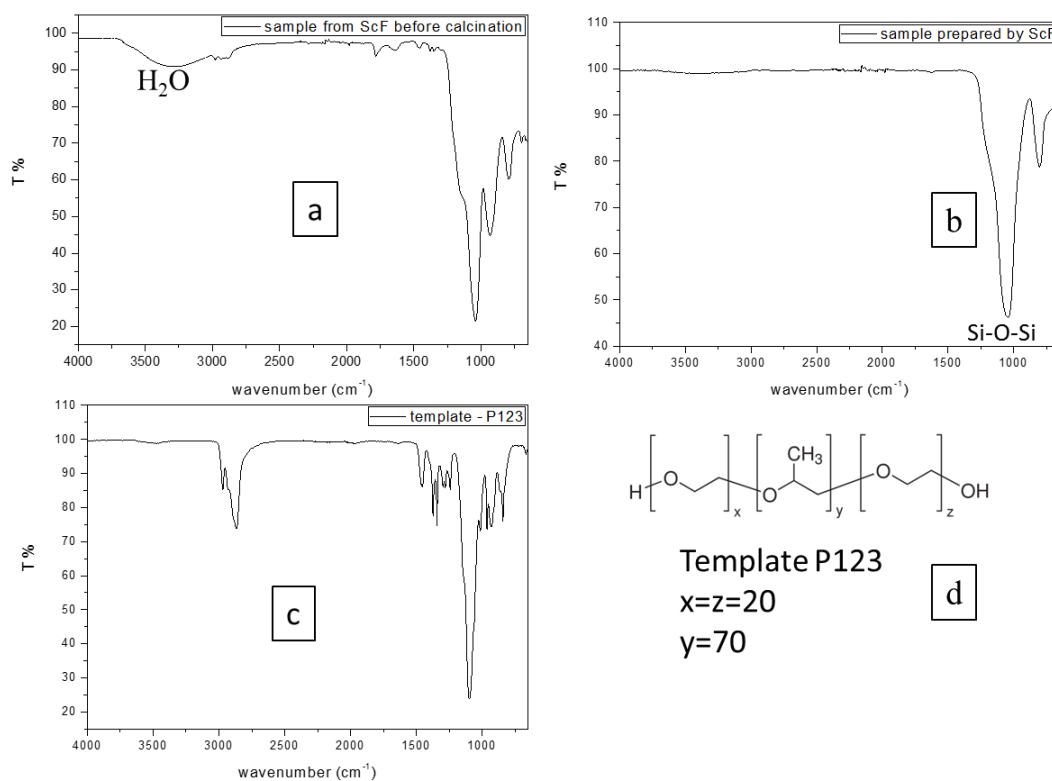
Figure 2.6 FTIR spectrum of uncalcined sample (a), calcined sample (b), the P123 template (c) and its polymer structure (d)

2.3   Preparation of silica in SCF by using HCl as acid

The next stage was to attempt to synthesise silica materials in the presence of supercritical fluids. The liquid phase for the synthesis of conventional SBA-15 was transferred to the high pressure reactor, and carbon dioxide was then introduced. Subsequently the pressure and the temperature were adjusted to the desired value. After the reaction, it was surprising to observe that the solution has turned to green (shown in Figure 2.7), which implied that corrosion may appear because of too high acid concentration added into the reactor.
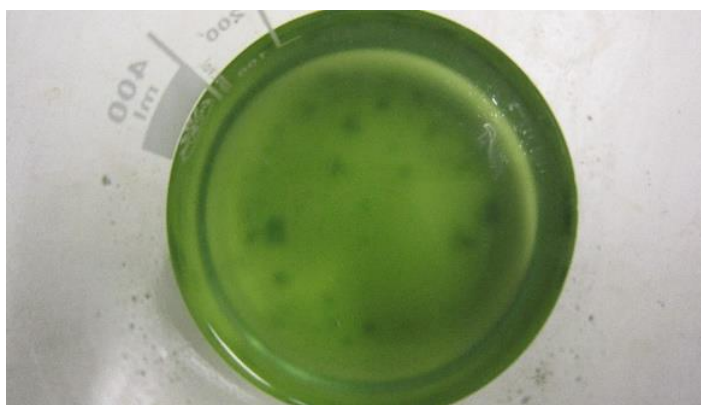
Figure 2.7 Green solution from the silica synthesis in SCFs

The porosimetry data in Table 2.5 shows that the silicas possessing a BET surface area of up to 438 m^2/g and pore volume of up to 0.58 cm^3/g were prepared. No spherical structure was observed from TEM images of silica samples prepared either with or without stirring (shown in Figure 2.8). Based on the observation above, the acid would probably react with the reactor, resulting in the formation of Fe or Ni ions. This may prevent the process of synthesising the vesicular silicas. ICP analysis of the green solution, demonstrated the presence of Fe, Ni and Cu in concentrations of 1.06×10^4 ppm, 1.6×10^3 ppm, 40 ppm, respectively.

Table 2.5 Textural properties of the silica samples prepared with or without stirring

	BET surface area (m²/g)	Pore volume (cm³/g)	Pore diameter (nm)
Unstirred	438	0.58	5.32
Stirred	343	0.23	2.71

In order to prepare predicted samples and keep the reactor safe, another experiment with half acid concentration has tried, and the result demonstrated that no product was produced. It should be noted that the result of the low concentration sample synthesised in aqueous phase in 2.2.2 indicated the well-ordered mesoporous silica was synthesised by the conventional method under the same acid concentration.

Therefore, owing to the limitation of the high pressure reactor, it was necessary to find another suitable acid for mesoporous silica preparation. Trifluoroacetic acid, as a suitable acid, was introduced for the synthesis of porous silica in SCF system due to the high solubility in SCF as mentioned in previous section.
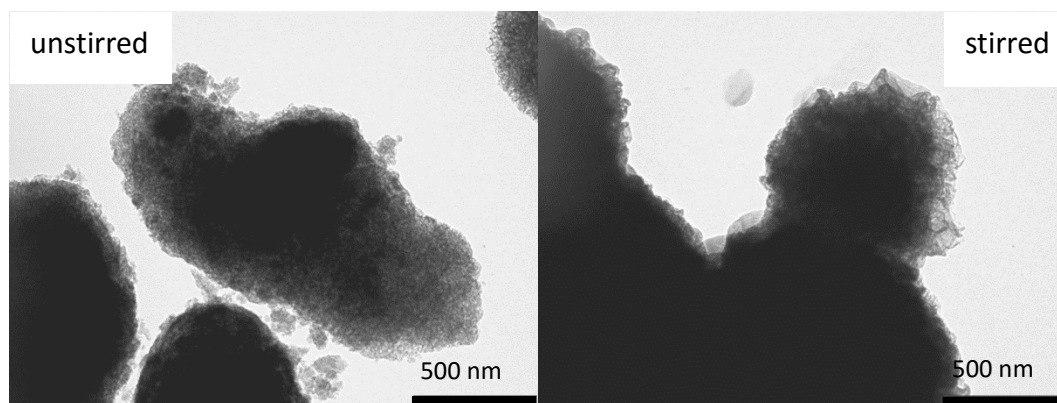
Figure 2.8 TEM images of the silica samples prepared with or without stirring

2.4 Preparation of silica in SCFs by using TFA as acid

2.4.1 Isolated preparation process in SCF

As shown in Figure 2.9, the silica precursor TEOS was placed on the bottom of the reactor due to the high diffusion of supercritical fluid so that it is isolated from the liquid in the container during the process. The liquid mixture was composed of TFA acid, P123 and water. The various conditions were adjusted and the resultant materials were characterized.

Supercritical reactor
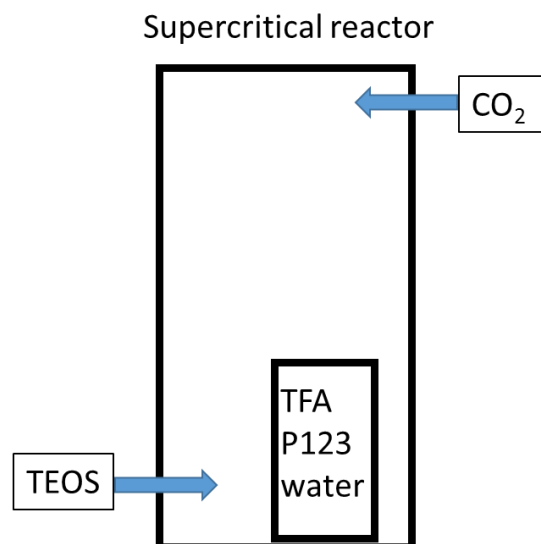
Figure 2.9 Schematic diagram of the isolated preparation process in SCF

2.4.1.1 Effects of reaction time

The effects of the reaction time on the properties of resultant materials were investigated. Table 2.6 shows the porosimetry data of samples prepared under different reaction times. All the porosimetry data were quite poor except the pore diameter of S1-8 (11 nm) and S1-16 (7.17 nm). From the TEM micrographs illustrated in Figure 2.10, a less uniform ball structure was observed in S1-8 and S1-16. This result was consistent with the high pore diameters of S1-8 and S1-16 in Table 2.6, which could be attributed to the short reaction time leading to an incomplete silica aggregation compared to the sample prepared under longer time.

Table 2.6 Textural properties of samples prepared under 8 h, 16 h, 24 h

	Time (h)	BET surface area (m²/g)	Pore volume (cm³/g)	Pore diameter (nm)	Yield %
S1-8[a]	8	35	0.10	11.00	12
S1-16	16	11	0.02	7.17	7
S1-24	24	6	/	/	34

[a] All the experiments carried out under 350 bar and 80 °C, and the amounts of compounds added were 0.8 g of P123, 3.6 mL of TFA, 0.36 g of water and 3.4 g of TEOS.

The product yield of S1-24 was the highest at *ca.* 34%, but the specific surface area of this sample was as low as 6 m^2/g. Figure 2.10 also shows that a solid ball structure of this sample with the particle diameter of 1 μm was formed.
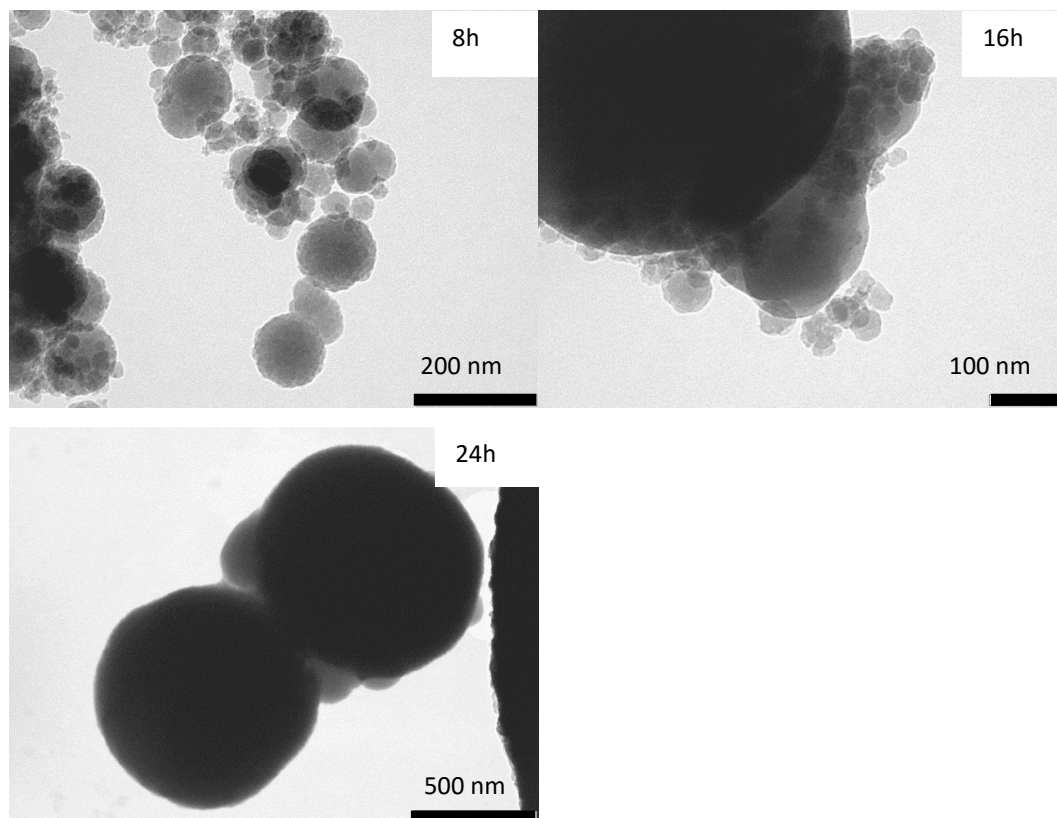
Figure 2.10 TEM micrographs of samples prepared under 8 h, 16 h, 24 h

2.4.1.2 Effects of pressure

Table 2.7 Textural properties of samples prepared in different pressures

	Pressure (bar)	BET surface area (m^2/g)	Pore volume (cm^3/g)	Pore diameter (nm)	Yield %
S1-150	150	/	/	/	/
S1-250	250	/	/	/	<1
S1-350	350	6	/	/	34

All the experiments carried out under 80 °C, and the amounts of compounds added were 0.8 g of P123, 3.6 mL of TFA, 0.36 g of water and 3.4 g of TEOS.

Variation of pressure had little effect on the yield of product prepared in this process (Table 2.7). This may be due to the absence of enough water in the gaseous phase. Even in the static condition, the water stayed in the vial rather than dispersing into the CO_2 phase so that the hydrolysis could not take place. It is known that the water solubility in carbon dioxide is dependent on the temperature and pressure. However, the solubility of water in CO_2 is as low as *ca.* 0.35% when the pressure and the temperature is 150 bar and 26 °C, respectively, and this value increases to *ca.* 0.41% as the pressure increases to 350 bar, indicating a lower solubility of water in CO_2.[153] Hence, it could be predicted that in our process, there is not enough water in the gaseous phase to initiate the hydrolysis process.

2.4.1.3 Effects of temperature

The same situation was also apparent for the segregation of water and precursors in the temperature adjustment process, leading to poor porosimetry data (Table 2.8). The table showed there were poor porosimetry data for all three samples with the BET surface area of up to 6 m^2/g. TEM micrographs (Figure 2.11) demonstrated that dense ball particles with less uniform size were prepared by this process. Few pores were observed in the TEM micrographs, which was consistent with the porosimetry results. It should be noted that the interface of the particles was quite smooth. In comparison with the three different samples, there was no dramatically difference, and the scale bar showed all the three samples had an average particle diameter of 1 μm.

Table 2.8 Textural properties of samples prepared under different temperatures

	Temperature (°C)	BET surface area (m^2/g)	Pore volume (cm^3/g)	Pore diameter (nm)	Yield %
S1-40	40	/	/	/	11
S1-60	60	1	/	/	9
S1-80	80	6	/	/	34

All the experiments carried out under 350 bar, and the amounts of compounds added were 0.8 g of P123, 3.6 mL of TFA, 0.36 g of water and 3.4 g of TEOS.
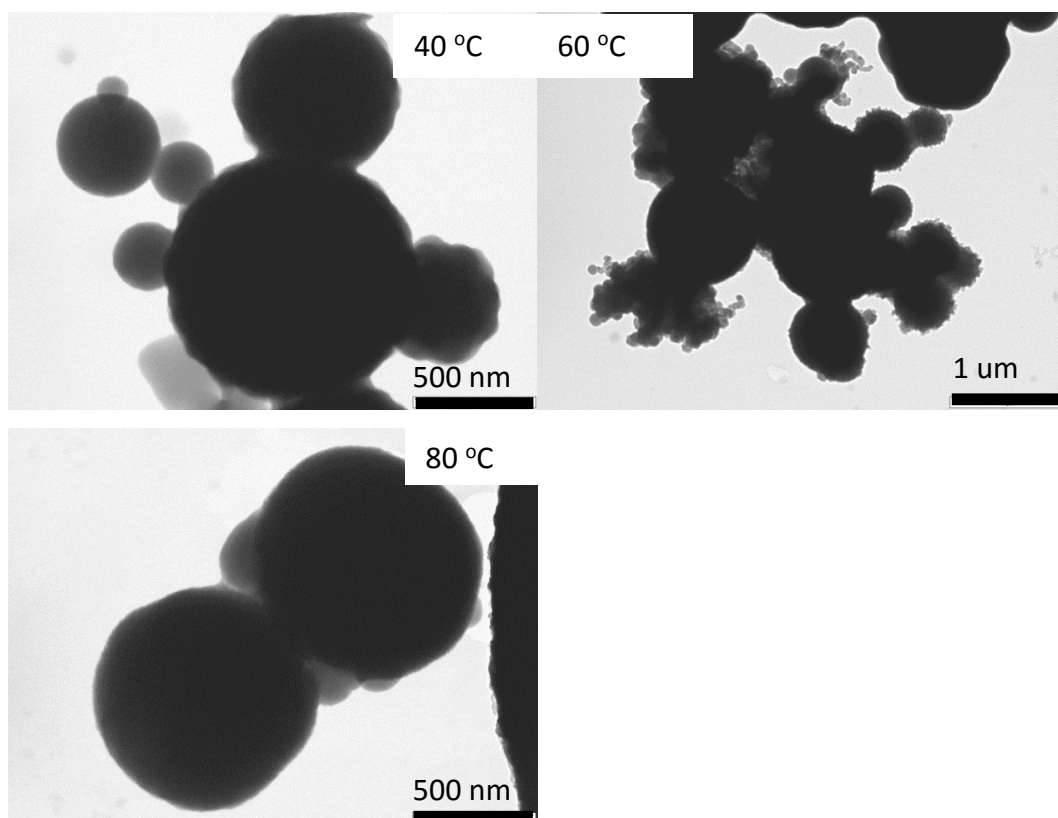
Figure 2.11 TEM micrographs of samples prepared under different temperatures

2.4.1.4 Effects of addition of EtOH

With ethanol introduced into the reaction, a small quantity of water in ethanol could be taken into the system for initiating the hydrolysis. Moreover, it has been reported that ethanol could play a role as co-solvent in modifying the CO_2 properties and making the water more soluble in the SCF. [61, 64, 154] Table 2.9 showed the textural properties of the samples synthesized with different amounts of ethanol and water. It demonstrated that S1-0.36 had a poor product yield (<0.01%) and low specific surface area, pore volume and pore size because of hydrolysis not taking place. An addition of ethanol increase from 0.36 g to 3.6 g for S1-0.36 and S1-3.6 samples slightly improved the BET surface area to 82 m^2/g, pore volume to 0.07 cm^3/g, but still remained relatively low. TEM images of these two samples demonstrated disordered silicas were formed under the conditions, indicating the templating process did not proceed successfully.

When 0.36 g water was added, a high yield of 37% was achieved for the S1-3.6II sample. TEM micrographs (Figure 2.12) showed there were some regular pore channels around the dense balls, suggesting that the silica tended to form ordered structures, which were not observed in the materials made without the addition of water. This is probably due to the miscibility of ethanol in SCF supporting the formation of a homogeneous phase including water, SCF and reagents. Hence, the water also could be easily transferred from vials.

Table 2.9 Textural properties of samples prepared with different amounts of EtOH

	EtOH (mL)	H₂O (mL)	BET surface area (m²/g)	Pore volume (cm³/g)	Pore diameter (nm)	Yield %
S1-0.36	0.36	/	/	/	/	<1
S1-3.6	3.6	/	82	0.07	3.30	9
S1-3.6II	3.6	0.36	65	0.06	3.58	37

All the experiments carried out under 350 bar and 80 °C, and the amounts of other compounds added were 0.8 g P123, 3.6 mL of TFA and 3.4 g TEOS.
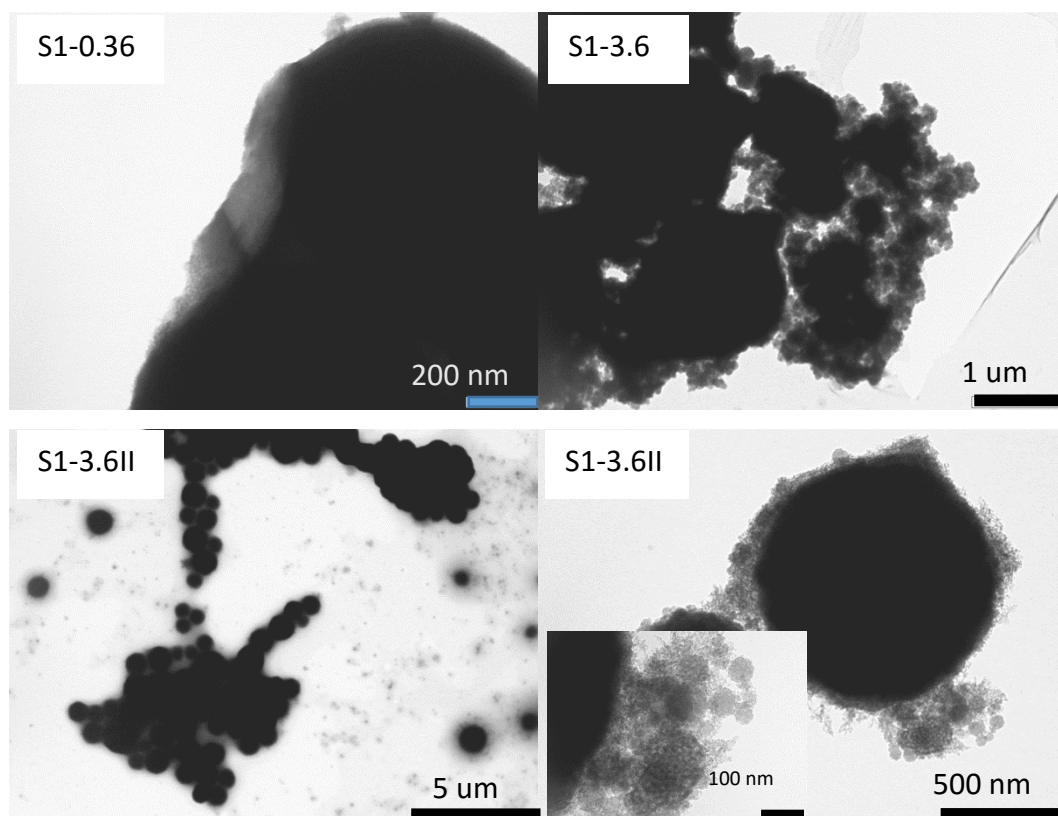
Figure 2.12 TEM micrographs of samples prepared with different amounts of EtOH

In comparison to well-shaped spherical silica synthesised by the conventional method with TFA, the templating process in isolated system has failed. It is concluded that the silica synthesised by this isolated preparation system is essentially nonporous based on the research of the isolated system. Varying the conditions including the temperature, pressure, reaction time and addition of EtOH, a silica material with maximum BET surface area of 82 m^2/g and pore volume of 0.10 cm^3/g was obtained. The silica yield for this method is quite poor, and the highest yield for the silica is *ca.* 37% (S1-3.6II sample), which was achieved by the addition of EtOH and H_2O. Besides, without the introduction of water, it was difficult to complete the hydrolysis process. Therefore, the investigation of the addition of water will be carried out in further section.

2.4.2 Mixed preparation process in SCF

As such, a mixed system by mixing TEOS, TFA, P123 and water together prior to being placed into the high pressure reactor was investigated (shown in Figure 2.13). This enables the silica precursor closely contact with the acid, thus easily being hydrolysed.
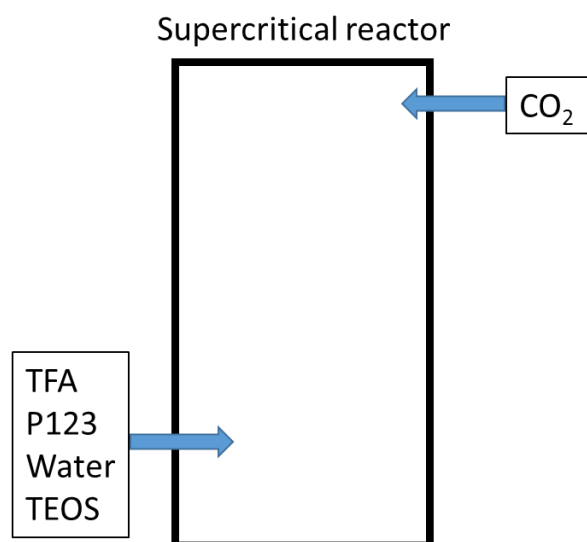
Figure 2.13 Schematic diagram of the mixed preparation process in SCF

2.4.2.1 Effects of kinetics in reaction

Table 2.10 Textural properties of the silica samples prepared with or without stirring[a]

	Stirring	BET surface area (m^2/g)	Pore volume (cm^3/g)	Pore diameter (nm)
S2-static	NO	118	0.16	5.72
S2-dynamic	YES	438	0.33	2.97

[a] Both the experiments carried out under 250 bar and 60 ^{o}C, and the amounts of compounds added were 0.8 g P123, 3.6 mL of TFA, 3.6 g water and 3.4 g TEOS.

In the silica synthesis, the kinetics could influence morphology of products. The stirring technique could change the micelle formation, which is a main effect on silica assembly procedure. Table 2.10 indicated that the dramatic differences in the textural properties between these two samples with or without stirring. The sample of S2-static had a modest specific BET surface area of 118 m^2/g and pore volume of 0.16 cm^3/g, which is probably attributed to the poor water distribution in SCF without stirring as mentioned before, whereas it should be noted that the pore size of this sample was almost double that of the dynamic one.

TEM images (Figure 2.14) showed both samples contained vesicle shapes with a silica shell and hollow space inside. Owing to the static condition during the process, the vesicle shell was much thicker and smoother than that in the dynamic sample. Moreover, a less uniform and fractured sphere was clearly shown in the dynamic sample, which indicated the negative effects of stirring for the formation of vesicle silicas. The high values of porosimetry data in Table 3.9 and the worm-like pore structures shown in TEM images demonstrated that a much more porous material could be synthesized in the dynamic condition. Besides, stirring would possibly accelerate the formation of a more homogeneous phase mixed of CO_2 and water, thus preventing the generation of the stabilised CO_2-in-water droplet.[49, 50] This could be evidenced from the fact that there were some bulk silica materials shown in TEM micrographs of S2-dynamic.

However, it is worthwhile to note that our results did not concur with the discussion on the paper published by Mokaya and co-workers in 2006.[49, 50] They proposed that the microemulsion is a thermodynamically unstable system, which needs an extra force (agitation or stirring) to maintain stability. In the absence of stirring, a stable microemulsion was not achieved so that a rod like shape was synthesized in the static system.[50]
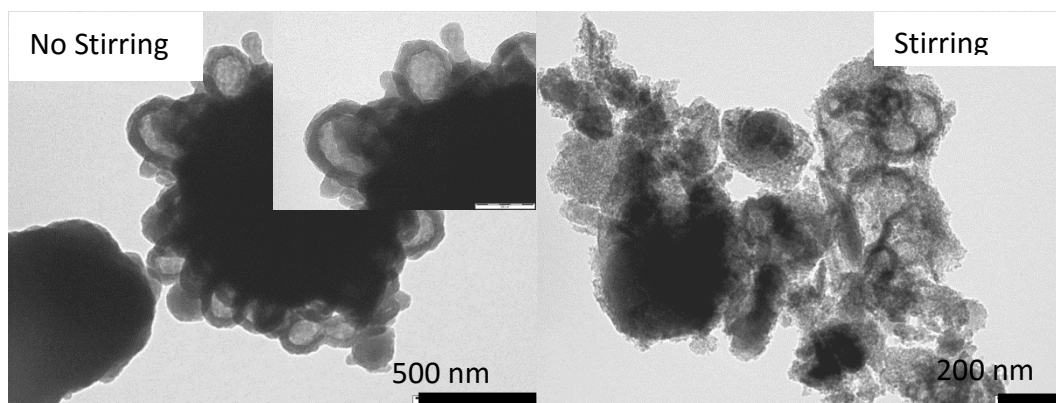
Figure 2.14 TEM micrographs of samples prepared with or without stirring

2.4.2.2 Effects of water amount

According to the discussion of the synthetic mechanism in 2.1, water is extremely important for the hydrolysis of silica precursor during the silica synthesis. Hence, it is necessary to introduce enough water into the system. Table 2.11 demonstrates that the BET surface area value became larger from 343 m^2/g to 524 m^2/g with the addition of more water up to 10.8 g in the reaction system, accompanied with a reduced pore volume (0.53 - 0.31 cm^3/g) and pore diameter (6.18 – 2.39 nm). Without the addition of water to the system, the hydrolysis cannot be carried out and the silica product would not form, even though a single phase containing carbon dioxide, acid and template could probably be formed.

Table 2.11 Textural properties of the materials prepared with different water percentages[a]

	H_2O/TFA/TEOS molar ratio	BET surface area (m^2/g)	Pore volume (cm^3/g)	Pore size (nm)
S2-0	0:2.4:0.8	/	/	/
S2-0.36	1:2.4:0.8	343	0.53	6.18
S2-3.6	10:2.4:0.8	438	0.33	2.97
S2-7.2	20:2.4:0.8	495	0.33	2.63
S2-10.8	30:2.4:0.8	524	0.31	2.39
S2-14.4	40:2.4:0.8	482	0.26	2.17

[a] The amounts of other compounds added were 0.8 g P123, 3.6 mL of TFA and 3.4 g TEOS. The pressure and the temperature for the experiment were 150 bar and 60 °C, respectively.
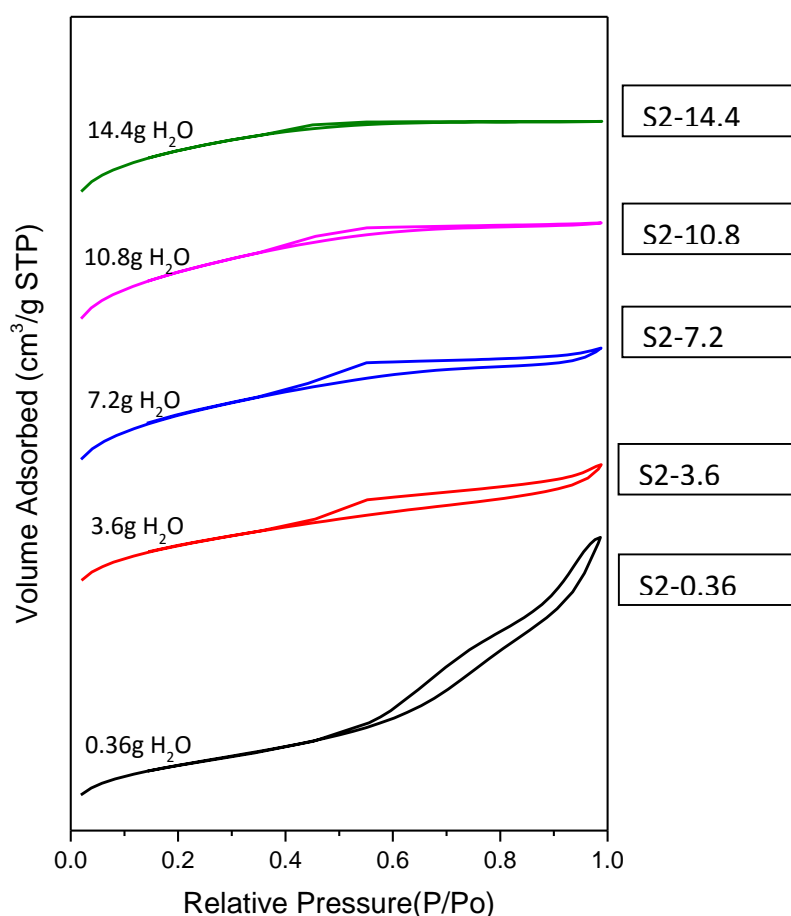
Figure 2.15 Adsorption/desorption isotherm plots of the materials prepared with different water percentages

The isotherm plots in Figure 2.15 showed that two different types appeared. There was a gradual rise and gradual drop in the isotherm plot of S2-0.36, indicating a wide range

90

of pore size distribution and a large proportion of micropores. The isotherm plots of the other four silica samples were similar while the hysteresis loop became smaller and smaller as the water amount increased, indicating that the mesoporous structures of these samples were the same but the micro/meso ratio increased. This is likely due to the increase of the water content, the acid concentration was subsequently lowered. As mentioned by Stucky, too low acid concentrations had a negative effect on the formation of mesoporous silica and thus may result in the formation of silica gel.[16]
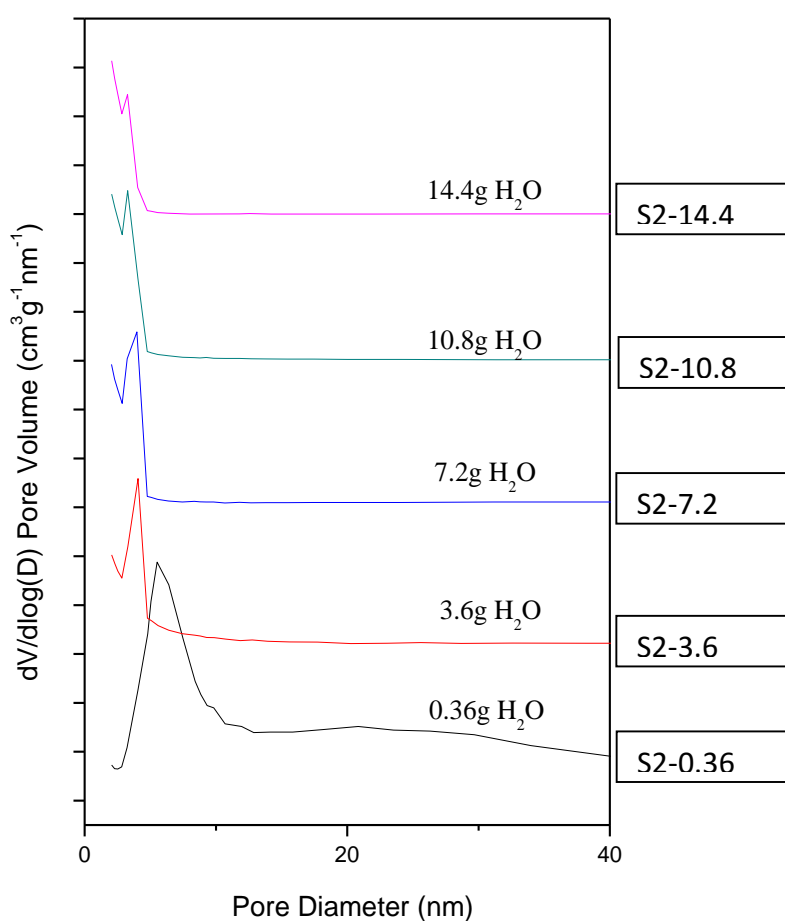
Figure 2.16 Pore sized distribution curves of the materials prepared with different water percentages

The pore size distribution discussed here are all shown by plotting dV/dlogD against pore diameter where dV/dlogD represents the change in the volume adsorbed with the change in diameter. Generally, the pores analysed are assumed to be rigid and have a

regular shape (cylindrical or slits).[124] Figure 2.16 showed the pore size distribution of the silica samples under different water amount. A distinct and broad peak appeared in S2-0.36 indicated the pore volume was higher than others and there also was a wide range of pore size in such a sample, which was consistent with the results discussed above. It should be noted that there was a reduction in pore size across the series, which was reflected from Table 2.11 and Figure 2.16, indicating that the pore size could be controlled in diameter as the acid concentration changed. However, this result could not be observed from the data of acid concentration effect by using conventional preparation route.
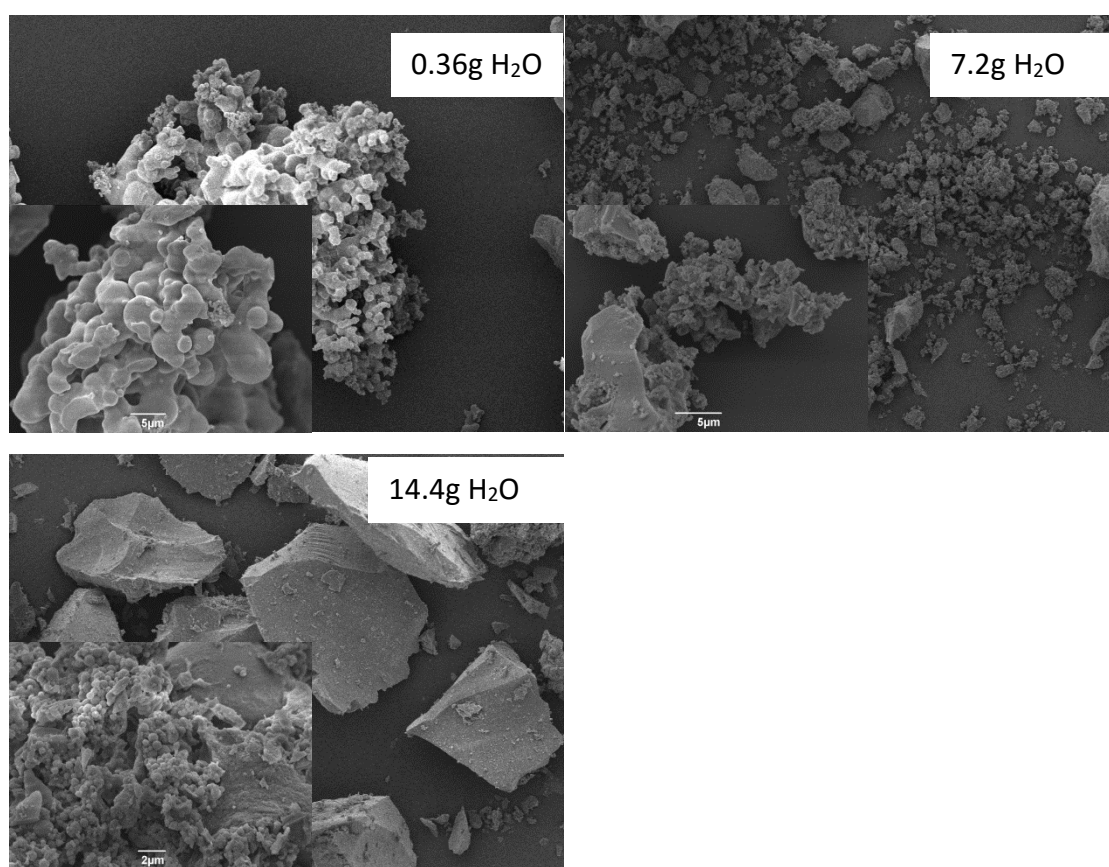
Figure 2.17 SEM images of the materials with different water percentages

The SEM images (Figure 2.17) showed that the silica sample tended to be bulk material when the water amount increased, which was also consistent with the results above. The SEM image of the sample synthesized by smallest amount of water exhibited the formation of vesicle-structured silica.

92

2.4.2.3 Effects of reaction time

Table 2.12 Textural properties of the materials under different reaction times

	Time (h)	BET surface area (m^2/g)	Pore volume (cm^3/g)	Pore size (nm)
S2-8	8	369	0.24	2.63
S2-24	24	495	0.33	2.63

The amounts of other compounds added were 0.8 g P123, 3.6 mL of TFA, 7.2 g water and 3.4 g TEOS. The reaction was carried out under 250 bar and 60 °C.

Table 2.12 illustrated the differences of textural properties between the silica materials synthesised under two reaction times. There were higher BET surface area of 495 m^2/g and pore volume of 0.33 cm^3/g for the sample prepared under longer reaction time. A similar data trend was reported by Pendleton for the mesoporous silica synthesis in sub- and supercritical carbon dioxide[56]. They proposed that this may be due to the formation of micropores.[56] The N_2 adsorption/desorption isotherm plot (Figure 2.18) showed there was only a slight difference between two silica samples, with the exception of total pore volumes. The isotherm plot shape including the hysteresis loop of 8-hour reaction and 24-hour reaction indicated similar pore structures. That is possibly attributed to advantageous physical properties of supercritical fluid. As mentioned before, the excellent diffusivity and viscosity compared to other liquid solvent makes the reaction short. Generally, slow systems are frequently used to allow high degrees of templating or structural arrangement. The Figure 2.19 demonstrated there was the similar pore size range in both samples. The pore volume of the long reaction time sample was larger than that of short reaction time, which was consistent with the results demonstrated in Table 2.12.
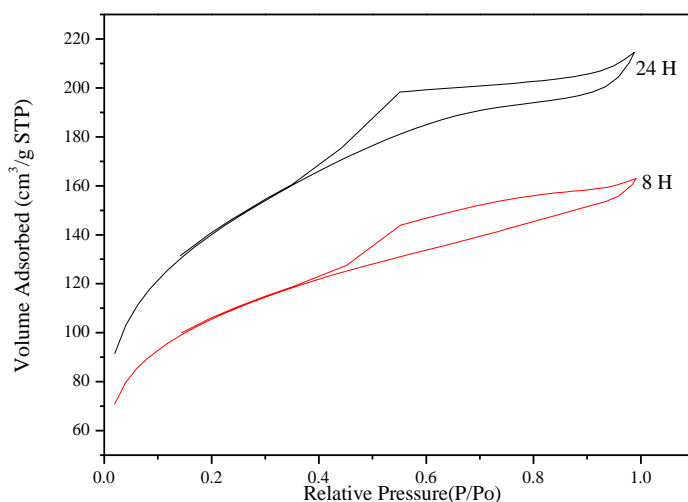
Figure 2.18 N₂ adsorption/desorption isotherm plots of the materials under different reaction times
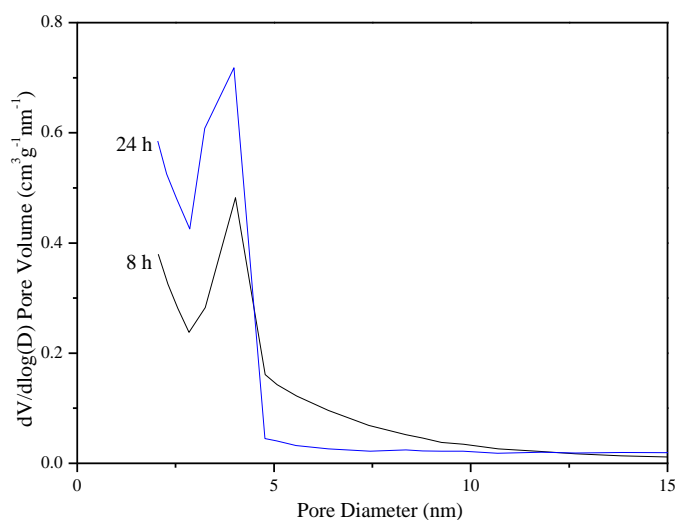
Figure 2.19 BJH pore size distribution of the materials under different reaction times

However, Figure 2.20 shows an oval-shaped silica material in the product synthesized over an 8 hour reaction time, while there were smooth and round hollow spheres in the long reaction time sample. Therefore the shorter reaction time could lead to the incomplete micelle formation, thus resulting in the oval silica structure. Interestingly, there was a channel with thick wall formed by the aggregation of vesicles in Figure 2.20

probably owing to the short reaction time. Predictably, this channel would split to form individual vesicle as the reaction time increases.
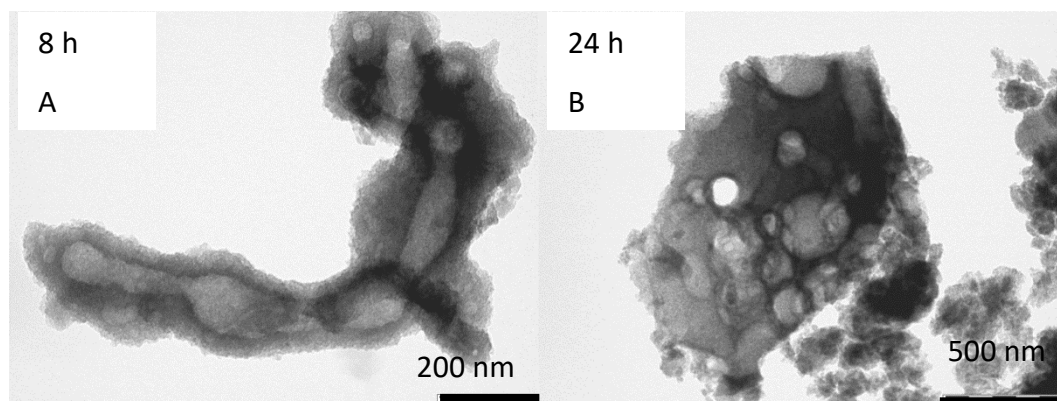
Figure 2.20 TEM micrographs of the samples prepared under 8 hours and 24 hours

2.4.2.4 Effects of pressure

Various papers reported that the successful synthesis of the porous particles strongly depends on the pressure and the density of carbon dioxide, and the mesoporosity and morphology of silica can be controlled by varying the operating carbon dioxide pressure.[50, 146, 155]

The pore sizes of the silica samples increased slightly as the pressure increased from 150 bar to 350 bar. While a significant increase in specific surface area and pore volume appeared, resulting in a bigger expansion of silica material when the pressure increased in the same situation (Table 2.13). That is attributed to the swelling function of CO_2 and increasing P123 sorption of CO_2 at higher pressure.[50] The same results can be concluded in the nitrogen adsorption/desorption isotherm (Figure 2.21). Due to the transport limitations of the polymer template in supercritical carbon dioxide at lower pressure, the silica precursor dissolving in CO_2 cannot penetrate into the porous structures so that the volume adsorbed for the low pressure sample is much smaller than that for other two, which could also be reflected from BET surface area of the samples.[146] Interestingly, the shape of the isotherm plots of both under 250 bar and 350 bar were extremely similar and close to each other, proving the pressure influence might weaken at high pressure

range. That indicated the similar pore structure has been prepared under such two different pressures.

Table 2.13 Textural properties of the materials under different pressures[a]

	Pressure (bar)	Temperature (°C)	BET surface area (m²/g)	Pore volume (cm³/g)	Pore size (nm)	Yield %
S2-150	150	60	267	0.18	2.68	44
S2-250	250	60	495	0.33	2.63	33
S2-350	350	60	504	0.35	2.74	50

[a] The amounts of other compounds added were 0.8 g P123, 3.6 mL of TFA, 7.2 g water and 3.4 g TEOS.
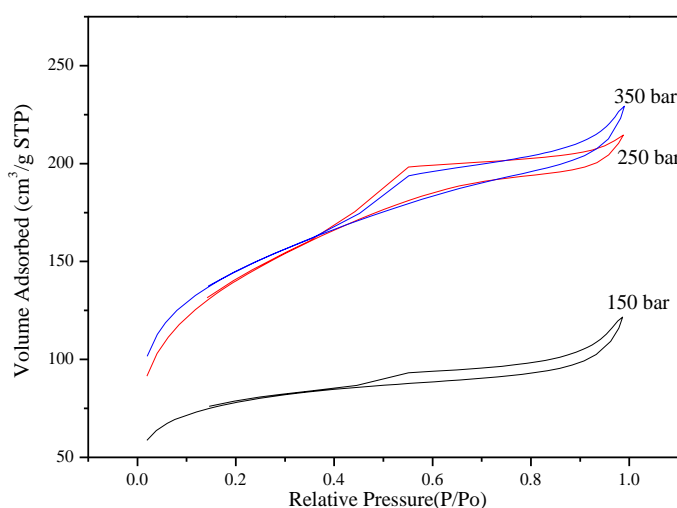
Figure 2.21 N$_2$ adsorption/desorption isotherm plots of the materials under different pressures

The pore size distribution of the materials (Figure 2.22) showed that all the samples had a narrow range of pore sizes with the peak around 4 nm, while as explained before, the peak for the low pressure sample was far lower than others indicating a small pore volume for such a sample.
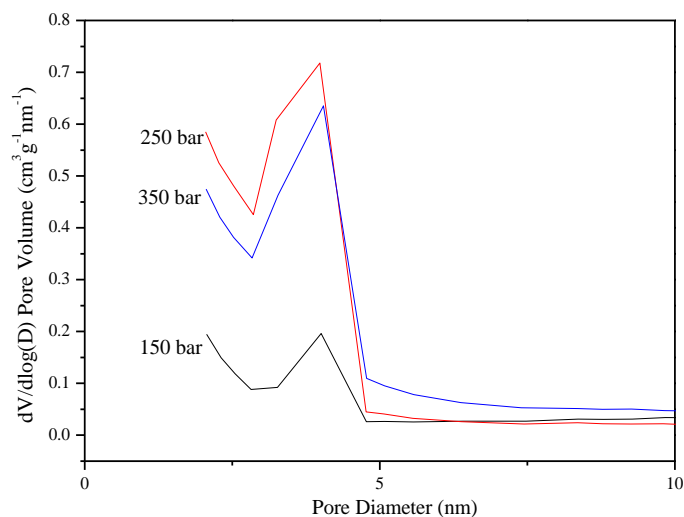
Figure 2.22 BJH pore size distribution curves of the materials under different pressures

TEM micrographs (Figure 2.23) showed there were vesicles in all silica materials prepared by different pressures. The four images clearly indicated that at low pressure, the proportion of the vesicle-shape structure was higher than at high pressures. That is probably due to the change in the density of the $SCCO_2$ at different pressures.[155] Table 2.14 illustrates at 60 ^oC, the CO_2 density is increasing as the pressure goes up, which means the density would be more and more close to that of water. Therefore, at high pressure, having similar densities of two solvents may help to form a well dispersed system with two phases uniformly mixed. That can simply explain the fact that the formation of vesicles at low pressure resulting from an effective templating process, but forming bulk silica at higher pressure. Interestingly, there were channels located in the middle of silica materials shown in Figure 2.23C. This is probably the same structure as shown in Figure 2.20A in 2.4.2.3 but with different thickness of silica wall. It is worthy carrying out the further investigation for this particular silica structure as this could potentially extend the applications of silica materials. Hence, as a consequence of decreasing the pressure, lower densities of CO_2 is achieved, which is preferable for the synthesis of vesicular silicas in this work, more specifically for S2-150 sample with the BET surface area of 267m^2/g, pore volume of 0.18 cm^3/g and pore size of 2.68 nm.
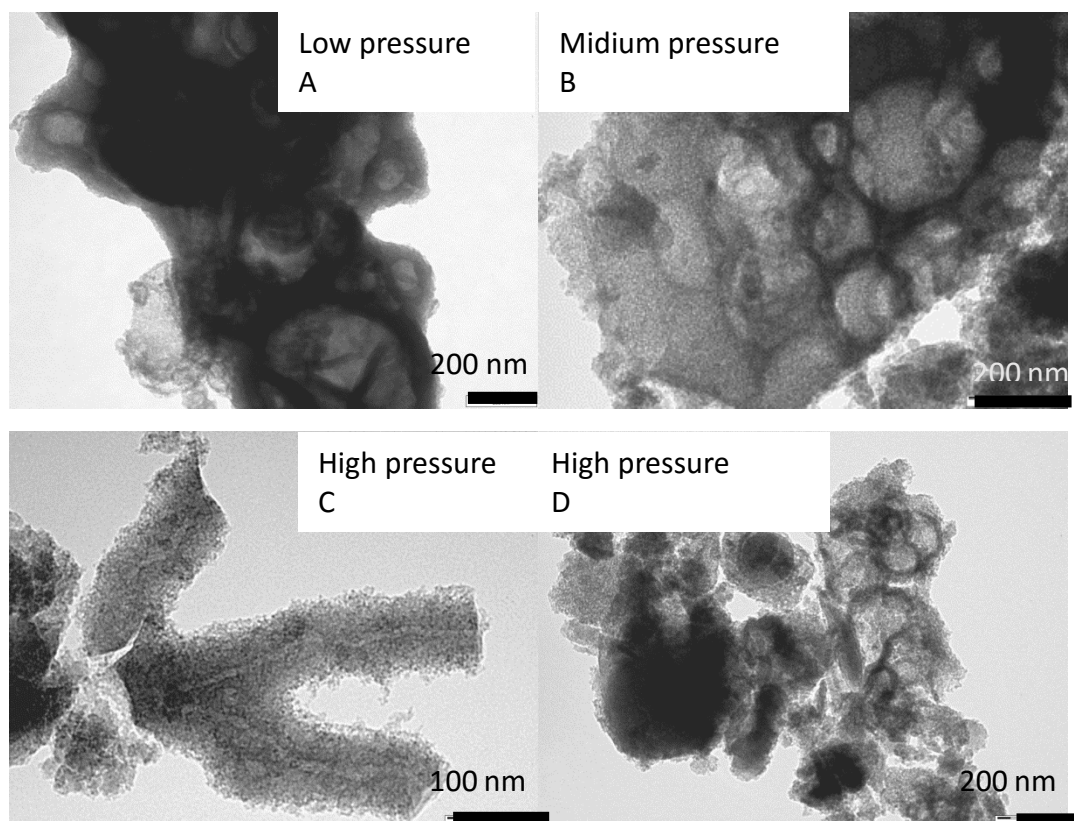
Figure 2.23 TEM micrographs of the samples prepared under 150 bar, 250 bar and 350 bar

Table 2.14 CO$_2$ density vs pressure change from 150 bar to 350 bar at 60 °C (From NIST Webbook)[155]

Pressure (bar)	Density (g/mL)	Pressure (bar)	Density (g/mL)	Pressure (bar)	Density (g/mL)
150	0.6041	220	0.7524	290	0.8220
160	0.6375	230	0.7647	300	0.8297
170	0.6646	240	0.7760	310	0.8369
180	0.6873	250	0.7865	320	0.8439
190	0.7067	260	0.7963	330	0.8505
200	0.7237	270	0.8054	340	0.8568
210	0.7388	280	0.8139	350	0.8629

2.4.2.5 Effects of temperature

Under the mixed preparation process, the variation of the system temperature could potentially influence the textural properties and the pore structures of silica materials. Porosimetry results in Table 2.15 showed a significant difference among three materials, demonstrating an increase in temperature leads to a higher BET surface area of up to 633 m^2/g, higher pore volume of up to 0.82 cm^3/g and larger pore size of up to 5.30 nm until the temperature reaches to 80 °C. This is consistent with Stucky's result: due to the temperature dependent hydrophobicity of the PEO block, higher temperatures result in large pore size in the synthesis of SBA-15 materials.[16] The PEO block become more hydrophobic at higher temperatures, resulting in increased hydrophobic domain volumes and thus increased pore sizes.[16] It is reported that physical properties of SCF such as diffusion coefficient, viscosity and surface tension, which could also be manipulated by the system temperature, may affect the overall supercritical solution structure, thus giving rise to different morphologies of silica materials.[56, 156] These differences in pore structure is likely due to the differences in nucleation or transport processes.[157] Hence, further work is needed to investigate the change of CO_2 physical property caused by the system temperature could potentially influence the pore structure of synthesised silica.

Table 2.15 Textural properties of the materials under different temperatures[a]

	Pressure (bar)	Temperature (°C)	BET surface area (m^2/g)	Pore volume (cm^3/g)	Pore size (nm)
S2-40	250	40	279	0.17	2.43
S2-60	250	60	495	0.33	2.63
S2-80	250	80	633	0.82	5.30

[a] The amounts of other compounds added were 0.8 g P123, 3.6 mL of TFA, 7.2 g water and 3.4 g TEOS.
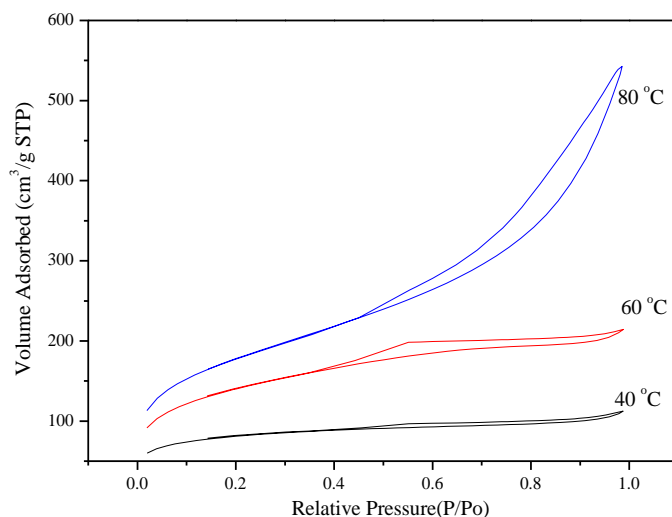
Figure 2.24 N$_2$ adsorption/desorption isotherm plots of the materials under different temperatures

Figure 2.24 showed the adsorption/desorption isotherm plots, indicating a significant difference in the nature of porosity. That implied different shapes of nanomaterials were prepared by adjusting the temperature. The height of hysteresis loop of S2-40 sample was much smaller than others, which suggested low mesoporosity for the sample prepared in that condition. Although the isotherm plot of S2-80 had a higher total pore volume consistent with the data in Table 3.14, there was a more gradual increase and decrease over a much wider range of relative pressure, indicating there is a much wider pore size distribution in the material. The same result was demonstrated in Figure 2.25, there was a clear single peak for S2-40 and S2-60 whereas the pore size distribution for S2-80 was over a much wider range. The figure also indicated that the a large quantities of the mesopores in S2-8 sample became larger from *ca.* 5 nm to *ca.* 10 nm, which was consistent with the previous literature results, showing that elevated temperatures translated to mesopores of wide pore size.[14, 158]
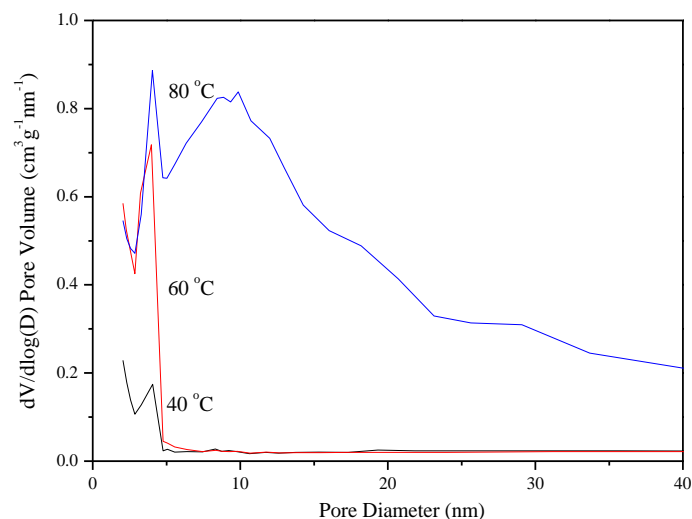
Figure 2.25 BJH pore size distribution curves of the materials under different temperatures

As mentioned before, CO_2 density may vary by controlling the pressure or temperature, and the values are shown in Table 2.16. Keeping the pressure consistent, higher temperature may lead to a lower density of CO_2. Its density decreases from 0.8794 g/mL to 0.6862 g/mL when the temperature increases from 40 °C to 80 °C. This has an identical effect as the decrease of pressure in terms of density effect. However, the TEM micrographs did not illustrate the same results, suggesting that this could not be explained by CO_2 density adjustment. Figure 2.26 shows a disordered amorphous silica material was synthesized at 80 °C. This is probably because high temperature is enough to disrupt the assembly mechanism, which is dependent on relatively weak forces, and is consistent with the research by Stucky.[16]
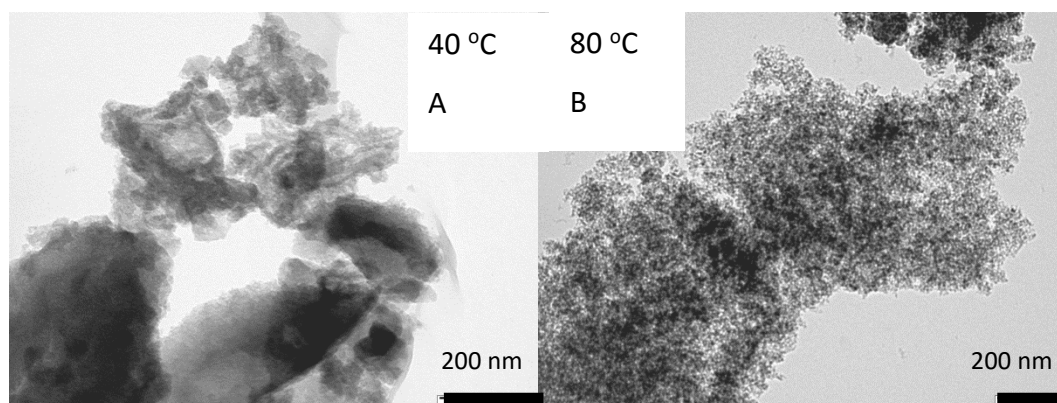
Figure 2.26 TEM images of the materials under different temperatures

Table 2.16 CO$_2$ density vs temperature change from 40 °C to 85 °C at 250 bar (From NIST Webbook)[159]

Temperature (°C)	Density (g/mL)	Temperature (°C)	Density (g/mL)
40	0.8794	65	0.7619
45	0.8571	70	0.7369
50	0.8341	75	0.7116
55	0.8106	80	0.6862
60	0.7865	85	0.6609

2.4.2.6 Effects of template

Both the isotherm plot without hysteresis loop and pore size distribution with minor peak for S2-no template sample showed that the silica material contained mostly microporous instead of mesopores if no template was used in the reaction.

Table 2.17 Textural properties of the materials prepared with different templates[a]

	P123 (g)	TEA-PFOS (g)	BET surface area (m^2/g)	Pore volume (cm^3/g)	Pore size (nm)	Yield %
S2-no template	0	0	367	0.20	2.22	26
S2-P123	0.8	0	495	0.33	2.63	33
S2-TEA-PFOS	0	0.8	807	0.62	3.06	67

[a] The amounts of other compounds added were 3.6 mL of TFA, 7.2 g water and 3.4 g TEOS. The reaction took place under 250 bar and 60 °C.

Two different kinds of surfactants have already been used for preparing the silica materials in the supercritical fluid, which are non-ionic surfactant P123 and ionic surfactant tetraethylammonium perfluorooctylsulfonate (TEA-PFOS).[160, 161] In Table 2.17, all the textural properties of sample prepared by TEA-PFOS are better than that prepared by P123, yielding samples which are much more comparable to commercial SBA-15. The BET surface area and the pore volume of S2-TEA-PFOS are 807 m^2/g and 0.62 cm^3/g, respectively, which are nearly twice those of S2-P123 as well as the yield. Its nitrogen adsorption/desorption isotherm plot (Figure 2.27) demonstrated a gradual rise for the adsorption branch while a sharp steep drop appeared in the desorption branch, which can be assigned as H2 type hysteresis loop resulting in the morphology of the pore structure with the wide bodied pores and narrow necks (ink-bottle type). The silica sample prepared without template was also synthesised and analysed for comparison. It was believed that the no template sample possessed disordered silica structures with less uniform pore sizes, which could be obtained from porosimetry results, and Table 2.17 indicated that its textural property and the yield were lower than that the other two.
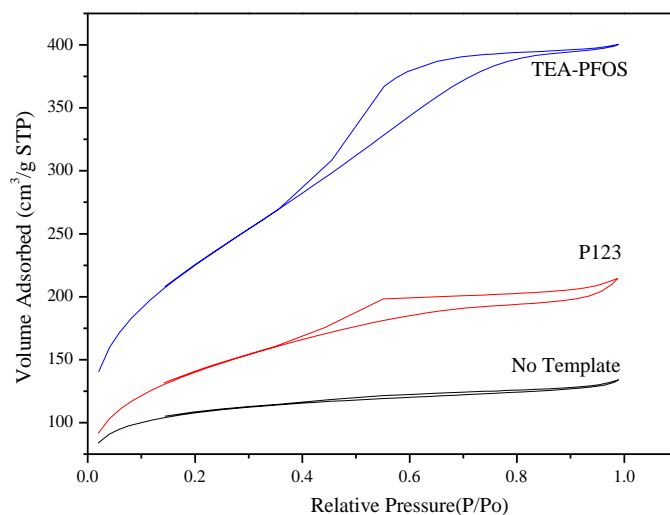
Figure 2.27 N₂ adsorption/desorption isotherm plots of the materials prepared with different templates
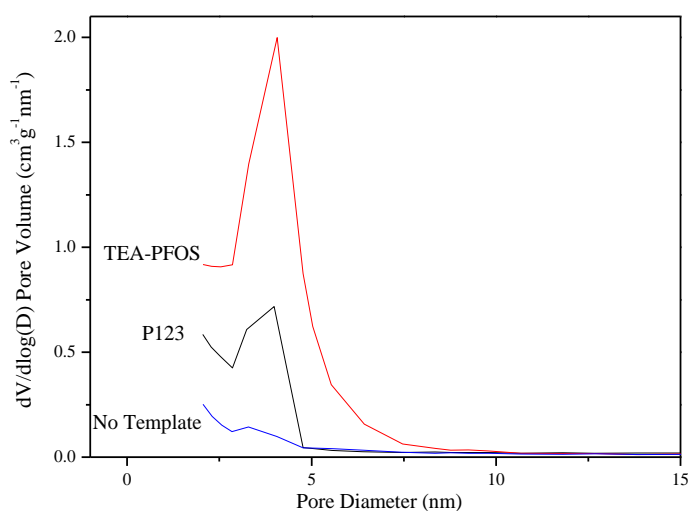
Figure 2.28 BJH pore size distribution curves of the materials prepared with different templates

The BJH pore size distribution (Figure 2.28) showed that there was a much higher pore volume for S2-TEA-PFOS, which was consistent with the results shown in Table 3.16. It is noteworthy that the peaks for both of these silica samples appeared around 4 nm, indicating a similar pore diameter was obtained for both of them. TEM images showed (Figure 2.29) that only S2-P123 had vesicle shape with non-uniform sizes whereas there was bulk silica with disordered pore structure in the S2-TEA-PFOS material, supporting that no regular micelles were formed by using TES-PFOS as template in SCF. Thereby, further work is needed to investigate the micelle formed by non-ionic or ionic surfactants in SCFs, which could be potentially used as template in the synthesis of mesoporous silica.
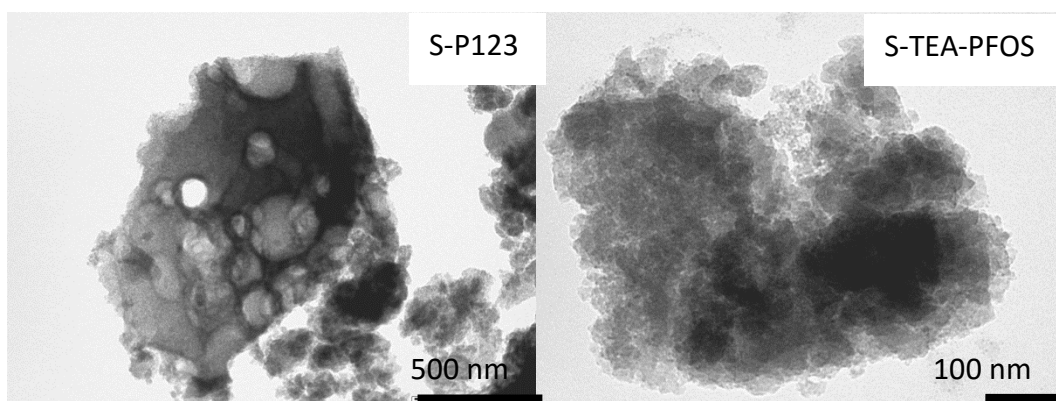
Figure 2.29 TEM micrographs of S-P123 and S-TEA-PFOS

104

2.4.3 Comparisons of different silica preparation methods

Table 2.18 demonstrated textural properties of silica samples prepared by different methods. SBA-15 and SBA-15-TFA were synthesised by the conventional method using HCl and TFA as acid, respectively. S-TFA was synthesised by using supercritical fluid as solvent and TFA as acid. The table indicated that SBA-15-TFA had a comparable specific BET surface area (768 m^2/g), pore volume (1.01 cm^3/g) and pore size (5.28 nm) than normal SBA-15. However, in Figure 2.30, the hysteresis loop with gradual rise for the SBA-15-TFA sample indicated that wider pore size range and less well ordered structures of SBA-15-TFA were obtained compared to the normal SBA-15. The porosimetry data also demonstrated that the sample prepared from supercritical fluid had lower BET surface area of 504 m^2/g, lower pore volume 0.35 cm^3/g and smaller pore size of 2.74 nm than others.

The adsorption/desorption isotherm plots (Figure 2.30) of three different kinds of nanomaterials were very different, suggesting the silica pore structures of three samples were not similar. The conventional SBA-15 curve typically belongs to the H1 hysteresis loop type. The curve of the sample from microemulsion method seems more like H2 hysteresis loop, which exhibited that the material may contain a large quantity of ink bottle type pores. Compared to the other two, there was a smaller hysteresis loop for sample prepared in supercritical fluid, which was consistent with the data in Table 2.18.

Table 2.18 Textural properties of silica samples prepared by different methods

	BET surface area (m²/g)	Pore volume (cm³/g)	Pore size (nm)
SBA-15[a]	942	0.82	3.51
SBA-15-TFA[b]	768	1.01	5.28
S-TFA[c]	504	0.35	2.74

[a] The sample was synthesized as the conventional method by using HCl.

[b] The sample was synthesized as the conventional method by using TFA.

[c] The sample was synthesized as the mixed preparation method by using TFA.
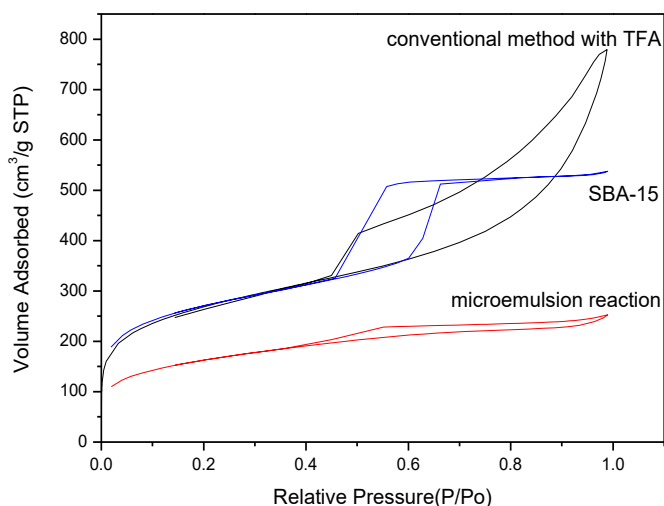
Figure 2.30 Adsorption/desorption isotherm plots of the samples prepared by different methods

From the low angle XRD analysis (Figure 2.31), normal SBA-15 has a significant peak occurred around $2\theta = 1.2^o$, indicating this kind of nanomaterial possesses a well ordered structural ordering. However, there is no significant peak observed from other two curves, suggesting these two samples had less ordered pore arrangement compared to the SBA-15 one. The fact that poor mesoporous structural ordering for these two samples may be due to the use of the acid TFA, which prevented the stabilisation of the micelles and structures formed by the template.

TEM images (Figure 2.32) showed there were significant differences between the samples prepared by different acids, which was consistent with powder XRD results shown in Figure 2.31. There was an ordered long range structure with hexagonal matrix for SBA-15 whereas both of the samples prepared by TFA whether under water phase or supercritical fluid demonstrated a vesicle shape without uniform structures.
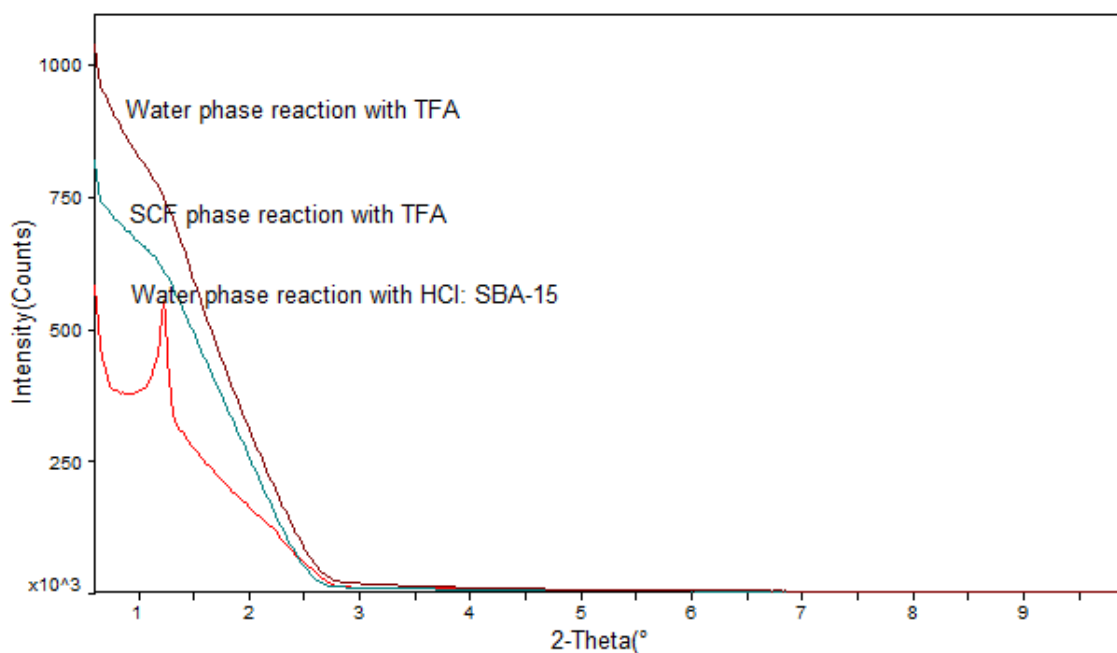
Figure 2.31 Powder XRD patterns of the samples prepared by different methods
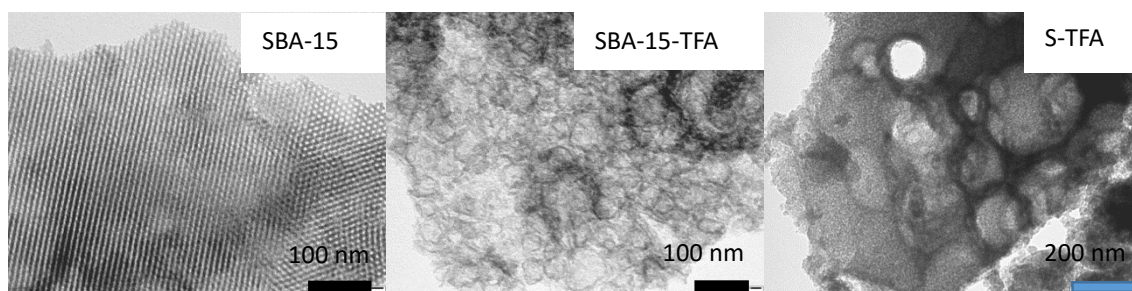
Figure 2.32 TEM micrographs of samples prepared by different methods

2.4.4 Investigation of silica hollow spheres

The optimal conditions in terms of the generation of vesical structures have been investigated through adjusting various parameters in the silica synthesis such as pressure, temperature, kinetics, reaction and water amount. Mixed preparation process is obviously advantageous to the isolated process, obtaining a mesoporous silica material with vesicular structure.

It is necessary to note that a spherical silica with hollow structure was successfully synthesized under static condition. In order to achieve a high proportion of this

morphology, a range of experiments by adjusting the temperatures and pressures under static condition was carried out.
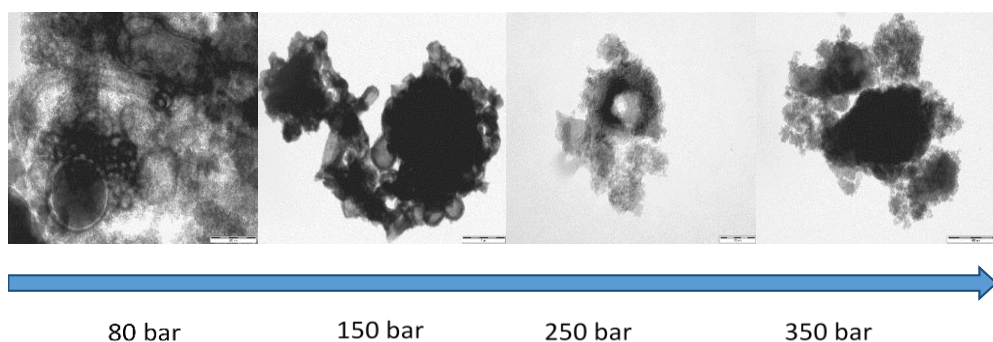
	80 bar	150 bar	250 bar	350 bar
BET surface area (m^2/g)	761	626	727	617
Pore volume (cm^3/g)	0.48	0.42	0.59	0.54
Pore diameter (nm)	2.53	2.68	3.27	3.48

Figure 2.33 Porosimetry results and the TEM images of the silica materials prepared with different pressures

Figure 2.33 illustrates the porosimetry results and the TEM images of the silica materials prepared under static condition with different pressures. The intact silica hollow spheres existed in the low pressure samples, while the spheres partially broke as the increase of pressure, and eventually became an amorphous silica with nonlinear array when the pressure achieved up to 350 bar. This could be explained by the increased density of $SCCO_2$ with the increase of the system pressure, which was discussed in 2.4.2.4. It should be noted that during the silica synthesis, a relatively slow depressurisation process was considered as big pressure change at short time could result in the collapse of pore structures. The density of $SCCO_2$ is close to that of water, resulting in a uniformly mixed phase during the synthesis of silica, thus forming the disordered amorphous silica. The porosimetry data shows the pore size of the silica increased as the pressure increased. This is probably due to the swelling function of $SCCO_2$ in higher pressure.[50]

	40 °C	60 °C	80 °C
BET surface area (m^2/g)	346	580	847
Pore volume (cm^3/g)	0.23	0.30	0.67
Pore diameter (nm)	2.7	2.1	3.2
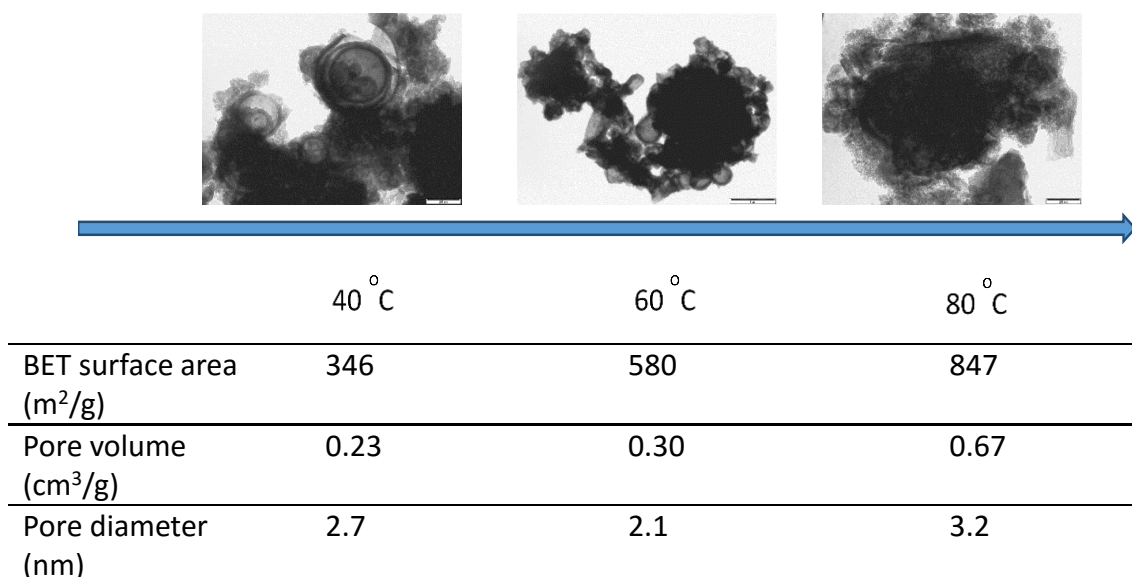
Figure 2.34 Porosimetry results and the TEM images of the silica materials prepared with different temperatures

Porosimetry results and the TEM images of the silica materials prepared under static conditions with different pressures are presented in Figure 2.34. This indicated that intact spherical silica structures were synthesised at lower temperature (especially for 60 °C sample), while the 80 °C sample only had fractured spheres. This could be attributed to the density variations under different system temperatures, which has been discussed in 2.4.2.5. The BET surface area and the pore volume of the materials was increasing from 346 to 847 m^2/g and 0.23 to 0.67 cm^3/g, respectively, as the temperature goes up due to the temperature dependent hydrophilicity of the PEO block.
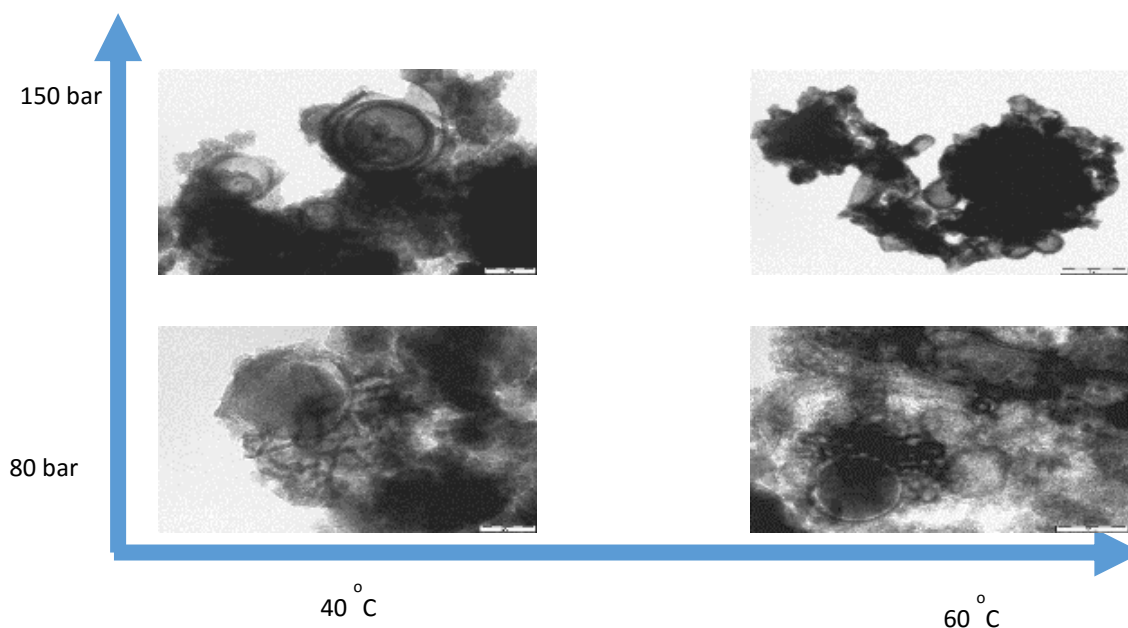
Parameters	
Mixing	Without stirring
Reaction time	24 h
Template	P123
Water amount	7.2 g
Acid	TFA

Figure 2.35 Optimal condition for the synthesis of spherical silica materials

Overall, the optimal condition for the synthesis of spherical silica in the supercritical fluids has been investigated and the results were illustrated in Figure 2.35. The CO_2 / H_2O microemulsion system will form during the synthesis without stirring, thus producing hollow spherical silicas. At low temperature and low pressure condition, the synthesised silica has intact spherical structure because of the lower $SCCO_2$ density, which was discussed in detail in the previous section. This silica sphere would be partially destroyed as the increase of temperature and pressure until the amorphous silica with nonlinear pore arrangement was produced. The pressure from 80 bar to 150 bar and the temperature from 40 °C to 60 °C is preferable for producing silica hollow spheres. It should be noticed that when the carbon dioxide approaches to its critical point, some of the physical properties would significantly change due to the formation of large molecular CO_2 clusters. This is not happening when the pressure or temperature is made to deviate from the critical value. Such a phenomenon is known as critical

opalescence,[162-164] however, this state has not been extensively studied. The optimal conditions in terms of the generation of vesical structures in this work - the pressure from 80 bar to 150 bar and the temperature from 40 °C to 60 °C – are very close to the supercritical point of CO_2, suggesting that the critical opalescence state has effect on the formation of the vesical silicas. Thereby, further work is needed to figure out the relationship between the properties of CO_2 under this state and the morphology of the synthesised silica.

According to previous research, Richtering *et al.* demonstrated that the formation of multilamellar vesicles were observed in the P123-butanol-water ternary system.[165] They highlighted that butanol acts rather as co-surfactant than as oil in their system since it is interfacially active. Analogously, SCF in our system could also act as both co-surfactant and solvent. The resultant vesicle silica have distinctive morphology and are expected to display novel physical and chemical properties, leading to the new applications in a wide range of applications such as drug delivery, catalysis, adsorption, and chromatography.[149, 166-168]

2.5 <u>Conclusion and further work</u>

2.5.1 Conclusion

The aim of this chapter was to investigate a novel and alternative method for preparation of porous silica materials using SCF.

Firstly, acid effect including the types of acid and the concentration of acid on the synthesis of SBA-15 in the aqueous phase was investigated. The TEM images indicated the silica materials had different matrix and structure based on the inorganic or organic acid applied in the preparation. A linear mesoporous channel and ordered hexagonal matrix was found in the silica material prepared using inorganic acid, while there was a vesicle matrix with a particle diameter of 40 nm in the sample prepared by TFA. At lower and higher HCl concentration, amorphous or less uniform silica with worm-shape was formed. In the adjustment of the TFA concentrations, smooth and intact vesicles were found in middle concentration sample, while fractured vesicles were synthesized under

low acid concentration, indicating the significant influence of the acid concentration. XRD analysis shows that normal SBA-15 had a distinct peak at low angle, while there was no clear peak observed in the samples made by TFA either in water or in SCF, indicating a poor structural ordering in the samples. The infrared analysis demonstrated that template removal such as calcination was a necessary procedure because SCF could not remove the template away from the pores of silica material after the reaction.

In supercritical fluid, mixed or isolated reaction processes were both carried out and some of the parameters were investigated. The resultant samples were characterised by common analytical techniques including porosimetry analysis, XRD, SEM and TEM. Overall the silica samples prepared by isolated process had poor textural properties, indicating a badly structured silica material with disordered and less uniform matrix, even the samples were synthesized by changing the various conditions. The lower water dispersion and too little water in this process may lead to inadequate hydrolysis during the reaction. In the mixed process, the silica samples had much higher textural properties than those prepared in the isolated process. Smooth vesicles were found and the shells were much thicker than the samples made without stirring in the process. On the contrary, there were higher proportions of bulk silica materials with less uniform structures in the stirring sample. That is probably due to formation of more homogeneous phase by stirring. In terms of water amount effect, the sample prepared under 0.36 g amount of water had a different type of adsorption/desorption isotherm plot with a gradual drop compared to other samples, indicating a different synthesis route took place. This is likely due to the increase of water content, the acid concentration increased. There was no silica product synthesized without water supporting the necessity of the existence of water to promote the hydrolysis. Besides, because more water is added into the system, lower acid concentration would be achieved, the silica samples prepared by higher amount of water formed silica gel rather than precipitate after the completion of the reaction. The porosimetry data revealed that there were slight differences between two silica materials prepared under 8 hours and 24 hours. However it should be noted that short reaction time may lead to the synthesis of fractured or incomplete hollow spheres. The effects of the adjustment of pressure were mainly due to the CO_2 density with the variation of pressure. At high pressure, the

system may form a uniformly mixed phase, which leads to the synthesis of bulk silica material. Moreover, a bigger expansion of silica pores at higher pressure indicates the better swelling function and better penetration ability of CO_2 as the increase of pressure, which also appeared in the higher temperature condition. Owing to the critical influence of the micelles formed by templates in the silica preparation process, varying the different templates would definitely change the morphology of the silica products. TEA-PFOS has been used as a new template, and the sample prepared by such a temple had an extremely high specific surface area, pore volume and pore size, which is comparable with the conventional SBA-15. This is probably due to the solubility of the fluorinated group in the template. However, the TEM micrographs revealed that there was no vesicle-shape or regular micelles when the TEA-PFOS was applied as template in SCF microemulsion.

2.5.2 Further work

In order to further explore potential morphologies of silica materials, alternative fluorinated surfactants such as sodium perfluorooctanoate are worth trying as templates for forming micelles in SCF in further work due to the critical importance of templates in preparation of silica. Similar phase behaviour investigation between micelles and SCF and micelle formation has been done before,[50, 73, 86, 94, 169, 170] but it is still needed to be studied further.

In 2.4.2.1, it is worth optimising the morphology and properties of the silica materials synthesized in the static preparation process through adjusting the pressure or temperature since such hollow spheres with intact silica walls have a quite high product yield and they are likely to find applications in catalysis, adsorption and drug delivery.

So far, all the acids used in preparation processes in SCF are TFA due to the high solubility both in SCF phase and aqueous phase. However, some other acids such as HCl and p-TSA are also worthy to be studied in SCF preparation and some research has been done in recent years.[49, 50, 91, 146, 171]

In terms of the effects of water in mixed process, the silica morphology of the samples prepared with 0.36 g water was different with that with more water amount added. Hence, it is worth doing more experiments with the addition of 0 to 0.36 g water to investigate the synthesis mechanism for lower water preparation process.

Due to the miscibility of ethanol in SCF, it would be interesting to introduce ethanol to the mixed preparation process to achieve a much higher level of miscibility of SCF phase and aqueous phase. Besides, in this process, the adjustments of water amount have been studied, and it is worthy investigating the influence of the different acid concentrations.

Finally, it would also be of interest to modify as-synthesised silica materials with metal and metal oxides directly in SCF, and such modified materials would be used as either catalysis or separation process. Alternatively, metal precursors such as metal salts or metal complex could also be applied in supercritical fluid process to synthesize metal nanoparticles which is analogous with the silica preparation process.

Chapter 3   Synthesis of tuneable carbon silica composite

Publication:

Conference poster presentation:

4th International Conference on Nanotek & Expo – "Green Preparation of Carbon-Silica Composites, December", San Francisco, USA

3.1 <u>Objective of this chapter</u>

The scope of this chapter is to develop the green approach of synthesising carbon-silica composite (CSC) by using bio-oil as carbon precursor. The bio-oil, as a sustainable resource, is generated from microwave assisted pyrolysis of waste office paper. The complex mixture of compounds within the bio-oil (including those molecules containing alcohols, aliphatics, carbonyls and aromatics) gives rise to the functionality of the CSCs. Thus the resultant CSC exhibits not only similar pore structural ordering as parent porous silica materials, but also unique advantages including temperature-dependent surface functionality. The carbon species in the materials vary significantly based on the carbonization temperature, resulting in a continuum functionality ranging from polar hydroxyl groups to aromatic surfaces of CSC. This creates unique advantages compared to traditional synthesis methods.

3.2 <u>Waste office paper utilization</u>

3.2.1 Paper manufacturing

Paper was first developed in China during the early 2nd century AD, by Cai Lun. Although there is a massive difference in the starting materials, the modern paper manufacture still retains a similar preparation process. In principle, making paper begins with pulp preparation, followed by the refining of the fibres. After the screening and cleaning to remove the moisture, the additives and auxiliaries are coated to provide a suitable surface for the specific end use.[172]

Generally, paper is made from wood pulp, accompanied by several kinds of additives and / or auxiliaries during the process. The wood pulp, as the major component in paper, is composed of cellulose, hemicellulose, lignin, and extractives (resins, tannins, and mineral materials). Cellulose is the predominant polymer, while hemicellulose and lignin were found in smaller amounts. Cellulose is a linear homopolymer of anhydro D-glucose units linked together by β-1,4 glucosidic bonds (Figure 3.1).[173] The highly ordered crystalline structure in the cellulose is mainly attributed to the hydrogen bonding (dashed line in Figure 3.1). Hemicellulose contains up to five different sugars, which are xylan, glucuronoxylan, arabinoxylan, glucomannan, and xyloglucan. Unlike cellulose with

crystalline structure, hemicellulose has a random, amorphous structure with little strength. Lignin is a dark coloured highly variable material consisting of complex organic chemicals, which varies depending on the source.[174] Due to the hydrophobicity of lignin, it could not be applied in the papermaking process. Through the increase of temperature, most of lignin would be removed from the pulp. The extractives such as waxes, pigments contribute little for the papermaking so that they are removed from the pulping process.[175]
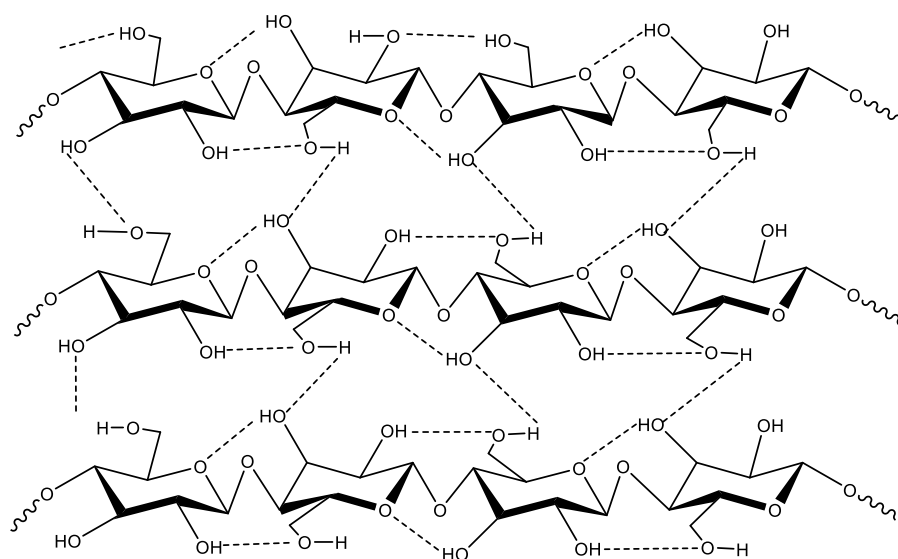
Figure 3.1 The schematic structure of cellulose[173]

Other than organic compounds in the paper, the inorganic compounds consisting of filling and loading materials such as calcium carbonate, clay, titanium oxide may be up to 30% of paper depending on the type of paper. Previous work revealed that the calcium carbonate was found in the residue (bio-char) after the pyrolysis of paper, while the carbohydrates such as cellulose and, hemicellulose, and also lignin contributed most to the bio-oil production.[112]

3.2.2 Utilization of waste paper

The production of paper and cardboard reached 91 million tonnes in CEPI countries in 2013 (Figure 3.2) and paper is an important tool in human's everyday life. However, this generates a big issue of treating the used paper at the end of its life in terms of environment protection and forest conservation. Until now, paper waste, which used to

118

be landfilled or incinerated at the end of life, has become the most important raw material for the paper industry. Hence, a significant success of paper recycling was achieved in the last decades. Almost any used paper can be recycled, including newspapers, cardboard, packaging, magazines and wrapping paper. In their 2012 paper recycling monitoring report, the European Recovered Paper Council declared that a paper fibre is collected and recycled on average 3.5 times.[176] The life cycle assessment of waste paper indicates that reprocessing of waste paper into new paper product have massive advantages over producing paper from virgin resources.[177]
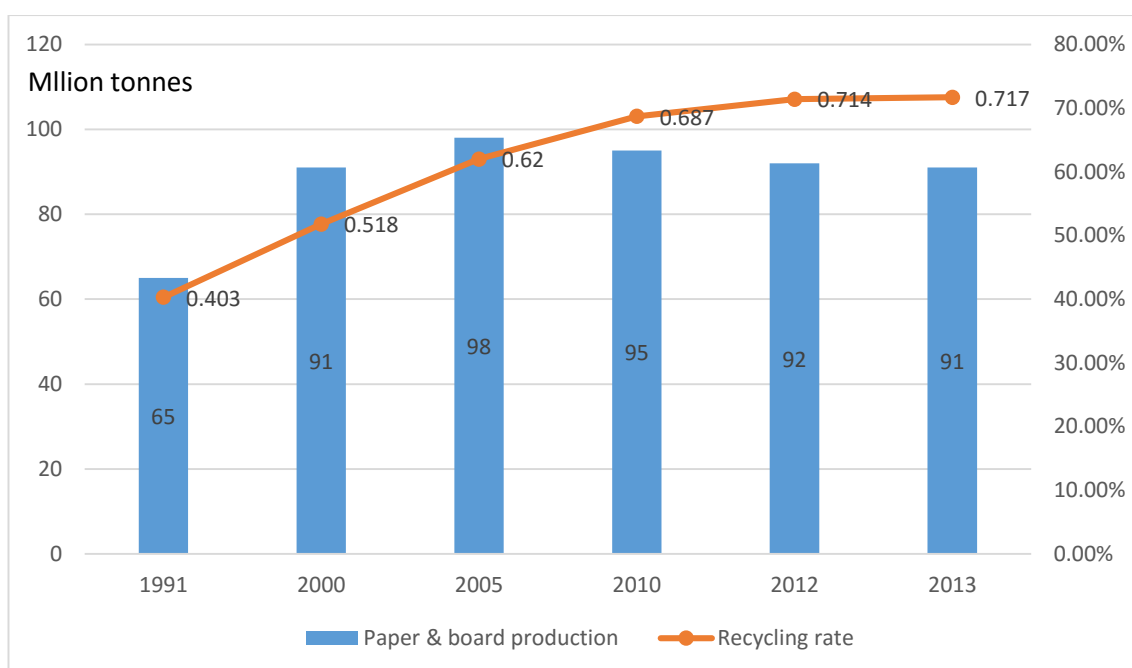
Figure 3.2 Production and recycling rate of Paper and cardboard from 1991 to 2013 in CEPI (Confederation of European Paper Industries) countries[178]

Theoretically, paper could be recycled and reused up to six or seven times, but it cannot be recycled indefinitely because the fibres would become too weak.[112] This is a limitation on recovery of used paper so that a large amount of used paper ends up with incineration or landfill. Due to impacts including the shortage of suitable disposal sites, the greenhouse effect and increasing public hostility to landfill due to increased environmental awareness, alternative ways of converting paper have become an urgent necessity. A significant body of research has demonstrated that waste paper has a huge potential as a source of high valuable chemicals through bioconversion processes, examples include lactic acid,[179] gluconic acid,[180] methane,[181] and ethanol.[182] The waste

119

paper could also be converted to adhesives *via* phenolation and methylolation. Cellulose, as the major component of waste paper, decomposed and reacted with phenol through phenolation to produce substances with a phenolic moiety. Subsequently, the methylolation proceeded by the substances reacting with fomaldehyde, which gave rise to the production of alkaline curable adhesive resins. The results indicated that the resultant product possesses comparable properties to a commercial phenolic resin in cure behaviour, resin viscosity and tensile bond strength.[183]

Some researchers have investigated the pyrolysis characteristics of waste paper.[112, 184, 185] Li and co-workers demonstrated that the bio-oil from pyrolysis of waste paper yield of 49.13% at temperature around 420 °C with the heating rate of 30 °C min^{-1}. It was reported the resultant bio-oil mainly contains four different classes: anhydrosugars, carboxyl compounds, carbonyl compounds and aromatic compounds.[185] Recently, the Green Chemistry group in the University of York converted waste office paper into bio-oil, bio-char and gas product via microwave-assisted low temperature (<200 °C) fast pyrolysis process, and the yield of bio-oil product was up to 42%, followed by the further utilization of bio-oil as an aluminium adhesive.[112] Bio-oil is potentially one of the most valuable products in the microwave pyrolysis of waste paper.[100] There are several review papers summarising its use both as an energy source for substitution of conventional fossil fuels and as a feedstock for chemical production with further separation.[186-188] It is important to note that the recovery of pure compounds from bio-oil and the upgrading of bio-oil to a high quality fuel is technically feasible but still not economically attractive due to the high energetic and financial cost.[189, 190] As such, a possible application of bio-oil without further upgrading as an environmentally sustainable and economically viable carbon source for fabrication of this composite and modification of silica surfaces have been explored.

3.3 <u>Microwave assisted pyrolysis experiment</u>

The detailed procedure of fabrication of bio-oil is described in Chapter 6. Basically, 160 g of waste office paper was weighed and compressed into the microwave vessel. The vessel was then placed in the "Milestone" microwave equipment. The sample was

gradually heated from 40 °C to 200 °C under vacuum (20 – 100 mbar) at a power of 1200 W for 12 minutes.

3.4 Characterization and identification of bio-oil

Bio-oils presented here are typically formed by depolymerizing and fragmenting cellulose, hemicellulose and lignin, which are the major constituents of waste office paper, with a rapid increase in temperature. As indicated in 3.2.1, the dominant component in the waste office paper is cellulose, and as such a significant proportion of the compounds present in the bio-oil are degradation products of this polymer.[100] A variety of analytical techniques have been applied for the characterization of bio-oil, including thermogravimetric analysis (TG), GC-MS analysis, NMR analysis and FT-IR analysis.

3.4.1 TG analysis
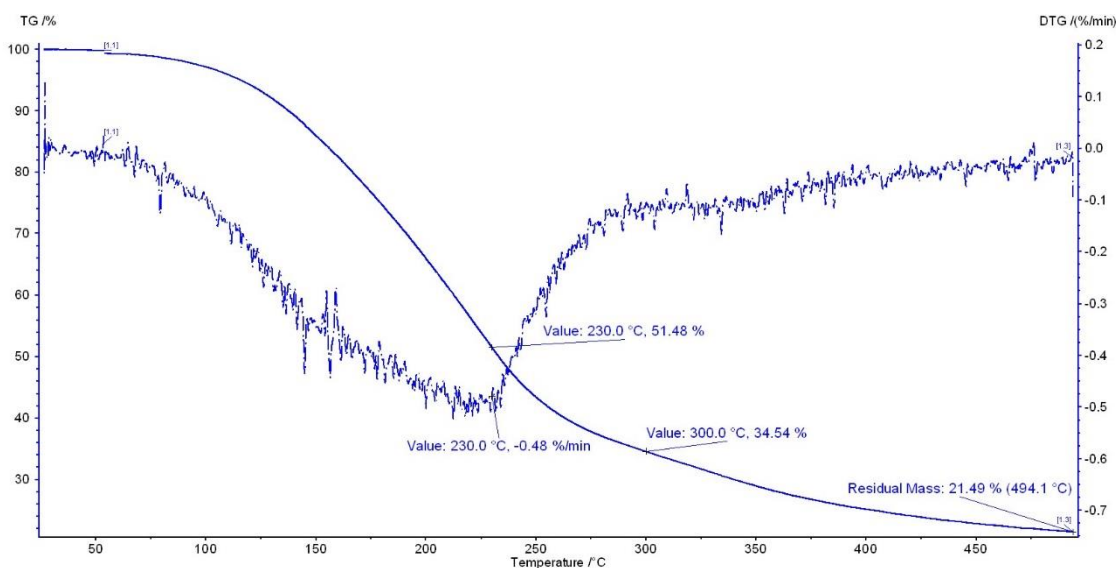
Figure 3.3 The thermogravimetric analysis curve of the bio-oil

TGA results for the bio-oil are shown in Figure 3.3. The sample was heated up to 500 °C at a heating rate of 1 K / min under nitrogen flow. The results indicated that a mass loss of approximately 80% was observed by 500 °C. There is one major peak in DTG curve, which indicates a significant weight loss during the thermal treatment in nitrogen at ~230 °C and occupies 48.52% of the total weight. At the end of the process, the mass of

121

residue is 21.49%.[191] Bridgwater surmised that the pyrolysis process at 500 °C eventually produces a solid residue of around 12 wt.% of the original biomass,[192] and he also concluded that lower process temperature favours the production of charcoal, which could be the reason for the fact that the solid residue percentage prepared in this work (21.49%) is higher than that in the literature (12%). Besides, the evaporation of light volatiles gave another mass loss, showing a minor peak at around 150 °C. It is should be noted that the bio-oil lost 65.46% of total weight when the temperature reached to 300 °C, which is the highest temperature for GC-MS analysis. This indicates that a significant proportion of the bio-oil is unlikely to be visible by GC-MS analysis. There is no mass loss at around 100 °C, indicating that little amount of water existed in the bio-oil. This is because ethanol was used for removing the water when collecting the bio-oil from microwave vessel.

3.4.2 GC-MS analysis

As described in Chapter 1, there are a large number of different types of compounds in bio-oil, which is indicated by the peaks on GC spectrum. Major peaks in Figure 3.4 are identified from the mass spectrometer database library. Some of silane compounds (11.32 minutes) appeared in the bio-oil are consistent with the column breakdown. As mentioned in 3.4.1, although many compounds in the bio-oil could be detected by GC analysis, there are still large amounts of different types of organics which could not be analysed via GC as most carbohydrate oligomers, which have insufficient volatility under the operation conditions of the equipment and some of the polar components only accessible by HPLC or GPC analysis. This has been investigated in previous research.[100]
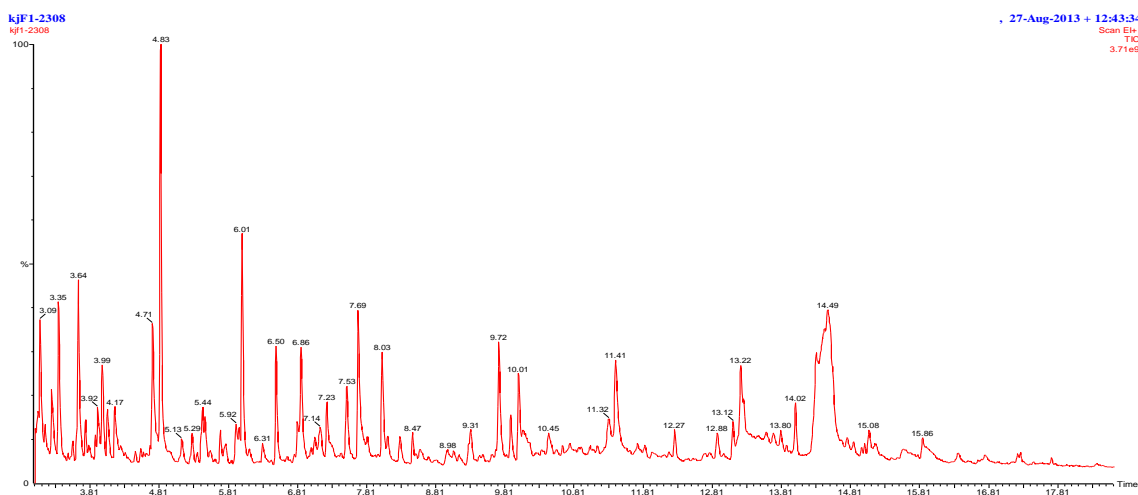
Figure 3.4 GC spectrum of bio-oil pyrolyzed from waste paper

As mentioned above, Li and co-workers categorised the bio-oil into four different classes: anhydrosugars, carboxyl compounds, carbonyl compounds and aromatic compounds.[185] However, it is found that there are several overlaps among these classes. For instance, anhydrosugars could possibly be carbonyl compounds and some carbonyl compounds could be aromatics. Hence, due to the complexity of types of the compounds in the bio-oil, they are broadly divided in to three groups by us. The 1st group is the carbohydrate class and its derivatives such as levoglucosenone, 1,4:3,6-dianhydro-α-d-glucopyranose, and levoglucosan, which mostly appeared at 8-15 minutes in the GC spectra. The 2nd group is the furanic compound including 2,5-dimethylfuran, 2(5H)-furanone, 2-(dichloromethyl)tetrahydrofuran, and 5-(hydroxymethyl)-2-furaldehyde (HMF). The 3rd group is the possible phenolic compounds.

Table 3.1 Typical identified compounds in the bio-oil according to the NIST database

Retention time/minutes	Identified compound	Retention time/minutes	Identified compound
3.09	Acetic acid	6.86	Propanoic acid
3.64	2,5-Dimethylfuran	8.03	Levoglucosenone
4.71	2(5H)-Furanone	9.72	1,4:3,6-Dianhydro-α-d-glucopyranose
4.83	1,2-Cyclopentanedione	10.01	5-(Hydroxymethyl)-2-furaldehyde (HMF)
6.01	1-Hydroxy-2-pentanone	14.49	Levoglucosan
6.50	3-Methyl-1,2-cyclopentanedione		

The NIST (National Institute of Standards and Technology) mass spectral database is a fully evaluated collection of electron ionization (EI) mass spectra. The compounds can be predicted by searching against the NIST library. The major identified compounds in the bio-oil based on the prediction of NIST database are listed in Table 3.1. The characterization and fragmentation of the major components derived from the waste paper was investigated in detail in the following section in order to help propose the identity of the compounds.

3.4.2.1 2,5-Dimethylfuran
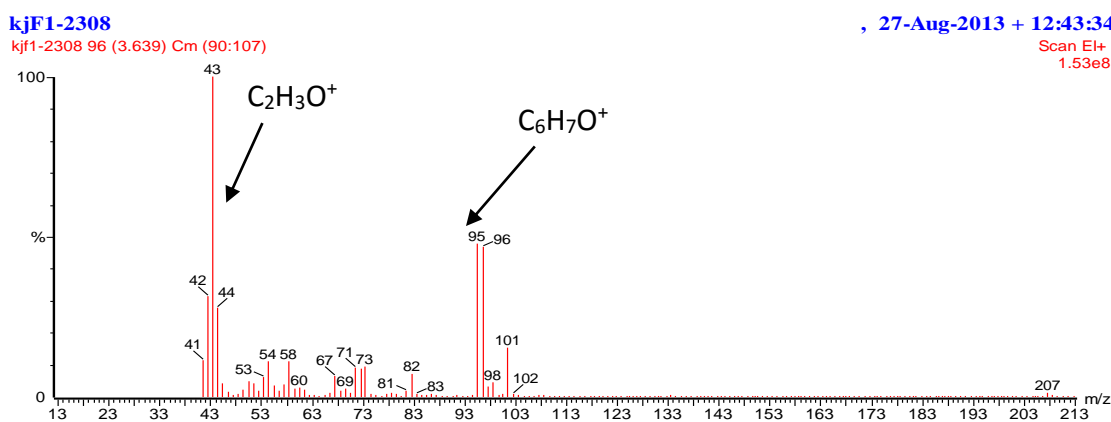
Figure 3.5 EI mass spectrum of 2,5-dimethylfuran from GCMS of bio-oil
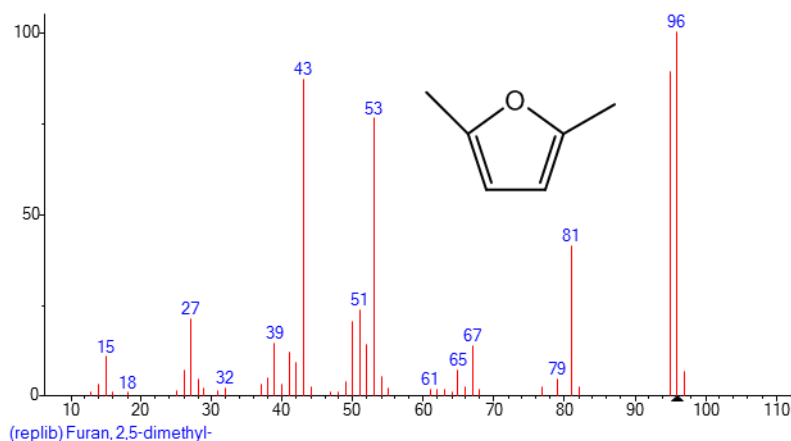
Figure 3.6 EI mass spectrum of 2,5-dimethylfuran from the NIST library

As indicated above, furanic compounds make up one of the major classes in the bio-oil by the depolymerisation of cellulose. A distinct peak at 3.64 minutes in the GC spectrum is assigned to 2,5-dimethylfuran. Figure 3.5 shows an EI mass spectrum for 2,5-dimethylfuran which is compared with the EI spectrum from the NIST library in Figure 3.6. Only the ions larger than 40 could be seen from the EI mass spectrum due to the instrument limitation. The parent ion $C_6H_8O^+$, which is abundant during the fragmentation, is due to furan's 6π-electron system, stabilising the molecular ion. The expected fragmentation pattern is described below (Figure 3.7), since usually in the fragmentation, weak bonds break in preference to strong bonds and bonds that break to form more stable fragments break in preference to those that form less stable fragments.[193]
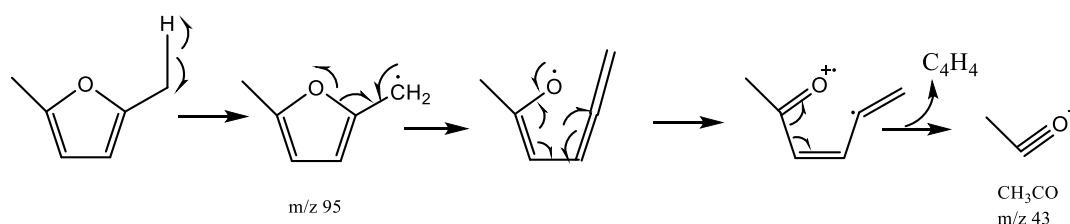
Figure 3.7 Formation of fragment ions m/z = 95 and m/z = 43

The ion $C_6H_7O^+$ assigned to m/z = 95 is produced with the loss of allylic hydrogen radicals from methyl group, which is in agreement with the result in the literature.[193] It is believed that typically $[M-1]^+$ ion is a strong fragment in methylfurans.[193] The base peak at m/z = 43 is assigned to the $[CH_3CO]^+$ group, which is produced by the loss of the oxygen

from the molecule together with the neighbouring carbon. The possible fragmentation mechanism is illustrated in Figure 3.7. Garscadden *et al.* studied the electron impact ionization of 2,5-dimethylfuran and five main product ions were produced, which were $C_6H_8O^+$, $C_6H_7O^+$, $C_5H_5O^+$, $C_2H_3O^+$, and $C_4H_5^+$.[194] This is consistent with the results discussed above.

3.4.2.2 2(5H)-Furanone
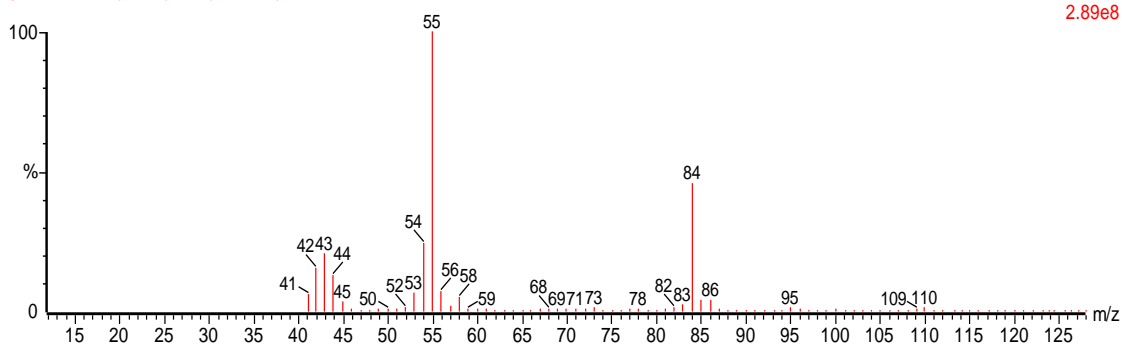
Figure 3.8 EI mass spectrum of 2(5H)-furanone from GCMS of bio-oil
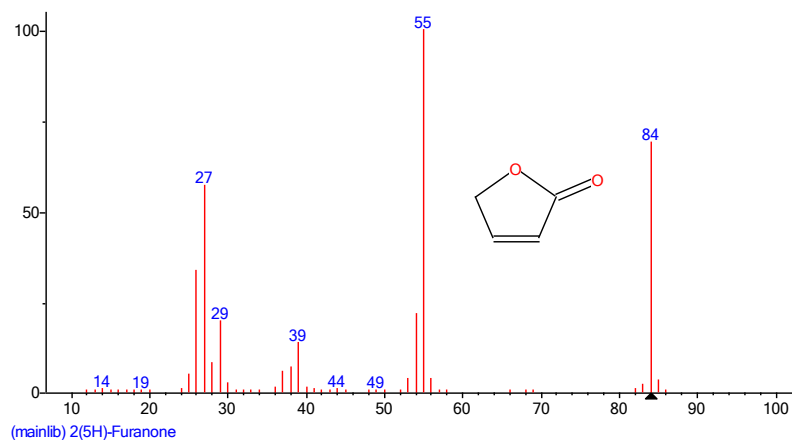
Figure 3.9 EI mass spectrum of 2(5H)-furanone from the NIST library

2(5H)-furanone is a kind of lactone. As can be observed from Figure 3.8, the abundant ions are located at m/z = 55 and m/z = 84. By comparison with the EI mass spectrum of 2(5H)-furanone from the NIST library (Figure 3.9) and the published paper,[195] the same peaks are demonstrated except for the undetectable peak at m/z = 27. The molecular mass of 2(5H)-furanone is 84 ($C_4H_4O_2$), which is indicated from Figure 3.8. The major fragment of this compound is C_3H_3O, the peak of which is located at m/z = 55. This is due

to the ring opening by the breakage of C-O bond and the elimination of the CO group from the molecule, followed by the further cleavage of an allylic hydrogen atom shown in Figure 3.10. Based on previous research, Gates *et al.* also concluded that the loss of CO group is the predominant process in the fragmentation of 2(5H)-furanone,[196] which is consistent with the mechanism proposed above.

$$C_3H_3O$$
$$m/z\ 55$$
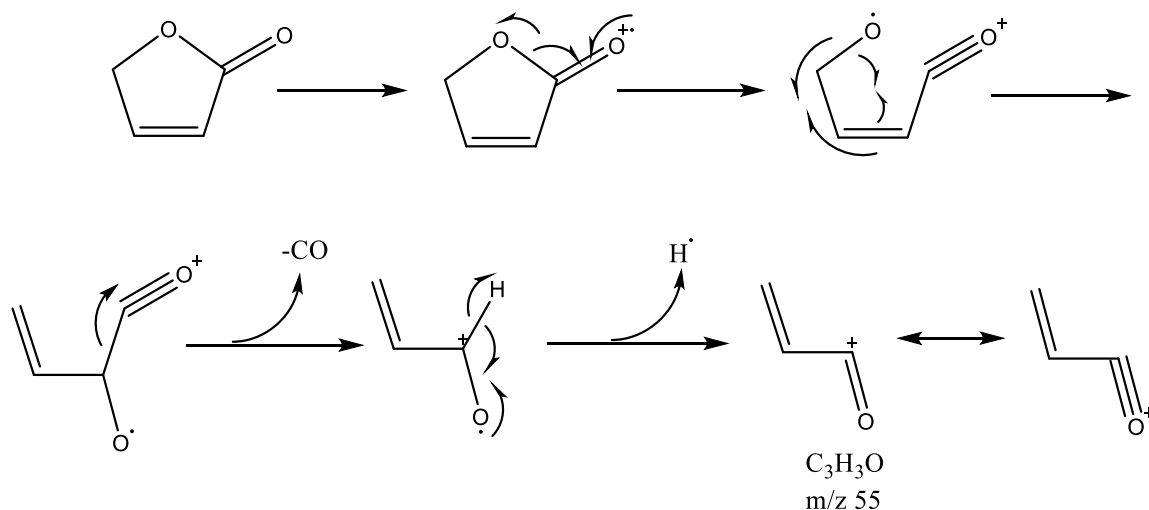
Figure 3.10 Formation of base peak ion m/z = 55

3.4.2.3 1,2-Cyclopentanedione

As shown in Figure 3.4, the most significant peak is located at ~4.83 minutes, which is assigned to 1,2-cyclopentanedione from the prediction of NIST library. Figure 3.11 shows the EI spectrum of 1,2-cyclopentanedione and Figure 3.12 shows the NIST library match of 1,2-cyclopentanedione.
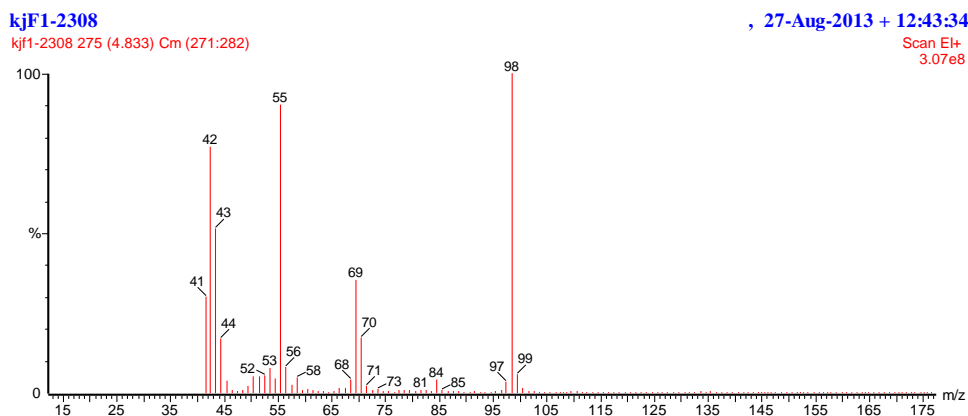
Figure 3.11 EI mass spectrum of 1,2-cyclopentanedione from bio-oil

127

(mainlib) 1,2-Cyclopentanedione
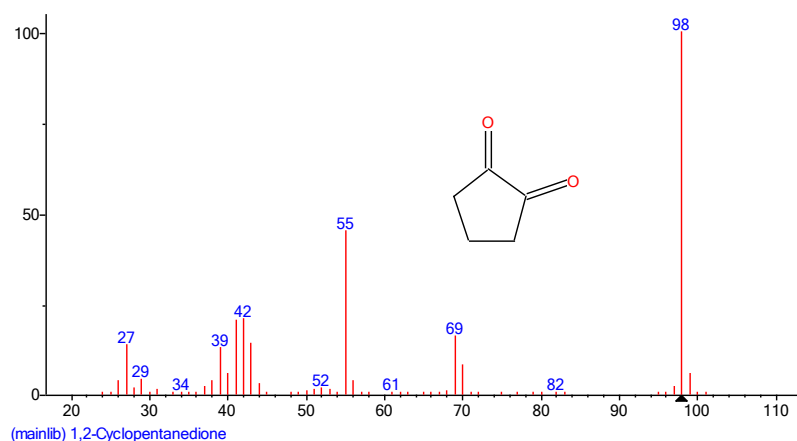
Figure 3.12 EI mass spectrum of 1,2-cyclopentanedione from the NIST library

The molecular weight of 1,2-cyclopentanedione is 98 ($C_5H_6O_2$), and the fragmentation ions are recorded as m/z = 42, 55, and 69 (Figure 3.11), which demonstrated good correlation with the literature.[197, 198] Main distinct EI fragment m/z = 55 is formed as a result of McLafferty rearrangement with the migration of a hydrogen atom then followed by the β-cleavage, as indicated in Figure 3.13 (pathway 1). Another important ion of $[CH_2CO]^+$ at m/z = 42 could also be identified and is also believed to be generated due to McLafferty Rearrangement. Weak ions at m/z = 70 and m/z = 69 are observed from Figure 3.11 and they could possibly form due to the direct loss of CO group form pathway 2.
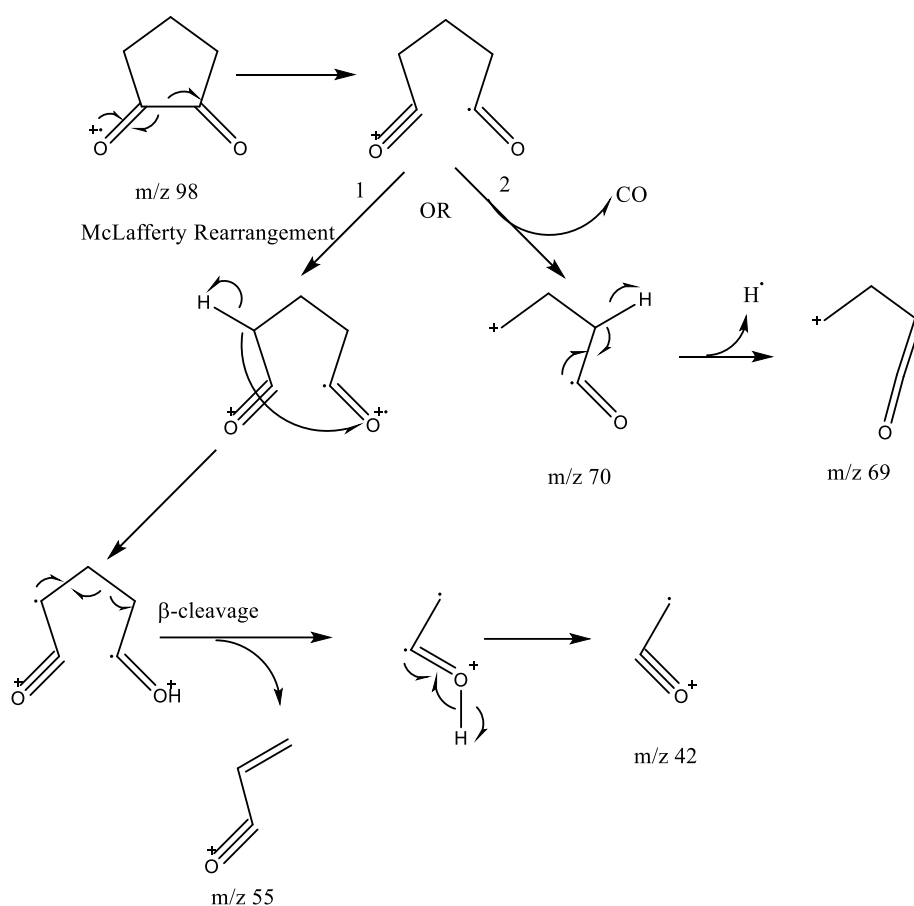
Figure 3.13 Formation of fragment ions m/z = 43 and m/z = 55

3.4.2.4 Levoglucosenone

Levoglucosenone is considered as another product of pyrolysis of cellulose, which is formed in large proportions when there is an acidic catalyst present in the sample.[199, 200] The structure was firstly confirmed forty years ago, and the high resolution MS technique conducted by Halpern revealed that the accurate molecular mass of the levoglucosenone is 126.0327 corresponding to a formula of $C_6H_6O_3$.[201] This is in good correlation to the data shown in Figure 3.14. Due to the unique nature of the structure including all carbon atoms with different chemical environments and easily modifiable functional groups, levoglucosenone has become attractive in the synthesis of chiral products.[202]
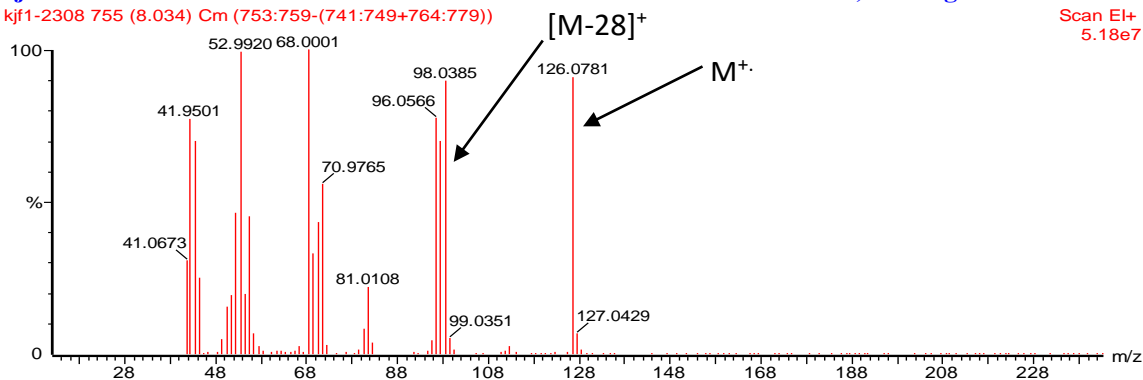
Figure 3.14 EI mass spectrum of levoglucosenone from bio-oil
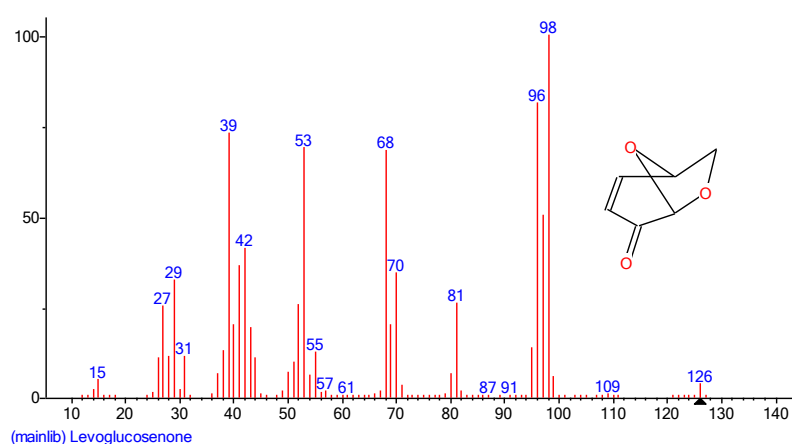
Figure 3.15 EI mass spectrum of levoglucosenone from the NIST library

The EI spectrum is compared with the standard spectrum (Figure 3.15), showing the major ions at m/z = 42, 53, 68, 98 and 126. The peak located at m/z = 98 is attributed to the elimination of C=O group shown in Figure 3.16. Subsequently the ion m/z = 68 forms as the most abundant ion from the cleavage of CHO^+ to give a 3-ring ion and further loss of allylic hydrogen radical.[203]
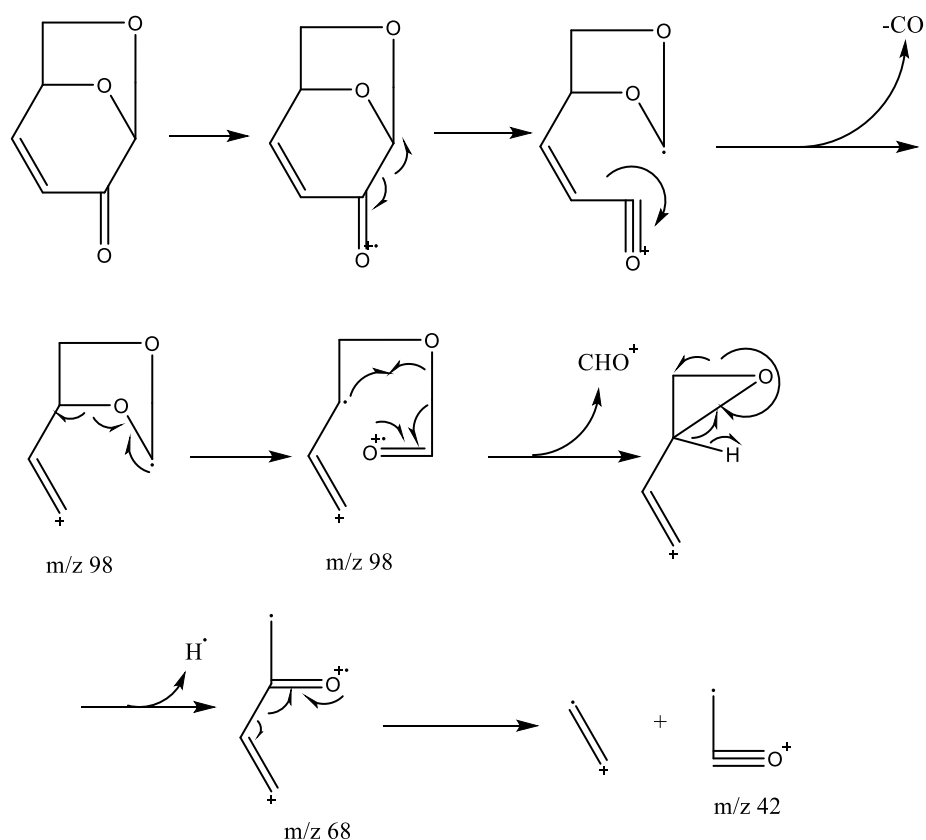
Figure 3.16 Formation of major EI fragment ions for levoglucosenone

3.4.2.5 Levoglucosan

Levoglucosan (1,6-anhydro-β-D-glucopyranose) is the most important pyrolytic product from cellulose, which is formed through the depolymerisation process. It should be noted that levoglucosan is also a potentially valuable and beneficial sugar compound. It could be used as a chiral synthon for the synthesis of stereoregular polysaccharides and as precursor to produce glucose and bio-ethanol through the hydrolysis reaction.[204, 205] It occupied a high proportion in the GC-MS visible component of the bio-oil, and has to be dissolved in methanol due to high polarity of this compound.[116] The similar shape and retention time in the GC spectrum of standard levoglucosan sample and bio-oil sample give further evidence of the presence of levoglucosan in the bio-oil. According to the literature, this compound is known as an important intermediate in the pyrolysis of cellulose, which is formed up to 60% of the yield in total,[206] and it could be possibly degraded to lower molecular-weight products or polymerized into polysaccharide.
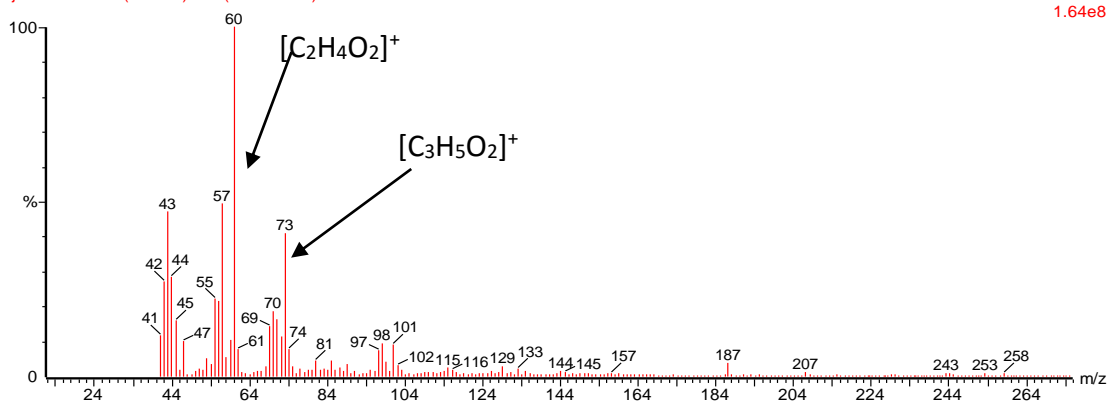
Figure 3.17 EI mass spectrum of levoglucosan from bio-oil
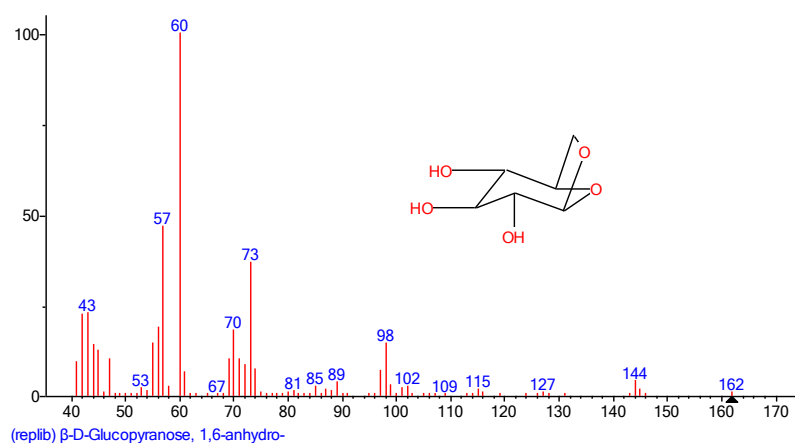
Figure 3.18 EI mass spectrum of levoglucosan from the NIST library

The EI spectrum of levoglucosan is shown in Figure 3.17 which is compared with the EI spectrum from the NIST library (Figure 3.18). As can be observed from the possible fragmentation process of levoglucosan in Figure 3.19, the fragment ion $[C_2H_4O_2]^+$ with m/z = 60 is generated through pathway 2 and this is the base peak ion. The possible fragmentation could be identified. Figure 3.19 also demonstrates another ion with distinct peak at m/z = 73 forms *via* pathway 1. It is reported that the ions at m/z = 60 and m/z = 73 have been widely used as marker fragments of levogluscosan.[207] It should be noted that due to the high energy of EI MS, the molecular ion of levoglucosan could not be shown in the spectrum.
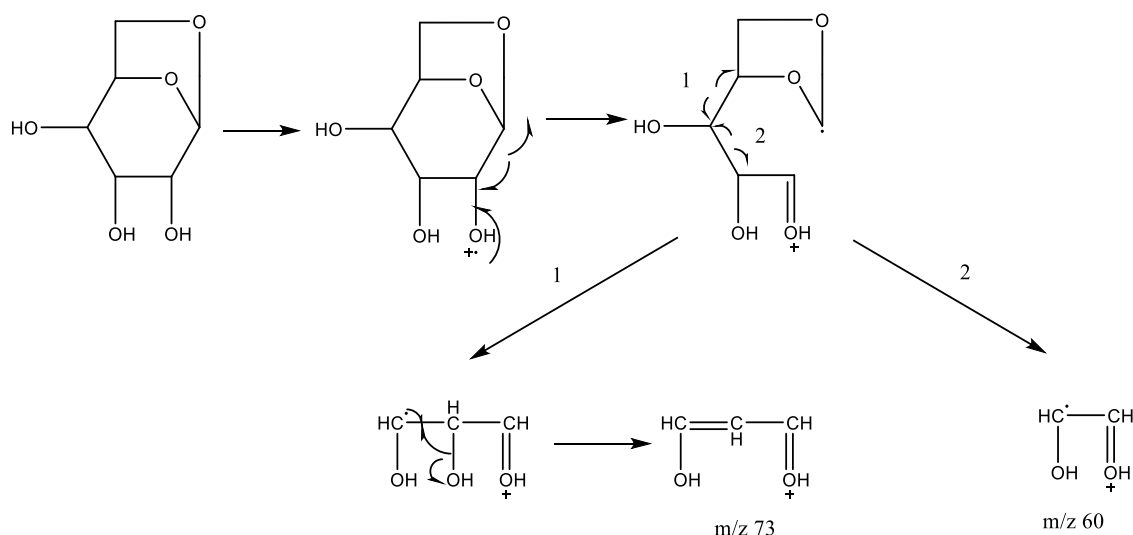
Figure 3.19 Formation of EI fragment ions m/z = 60 and m/z = 73

According to the previous research, it is demonstrated that levoglucosan could be thermally converted into 1,4:3,6-dianhydro-α-d-glucopyranose and –furanoses, thus further indicating the presence of 1,4:3,6-dianhydro-α-d-glucopyranose and 5-deoxy-α-d-xylofuranose appeared at 9.72 minutes and 11.41 minutes in the GC spectra, respectively.[208] Also after the dehydration reactions in the pyrolytic environment, it is reported that levoglusocan could be converted to levoglucosenone, probably suggesting the existence of these two compounds.[203, 209]

3.4.3 NMR spectra of the bio-oil

Both ^{1}H NMR (Figure 3.20) and ^{13}C NMR (Figure 3.21) spectra could give more structural information of the bio-oil. Due to the complexity of the composition of bio-oil, the corresponding NMR spectra are composed of many signals with different intensities. Thus, while it is very difficult to definitively identify specific components, the organic compounds could be categorized into several groups according to the chemical shift range.
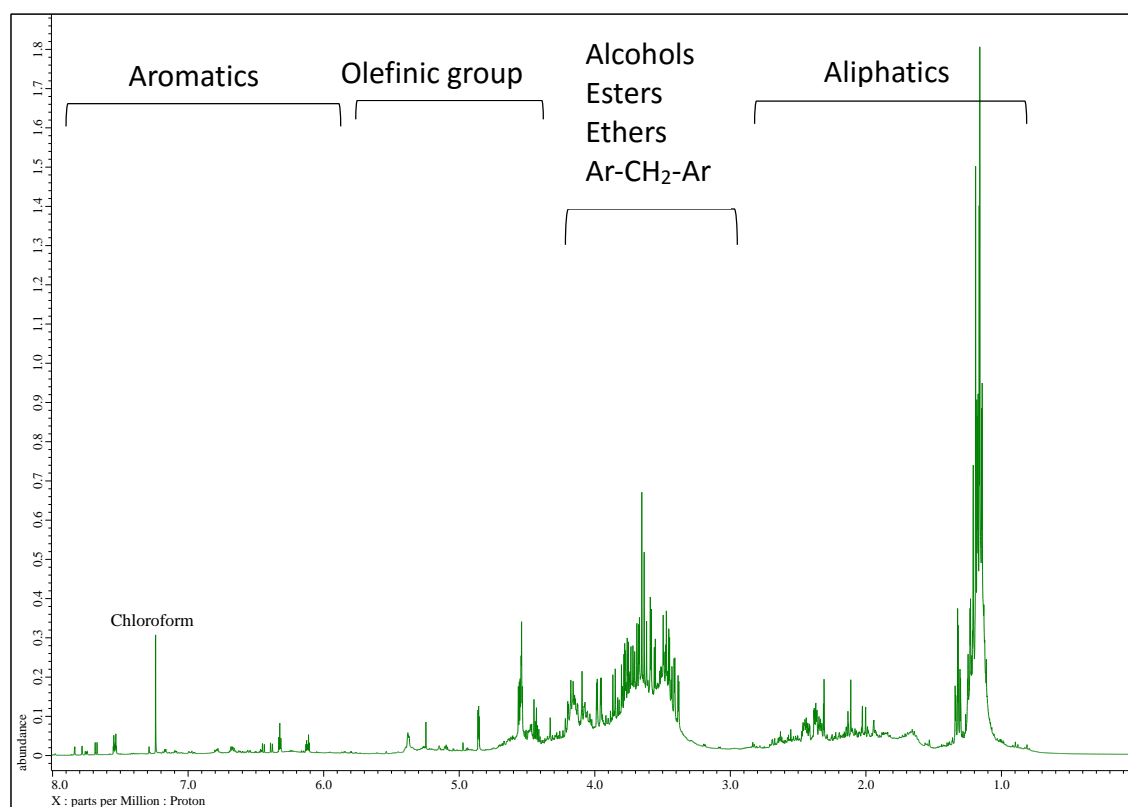
Figure 3.20 ^{1}H NMR spectrum of the bio-oil

^{1}H NMR spectrum of the bio-oil in Figure 3.20 shows the signals between 6 ppm to 8 ppm are assigned to the aromatics, and the weak peaks in this region reveal that the proportions of aromatics in the bio-oil is lower than other organic groups.[210] The presence of aromatics could also be reflected from ^{13}C NMR analysis (Figure 3.21). Olefinic resonances with low intensities occur in the chemical shift regions of 4-6 ppm.[211] Signals between 3 ppm to 4 ppm are assigned to the protons adjacent to C-O groups from saccharides, ethers, alcohols or esters, which could be evidenced from the IR bands assigned to –OH groups at 3300 cm^{-1} and the C-O bonds at 1053 cm^{-1} in Figure 3.22. Aromatic bridging methylene protons have a large proportion in the bio-oil and this band is also observed in the range of 3-4 ppm.[211, 212] Aliphatic protons were present in high proportions in the bio-oil corresponding to the characteristic peaks with high intensities between 1ppm to 3 ppm.[213] This is in agreement with the results of the IR spectrum, where the band at 2850 cm^{-1} was assigned to –C-H stretching vibrations. Such signals are possibly attributed to the long chain species including fatty acids or alkyl groups adjacent to carbonyls.
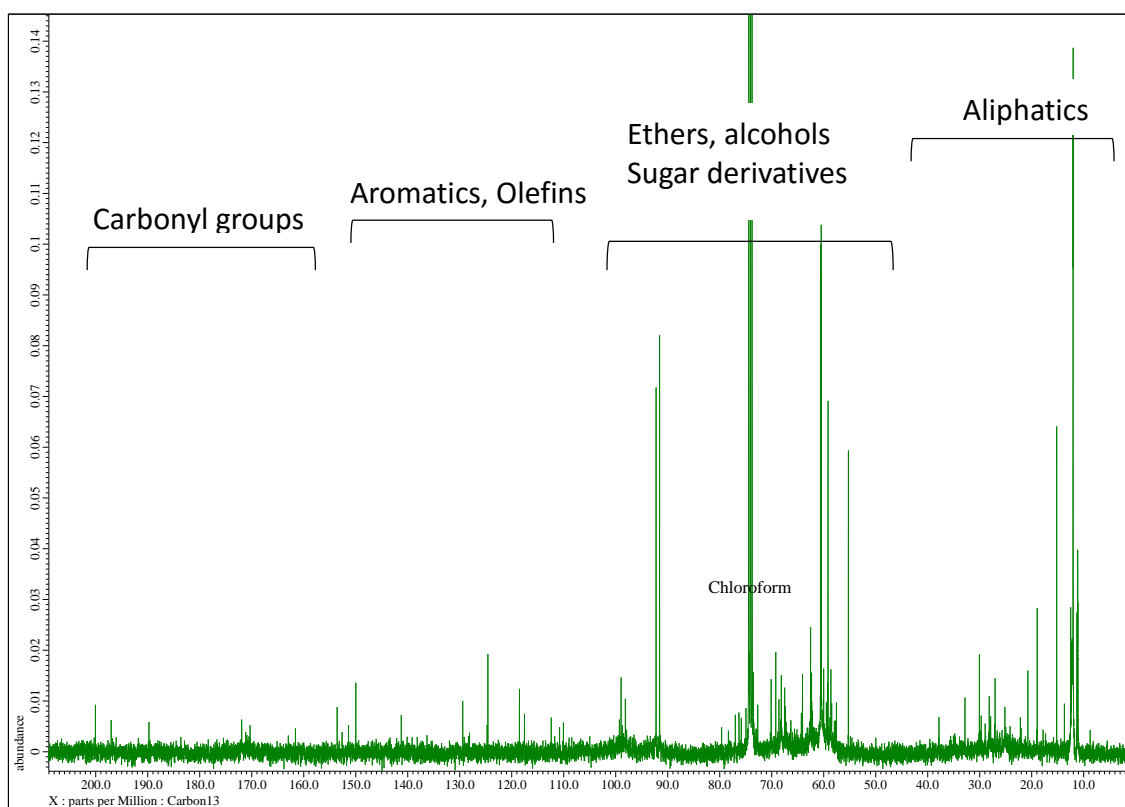
Figure 3.21 ^{13}C NMR spectrum of the bio-oil

Figure 3.21 shows the ^{13}C NMR spectrum of the bio-oil and the assignments for the carbons are illustrated.[214, 215] The chemical shifts above 120 ppm are difficult to observe due to the low intensities of these peaks. This is consistent with the result of ^{1}H NMR spectrum, which shows weak peaks at aromatic region. The sugar-derived compounds are present, indicating from the resonances between 50 ppm to 100 ppm, which is ascribed to the carbon atoms adjacent to an oxygen atom.[214] The high number of peaks suggests a large number of carbohydrate-derived products in the bio-oil. This correlates with the data shown in GC-MS analysis. The bio-oil contains carbonyl groups but the types are complex, such as carboxylic acid, esters, ketones and aldehydes. This could be reflected from the peaks located at 160 ppm to 210 ppm (160 - 170 ppm for carboxylic acid or esters, 190 – 210 ppm for aldehydes or ketones). Also as could be seen in Figure 3.22 of the IR spectrum of bio-oil, a significant peak assigned to the C=O groups could be detected, confirming the presence of carbonyl groups. According to the ^{1}H NMR and FTIR results, there is no doubt that the aliphatic structures are present with a high percentage in the bio-oil. This could be evidenced by the signals between a chemical shift range of 0-20 ppm in the ^{13}C NMR spectrum.

It could be concluded from both ^{1}H NMR and ^{13}C NMR spectra of the bio-oil that the composition of the bio-oil is complex. The carbohydrates and their derivatives are indicated as the majority in the bio-oils, along with a significant aliphatic content. The aromatic compounds such as furanic compounds are also present but with a relatively low proportion.

3.4.4 FT-IR analysis
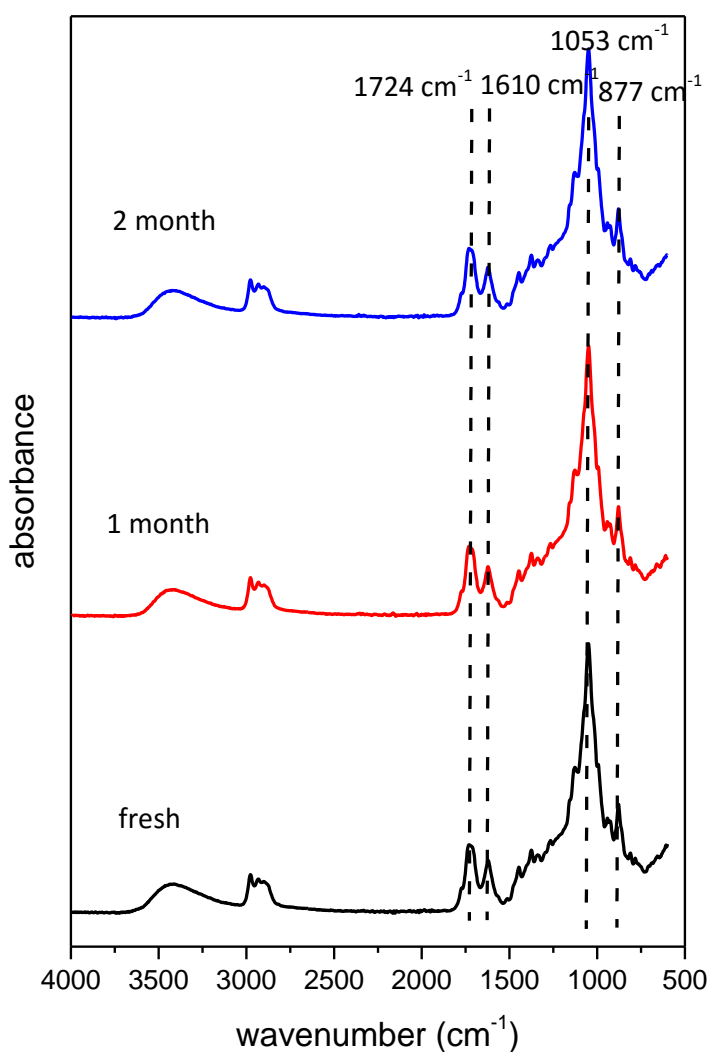
Figure 3.22 FTIR spectrum of crude bio-oil

FTIR spectra representing functional group compositional analysis of bio-oil was displayed in Figure 3.22. The major related peaks were identified and listed in Table 3.2.

The most significant peak is located at ~1053 cm^{-1} assigned to the C-O-C groups from pyranose rings, which suggests the presence of sugar compounds. The peaks at and around 2850 cm^{-1} assigned to -CH stretching vibrations indicating the existence of –CH, –CH$_2$ and/or –CH$_3$ group, and this group is also evidenced by peak of the –CH bending vibrations at 1382 cm^{-1} and 1450 cm^{-1}. The signals at 1724 cm^{-1} are attributed to the C=O stretching vibrations,[212, 213] which are consistent with NMR data pointing to the presence of carbonyl groups. These could possibly be contributed from ketones, aldehydes, carboxylic acids or esters. There is a weak peak at ~1610 cm^{-1} attributed to C=C stretching of the aromatic compounds in the bio-oil. The absorption band at ~3300 cm^{-1} is attributed to the –OH stretching vibration, consistent with the sample containing the carbohydrates and their derivatives.[216] It is reported the hydroxyl groups could be involved in hydrogen bonds, also resulting in the low frequency values for those bands.[212] It should be noted that a few quantities of water in the sample also contribute to the –OH peak. It is well documented that pyrolysis of lignin structure gives rise to the phenolic compounds.[216] However, there is no distinct evidence of the presence of phenolic compounds, consistent with the low intensity aromatic signal on the ^{1}H NMR spectrum, further suggesting small proportion of lignin in waste office paper. This result is also in agreement with GC-MS data (Figure 3.4) and ^{13}C NMR spectra (Figure 3.21), which shows few traces of phenolic compounds. A sharp peak at 877 cm^{-1} could be ascribed to the bending vibration of methylene groups.[217]

Table 3.2 FTIR peaks of functional groups identified in bio-oils

Hydrocarbon		Oxygen-containing	
Functional Group	Wavenumber (cm^{-1})	Functional Group	Wavenumber (cm^{-1})
C-H (aliphatic)	3000-2850 (br.)	O-H (alcohol)	3400-3300 (br.)
C=C (aromatic)	1610	C=O	1724
Aromatic Ring	850-700	C-O	1053

In order to investigate the chemical stability of the bio-oil, the sample was analysed by IR spectroscopy directly after formation, after 1 month time and 2 month time. The sample was kept in a refrigerator at 5 °C during this period. The very similar IR results

indicated that the chemical composition of bio-oil did not change dramatically for at least a two-month period. The stability analysis of bio-oil has been investigated by several research groups, which reported that the viscosity and the molecular weight of the bio-oil tend to increase with the time of storage.[192, 218] Since the bio-oil contains a variety of different components, it is believed that this change results from the chemical reactions, which still proceed in the bio-oil such as aldol condensation of aldehydes or ketones and polymerization of double bonded compounds.[100, 219] Temperature is the most important factor during the storage as it affects the rate of the chemical reactions.[219, 220] As a result, there is little change of the functional groups when the bio-oil is stored at 5 °C for 2 month.

3.5 <u>Carbon-silica composites (CSCs)</u>

Porous carbonaceous materials have played an important role in many fields of modern science and technology, such as separation processes, electronics, energy storage, biomedical devices and more.[221, 222] Therefore, a novel family of ordered mesoporous carbon materials designated as CMK series was firstly investigated by Ryoo *et al.* in 1999.[223, 224] The standard preparation procedure of this material involves the infiltration of mesoporous silica pores with mono- and di-saccharides, followed by their carbonization and silica removal. One of the advantages of this carbonization technique is that the resultant carbon materials could replicate the inverse mesostructural order after removing the silica templates with HF or NaOH solution. And later, further study was carried out on the modification of CMK with crosslinked polymers or metals to form chemically enhanced carbon materials.[225-227]

However, while relevant research focused predominantly on the preparation of porous carbonaceous materials,[228-230] far less has been published on the investigation of the carbon-silica intermediate product. Hence, the carbon-silica composite (CSC) would be the main target in this work. CSCs are prepared from bio-oil derived *via* microwave pyrolysis of waste paper, which is impregnated into the pores of a range of nanostructured silicas, followed by carbonization in nitrogen. This novel route allows the composite to retain the porosity characteristics of parent silicas, but attaches a thin carbonaceous film to the surface. In this case, the silica mesoporous structure feature

could be well controlled and retained *via* a new synthesis route. In contrast to the previous method, mesoporous materials with carbonaceous surfaces can be prepared via a short and cheap synthesis route. The incorporation of carbon onto silica pore wall not only results in interesting mesoporous carbon-silica composites, but provides a mechanically or chemically enhanced carbonaceous material.[231-235] The presence of the rigid silica framework in the composites could also greatly reduce structural shrinkage during high temperature pyrolysis.[236] As such, this porous composite may offer great opportunities for a variety of potential applications in electronics, chemical sensors, heterogeneous catalysis and for silica modification.[234, 235]

Many carbon materials have been synthesised from biomass, typically through hydrothermal carbonization, or pyrolysis.[237-240] The challenges in this field are particularly the control of the porosity of the material and the tuning of graphitic content. Conventionally, carbon sources used for synthesis of carbonaceous material are frequently pure chemicals and polymers such as (poly)furfural alcohol (PFA),[241, 242] dichloromethane,[243] and sugars (sucrose).[221] However, drawbacks such as toxicity, using products that compete with food and those that are highly purified may restrict the further development of carbon nanomaterials.[244-246] Therefore, it is important to identify carbon sources derived from waste that do not require purification, can easily undergo self-polymerization and do not compete with food. Bio-oil is a waste product of bio-char production obtained by microwave fast pyrolysis of a range of biomass types, including wood, rice husk, waste office paper and so on. Bio-oils usually contain many types of oxygenated compounds with various chemical properties, such as aldehydes, ketones, phenols, esters, sugars, furans and multifunctional groups.[100, 103, 109, 216, 247] Herein, a possible application of bio-oil as an environmentally sustainable and economically viable carbon source for fabrication of this composite has been explored.

3.5.1 Thermal analysis of CSC materials

Figure 3.23 demonstrates the thermogravimetric analysis for the sample from 100 ^{o}C to 800 ^{o}C. The mixture was placed in the furnace and heated from room temperature to 800 ^{o}C at a heating rate of 5 ^{o}C / min under nitrogen. There are two major peaks observed from DTG curve, showing two parts of mass loss during the heating process at 156 ^{o}C

139

and 220 °C. This could also be observed from the TG analysis of bio-oil in 3.4.1. These two mass loss could attribute to the evaporation of light volatiles and the decomposition of organic compounds in the bio-oil, respectively. As discussed in 3.4.1, the thermogravimetric analysis of pure bio-oil was discussed, indicating that 48.53 w/w % of the sample possibly decomposed or evaporated at 230 °C. For CSC sample, smaller amounts of bio-oil decomposed, suggesting much more components in the bio-oil tend to crosslink in the presence of silica. This suggests that the incorporation of silica framework gave rise to the polymerization of bio-oil, which has been an excellent property of the utilization of bio-oil for the synthesis of CSCs.

At the end, the residue mass is 47.44%, consisting of carbonaceous films and SBA-15 framework. Moreover, it is necessary to note that a relatively flat DTG curve after 400 °C suggests that the mass of the sample changed little (~7%) at the temperature ranging from 400 °C to 800 °C. This result is consistent with the IR and NMR data discussed in 3.5.3, which shows very similar spectra for CSC-400, CSC-500, CSC-600, CSC-700 and CSC-800 sample. It could be observed that there is a minor mass loss at around 100 °C due to the evaporation of water, which was not observed from the TG graph of bio-oil. This is probably attributed to the moisture content in the parent silicas.
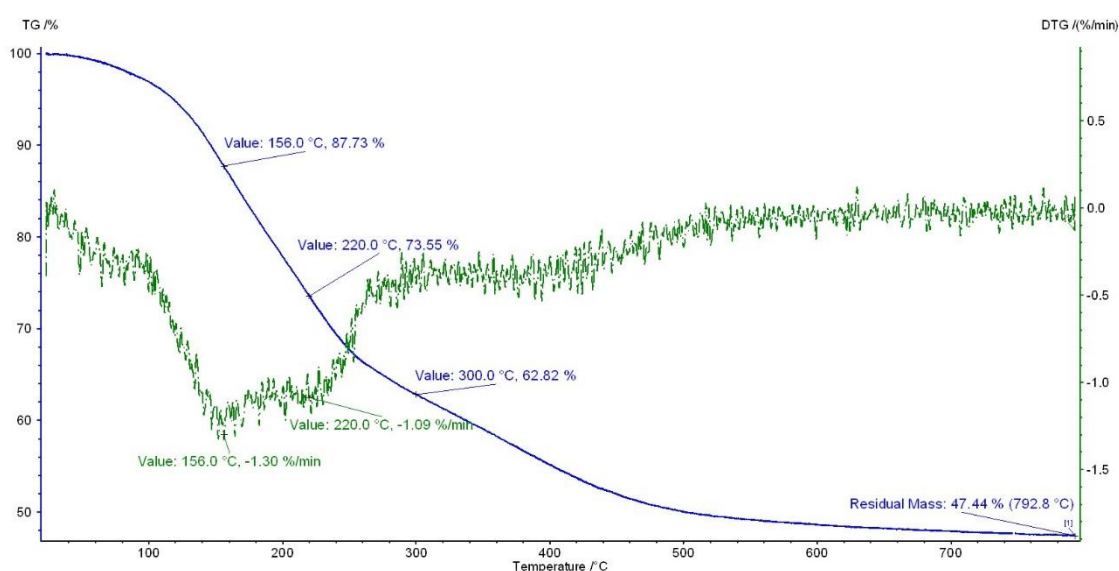
Figure 3.23 Thermogravimetric analysis of CSC material

TG-IR 3D spectrum demonstrates the IR spectrum of released gas during the carbonization of the CSC sample from room temperature to 800 °C. It is an important

analytical technique to detect the type of components released from the CSC material when the carbonization temperature increases. At the initial 100 ^oC, the intensity of peak is very low, proving that only small amounts of gas (mainly water) were volatilized from the sample. As observed from Figure 3.24, there are a large number of peaks before 400 ^oC, indicating that most of the components were decomposed or evaporated from the sample in this temperature range. This is in good correlation to the TG results above. Especially when the system was heated to about 160 ^oC, there are two strong signals A and B observed from the spectrum, suggesting large amounts of components were released from the system. This could be evidenced by the largest mass loss at this temperature in TG curve.

The IR spectrum of the released gas at 160 ^oC was extracted and shown in Figure 3.25 (I). It is clear that there is a significant peak located at 1082 cm^{-1}, which is ascribed to C-O-C groups, possibly due to the presence of decomposition product from saccharides. From the discussion of IR analysis of bio-oil in 3.4.4, another characteristic peak at 2979 cm^{-1} could be assigned to -CH stretching vibrations, indicating the presence of –CH, –CH_2 or –CH_3 groups. As can be seen in Figure 3.24, although the intensities of these peaks were decreased from 160 ^oC, they could be detected continuously until 400 ^oC, indicating the sample still contain these components before 400 ^oC. This is consistent with the NMR results in 3.5.3. A peak at 1807 cm^{-1} could be attributed to the carbonyl group associated with anhydrides in the spectra, suggesting that these groups were released at this temperature. The fact that the second band close by the peak at 1807 cm^{-1} is another evidence for the presence of anhydrides as anhydrides have asymmetric and symmetric stretches. A sharp peak at 877 cm^{-1} could be ascribed to the bending vibration of methylene groups.[217] The minor peak at 2350 cm^{-1} should be attributed to the vibrations of carbon dioxide, compared from the standard IR spectrum of carbon dioxide.

Temp. °C
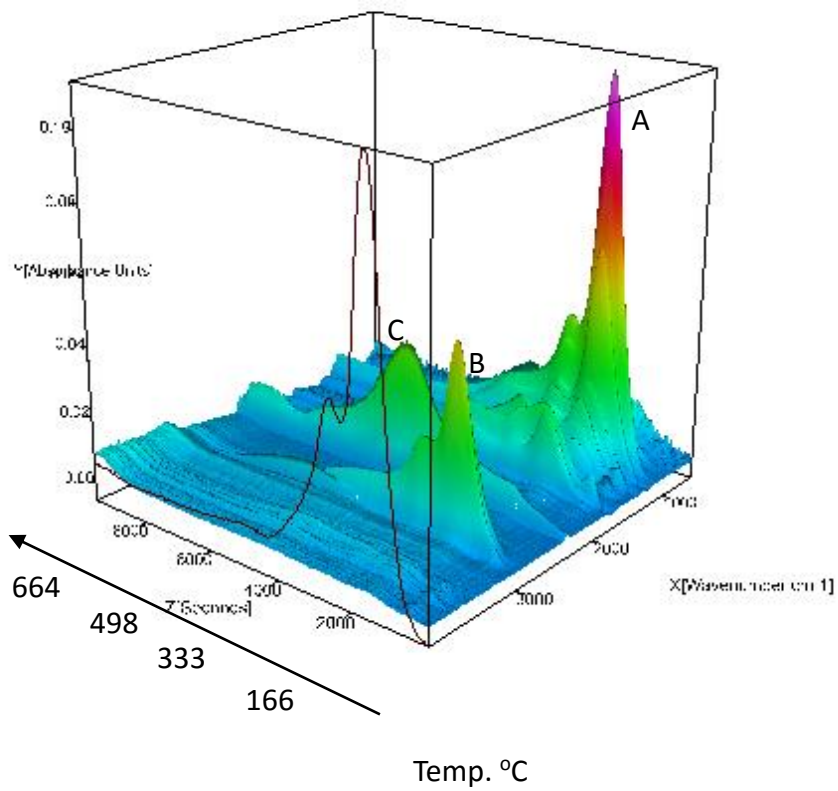
Figure 3.24 3 Dimensional IR spectra of CSC sample (Ramp rate: 5 °C/min)
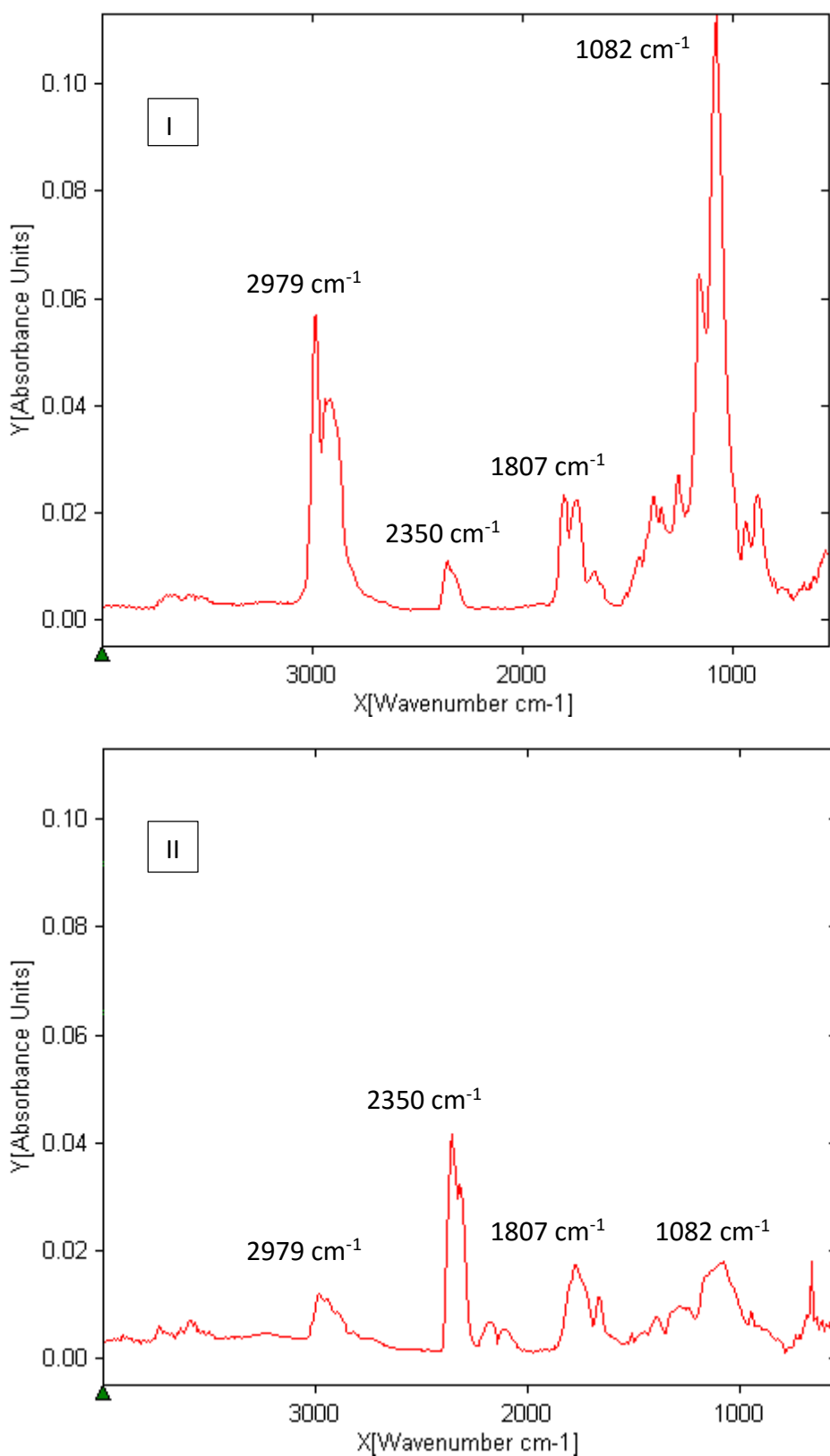
Figure 3.25 IR spectrum at 160 ⁰C (I) and 400 ⁰C (II) (extracted from 3D spectra)

Figure 3.25 (II) demonstrates the IR spectrum of released gas at 400 ⁰C. As can be seen in this figure, the peak locations of the spectrum at 400 ⁰C is qualitatively similar to that

at 160 °C expect for the intensity and resolution of these signals, indicating the similar components came out from the CSC sample. It should be noted that the intensity of two peaks at 2979 cm^{-1} and 1053 cm^{-1} dramatically decreased, indicating only a small amount of corresponding components is released from the sample, thus suggesting there is not so much in the sample. This is consistent with the results in 3.5.3. It is noted that the dominant peak is located at 2350 cm^{-1} (Peak C in Figure 3.24), which is assigned to CO_2, and the double peak located just slightly lower than 2350 cm^{-1} is attributed to CO. As such, the results in Figure 3.23 indicated that the mass of the sample changed gently after 400 °C.

3.5.2 Variations of heating rates

In a typical pyrolysis process, heating manner is an important factor especially for mesoporous materials. A quick heating rate in the pyrolysis could result in the pore collapse and thus destroy the mesoporous structure of the material. Ranjit *et al.* reported that the calcination process at heating rate of 5 K/min or higher usually led to the collapse of MCM framework.[248]

Table 3.3 Textural properties of SBA-15 samples prepared with different heating rates

	BET surface area (m^2/g)	Pore volume (cm^3/g)	Pore diameter (nm)
1 K/min	795	0.80	4.04
3 K/min	701	0.69	3.96
5 K/min	829	0.84	4.04

In order to investigate the influence of heating manner on the CSC material, it is important to know about the thermal stability of SBA-15 silica materials. Thus the parent SBA-15 is heated at a heating rate of 1 K/min, 3 K/min and 5 K/min under the nitrogen flow and the resultant samples were analysed by nitrogen porosimetry and XRD. Table 3.3 shows that the SBA-15 pyrolyzed via the heating rate of 1 K/min, 3 K/min and 5 K/min possess the similar specific BET surface area, pore volume and pore diameter, indicating the heating rate up to 5 K/min has a small effect on these parameters. The same result

is evidenced by the isotherm plots, which demonstrates the typical type-IV isotherm plot with an H1-type hysteresis loop, and a steep capillary condensation step in adsorption and desorption branch implies a uniform mesoporous size.
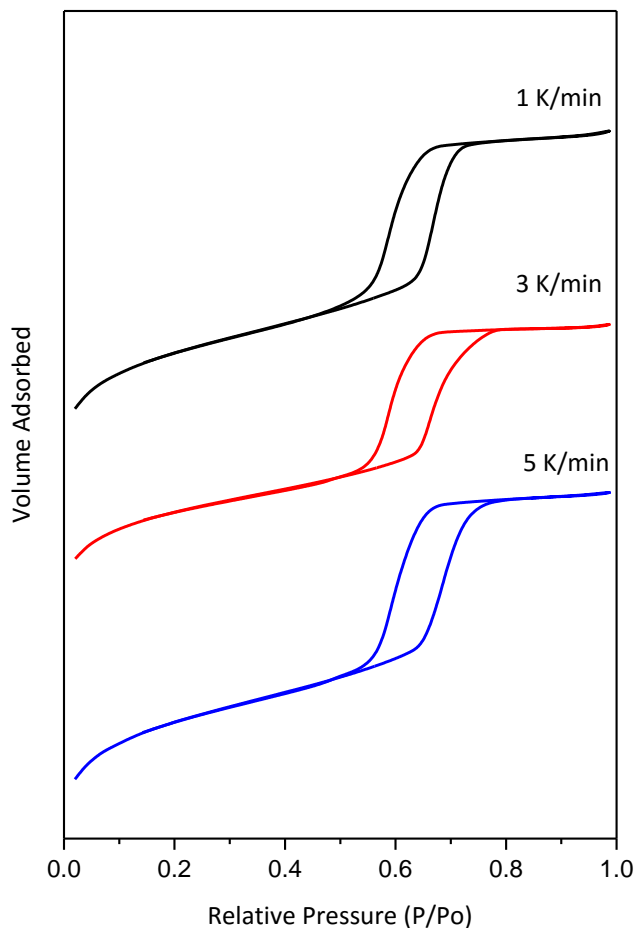
Figure 3.26 N$_2$ adsorption/desorption isotherm plots of SBA-15 pyrolyzed via the heating rate of 1 K/min, 3 K/min and 5 K/min

However, the small angle XRD patterns illustrate different result compared to the porosimetry data. It shows the slight shift of the peak in the samples under different heating rate. The peak of the sample pyrolyzed by the heating rate of 1 K/min, which is the slowest one, has shifted to large angle, indicating a smaller unit cell, resulting from a subtle shrinkage of the cell wall coupled with the relative kinetics of residual template. It is worthwhile to note that the XRD pattern of the sample pyrolyzed by the heating rate

of 3 K/min and 5 K/min has a less intensive peak compared to that of 1 K/min sample. This could also be attributed to the mesoporous structure collapse during the pyrolysis.
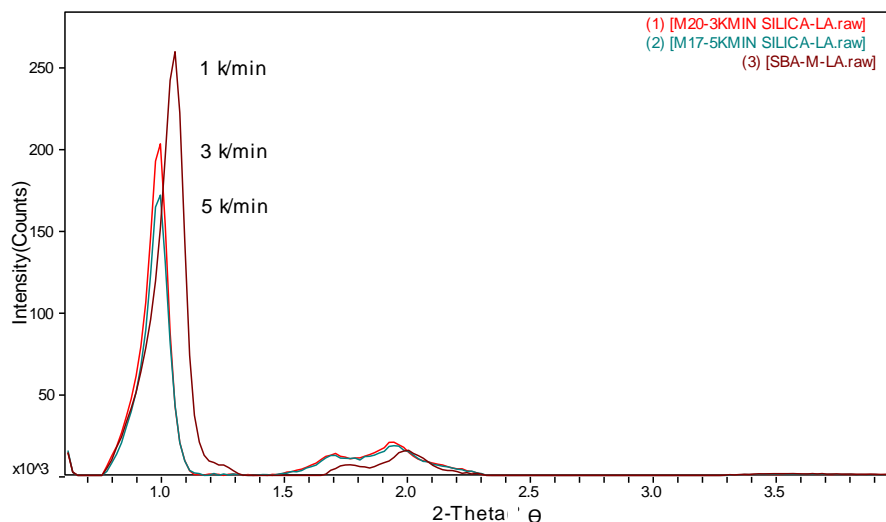
Figure 3.27 Small angle XRD patterns of SBA-15 samples prepared under different heating rates

Hence, it could be concluded that a fast heating rate in the pyrolysis has some influences on the structural ordering of the final product but this impact is not as significant as other conditions discussed.

Table 3.4 illustrates the specific BET surface area, pore volume and pore diameter of the CSCs pyrolyzed via the heating rate of 1 K/min, 3 K/min and 5 K/min. All the results are quite close, indicating there is no massive difference among these three samples, which is consistent with the result of SBA-15 samples. Figure 3.28 also demonstrates the similar isotherm plots of the CSC samples pyrolyzed under different heating rates.

Table 3.4 Textural properties of CSCs prepared under different heating rates

	BET surface area (m²/g)	Pore volume (cm³/g)	Pore diameter (nm)
1 K/min	517	0.37	2.85
3 K/min	564	0.42	2.95
5 K/min	524	0.37	2.85
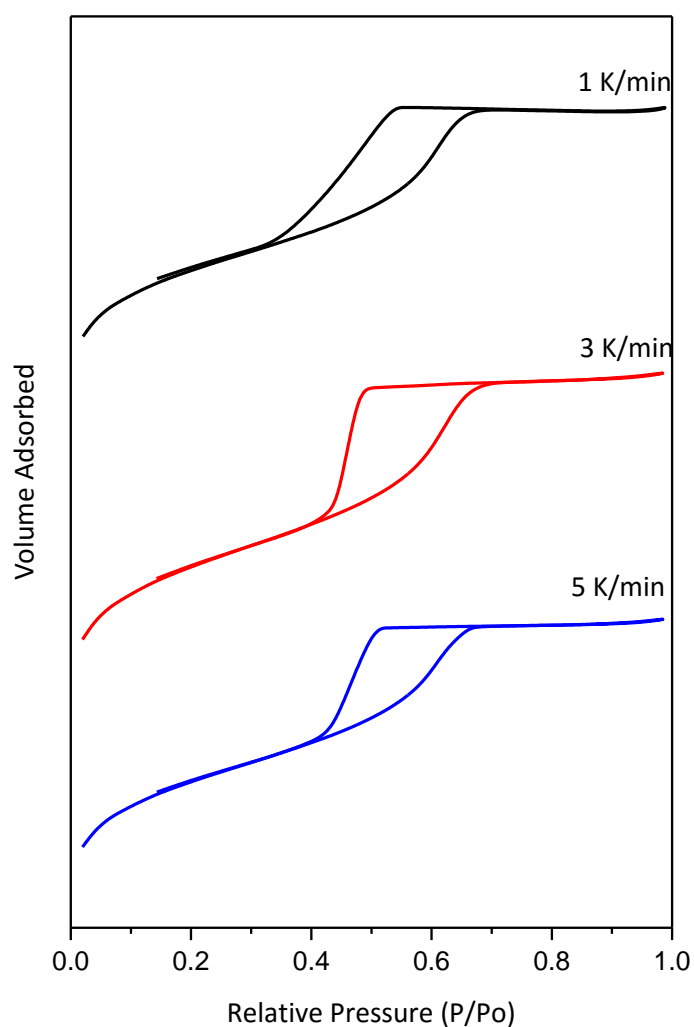
Figure 3.28 N₂ adsorption/desorption isotherm plots of CSCs prepared under different heating rates

The small angle XRD patterns in Figure 3.29 shows that the intensity of the characteristic peak increased by the decrease of the heating rate, indicating a better-ordered material was prepared at lower heating rate. Surprisingly, the signals are located at the same

position and do not shift, suggesting there is no difference of the unit cell among these three samples. This is not in agreement with the results of SBA-15 samples. Through the coating of the bio-oil to SBA-15 surface, not only was the carbonaceous layer shaped and stabilized by the silica, but also the silica was performed as scaffold, thus resulting in the thermal stability of the whole CSC material even when a faster heating rate was applied.
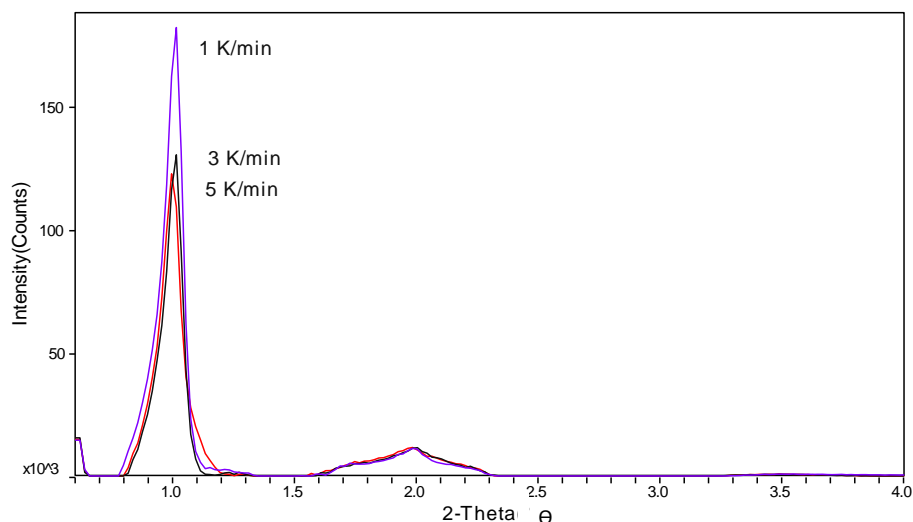
Figure 3.29 Small angle XRD patterns of CSCs prepared with different heating rates

3.5.3 Textural properties of CSCs

The characterization of CSCs by using nitrogen porosimetry, microscopy and XRD analysis has been studied in order to obtain the structural information and textural properties of CSC material prepared at a series of temperatures.

The porosimetry data demonstrates the CSC materials have a high surface area except 300 °C sample (Table 3.5). It could be clearly observed that most of silica pores have been blocked by unpolymerized bio-oil at 300 °C. The estimated thickness of carbonaceous layer could be calculated based on the pore diameter of parent SBA and CSC. The thickest layer is 1.82 nm and the thinnest one is 1.63 nm. However, the change of thickness of the layer did not correlate with the increase of carbonization temperature.

Table 3.5 Textural properties of parent SBA-15 samples and CSC materials prepared at different temperatures

Sample	BET surface area (m^2/g)	t-plot micropore area (m^2/g)	Pore volume (cm^3/g)	Pore diameter (nm)	Estimated thickness of carbonaceous layer (nm)
SBA-15	732	186	0.80	5.10	-
300	39	36	0.03	-	0
400	449	206	0.19	3.28	1.82
500	636	290	0.31	3.47	1.63
600	457	201	0.24	3.46	1.64
800	411	164	0.23	3.42	1.68

The proposed mechanism for the formation of materials with increasing temperature is illustrated in Figure 3.55. The scanning electron microscopy (SEM) and transmission electron microscopy (TEM) images in Figure 3.30 allow observation of the structural ordering of samples and they clearly reveal that the composites exhibits a highly ordered hexagonal mesoporous structure, thus retaining the structural order characteristic of the parent silica. SEM images demonstrate that the uniform silica pore channels still exist in the CSCs. The estimated pore diameter measured from the TEM images are approximately 3.75 nm, 3.40 nm and 3.35 nm for parent SBA-15, the carbon-silica composite subjected to pyrolysis at 600 °C (CSC-600) and 800 °C (CSC-800), respectively.[249] These results are in good correlation with porosity data from the N$_2$ adsorption/desorption isotherms (Shown in Table 3.5), indicating that carbon-containing species did not affect the mesoporous structure of the silica substrate dramatically.
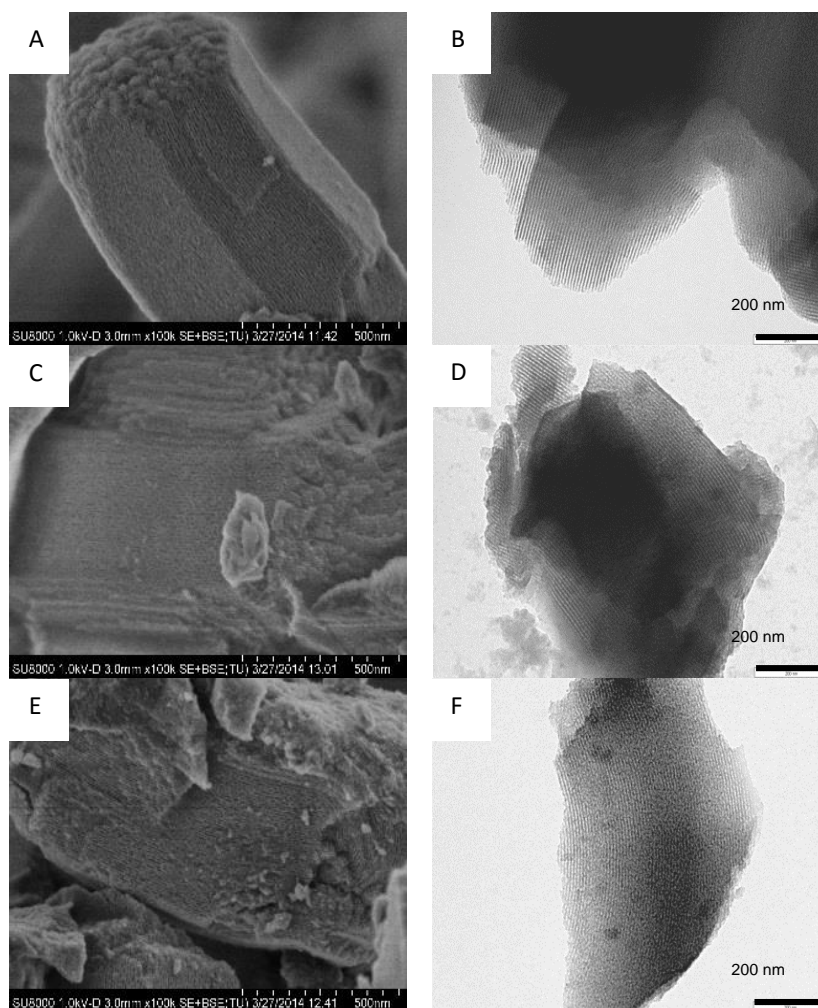
Figure 3.30 HRSEM images (left column) and TEM images (right column) of SBA-15 (A, B), CSC-600 (C, D) and CSC-800 (E, F) materials

Nitrogen adsorption isotherm plots (Figure 3.31A) indicate that SBA-15 exhibits a typical type-IV isotherm plot with an H1-type hysteresis loop, and a steep capillary condensation step in adsorption branch implies a uniform mesopore size.[250] However, all the carbon-silica composites carbonized above 400 °C display H2-type hysteresis loop with a gradual rise in adsorption branch during capillary condensation, revealing a broader pore size distribution and / or non-uniform pore structure.[235] The CSC-300 has an incomplete hysteresis loop (not shown in Figure 3.31) and the BET specific surface area is extremely low at 39 m^2/g supporting the theory that the silica pores have been fully filled with bio-oils and the carbon source has not been removed dramatically enough at this temperature, and that little shrinkage of the carbonaceous system has

occurred. This implies that the volume of the bio-oil did not change a lot although TG data shows quite a significant weight loss by 300 °C.
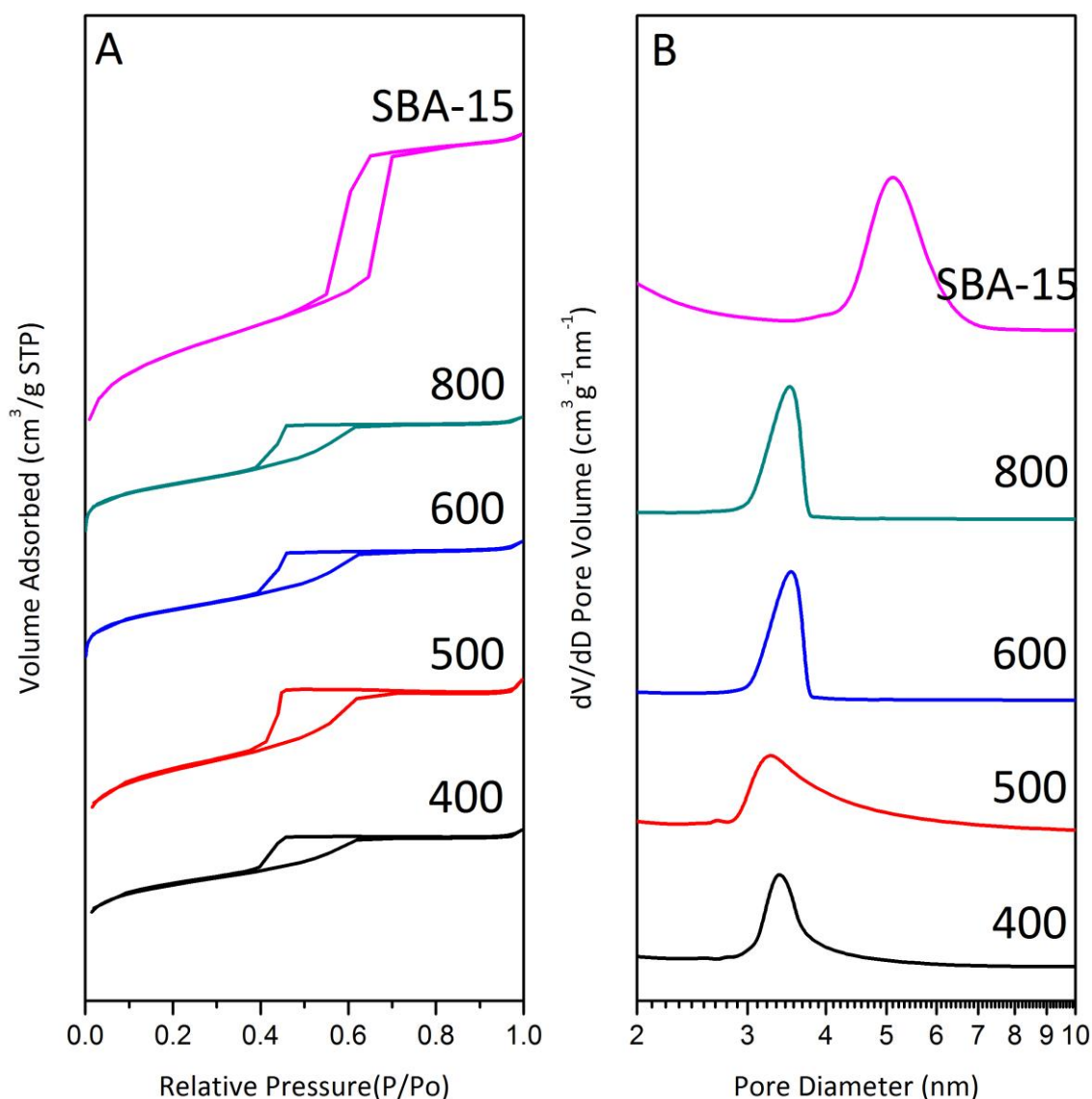
Figure 3.31 N$_2$ adsorption/desorption isotherm plots (A) and pore size distribution (B) of the carbon-silica composites and SBA-15 materials

The pore size distributions (Figure 3.31B) were calculated using the desorption branch, showing a narrow pore size distribution for all materials. Compared to SBA-15, the composites possess a smaller mesopore size. CSC-300 sample also shows no significant peak in the pore size distribution providing further evidence that the silica pores were filled with polymerised bio-oils as highlighted in Figure 3.55.
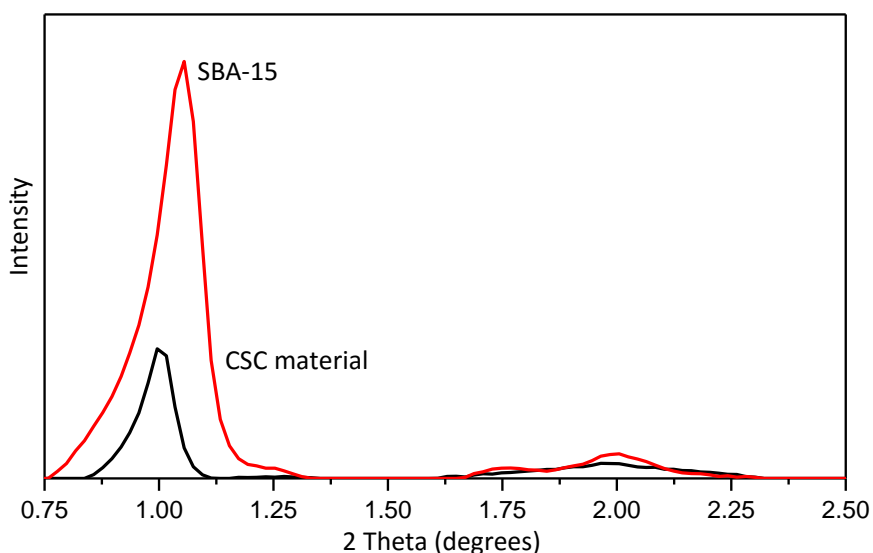
Figure 3.32 XRD patterns of parent SBA-15 materials and CSC-500

The XRD patterns (shown in Figure 3.32) of CSC and its parent SBA-15 provide further evidence that the inorganic structure of the SBA-15 silica remains intact after bio-oil modification process, which could be deduced from microscopy images. The pattern of CSC matches well with that of SBA-15 indexed to a hexagonal lattice,[251, 252] except the decreased intensity of the peak of CSC due to a ratio change in the contrast between silica / empty space and silica / carbon.[253]

3.5.4 Tuneable surface functionalities depending on pyrolysis temperatures

The carbon species in the materials could be tuned significantly based on the carbonization temperature, resulting in a continuum functionality ranging from polar hydroxyl groups to aromatic surfaces of CSC. This creates unique advantages compared to traditional synthetic methods. The resultant CSC exhibits not only similar pore structural ordering as parent SBA-15, but also unique advantages including temperature-dependent surface functionality. Therefore, the carbonization temperature definitely has a dominant impact on the functionality of the resultant CSCs.
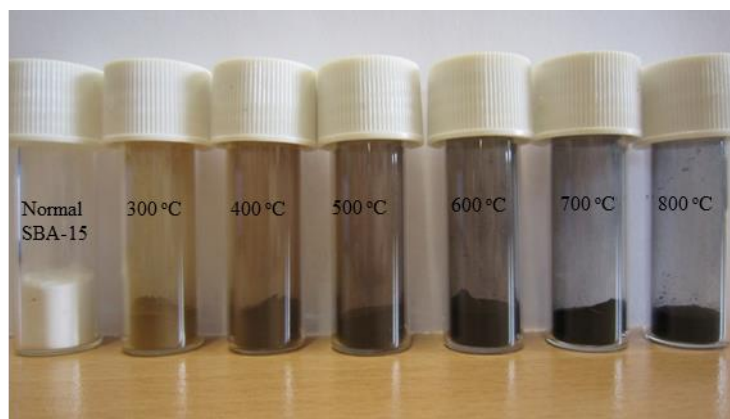
Figure 3.33 The carbon-silica composites materials carbonized from 300 °C to 800 °C and parent SBA-15 materials

The appearance of the CSC materials and parent SBA-15 is shown in Figure 3.33. SBA-15 is a normal white silica powder. After the modification of bio-oil, the colour changes to be light brown at low carbonization temperature and turns to be black until 800 °C. This is because the carbon proportion in the CSC material is large at low temperature and the carbon tends to be extended polyaromatic structures as the temperature increases. This could also be evidenced by the compositional analysis of CSCs.

After the pyrolysis under different temperature, the estimated ratio of pure silica residue should be 11% (neglecting the mass loss of the silica during the thermal treatment). The 300 °C sample has a ratio of 0.93 silica to carbonaceous material. The ratio of silica to carbon increased with the increase of the carbonization temperature, which indicates that the proportion of carbon has decreased with increasing temperature. According to the thermogravimetric analysis above, this is due to the volatilization of light compounds and the decomposition of hydrocarbons. Hence, the chemical composition of CSC could be easily tuned *via* controlling the pyrolysis temperature and the Silica:C ratio could be varied from 0.93 to 1.86.

Table 3.6 Compositional analysis of CSC-300, CSC-400, CSC-500, CSC-600, and CSC-800

Sample No.	Residue mass in average (w/w) %	Silica%	C%	Silica:C
CSC-300	22.85	11	11.85	0.93
CSC-400	21.11	11	10.11	1.09
CSC-500	19.34	11	8.34	1.32
CSC-600	17.35	11	6.35	1.73
CSC-800	16.91	11	5.91	1.86

Figure 3.35 demonstrates the comparisons of XRD patterns of CSCs carbonized at 300 °C, 400 °C, 500 °C, 600 °C, 700 °C and 800 °C. The (100) diffraction peak of the materials shifts to larger 2θ degree with the increase of temperature, indicating a smaller interplanar distance d_{100} and a smaller unit cell.[250, 251] This is attributed to the shrinkage of silica structure during the carbonization. A control experiment of XRD analysis of pure silica materials heated at 500 °C and 800 °C under nitrogen flow has also been carried out to provide further evidence for this phenomenon (Figure 3.34). Moreover, the shift of CSCs is more significant than that of silica sample, indicating that not only the shrinkage of silica itself, but also the acids and water from bio-oils could accelerate the crosslink effect of silanol groups.
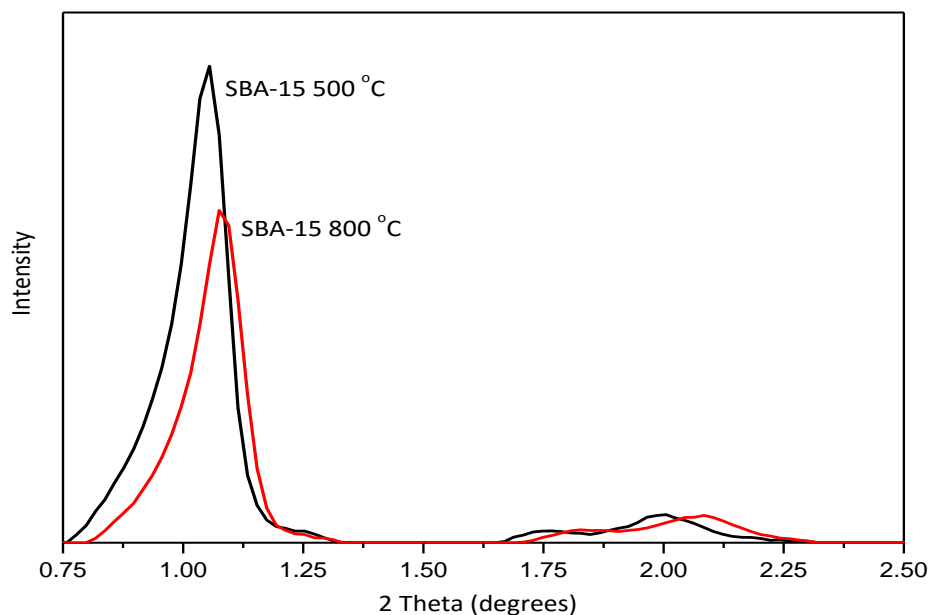
Figure 3.34 XRD patterns of SBA-15 materials heated at 500 ºC and 800 ºC under nitrogen flow

Figure 3.35 XRD patterns of CSC-300, CSC-400, CSC-500, CSC-600, CSC-700 and CSC-800 materials

The intensities of the peaks in XRD pattern increase first as the temperature increases to 700 ºC, proving that the temperature rise has a positive effect on the composite structural ordering.[253] The strong increase of intensities is explained by the removal of

organic species from the inside of the mesopores and the formation of a more uniform carbonaceous layer. As indicated in Figure 3.55 below, the pores were filled with organic compounds at lower temperature at first. Then some of organic species could decompose with the increase of temperature and a uniform layer containing the chemically stable compounds formed by coating with silica surface. Hence, the XRD result could strongly support the validity of successful fabrication of carbonaceous silica composite.
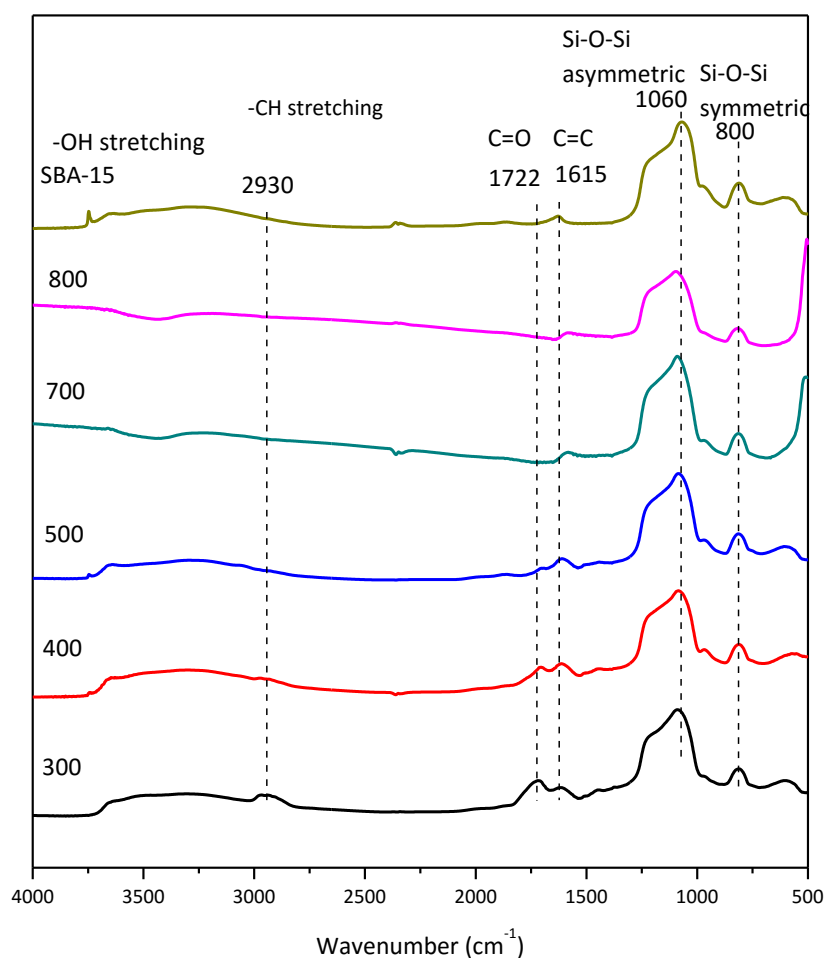
Figure 3.36 DRIFT spectra of the carbon-silica composites and SBA-15 samples

The characteristic of continuous functionality depending on different pyrolysis temperature is clearly shown in DRIFT spectra (shown in Figure 3.36). 300 °C sample as the lowest carbonization temperature, contained a variety of functional groups, such as OH groups, C-H groups, C=O groups and C=C groups. As the temperature increases to 800 °C, the functionalities of the material converted to aromatic form. Weakening or

156

disappearance of the peak at 2930 cm^{-1} assigned to CH stretching indicates that the aliphatic chains decompose completely above 500 °C. The existence of C=O groups from acid, ester, ketone or aldehydes could be confirmed by the peak at around 1720 cm^{-1}. On carbonization from 500 °C this peak disappears, indicating the decomposition of C=O containing species at high temperature. As mentioned, most previous research investigated the carbon-silica fabrication by utilizing soluble resin polymers or sugars as carbon precursor.[234-236, 249] However, due to the use of pure chemicals and carbonization at certain temperature, the typical product only possesses a carbonaceous layer with a single functionality on the silica surface and the surface property could not become temperature-dependent. In this work, it has been demonstrated that the surface properties of CSCs continually change from polar hydroxyl groups to aromatic surfaces with the increase of pyrolysis temperature. In addition, DRIFT analysis further demonstrated the existence of silica substrates in CSCs. The characteristic peaks shown at 3700 cm^{-1} (OH), 1060 cm^{-1} (Si-O-Si asymmetric) and 800 cm^{-1} (Si-O-Si symmetric) in the spectra of CSCs match well to the parent SBA-15 except for the OH peak.[254] The elimination of OH group in CSC is due to the crosslink effect of silicas under high temperature above 500 °C leading to the OH group loss. It is worthwhile to note that due to the existence of alcohols in CSC-300 sample and CSC-400 sample from ^{13}C NMR analysis below, the peak at 3500 cm^{-1} should also be assigned to alcohols.
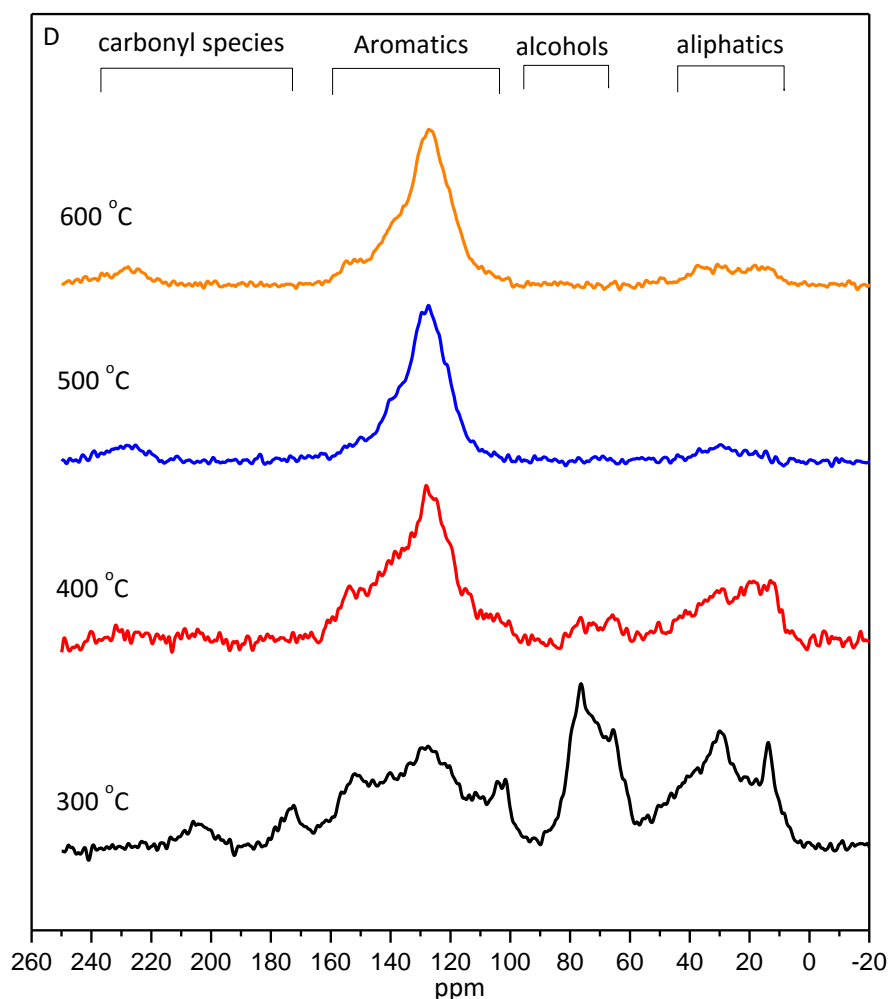
Figure 3.37 **¹³C solid state MAS/NMR spectra of CSC-300, CSC-400, CSC-500 and CSC-600 materials**

The sample information on the carbon speciation was also indicated from ^{13}C MAS/NMR spectra (Figure 3.37) of the carbon silica composites carbonized at 300 °C, 400 °C, 500 °C and 600 °C. CSC-800 (800 °C) sample could not be analysed due to the highly conductivity of the material, thus resulting in the inability to properly tune the probe. This phenomenon implies that high temperature CSCs could be applied in electrochemistry, chemical sensor and nano-electronic applications.[235, 255] The NMR spectra of 300 °C sample indicated that a wide range of organic functionalities are still present, including ketones at *ca.* 205 ppm, acid/esters at *ca.* 165 ppm, aromatics at *ca.* 150 ppm, alcohols at *ca.* 60 ppm and aliphatics at *ca.* 20 ppm. The data for these functional groups was consistent with DRIFT analysis above. The 400 °C sample is dominated by increased aromatic character accompanied by aliphatic and alcohol groups. It is evident that the disappearance of characteristic peak at 165 ppm and 205

ppm indicated the decomposition of carbonyl species by 400 °C, and most of alcohols decomposed at the same time evidenced by the decreased intensity of the peak at 76 ppm. In terms of CSC-500 (500 °C) and CSC-600 (600 °C) sample, the aromatic peak (plus spinning sidebands) is the only signal except a weak aliphatic signal around 10-20 ppm, indicating the carbon species were mostly converted to aromatic carbon form. It could also be observed from TG graph (Figure 3.23) that during the pyrolysis, the organic compounds were lost massively before 500 °C, while the mass of the sample changed little from 500 °C to 800 °C. Overall, the NMR and IR results demonstrated that the organic functionality of CSCs keeps changing by the adjustment of carbonization temperature (described in Figure 3.55). This is a unique advantage compared to the carbon-silica composite prepared through other methods which only prepared single functionality silane-modified composites. It is worthwhile to note that no resonance signal ascribed to C-Si bond was detected as explained by ^{29}Si NMR spectra (Figure 3.38).[256] Further work will explore the possibility of silicon-carbide formation at higher temperatures above 1000 °C.
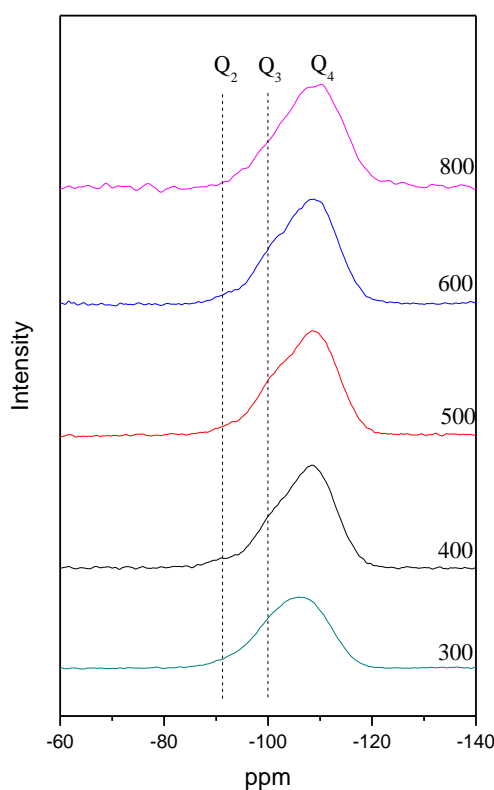
Figure 3.38 ^{29}Si solid state NMR spectra of carbon-silica composites prepared at 300 °C, 400 °C, 500 °C, 600 °C and 800 °C

Previous work demonstrated the utility of fluorine-containing compounds as probe molecules to investigate the surface functionality using ^{19}F NMR illustrating that the chemical shift difference ($\Delta\delta$) between the characteristic peak of fluorine in the liquid-phase peak and on the material surface correlates well with both surface energy and polarity values of the materials.[257] The pure carbon material contains an electron-rich graphite-like structure, which contributes greatly to surface energy value, thus resulting in a significant chemical shift, compared to pure silica material. Figure 3.40 shows the chemical shifts in the spectra of ^{19}F solid state NMR of SBA-15 materials heated at 500 ºC, 600 ºC and 800 ºC, CSC materials carbonized at 300 ºC, 400 ºC, 500 ºC, 600 ºC and 800 ºC and commercial activated carbon samples (activated charcoal Norit®, from coal). The chemical shifts of CSC materials decrease and move towards the value for activated carbon (-4.61 ppm) with the increase of pyrolysis temperature, indicating that the surface functionality of composites tend to become more like that of carbon species. This is due to the high temperature CSCs containing higher percentage of graphitic or polyaromatic carbon species, which is in agreement with ^{13}C NMR results. It is another strong evidence of the tuneable functionality of CSCs prepared through this new method. The fluorine peak of CSC-300 on the material surface is sharp and intensive (Figure 3.39), indicating that the carbonaceous layer distributes uniformly on the silica pores. However, due to the evaporation and decomposition of organic compounds with the increase of temperature, the thickness of this carbonaceous layer decreases, resulting in the low intensity peaks for high temperature samples.
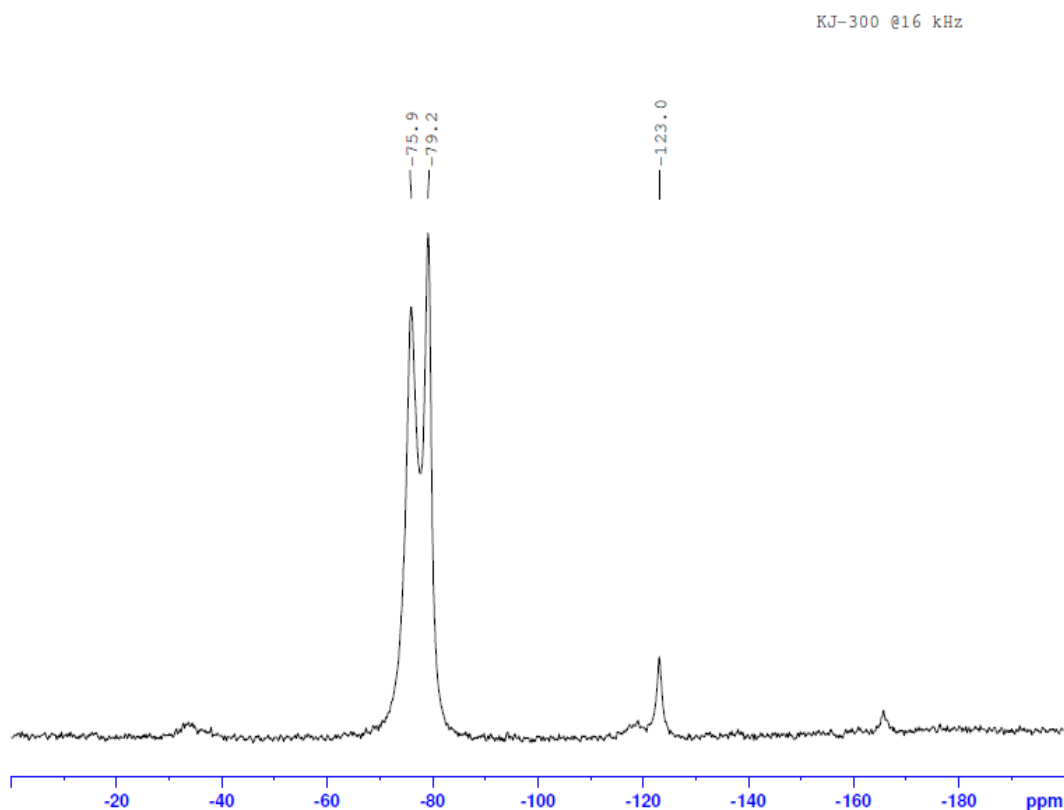
Figure 3.39 ^{19}F solid state NMR spectra of CSC-300

Besides, the SBA-15 materials have an increased chemical shift with the increase of temperature, demonstrating that high temperature leads to a more polar SBA-15 material because of the further crosslink effect between silica species. Interestingly, it is worthwhile to note that the chemical shifts of CSCs prepared at 300 and 400 $^{\circ}$C are even higher than that of parent SBA-15, suggesting that a more hydrophilic surface was prepared at lower pyrolysis temperature. This is due to most of polar organic carbon-containing compounds still remaining in the composites, leading to polar materials – indeed the ^{13}C NMR data suggests a product rich in hydroxyl groups and carbonyl species. Such a kind of functionalized silica materials with highly polarity could have a potential in some specific separation process except CSC-300 material with poor porosity and low surface area.

	CSC-800	CSC-600	CSC-500	CSC-400	CSC-300
	2.16	2.62	2.88	3.10	3.14

Δδ

Activated carbon	SBA-15-500	SBA-15-600	SBA-15-800
-4.61	2.64	2.75	2.92

Figure 3.40 Chemcial Shifts (Δδ) in the spectra of ^{19}F solid state NMR of SBA-15 materials carbonized at 500 ºC, 600 ºC and 800 ºC, CSC materials carbonized at 300 ºC, 400 ºC, 500 ºC, 600 ºC and 800 ºC and activated carbon materials

In the graph of the C, Si and O element concentration for CSCs as measured by XPS and CHN analysis (Figure 3.41), %C generally decrease whereas %Si increase with increasing pyrolysis temperature, providing further proof of decreased ratio of carbon-containing compounds at high pyrolysis temperature. The carbon concentration detected from CHN analysis for all CSCs was much lower than that from XPS analysis. In XPS analysis, only the initial ~10 nm depth of material surface can be investigated,[254] thus indicating that the surface of the composites is a richer carbon-containing layer, which further suggests that the carbon species are actually coated around the silica surface, and also is a strong support for the mechanism demonstrated in Figure 3.55. Moreover, C/H mass ratio of CSC-300, CSC-400, CSC-600 and CSC-800 obtained from CHN analysis was 11.73, 13.26, 16.8 and 37.80, respectively. This further suggested that the functionalities of the CSCs changed from 300 ºC to 800 ºC.
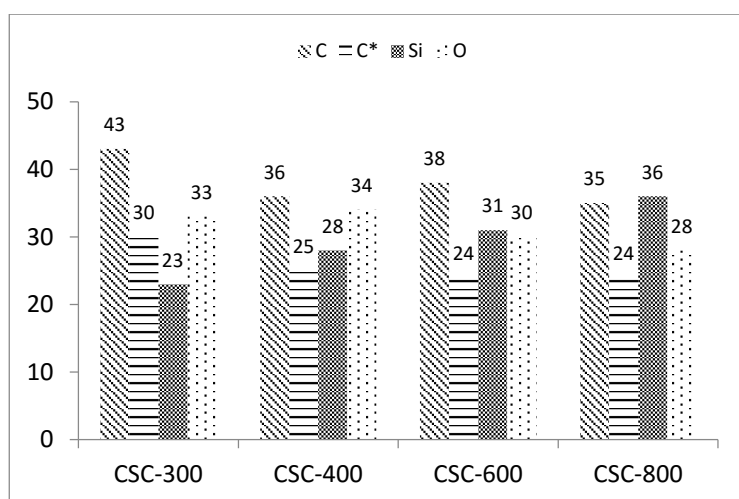
Figure 3.41 Graph of C, Si and O element concentration for CSC materials from XPS analysis except C* column stands for the data from CHN analysis

A spectra series of C_{1s} core level peaks of the CSCs prepared at 300 ºC, 400 ºC, 600 ºC and 800 ºC is shown in Figure 3.43. Three contributions can be identified as due to: C-C

group, C-O group (C-O-C or C-O-H) and C-O-Si group at 284.4 eV, 285.7 eV and 288.9 eV binding energies, respectively.[254, 258] The dominant peak in these samples is attributed to C-C group. The intensity of the peak observed at 285.7 eV tends to decrease as the increase of temperature as a result of the loss of organic compounds. It is clear to observe that the C-C/C-O ratio keeps increasing with the increase of temperature (Figure 3.42). This result is consistent with DRIFT and carbon NMR data, showing a temperature-dependent functionalized CSC was synthesized.
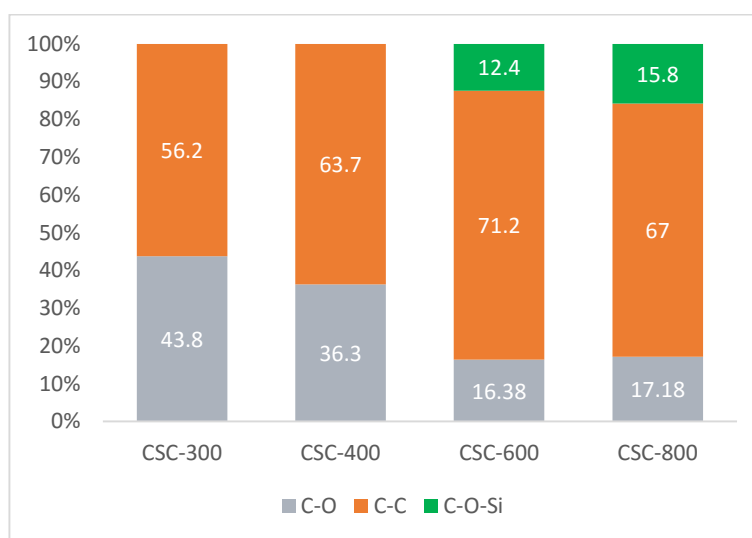
Figure 3.42 Ratios of C-O, C-C and C-O-Si groups in CSC-300, CSC-400, CSC-600 and CSC-800

Notably, the appearance of a small and broad peak at 288.9 eV is assigned to C-O-Si species.[254] This could be attributed to the interactions between bio-oils and silicas,[259] further emphasising the feasibility of carbon-silica composite fabrication by using bio-oil and silica, which is illustrated in Figure 3.55.
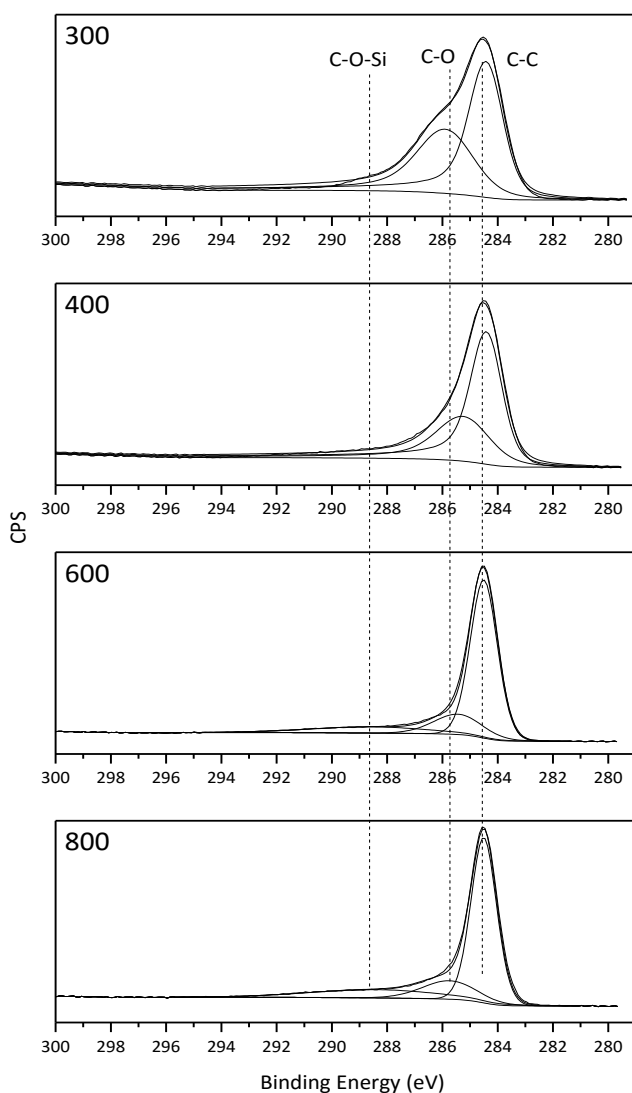
Figure 3.43 C$_{1s}$ XPS spectra of CSC-300, CSC-400, CSC-600 and CSC-800 samples

Another research by Macquarrie studied that waste ash obtained from combustion of bio-char, which is generated from microwave of biomass, could be converted into structured mesoporous silicas.[260] Thus by combining these two approaches together, a comprehensive utilization of waste biomass from microwave pyrolysis to prepare mesoporous carbonaceous silica materials is proposed here (Figure 3.44).
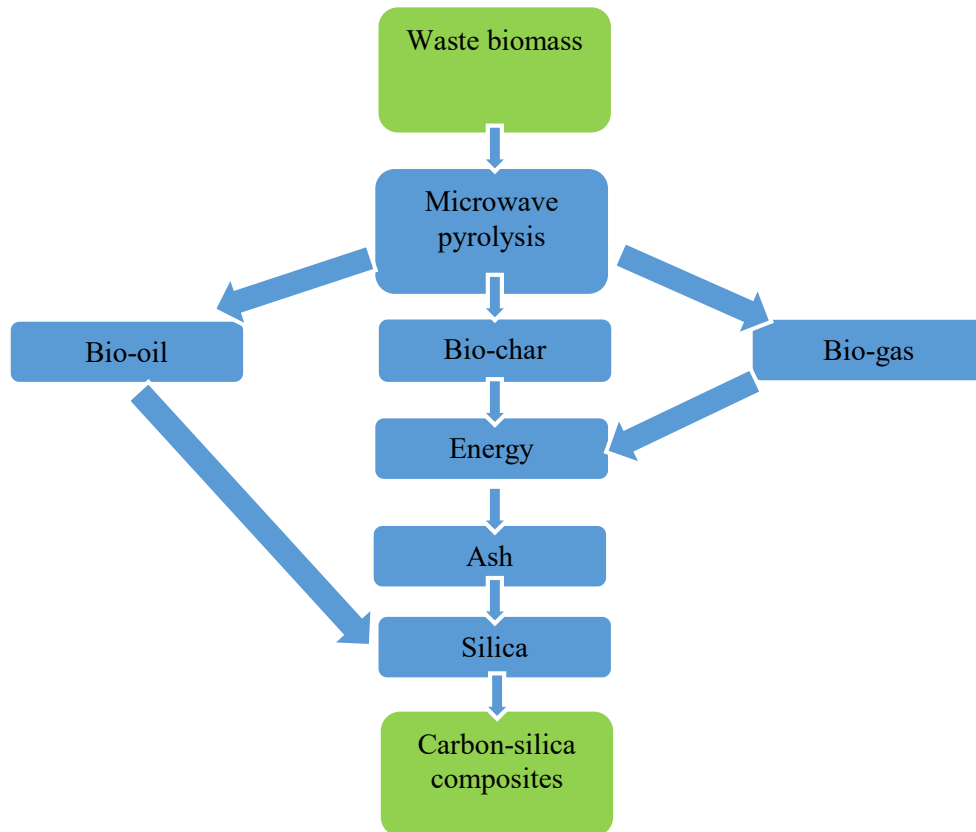
Figure 3.44 Flow graph of fabrication of carbon-silica composites from waste biomass

3.5.5 Combustion investigation - carbon removal

CSCs consist of two main components, which are silica and carbon. When the carbonaceous layer is removed by calcination, the silica could return to the original structure. The procedure of the combustion involves oxidising the CSC sample through calcining at 600 °C under air flow to effectively remove the carbon portion and get the original SBA-15.
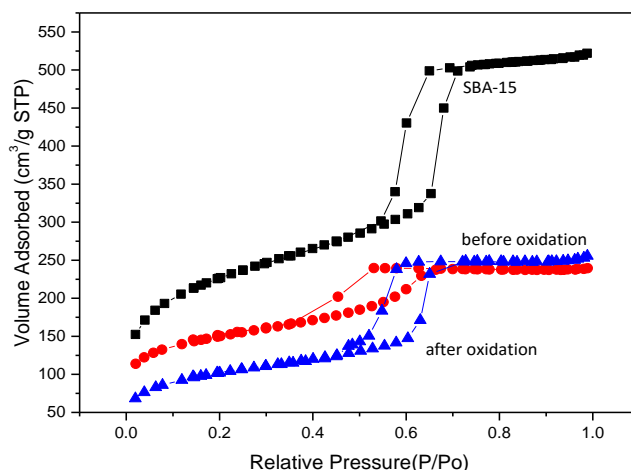
Figure 3.45 Nitrogen adsorption/desorption isotherm plots of SBA-15, CSC and its CSC-silica samples
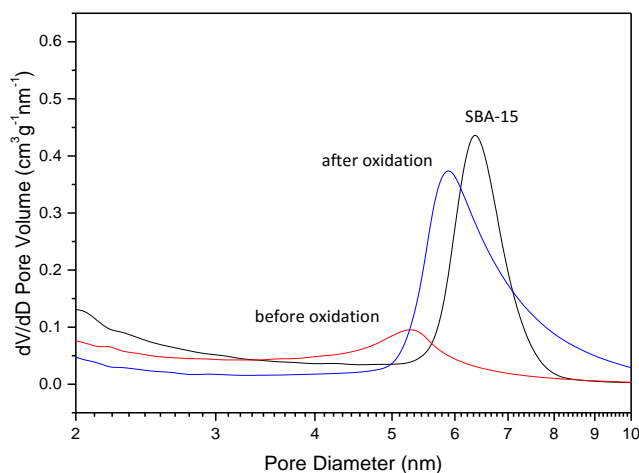
Figure 3.46 Pore size distribution of SBA-15, CSC and its CSC-silica samples

The adsorption/desorption isotherm plot (Figure 3.45) indicated that after the oxidation, the curve of CSC-silica sample tends to be Type H1, suggesting the carbonaceous layer was partially removed from the sample. This result also provided evidence that the mesoporous structure of SBA-15 existed in the either CSC sample or CSC-silica sample all the time, and was not affected by the incorporation of bio-oil and the pyrolysis. The pore size distribution shown in Figure 3.46 was in good agreement with the isotherm plots. The strong peak on the XRD pattern (Figure 3.47) of these three samples highlighted the well-ordered structure in these samples, and after the oxidation, this feature was still retained.
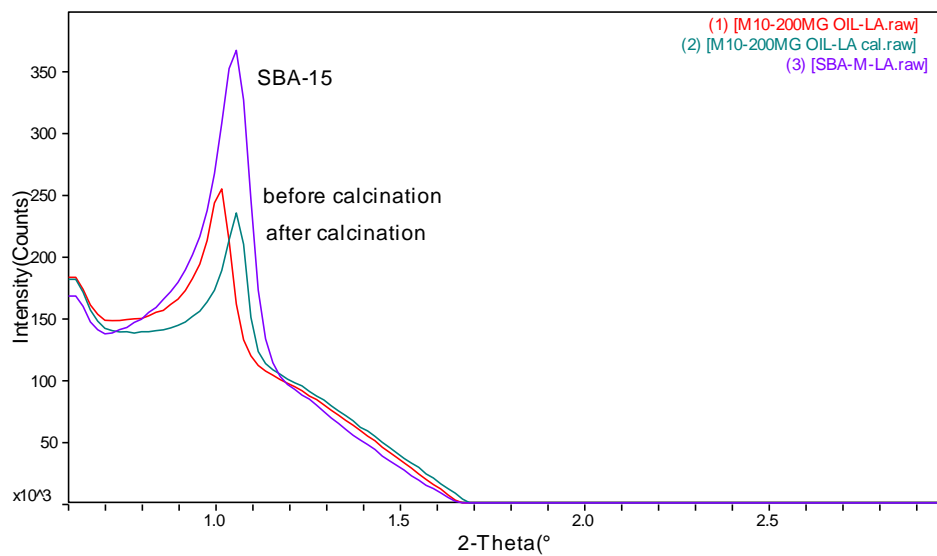
Figure 3.47 Small angle XRD patterns of SBA-15, CSC and its CSC-silica samples

.
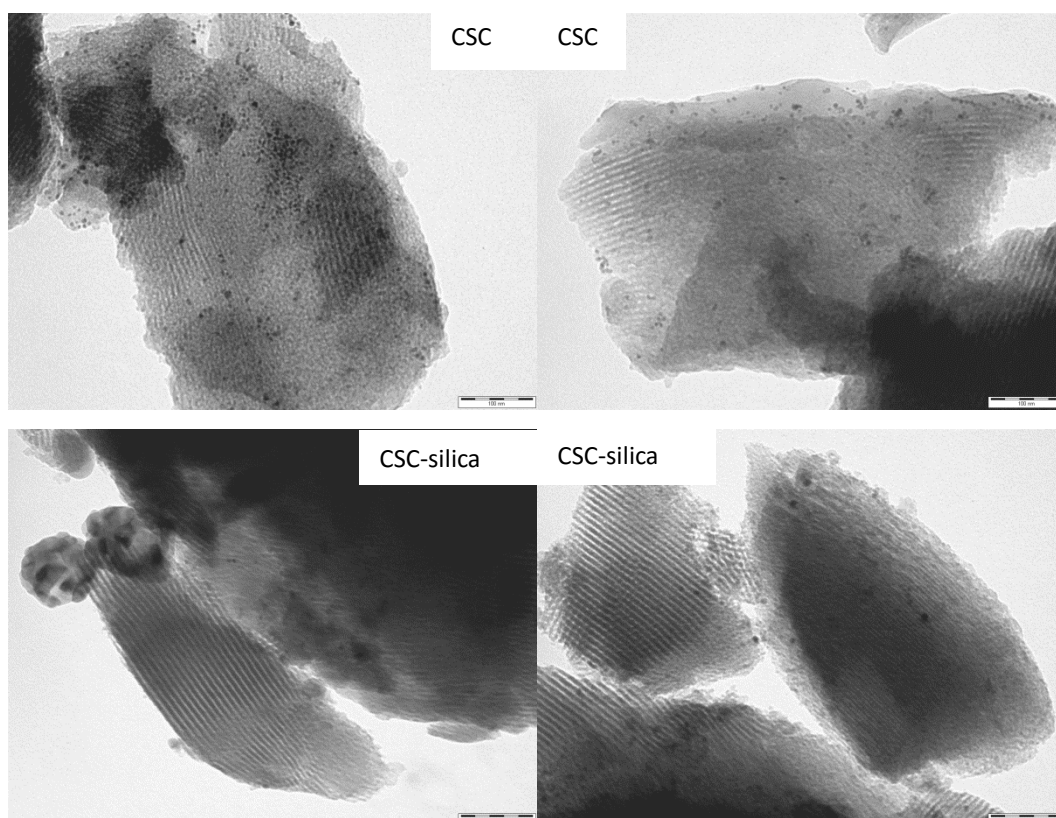
Figure 3.48 TEM images of CSC and CSC-silica samples

The TEM images of CSC and CSC-silica material suggested that the typical mesoporous structure of SBA-15 silica has remained after the removal of organic matters with high temperature calcination, which is in agreement with the XRD and porosimetry data. This demonstrates that the oil modification is a reversible process and the pores of silica solid support did not significantly collapse after the repeatedly high temperature slow heating.

3.6 Utilization of other types of silica substrates

For the purpose of enlarging the application of this carbon modification method, three different mesoporous silicas including MCM-41, macroporous-mesoporous SBA-15 (MMSBA) and KIT-6 were utilized in this synthesis approach and their respective composites were characterized in this work. MCM-41 is a popular and classic silica material, possessing a hexagonal arrangement of uniformly sized mesopores (1-10 nm).[261] MMSBA with meso-macro porous structure and KIT-6 with interconnected pore network exhibited improved pore interconnectivity and enhanced pore accessibility, allowing for a better mass transport compared to conventional SBA-15. MMSBA, which was synthesized via dual-templating routes employing P123 and polystyrene beads, had advantages of high surface areas and interconnecting macro- and mesopore networks with respective narrow pore size distributions.[19, 262] KIT-6 possesses highly accessible and highly connected open porous networks due to its unique cubic *Ia3d* pore architecture.[263, 264]

All of these porous silicas could be utilized in the preparation of carbon-silica composites with unique pore matrixes, offering vast prospects for future applications. The similar XRD patterns (Figure 3.50) of three silicas and respective composites revealed that the CSCs contained the same mesoporous structure as their parent silicas. Porosimetry results shown in Figure 3.49 are in good correlation with XRD data and also demonstrated that the CSCs were successfully prepared via this method. Similarly to SBA-15 result, the pore volumes and the average pore diameters of the corresponding CSCs decreased after bio-oil modification of these silica substrates (see Table 3.7). Due to the smaller average pore diameter of MMSBA (4.2 nm) and MCM-41 (3.2 nm) compared to SBA-15 (5.1 nm), the mesopores would be coated with carbonaceous layer, resulting in a smaller pore size less than 2 nm (micropore size) after the modification.

168

Comparison between the porosimetry data of original parent silicas and CSCs can be viewed in Table 3.7.

Table 3.7 Textural properties of the parent silica substrates and the corresponding CSCs

Sample	BET surface area (m²/g)	t-plot micropore area (m²/g)	Pore volume (cm³/g)	Pore diameter (nm)
MMSBA	256	23	0.28	4.53
CSC-MMSBA	283	123	0.20	3.87
KIT-6	842	90	0.98	6.3
CSC-KIT-6	563	182	0.36	4.6
MCM-41	1024	0	0.99	3.2
CSC-MCM-41	743	112	0.23	2.6
SBA-15	732	186	0.80	5.10
CSC-SBA-15	636	290	0.31	3.47
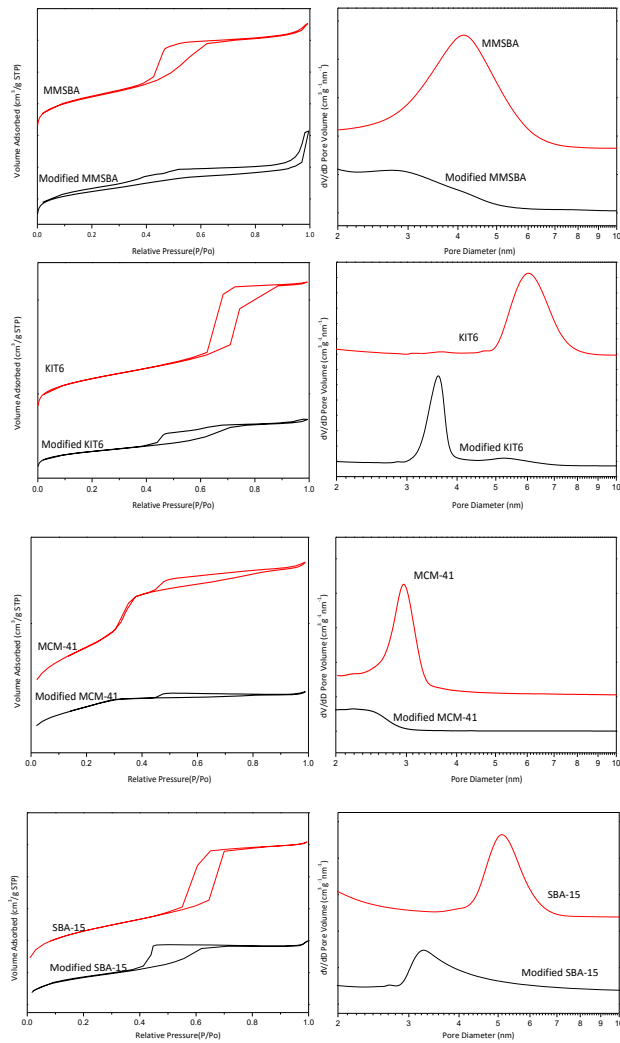
Figure 3.49 N₂ adsorption/desorption isotherm plots and pore size distribution of parent MMSBA, KIT-6, MCM-41, SBA-15 and corresponding modified CSCs
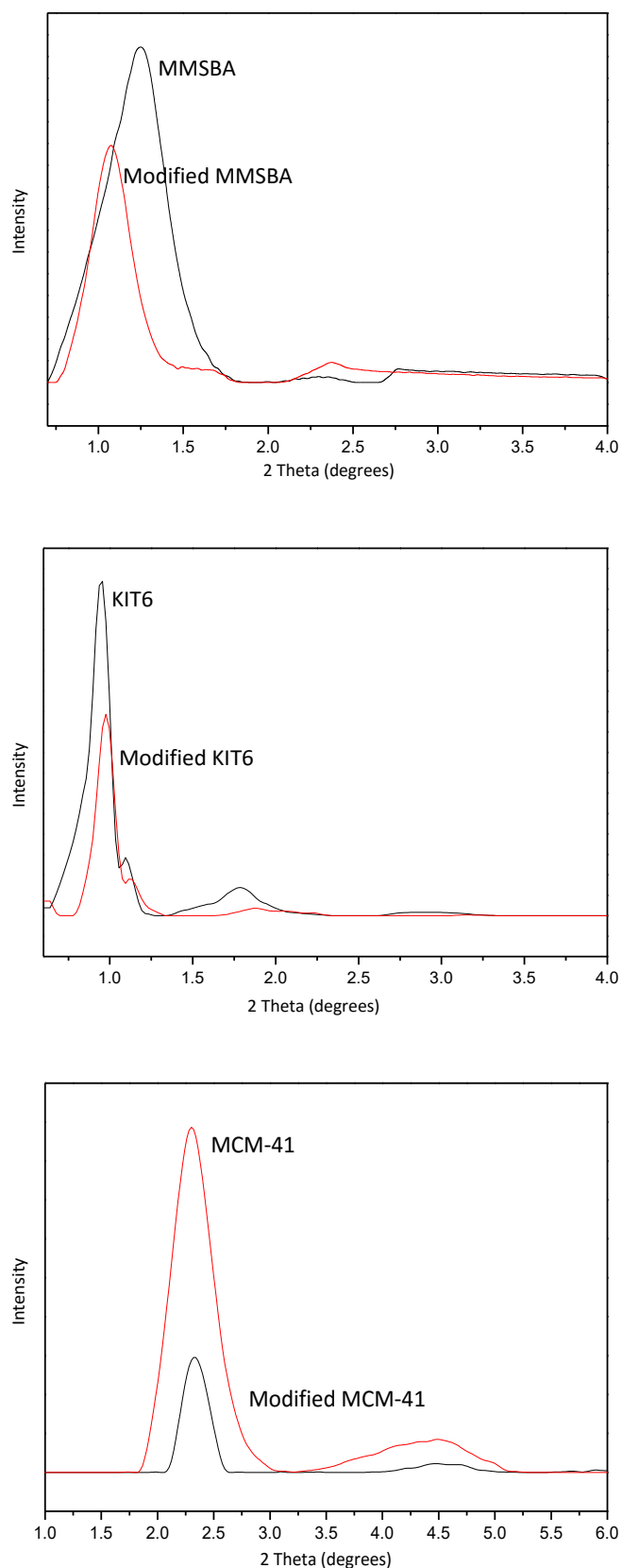
Figure 3.50 Small angle XRD patterns of parent MMSBA, KIT-6, MCM-41and corresponding modified CSCs

Notably a ratio of surface area (SA) and bio-oil amount plays an important role in tailoring the thickness of carbonaceous layer and pore size of CSC. Resulting from the high ratio of bio-oil to SA in MMSBA and MCM-41, a thicker carbon layer on the walls and smaller pore sizes were obtained, ultimately leading to a structure full of organics and more like CSC-300. Hence, the investigation between SA/bio-oil ratio and material's property will be further developed in Chapter 5.

3.6.1 Utilization of silicas synthesized in SCFs

The CSC materials were synthesised by using popular mesoporous silicas as substrates described above. In Chapter 2, several novel types of mesoporous silicas with specific structures have been fabricated via the supercritical carbon dioxide approach, particularly a hollow spherical silica with mesoporous shell has been of importance. Therefore, it is worthwhile to apply this kind of interesting silica material as solid support to prepare CSC material, and the resulting material was characterized by nitrogen porosimetry, microscopy and XRD analysis. Two typical silica samples fabricated in the supercritical carbon dioxide were utilized as solid support in this section.

Table 3.8 Textural properties of silica-I and CSC

	BET surface area (m^2/g)	Pore volume (cm^3/g)	Pore diameter (nm)
CSC	344	0.16	1.9
Silica-I	727	0.59	3.2

The 1st silica sample was synthesised under the pressure of 250 bar and the temperature of 60 ^{o}C. Table 3.8 illustrates the textural properties of silica support and its CSC material after the modification. The specific BET surface area of the CSC decreased significantly from 727 to 344 m^2/g. In the meanwhile, the pore volume and pore diameter decreased. This is because the carbonaceous layer was coated around the silica pore. The result is consistent with the modification by other types of silica materials.

TEM images in Figure 3.51 indicates that both the silica support and the corresponding CSC has hollow spherical structure with the estimated pore diameter of 200 nm, indicating that the CSC material still retains the same structure after the oil modification. It should be noted that the wall of the hollow spheres tend to be thicker after the pyrolysis of oil, which is due to the organic matter which was coated on the silica surfaces.
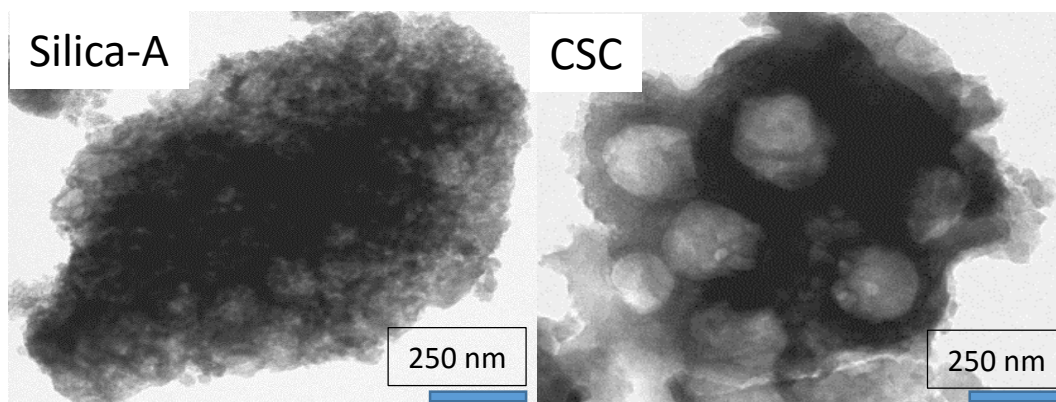
Figure 3.51 TEM images of silica and its corresponding CSC

The nitrogen isotherm plots of the silica support and the CSC material in Figure 3.52 demonstrate two different types of pore matrix for these materials. A narrower hysteresis loop on the isotherm plot of the CSC suggests a poor mesoporosity compared to the parent silica support. This is due to the incorporation of organic matter into silica mesopores, resulting in the partial blockage of pores. Table 3.8 also shows that the average pore diameter of the CSC is 1.9 nm (< 2 nm), which belongs in the micropore region.
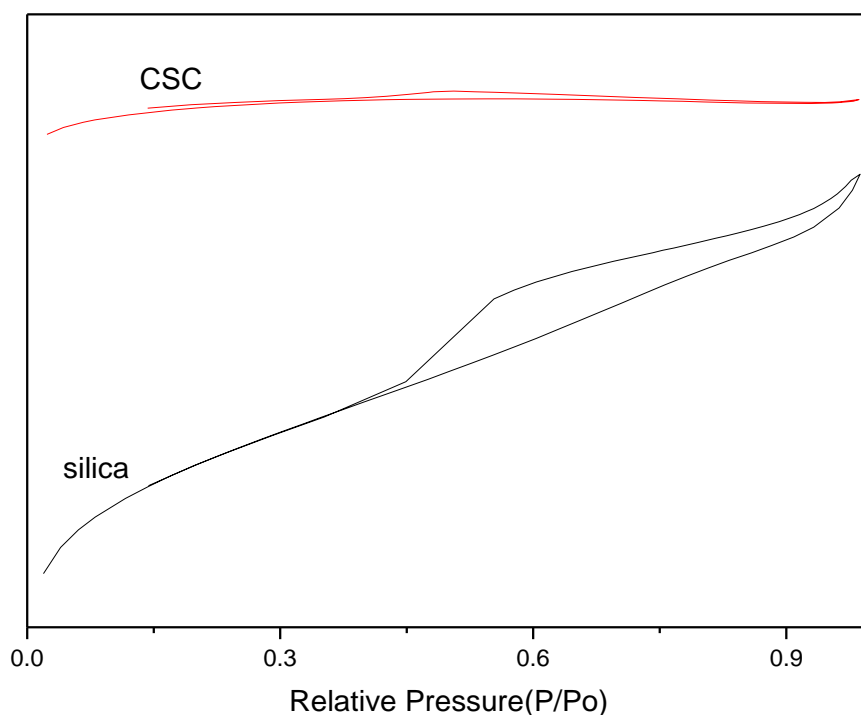
Figure 3.52 Nitrogen adsorption/desorption isotherm plots of silica and the corresponding CSC

The 2nd sample named as silica-B was synthesised under the pressure of 150 bar and the temperature of 40 °C. As mentioned above, the bio-oil/silica ratio could significantly affect the pore structure of the final material. Hence, three different ratios of bio-oil/silica were carried out and the resultant samples were compared.

Table 3.9 Textural properties of silica-II and CSCs

	Bio-oil/silica ratio	BET surface area (m²/g)	Pore volume (cm³/g)	Pore diameter (nm)
Silica-B		346	0.23	2.7
CSC-2	2	94	0.02	0.9
CSC-1	1	274	0.13	1.8
CSC-0.5	0.5	250	0.14	2.2

The textural properties of the silica material and the CSCs are shown in Table 3.9. As predicted, the CSC materials have a lower specific BET surface area, pore volume and

174

pore size compared the parent silica-II. Through adjusting the ratio of bio-oil/silica, the pore diameter of the CSC could be controlled from 0.9 nm up to 2.2 nm, suggesting that the average thickness of the carbonaceous layer is ranging from 0.5 nm to 1.8 nm based on the pore diameter of silica.

Due to the blockage of the pores of the material, the isotherm plot of the CSC-2 could not be obtained. The isotherm plots of other CSCs and parent silica is shown in Figure 3.53. All of these samples have a hysteresis loop and so have mesoporous structure. Compared to the silica samples, there is more of a gradual rise in volume of adsorbed N_2 in the curve of the CSC samples, indicating that the pore volume of the CSC sample is much smaller.
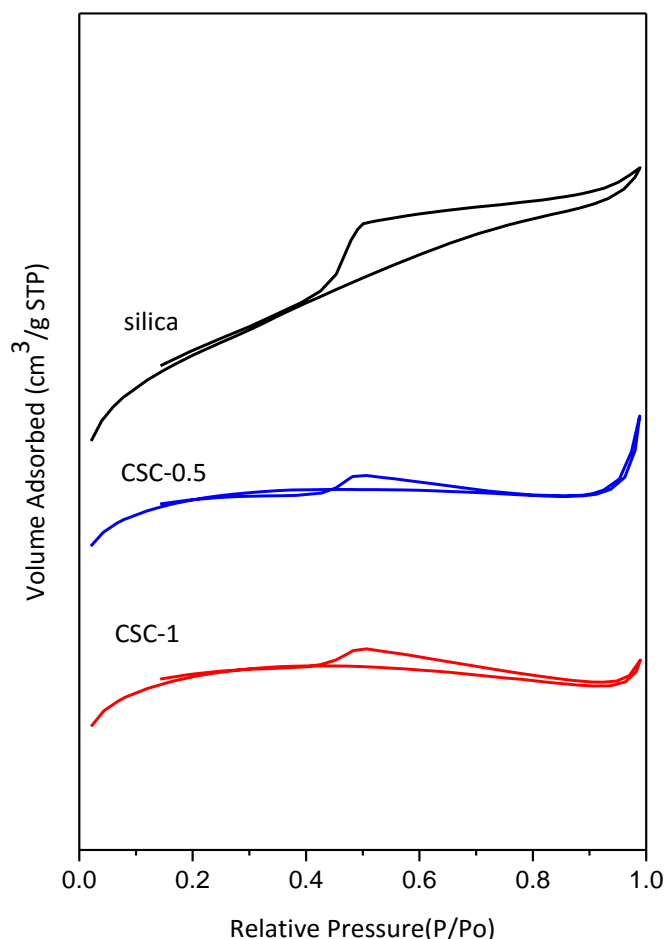
Figure 3.53 Nitrogen adsorption/desorption isotherm plots of silica and the corresponding CSCs

The TEM images shown in Figure 3.54 indicated the silica sample possess an onion structure with hollow spheres. Through the modification with different amounts of bio-oil, this interesting structure still remained in the CSC-0.5 sample. It is hardly observed in the CSC-1 and CSC-2 sample, which is probably due to the blockage by an excess of organic matters.
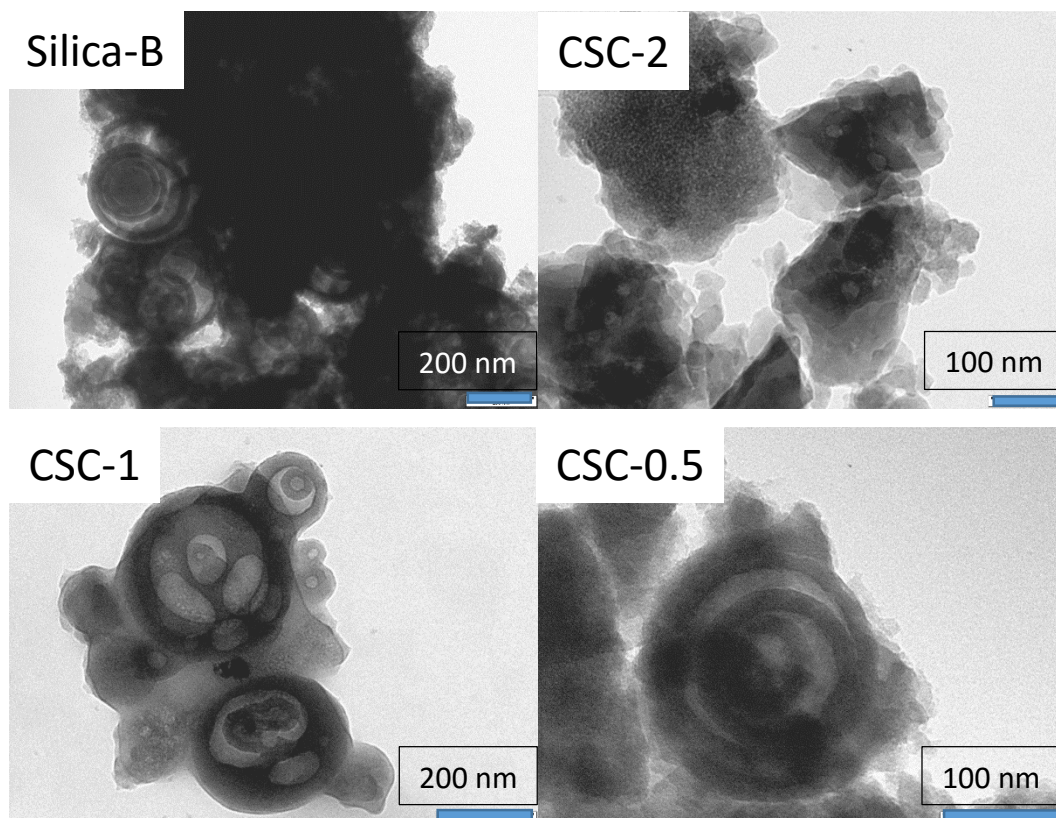
Figure 3.54 TEM images of silica support and its CSCs

3.7 Proposed mechanism for silica modification

According to the discussion above, the prospective vision of this preparation method could be proposed and illustrated in Figure 3.55. As can be seen, initially the parent SBA-15 materials are impregnated with bio-oil diluted with specific amount of acetone, followed by evaporation of the solvent and carbonization of the mixture of preparation. The carbon species in the materials vary significantly based on the carbonization temperature, resulting in a continuum functionality ranging from polar hydroxyl groups to aromatic surfaces of CSC. This creates unique advantages compared to traditional

176

synthetic methods. Due to the strong interactions between oxygenated compounds existing in bio-oil and residual silanol groups in silicas, the organic compound not in close contact with silica surface could be more easily removed via increasing temperature, hence a carbonaceous layer is coated around the interior of silica pores. The resultant CSC exhibits not only similar pore structural ordering as parent SBA-15, but also unique advantages including temperature-dependent surface functionality, cost-effective carbon source from waste and is prepared from a simple modification process. In order to fabricate different types of carbon-silica hybrid materials with specific mesoporous structures, a variety of porous silica has been utilized as alternative substrates including SBA-15 series in this approach. Several analytical techniques such as X-ray diffraction (XRD), N_2 porosimetry, microscopy, diffuse reflectance infrared Fourier transform (DRIFT), solid state NMR, and X-ray photoelectron spectroscopy (XPS) were utilized for characterizing the final product.
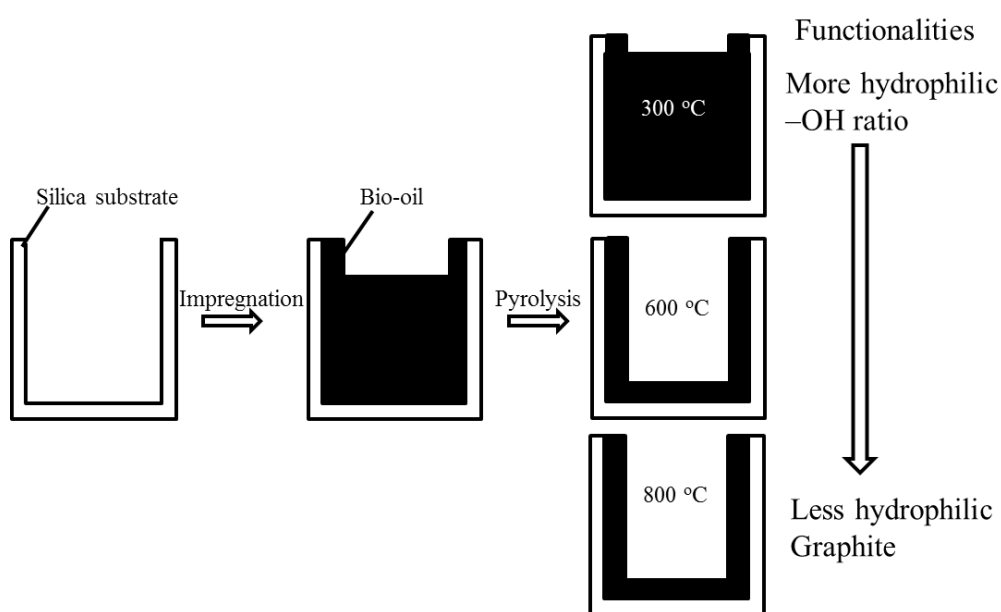
Figure 3.55 Proposed mechanism of oil modification on the surface of silica materials

3.8 Conclusion

In this chapter, a novel approach of preparation of carbon-silica material has been studied in order to enlarge the application range of mesoporous silica materials. A series of reaction conditions has also been investigated for preparing controllable CSCs with continuum functionalities. The obtained composites still possess high specific surface

177

area, narrow pore size distribution and ordered mesoporous structure mimicking the silica substrates. Moreover, the surface property could be tuned with continuum of functionalities ranging from polar hydroxyl groups to aromatic surfaces.

Bio-oil, which is generated from microwave fast pyrolysis of biomass and waste material (waste office paper is used in this work), is utilized as carbon source to prepare carbon silica composite. A range of techniques including GC-MS, NMR, FT-IR and TG were utilized to characterize the properties and determine the chemical composition of the bio-oil. The results demonstrated that the composition of bio-oil is complex, and the carbohydrate and its derivatives are the majority components with a quantity of furanic compounds and phenolics. The detailed discussion of the bio-oil selected is important for the synthesis of CSC materials with tuneable functionalities and surface properties in the later section.

The thermal analysis of CSC material demonstrated that almost 45 w/w % of the weight loss was observed before the material was heated to 400 °C. Thermogravimetric analysis of the bio-oil indicated that there is one major mass loss at 230 °C, which is associated to the decomposition of heavier compounds. The volatile components released at this temperature range were investigated by TG-IR. The results showed that the decomposition of the aliphatics and carbonyl groups contributed to the majority of the gas, which correlates to the NMR and DRIFT results of CSC materials shown in 3.5.4.

Both the silica support and the CSC material have been carbonized with different heating rate to investigate the influence of the heating rates on the structural property of material. The nitrogen porosimetry and XRD analysis of CSC material demonstrated that there is a minor effect on the mesoporous structure of the material by adjusting the heating rate up to 5 K/min. The XRD analysis of CSC and silica sample suggested that the variation of the structural ordering of the CSC under various heating rates is mainly due to the shrinkage of the silica support.

The synthesized composites possess a continuum of functionalities ranging from polar hydroxyl groups to aromatic surfaces through simply adjusting pyrolysis temperature. After the modification process, structural characterizations reveal that the resultant CSCs

178

exhibit well-ordered structures with high specific BET surface area, uniform pore size, comparable with the parent silicas. The chemical property and surface functionality of CSC could be easily tailored by carbonization temperature, offering this composite a variety of potential applications in chemical separation and heterogeneous catalysis. These have been characterized and evidenced by the small angle XRD, DRIFT, solid state NMR and XPS analysis. Moreover, the combustion of the CSC material has also been studied and has shown that this regenerates the original silica material. The subsequent analysis indicated that the material still showed the original pore matrix and linear pore arrangement like parent SBA-15.

In addition to the typical SBA-15 silica sample, examples of other mesoporous and meso-macroporous silicas such as MCM-41, MMSBA and KIT-6 and the silicas with spherical structures prepared in supercritical carbon dioxide were applied as solid support for the synthesis of CSC materials. This indicated that various types of porous silicas could be utilized in the preparation of CSC with unique pore matrixes via this simple approach, offering this method vast potential for further applications.

Owing to the well-ordered mesoporous structure, high surface area and variable surface functionality of CSC, this type of porous carbon-silica composite should have a potential application in separation processes and heterogeneous catalysis. The application of this novel composite deposited with palladium nanoparticles in catalysis field, particularly for Heck reaction, has also been investigated as detailed in Chapter 4.

Chapter 4   Catalytic activity test of Pd modified CSC catalyst

4.1 <u>**Background**</u>

Coupling reactions, allowing the combination of two different organic molecules into a new compound through the formation of a carbon-carbon bond, are important in organic synthesis. In 2010, the Nobel Prize in Chemistry was awarded to Richard F. Heck, Ei-ichi Negishi and Akira Suzuki for the development of palladium catalysed cross coupling. Such C-C bond constructions contribute to solving the problem of binding carbon atoms together. One of the most utilized coupling reactions is the Heck reaction, which offers the olefination of acryl, benzyl or vinyl halides through their reaction with various alkenes in the presence of palladium (Pd) catalyst.

The Heck reaction couples a vinylic halide or an aryl halide with an alkene in the presence of a base such as trimethylamine, and it is a substitution reaction: a vinylic hydrogen of the alkene is replaced by the R group of the aryl or vinylic halide. The general mechanism for Heck coupling reaction has been extensively studied and is depicted in Figure 4.1. The reaction initiates with an oxidative addition of palladium between the carbon and the halogen. The alkene inserts itself in the palladium-carbon bond by *syn* addition, followed by a C-C bond rotation. The regioselectivity of this insertion depends on the nature of the alkene, the catalyst and the reaction conditions. The organopalladium species then undergoes *syn* β-hydride elimination to form the new alkene product. The palladium(0) compound is then regenerated by reductive elimination of the palladium(II) compound by the base.[265, 266]
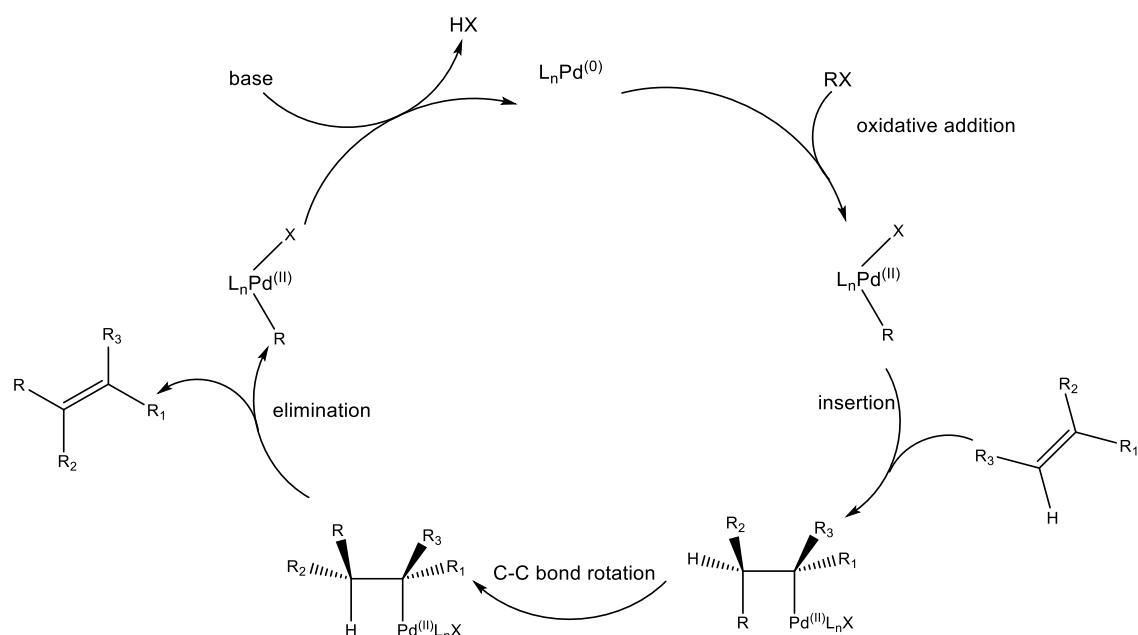
Figure 4.1 General catalytic cycle for Heck coupling reaction

Despite the great synthetic potential of this reaction in organic synthesis, environmental issues have been proposed such as recovery of catalysts and the utilization of alternative benign solvents since it was first discovered in 1970's. In recent years, the research on benign and sustainable chemical process has been the main focus. As an expensive metal catalyst, great efforts in terms of improving the elemental sustainability have been devoted into the design, recovery, recycle and reuse of Pd nanoparticles. Homogeneous catalysts have shown high catalytic activity in this process. However, this homogeneous catalytic process exhibits some drawbacks such as the lack of reusability and the contamination of the product.[267] As such, immobilization of Pd species onto a solid support to fabricate a heterogeneous catalyst is an ideal approach to solve this problem. In this case, the nature of the solid support could be critical for the performance of the catalyst. The encapsulation or confinement of Pd within the inner porosity of the support could avoid leaching or aggregation of the Pd, thus enhancing the stability of the catalyst and improving the metal elemental sustainability.[267] Pd catalysts supported on carbonaceous materials were developed and widely utilized in C-C coupling reactions and hydrogenation for industrial use due to the chemical inertness of carbonaceous materials under moderate experimental conditions.[268] However, the broad pore size distributions ranging from micropores to macropores and structural shrinkage under high temperature limited the applications and functions of traditional activated carbon

supports.[269] This drawback has been addressed by the incorporation of silica species to prepare a new carbon-based hybrid support. The incorporation of mesoporous silica substrates could offer massive advantages in scaffolding the nanostructure and tuning pore size and pore surface chemistry in comparison with conventional activated carbons.[270, 271] Therefore, a novel mesoporous carbon-silica hybrid support has been developed and studied, showing a better surface property with narrow pore size distribution and tuneable pore structure in comparison to activated carbons. Zhao *et al.* has developed a heterogeneous palladium catalysts supported on carbon-silica based materials, which were synthesized via a triblock copolymer templating approach by using phenolic resins and tetraethyl orthosilicate (TEOS) as carbon and silica precursors, respectively. The resultant materials exhibited an impressive yield of ~60 % in the Heck reaction of chlorobenzene and styrene without any assistance of a phase-transfer catalyst.[269]

In order to achieve a benign synthetic process, carbon silica composites (CSCs) could be used as an alternative solid support for depositing palladium nanoparticles. In this work CSCs are prepared by the utilization of bio-oil as alternative carbon source, which has been fully discussed and characterized in the previous chapter. Bio-oil is a by-product of bio-char production obtained by microwave fast pyrolysis of a range of biomass types, such as wood, rice husk, waste office paper and so on. The CSCs, which possess high BET specific surface areas and uniform pore sizes, could be an ideal alternative solid support for immobilization of Pd nanoparticles. The ordered mesoporous structure allows this composite to act as scaffold in which the metal is well dispersed. The carbon species gradually polymerize and carbonize with the increase of temperature, thus forming a carbonaceous layer around the silica surface, allowing a better immobilization and uniform dispersion of Pd nanoparticles. This offers the catalyst a higher catalytic activity and better recoverability.

In this chapter, three types of heterogeneous catalysts including Pd-CSC, Pd-SBA-15 and Pd-AC catalyst were introduced for the Heck reactions. The procedure for the fabrication of Pd-CSC catalyst was similar to that of CSC materials described in previous chapter. Pd-SBA-15 catalyst was prepared by the mix of SBA-15 silica and palladium with the

incorporation of small amounts of acetone, followed by the carbonization at 500 °C. Pd-AC (Pd on activated carbon) catalyst was purchased from Sigma-Aldrich. Their physical and chemical properties were compared and the catalytic activity of these catalysts for the Heck reaction was also tested later.

4.2   Heterogeneous catalyst for Pd-catalyzed coupling reactions

4.2.1   Mesoporous structure and chemical compositions of Pd-CSC, Pd-AC and Pd-SBA-15 catalysts

The detailed analysis of CSC material was studied in Chapter 3. It is believed that even with the incorporation of palladium nanoparticles, the structural properties of Pd-CSC catalyst is very close to that of CSC material.

The CSC support was prepared at 500 °C with a heating rate of 1 °C/min under nitrogen flow. The adsorption/desorption isotherm plot of Pd-CSC catalyst displayed typical Type IV curves with significant nitrogen uptake under the relative pressures of 0.4-0.8, which confirmed its well-ordered mesoporous structure, however there was a more gradual rise in adsorption branch during capillary condensation compared to the isotherm plot of parent SBA-15.[235] Owing to the deposition and insertion of palladium into the carbonaceous layers, the surface of the catalyst was harder to control as compared to the parent SBA-15. The BET specific surface area, pore volume and pore size of Pd-CSC catalyst calculated from porosimetry data was 355 m^2/g, 0.13 cm^3/g and 3.3 nm, respectively and shown in Table 4.1. However, it should be noted that the values are lower than those of Pd-AC and Pd-SBA-15 catalysts, which could be ascribed to the introduction of bio-oil, causing partial blockage of the pores of the support.
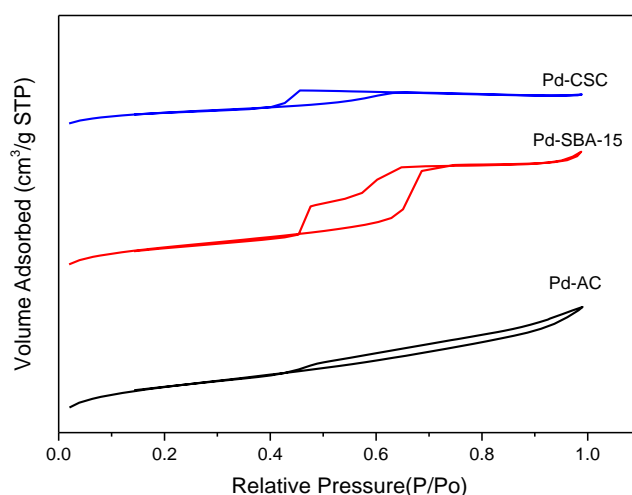
Figure 4.2 N$_2$ adsorption/desorption isotherm plots of Pd-AC, Pd-SBA-15 and Pd-CSC materials

Moreover, the desorption branch of the Pd-SBA-15 catalyst has two drop steps, suggesting there are two porous structures with different pore sizes. This may be due to the poor dispersion of palladium when utilizing this method without the help of bio-oil. Two of the significant peaks in the pore size distribution curve of Pd-SBA-15 catalyst, which was shown in Figure 4.3, suggests the two pore diameters are estimated to be 3.9 nm and 5.4 nm. This is also indicated that the catalyst possessed two different pore structures, resulting from the poor dispersion of palladium, which is in correlation with the isotherm plot.

Table 4.1 Textural properties of Pd-AC, Pd-SBA-15 and Pd-CSC materials

Sample	BET surface area (m^2/g)	t-plot micropore area (m^2/g)	Pore volume (cm^3/g)	Pore diameter (nm)
Pd-AC	844	483	0.41	5.1
Pd-SBA-15	408	121	0.53	4.7
Pd-CSC	355	193	0.13	3.3

Only one peak is observed on the pore size distribution curve of Pd-CSC catalyst, suggesting the metallic palladium is well-dispersed in the mesoporous structure of the

solid carrier as there is one peak located on the parent SBA-15 curve (Figure 4.3 inset). This is back up by the TEM images of the Pd-CSC catalyst. A minor peak was located on the curve of Pd-AC catalyst, suggesting this material possesses a low proportion of mesopores, thus could be regarded as a microporous-mesoporous material. Hence, the isotherm plots of commercial Pd-AC catalyst demonstrated the mesoporous carbon material with non-uniform pore sizes, which could be concluded from the weak peak in pore size distribution curve.
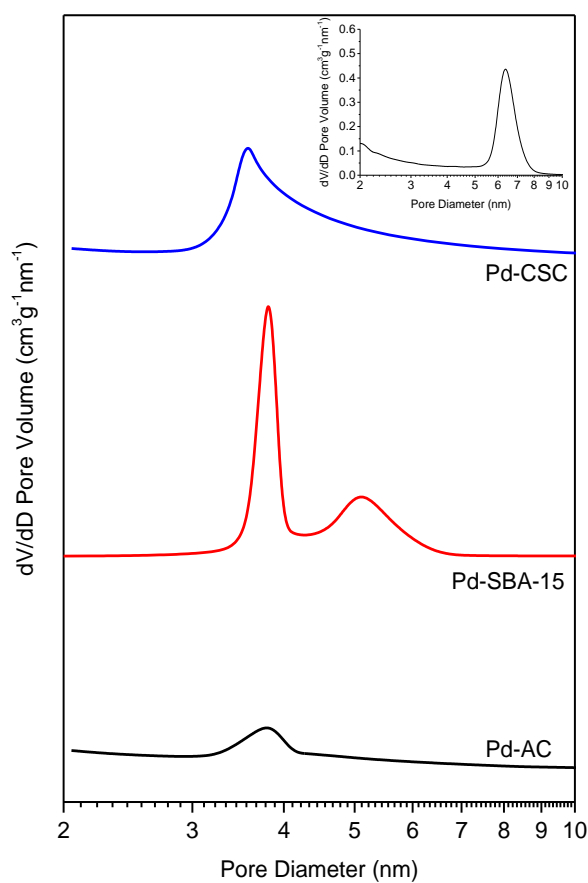
Figure 4.3 Pore size distribution curve of Pd-AC, Pd-SBA-15 and Pd-CSC materials (inset graph for parent SBA-15 material)
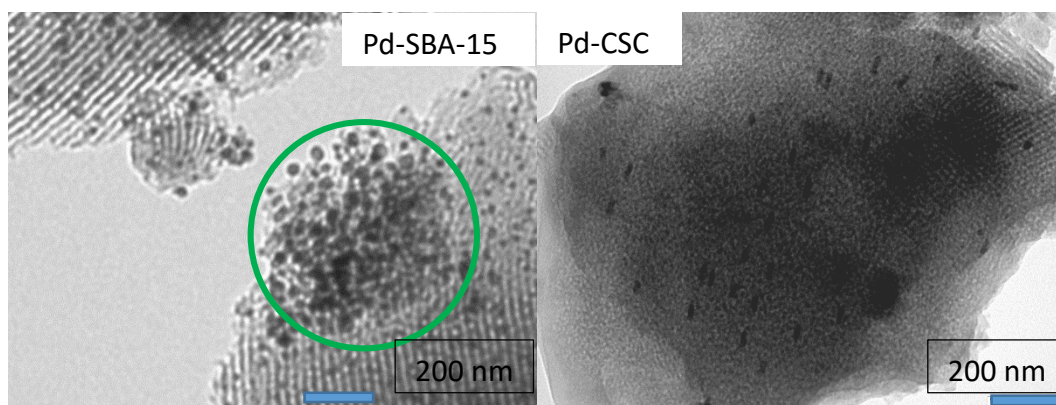
Figure 4.4 TEM images of Pd-SBA-15 and Pd-CSC materials

It could be concluded that the Pd-CSC catalyst still retains the physical properties of the SBA-15 after deposition of Pd nanoparticles. This could be observed intuitively from TEM images. Moreover, the palladium nanoparticles were well-dispersed on the surface of CSCs, rather than aggregated together, allowing this catalyst to be more beneficial to catalyse the Heck reaction. While this was the case to a limited extent in the Pd-SBA-15, there were significant amounts of bulk palladium nanoparticles sticking together on the surface of this material (green circle in Figure 4.4). This difference may be due to the polymerization of bio-oil, preventing the palladium nanoparticles from aggregation during the heating step.
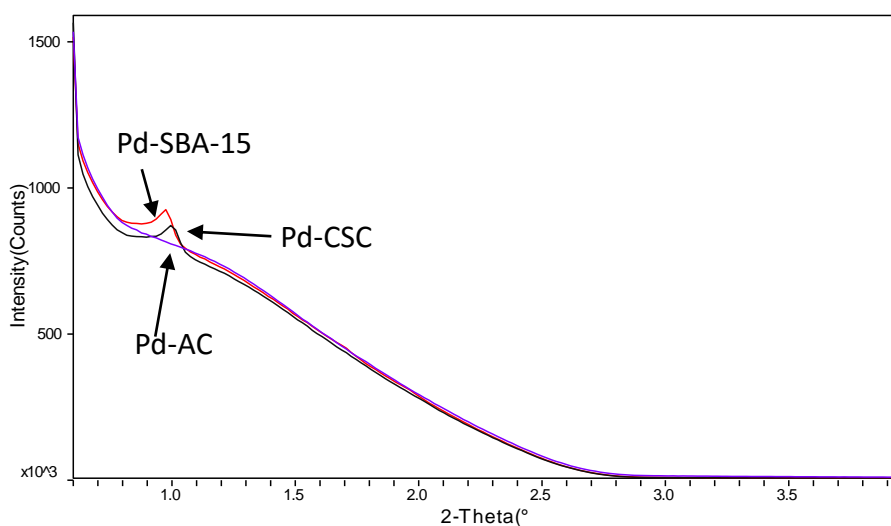
Figure 4.5 Small angle XRD patterns of Pd-AC, Pd-SBA-15 and Pd-CSC materials

All SBA-15-based supported palladium catalysts exhibit representative small angle XRD patterns of the two dimensional hexagonal mesoporous structures in Figure 4.5. There is one strong 100 diffraction at ~ 1.0º, proving the mesoporous structure property of the corresponding catalyst.[251, 252] This result is consistent with the porosimetry data shown in Figure 4.2 and the TEM images demonstrated in Figure 4.4. Clearly the peak of Pd-CSC catalyst shifted to larger angle compared to that of Pd-SBA-15 catalyst, suggesting the Pd-CSC catalyst has smaller cell dimensions. These results clearly indicate that the mesoporous structure of the solid support is still retained after the palladium incorporation. No significant peak observed in small angle XRD pattern of Pd-AC indicated it is amorphous, which is consistent with the broad pore size distribution.
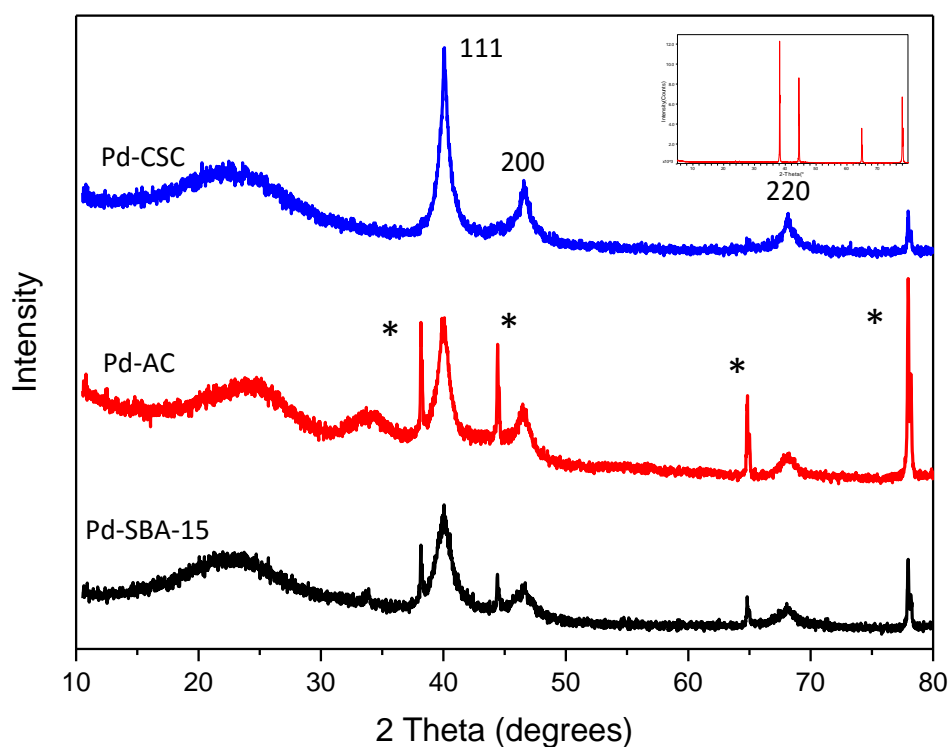
Figure 4.6 Wide angle XRD patterns of Pd-AC, Pd-SBA-15 and Pd-CSC materials (inset: wide angle XRD pattern of sample holder)

Figure 4.6 shows the wide angle XRD patterns of Pd-CSC, Pd-AC and Pd-SBA-15 catalysts. The well-resolved peaks at 2θ=40.1º, 46.5º and 68º were observed in all of the Pd catalysts, which were assigned to the 111, 200 and 220 reflections of the face-centre cubic (fcc) Pd lattice.[272, 273] The sharp peaks indicated the growth of metallic Pd in these catalysts. According to the Scherrer equation, the estimated palladium particle size is

190

approximately 8.8 nm, 8.4 nm and 5.4 nm for Pd-CSC, Pd-AC and Pd-SBA-15, respectively. The broad peak at ~23° could be assigned to either amorphous carbon or amorphous silica in these Pd catalysts.[269] The wide angle XRD patterns of the Pd-CSC catalysts are shown in Figure 4.7. It is easily observed that the intensity of characteristic peak of palladium increased from 1% Pd loading to 12.5% loading. Based on the Scherrer equation, the corresponding average grain size of Pd nanoparticles increased, indicating that the increased palladium concentration would accelerate the aggregation effect of the palladium nanoparticles. It should be noted that there were some unexpected peaks (labelled as * in Figure 4.6) observed in some samples. This is due to the signals of sample holder, caused by the insufficient amount of sample, which could be evidenced by the XRD pattern of the sample holder (see Figure 4.6 inset).
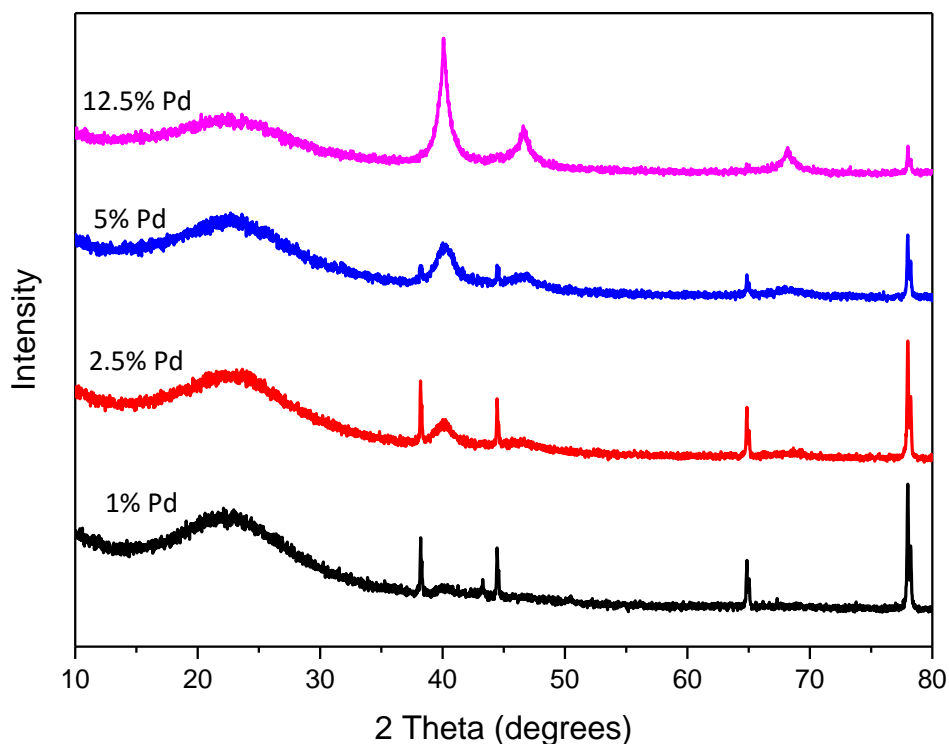
Figure 4.7 Wide angle XRD patterns of the Pd-CSC catalysts with different palladium loadings

Hence, the Pd-CSC catalyst possesses ordered mesoporous and uniform pore sizes compared to Pd-AC catalyst, allowing the palladium nanoparticles to easily interact with reagents, thus resulting in an effective catalytic activity for coupling reaction. In comparison with Pd-SBA catalyst, Pd-CSC has a high dispersion of palladium

nanoparticles in the mesopores, giving a better catalytic activity and recoverability.[269] This may be due to the polymerization of bio-oil during the carbonization helping to prevent the palladium aggregation.

4.3   Utilization of Pd-CSC catalyst in the Heck reaction

In typical organic processes, the solvents are employed both as the reaction media and for purification of desired products, so that they could occupy the majority of the material input.[274] Hence, a suitable solvent is another vital factor for a green process.[275] Cross-coupling reactions are preferentially carried out in dipolar aprotic solvents, such as *N*-methylpyrrolidone (NMP), *N,N*-dimethylformamide (DMF) or *N,N*-dimethylacetamide (DMAc). Due to the dipolarity of these solvents resulting in stabilizing the alkene intermediate, the alkene insertion by palladium, which is regarded as the rate-determination step of the Heck reaction, is easily achieved.[276]

4.3.1 Catalytic activity of catalyst in NMP

Scheme 4.1 Model Heck reaction used to determine the catalytic activity of the Pd-CSC catalyst
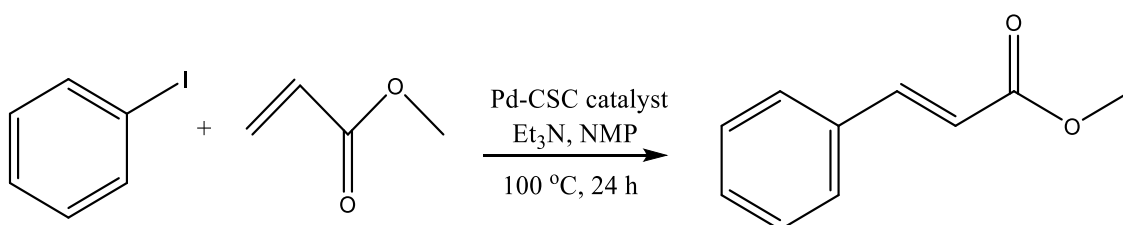
The Heck reaction of iodobenzene and methyl acrylate, using conventional *N*-methyl-2-pyrrolidone (NMP) as solvent and triethylamine as base (Scheme 4.1), was firstly carried out in order to investigate the catalytic activity of as-synthesized Pd-CSC catalyst.

The activity of the catalyst can be well illustrated by the coupling of iodobenzene and methyl acrylate in the presence of triethylamine in NMP and the conversion of reaction after 24 hours was 82%, proving that the designed material could successfully catalyse the reaction. For comparison, purified palladium acetate was utilized as catalyst at the same condition and it led to a conversion of 89%. Reuses of the catalyst were carried out by recycling the catalyst without additional thermal activation. This was done by the

filtration of the catalyst from the reactor and followed by re-loading the starting materials.
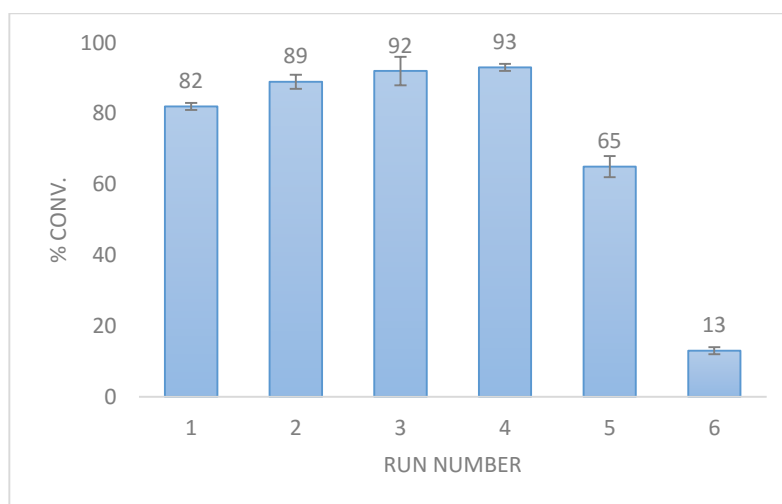
Figure 4.8 Conversion of the Heck reaction using Pd-CSC catalyst in NMP

Figure 4.8 shows that the catalyst could be reused four times in NMP before there is a significant drop of 28% conversion. It is worthwhile to note that high selectivity (>95%) in this reaction using NMP as solvent was observed when the catalyst was reused. The conversion of the reaction decreased to 13% at the 6th catalyst use. Based on the previous study, triethylamine hydroiodide (Et$_3$NHI) is formed in the reaction, and is likely to adsorb on the catalyst surface, thus blocking the pores and hindering the reaction.[277] In this case, a reactivation process has been done *via* re-heating the inactive catalyst at 500 °C with a heating rate of 1 °C/min under nitrogen flow, followed by the reuse of this catalyst. There is a significant increase of conversion from 13% to 84%, proving that the catalyst pores have been blocked and Pd has been covered by the insoluble component. Removal of this materials leads to recovery in activity to around the original value. Thereby, the leaching of that active catalytic palladium, which is a typical deactivation mechanism, hardly influences the drop of conversion at the 6th use. There was still enough Pd deposited in the surface of the catalyst and the heating step contributed significantly to the reactivation of the catalyst.

Samant *et al.* provided the investigation about the catalytic activity of Pd/C in the Heck reaction of aryl iodide with methyl acrylate with the help of ultrasound. It reached 71% conversion of iodobenzene and the yield of product was 70%, showing a high selectivity

193

of the reaction. In terms of the recoverability of the catalyst, the Pd/C catalyst could be only be recycled twice but the conversion was decreased to 60% at the 3rd run.[278] The recycling studies showed that the Pd/C catalyst prepared by Kohler even gave a 4% conversion at the 3rd run in the presence of dichloromethane/NaOAc after 6 hour reaction.[279] Under this circumstance, it is demonstrated that Pd-CSC catalyst has an effective catalytic activity and its recyclability is advantageous compared to the previous research. It should be noted the turnover number (TON) for this reaction is as high as *ca.* 4700 (mole of desired product/mole of Pd) when 0.02 mol% of the catalyst is used, which is comparable to some of the previous studies.[277, 279]

4.3.2 Catalytic activity of the Heck reaction at different amounts of Pd-CSC

Figure 4.9 demonstrated the conversion of Heck reaction by using a range of different amounts of Pd-CSC catalyst ranging from 0.02 mol% to 0.6 mol% at 100 ^oC. Under identical reaction conditions, the performance of the low amount of Pd-CSC catalyst is slightly poorer than that of higher amounts loading. The conversions of the starting materials for all runs are higher than 75%, suggesting that this catalyst has a great catalytic activity in coupling iodobenzene and methyl acrylate. These results indicate the ability to activate iodobenzene for the Pd-CSC catalyst with extremely low amounts. This could be interpreted by the high Pd dispersion and uniform Pd impregnation on the surface of the solid support. Compare to Hunt's research, in which at least 0.1 mol% of catalyst was added for catalysing the Heck reaction,[276] a high conversion could be achieved by the utilization of low amount of Pd-CSC catalyst.
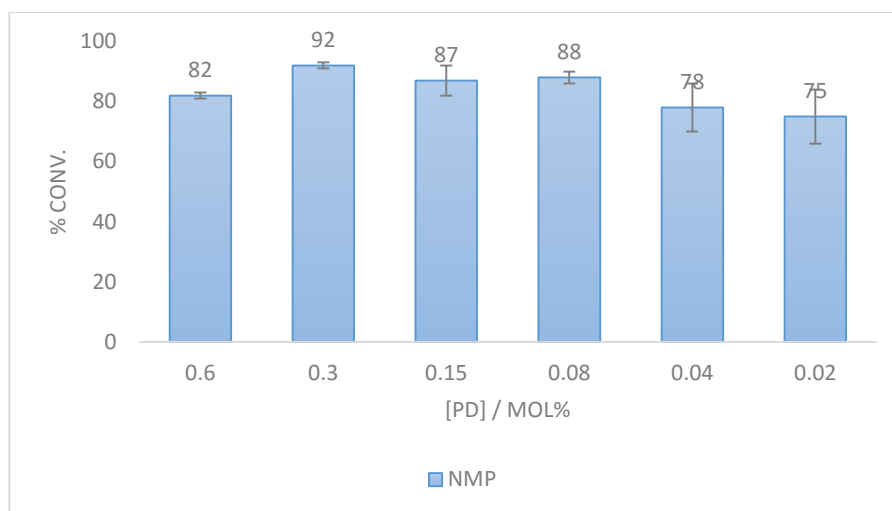
Figure 4.9 Conversion of Heck reaction using different amounts of Pd-CSCs in NMP

Based on the study of the recyclability and the Pd loading of the catalyst, it could be concluded that the as-synthesized Pd-CSC catalyst is extremely suitable for catalysing the Heck reaction in a high conversion and with excellent reusability. From the green chemistry point view however, it is important to not only fabricate the reusable catalyst, but also choose to use alternative solvent instead of conventional organic solvent.

4.4 Catalytic activity of Pd-modified catalyst in the Heck reaction by using alternative solvent

Pd-CSC catalyst has a good performance in the Heck reaction by using traditional solvent. However, a number of considerations such as environmental impact, toxicity to human health, and breach of some related regulations may restrict the further use of these solvents. The relevant research revealed that the greener solvents have been investigated for the Heck reaction, including water, ionic liquids, supercritical carbon dioxide and fluorous solvents. According to the previous research, these systems have some deficiencies as they often achieved a low yield or a ligand-modified catalyst is needed.[275]

In order to make the process efficient and simple, a benign alternative of organic cyclic carbonate with highly dipolarity was therefore proposed by Hunt and co-workers,[276] as a substitute for conventional dipolar aprotic solvents for the Heck reactions. Moreover, the propylene carbonate also has a low vapour pressure and odour level, leading to a

safe and easy-to-handle process. Another ecologically benign aspect of the use of cyclic carbonate is the environmentally friendly synthesis for these solvents.[280] Propylene carbonate could be synthesised from carbon dioxide (CO_2) *via* a solventless reaction.[281] A simple and metal-free method was also developed to convert alkenes and carbon dioxide into cyclic carbonates in water.[282] However, as a consequence of the relatively high boiling point of the cyclic carbonates, the removal of these solvents by distillation when the reaction has finished is very challenging economically, leading to the difficulty of obtaining the purified desired product. Therefore, it is necessary to solve the question of product separation in the cyclic carbonate system.[283]

propylene carbonate
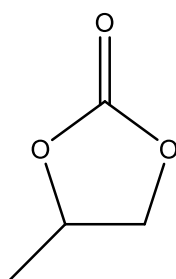
Figure 4.10 Structure of propylene carbonate

Cyclic carbonates have become popular alternative solvents in organic synthesis and catalysis in consideration of green chemistry aspect.[283] Borner *et al.* investigated the utilization of cyclic carbonates as solvents in Pd-catalysed asymmetric allylic substitution reaction. In comparison to the conventional dichloromethane, an enhanced yield and good selectivity were achieved. It should be noted that, in some cases, the palladium catalyst showed a better catalytic performance in terms of yield when cyclic carbonates were used.[284] Propylene carbonate was also proposed by the same research team to be utilized for asymmetric hydrogenation reaction instead of MeOH, THF and CH_2Cl_2.[285] Rhodium-catalysed intermolecular alkyne hydroacylation reaction has been shown to proceed in propylene carbonate as replacement for dichloroethane.[286] It has to be noted that there is limited research focusing on the utilization of cyclic carbonates as solvents for the Heck coupling reaction. Hence, a systematic study on the Heck reaction in propylene carbonate (Figure 4.10) has been investigated in this chapter.

4.4.1 Catalytic activity of catalyst using propylene carbonate as solvent
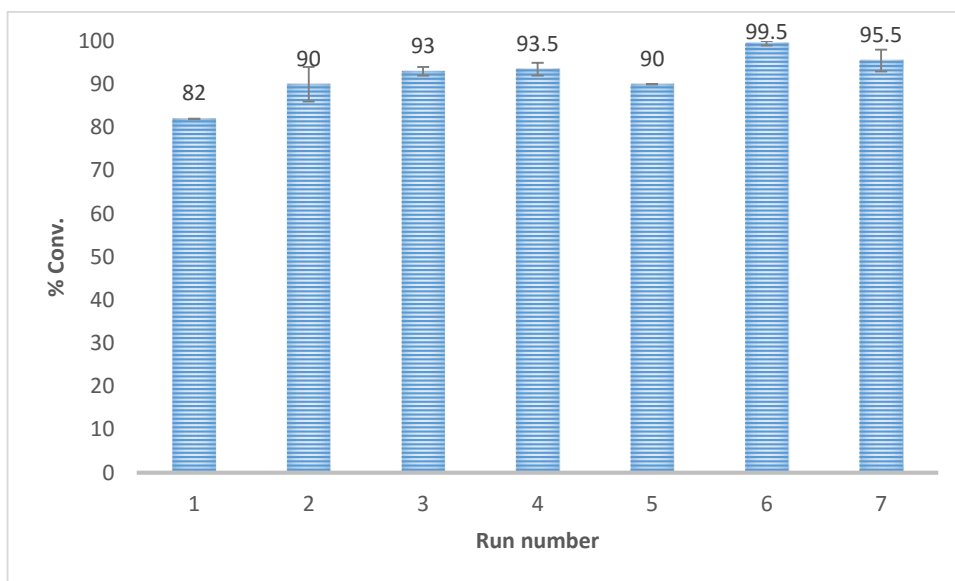
Figure 4.11 Conversion of the Heck reaction using Pd-CSC material in proplylene carbonate

In terms of the solvent influence on the Heck reaction, the polarity needs to be most considered.[276] Due to the close dipolarity (π^*=0.90) of both NMP and propylene carbonate,[276] they could theoretically have similar properties and promote a high productivity of the Heck reaction. The conversion of the methyl acrylate shown in Figure 4.11 demonstrated that there was a high catalytic activity of Pd-CSC in propylene carbonate. The catalyst can be used at least 7 times with a good catalytic activity and the conversion of the reaction was over 90% except for the 1st run, which is advantageous compared to that in the NMP. In Perez-Juste's review study, versatile heterogeneous catalysts for carbon-carbon coupling reactions were prepared using inorganic, organic and hybrid materials to support Pd nanoparticles.[267] He summarised that the majority of these catalysts could be recycled for reaction fewer than seven times. This suggests that Pd-CSC catalyst prepared in this work has an improved recyclability compared to other heterogeneous catalysts.

It is worthwhile to note that from the ICP analysis of the liquid phase of the Heck reaction, the palladium loss for the 1st run is as high as 26%, but other runs have a much lower Pd loss (< 2%). This suggests that there is a considerable amount of Pd leached into the liquid phase when the fresh Pd-CSC catalyst was used. A lot of loose Pd was dislodged in

the 1st run, which possibly led to produce benzene by hydrodeiodination and thus further producing a side product, which will be discussed in detail in the following section.[287]

Table 4.2 Catalytic performance in coupling reaction for Pd-CSC catalyst

Run number	Yield %[a]	Conversion %[b]	Selectivity %[c]
1	51 ±0.2	82 ±0.5	62
2	88 ±0.4	90 ±0.4	97
3	91 ±0.5	93 ±0.1	98
4	90 ±0.2	93 ±0.2	96
5	90 ± 0.4	90 ±0.3	>99
6	90 ±1.0	99 ±0.5	91
7	92 ±0.5	95 ±0.5	97

[a] yield of methyl cinnamate is determined by GC analysis. [b] conversion of methyl acrylate is determined by ^{1}H NMR. [c] selectivity is calculated by the yield and the conversion.

Other than detecting the conversion of starting materials, it is important to fully monitor the production of the desired product for the reactions. Table 4.2 depicts the yield of methyl cinnamate, conversion of methyl acrylate and the selectivity of the reaction. The selectivity of the reaction for the 1st run is much lower than that of other reactions. It is explained in the next section that the generation of the side product methyl 3,3-diphenylacrylate resulted in a drop of the proportion of the desired product so to achieve a low selectivity. In the following recycle runs, the amounts of leached palladium were dramatically decreased, as measured by ICP analysis. This indicates that the amounts of this side product are far more when Pd leaches.

4.4.1.1 Characterization and identification of methyl cinnamate

Figure 4.12 demonstrates the GC spectrum of the liquid phase after the 1st run. The strong signal ascribed to the desired product methyl cinnamate is observed at ~13 minutes, and also the solvent peak (~1.6 minutes) cannot be neglected. The elimination of the peaks for starting materials such as methyl acrylate (~1.3 minutes) and iodobenzene (~7.9 minutes) suggests that the Heck reaction proceeded successfully with the help of the Pd-CSC catalyst at 100 °C for 24 hours. Surprisingly, there is a significant peak at ~19 minutes, which is assigned to the side product of the reaction. The result is

198

consistent with the selectivity result of the 1st run in Table 4.2. As such, it is necessary to identify and characterize the desired product and the side product by using a range of analytical techniques including GC-MS and proton NMR. The corresponding standard sample was also purchased and the spectra were obtained for comparison.

Figure 4.12 GC spectra of the fractions from column chromatography

After the completion of the reaction, the desired product methyl cinnamate was extracted from the solvent and purified for further identification. GC analysis of standard methyl cinnamate has been done by using the same GC method. The retention time for the standard sample is *ca.* 13.4 minutes, which is consistent with the peak detected from the product solution.

Figure 4.13 EI Mass spectra of methyl cinnamate

The molecular ion at m/z =162 could be identified in Figure 4.13, which is consistent with the molecular weight of methyl cinnamate ($C_{10}H_{10}O_2$). The possible fragmentation

pathway of cinnamic acid has been studied by Schaldach and could be applied for the fragmentation of methyl cinnamate.[288] The base peak ion is located at m/z = 131, which is consistent with previous study.[289] This ion is produced by the loss of –O-CH$_3$ group of the molecule. The pathway of formation of the fragment ion is shown in Figure 4.14. Another ion at m/z = 103 is also observed due to the cleavage of C-C bond to release –COOCH$_3$ group. Besides, the ion at m/z = 77 is probably attributed to benzene ring (C$_6$H$_5^+$).

m/z = 162   m/z = 131   m/z = 103
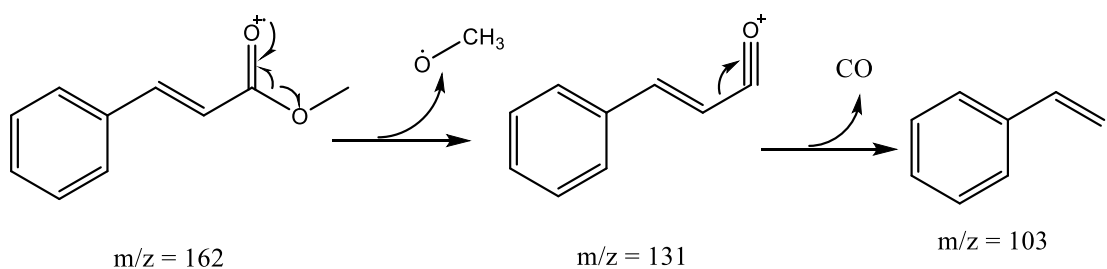
Figure 4.14 Formation of fragment ions m/z = 131 and m/z = 103
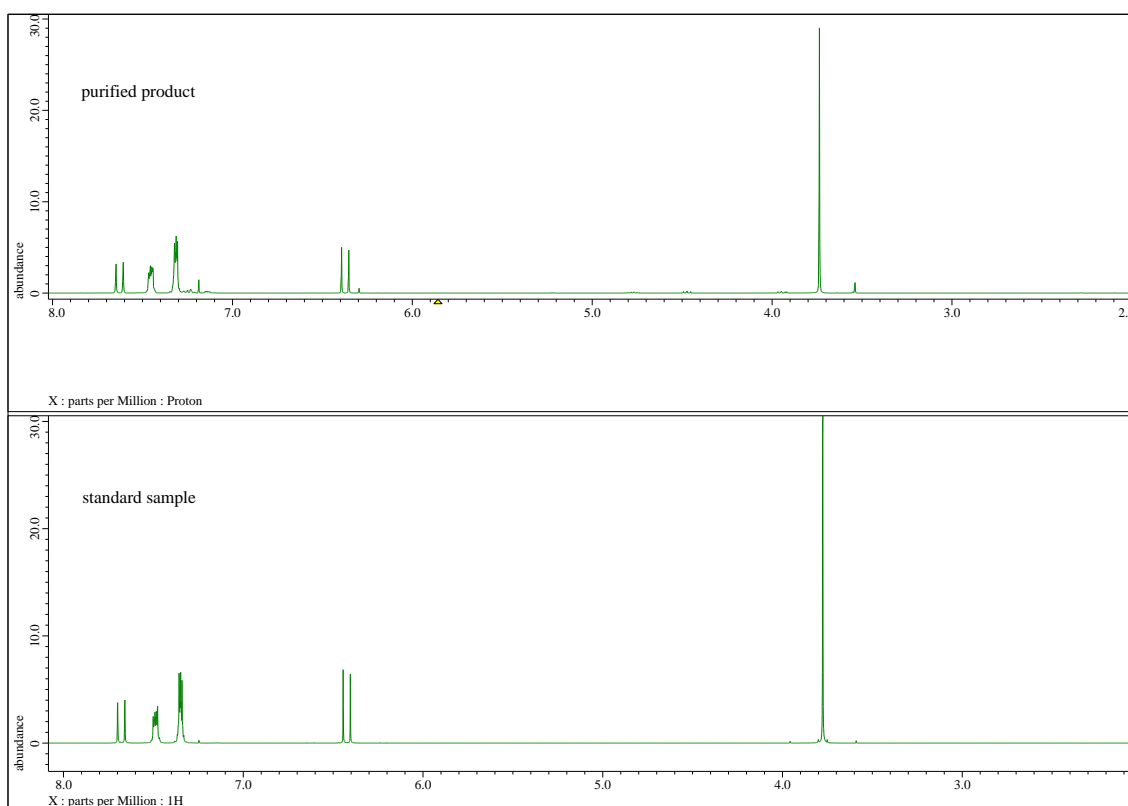
Figure 4.15 ^{1}H NMR spectra of as-synthesized and standard methyl cinnamate

^{1}H NMR spectra of both purified sample and the standard methyl cinnamate are shown in Figure 4.15. The chemical shifts of the characteristic peaks appeared on the spectra of the product are in good agreement with those on the standard sample, indicating that the Heck reaction proceeded smoothly. The chemical shifts for the corresponding hydrogen atoms in the sample were illustrated in Figure 4.16 and Table 4.3. The singlet peak at δ 3.73 is attributed to the protons on the methyl group with an integration of 3H. The proton NMR spectrum also shows two doublet peaks with an integration of 1H at δ 6.37 and δ 7.62, which are assigned to the protons on the olefin group. It should be noted that the J value of the coupling constant between 2 and 3 is 16 Hz, indicating the geometry of the double bond could be assigned to be in *trans* form. The signals of the protons on the benzene ring are observed at δ 7.2-7.5. In consideration of stereochemistry, the distance between the proton 4 and 4' on the benzene and the proton 3 on the olefin group is not identical so that the proton 4 and 4' are not located in the same chemical environment. Thus results in a slight chemical shift of the peaks assigned to these two protons.

Table 4.3 Assigned experimental ^{1}H-NMR signals from methyl cinnamate in chloroform-D

Proton	Chemical shift/ppm	Integration, J value
1	3.73	s, 3H
2	6.37	d, 1H
3	7.62	d, 1H / J = 16 Hz
4, 4'	7.45	m, 2H
5, 5'	7.32	m, 2H
6	7.30	m, 1H
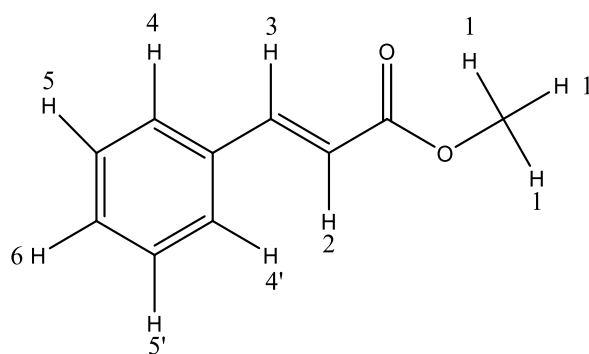
Figure 4.16 Molecular structure of methyl cinnamate

4.4.1.2 Investigation on side product generated from Heck reaction by using Pd-CSC as catalyst

In some cases, a side product was generated during the Heck reaction, which had not been observed in previous literature. This could be indicated from GC spectrum shown in Figure 4.12 (peak at *ca.* 19 min). The TLC test demonstrated that this side product has a similar polarity to the desired product (methyl cinnamate). Hence, it is difficult to separate from the reaction mixture by column chromatography using silica as stationary phase. The side product was extracted by short path distillation according to boiling point. Through analysing the reaction solutions using various conditions, it was found that the side product was produced when both Pd-CSC and propylene carbonate were used as catalyst and reaction solvent for Heck reaction, which led to the huge amounts of leached Pd.

The molecule - methyl 3,3-diphenylacrylate is proposed to be the side product from Heck reaction solution. In order to prove the existence of this side product, a range of analytical tools were utilized including GC, GC-MS, solution NMR for the product and standard sample. Some related literature was also taken into consideration.
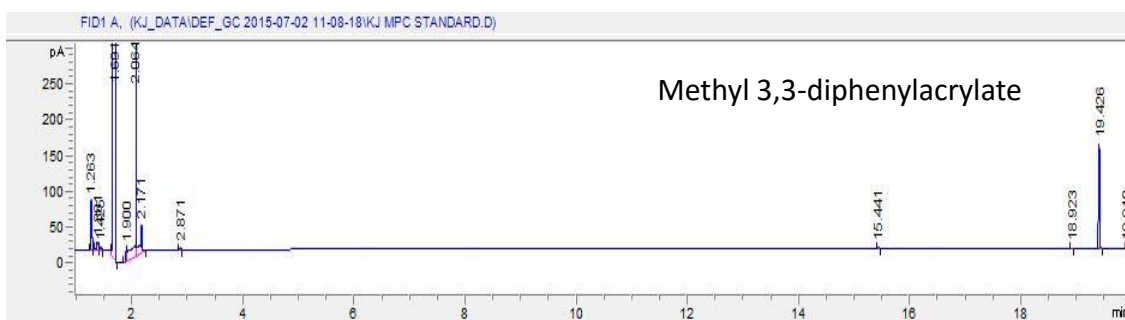
Figure 4.17 GC spectra of standard methyl 3,3-diphenylacrylate

GC spectra of standard sample indicates that the retention time is ~19 minutes (Figure 4.17). A strong and sharp peak on the spectra of the solution shown in Figure 4.12 gives the evidence of the production of methyl 3,3-diphenylacrylate.
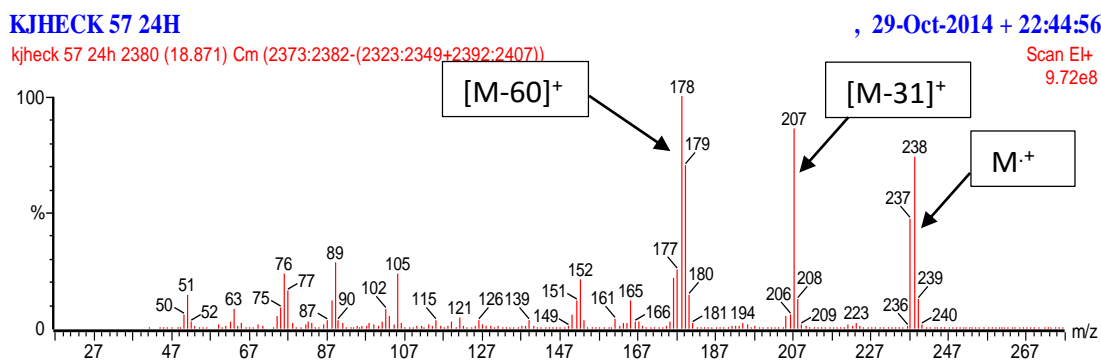
Figure 4.18 Mass spectra of side product

Figure 4.18 demonstrates the mass spectrum of this side product, and three characteristic peak is observed, which are m/z = 178, 207, and 238. The largest ion is assigned to the molecular ion of methyl 3,3-diphenylacrylate. Similar to fragmentation of methyl cinnamate, the other fragments m/z = 178 and 207 are formed as a result of the loss of the functional group $-COOCH_3$ and $-O-CH_3$, respectively, as shown in Figure 4.19. The possible fragmentation pathway of this compound is shown in Figure 4.19. The ion at m/z = 178 produces due to the further loss of a proton of the ion at m/z = 179. This could be a strong evidence of presence of methyl 3,3-diphenylacrylate after the reaction.

m/z = 238   m/z = 207   m/z = 179
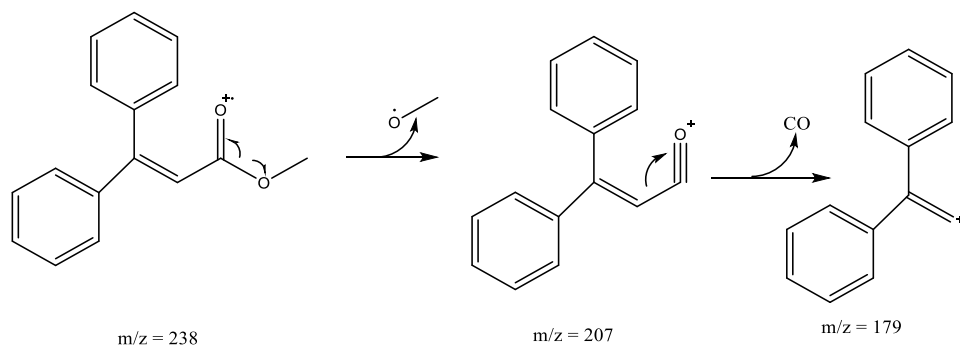
Figure 4.19 Formation of fragment ions m/z = 207 and m/z = 179

The ^{1}H NMR spectra of both the purified side product and standard sample are shown in Figure 4.21 and Figure 4.22, respectively. It is evident that the position of characteristic peaks of the side product purified from the liquid phase of the Heck reaction matches perfectly to that of the standard purchased from Sigma-Aldrich company, giving the identity of methyl 3,3-diphenylacrylate. The chemical shifts of the peaks at δ 3.54, δ 6.3 and δ 7.4-7.1 are illustrated in Table 4.4, which correspond to the protons on the methyl group, olefin group, and benzene ring, respectively. Same as methyl cinnamate, due to the steric effect, the ortho-H and meta-H are located in the different chemical environment, leading to the signal shift. As a result, the signals belonging to benzene ring on the NMR spectrum are partially overlapped with each other.
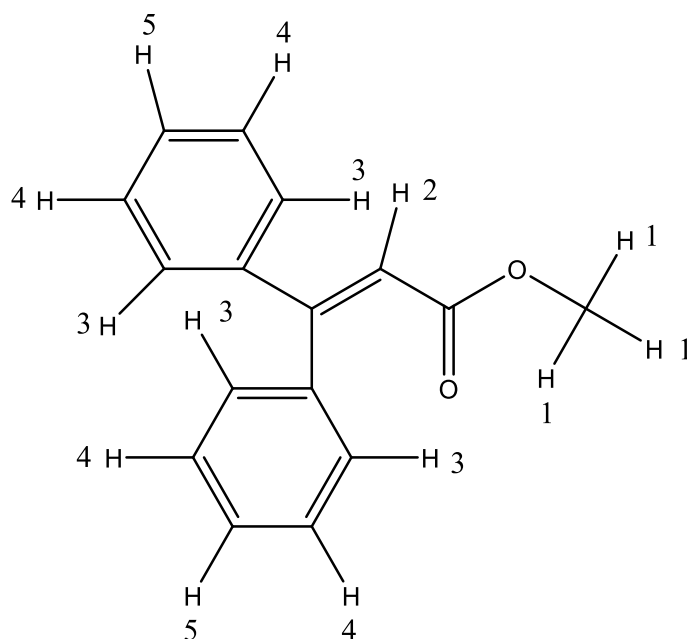
Figure 4.20 Molecular structure of methyl 3,3-diphenylacrylate

Table 4.4 Assigned experimental ^{1}H-NMR signals from methyl 3,3-diphenylacrylate

Proton	Chemical shift/ppm	Integration
1	3.54	3H
2	6.30	1H
3,4,5	7.4-7.1	10H
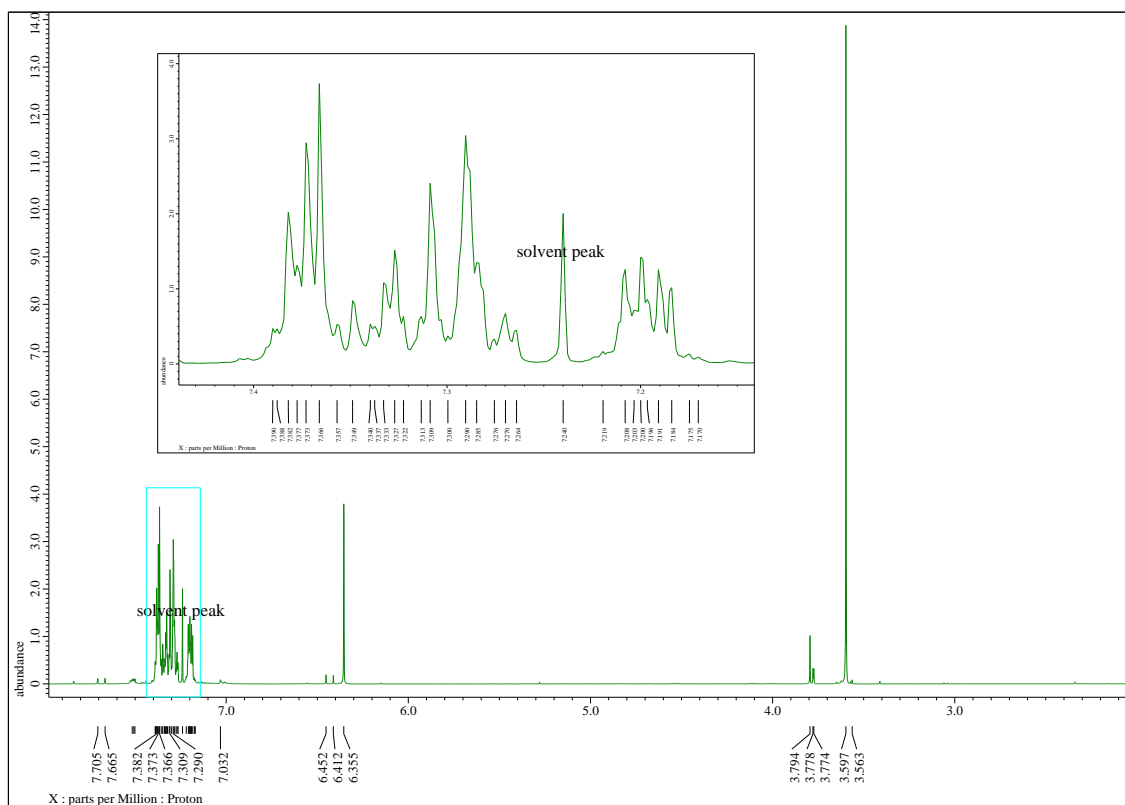
Figure 4.21 ^{1}H NMR spectra of purified side product
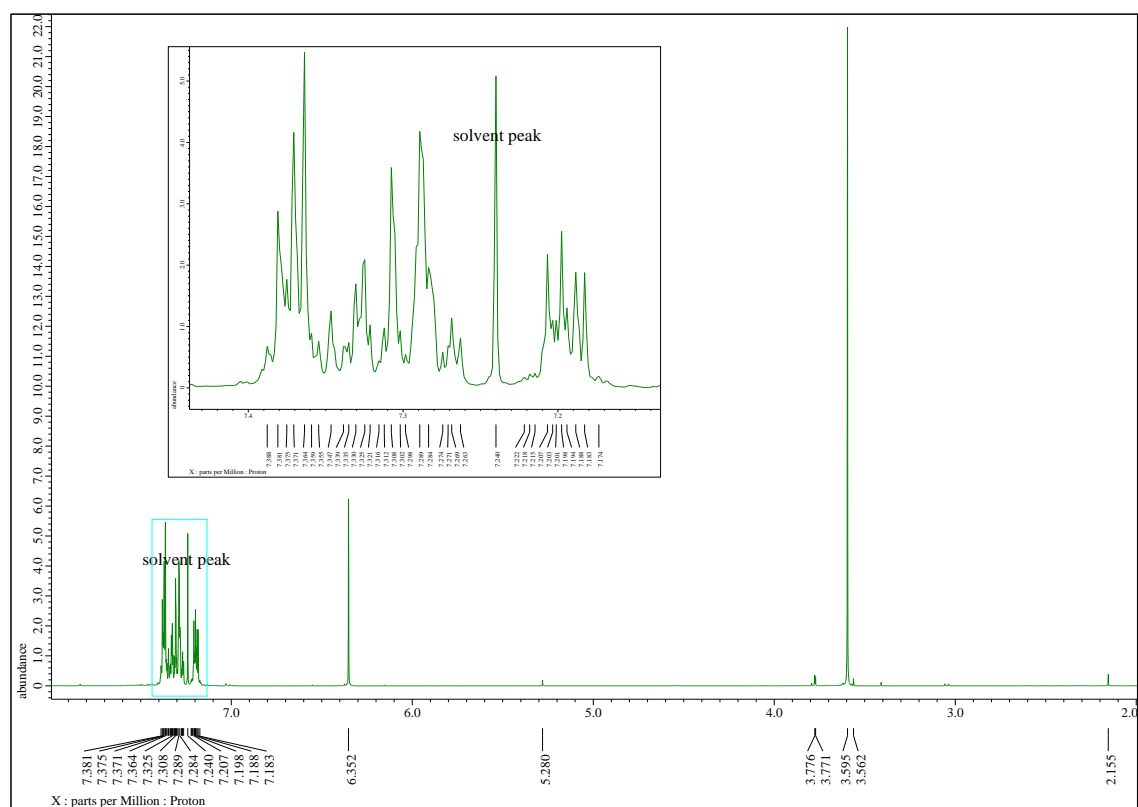
Figure 4.22 ^{1}H NMR spectra of standard methyl 3,3-diphenylacrylate

It has to be noted that in Kiviaho's study in 1995, he pointed out that the small part of palladium released from the surface of the catalyst supported by modified silicas resulted in the formation of benzene by a hydrogenation reaction. In the further reuse of the catalyst, the leached palladium was heterogeneous so that only Heck reaction proceeded.[290] Also several research groups including Kelkar[287] and Arai[291] studied the production of benzene by dehalogenation of aryl halides during the Heck reaction. There is competition between the vinylation and dehalogenation reaction. Especially in the presence of triethylamine as base, which has ability to act as a source of hydride, the dehalogenation was considered as the dominant reaction compared to the use of sodium carbonate as base, leading to the generation of benzene in the liquid phase.[287]

Table 4.5 Conditions of synthesis of methyl 3,3-diphenylacrylate using benzene from literature
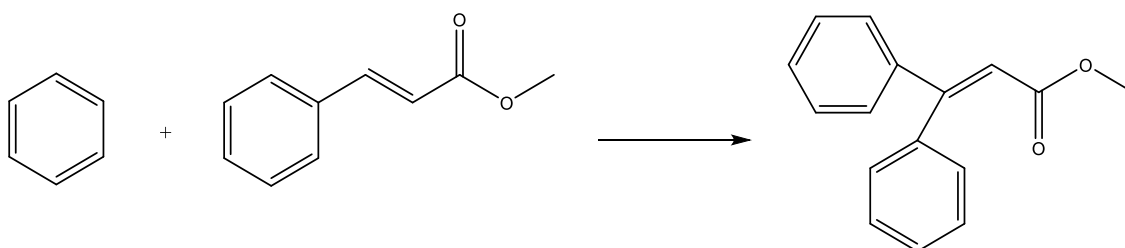
Conditions		Yields	Ref.
10 mol% Pd(OAc)$_2$	RT. 24h	67%	Song[292]
TFA			
(NH$_4$)$_2$S$_2$O$_8$			
5 mol% Pd(OAc)$_2$	80 °C 24h	67%	O'Shea[293]
AcOH/CH$_3$CN (4:1)			
K$_2$S$_2$O$_8$			
10 mol% Pd(OAc)$_2$	120 °C 15h	42%	Duan[294]
10 mol% ligand			
1 equiv. Cu(OAc)$_2$			

In our experiments, it is possible that the benzene produces subsequently during the reaction. According to the discussion above, the Pd leaching test by ICP analysis indicated that there was massive Pd loss of 26% in the initial use of the catalyst, while its concentration changed very little during the subsequent recycle runs. This is due to the dislodging of the loose palladium nanoparticles. The resultant benzene was then reacted with methyl cinnamate to produce methyl 3,3-diphenylacrylate using palladium as catalyst, which were been already studied by several research groups in the literature (Table 4.5).[292-294]

According to the previous literature, it is interesting to point out that there is another way of forming methyl 3,3-diphenylacrylate. During the Heck reaction, methyl 3,3-diphenylacrylate could be obtained by the further coupling of the product methyl cinnamate and iodobenzene at a rather slow reaction rate (67% yield in 98 h).[295] She *et*

al. also reported that the steric effect of olefin impeded the reaction and thus resulted in a poor yield (27%).[296]

As a consequence, based on the search of the previous literature, there are two possibilities of forming the side product. In order to investigate whether benzene or iodobenzene was involved in the generation of methyl 3,3-diphenylacrylate, some experiments (see Figure 4.23) were then carried out. Deuterated benzene was introduced to track where the benzene ring in the side product is from. The ESI results clearly show the side product is generated with hydrogen instead of deuterated atom, thus proving only iodobenzene reacted with methyl cinnamate to generate methyl 3,3-diphenylacrylate. Moreover, it is worthwhile to note that this side product only produced in the presence of small amounts of methyl acrylate, which is the starting material for the Heck reaction, while there is no side product generated in the absence of methyl acrylate. This implies that the generation of the side product requires at least one complete catalytic run of the Heck reaction, which is also consistent with the relative activities of methyl acrylate and methyl cinnamate. It is worthwhile to note that on the GC-MS results of the liquid solution showed that there is no significant trace for benzene, also indicating that the first benzene route for the production of side product is less possible.
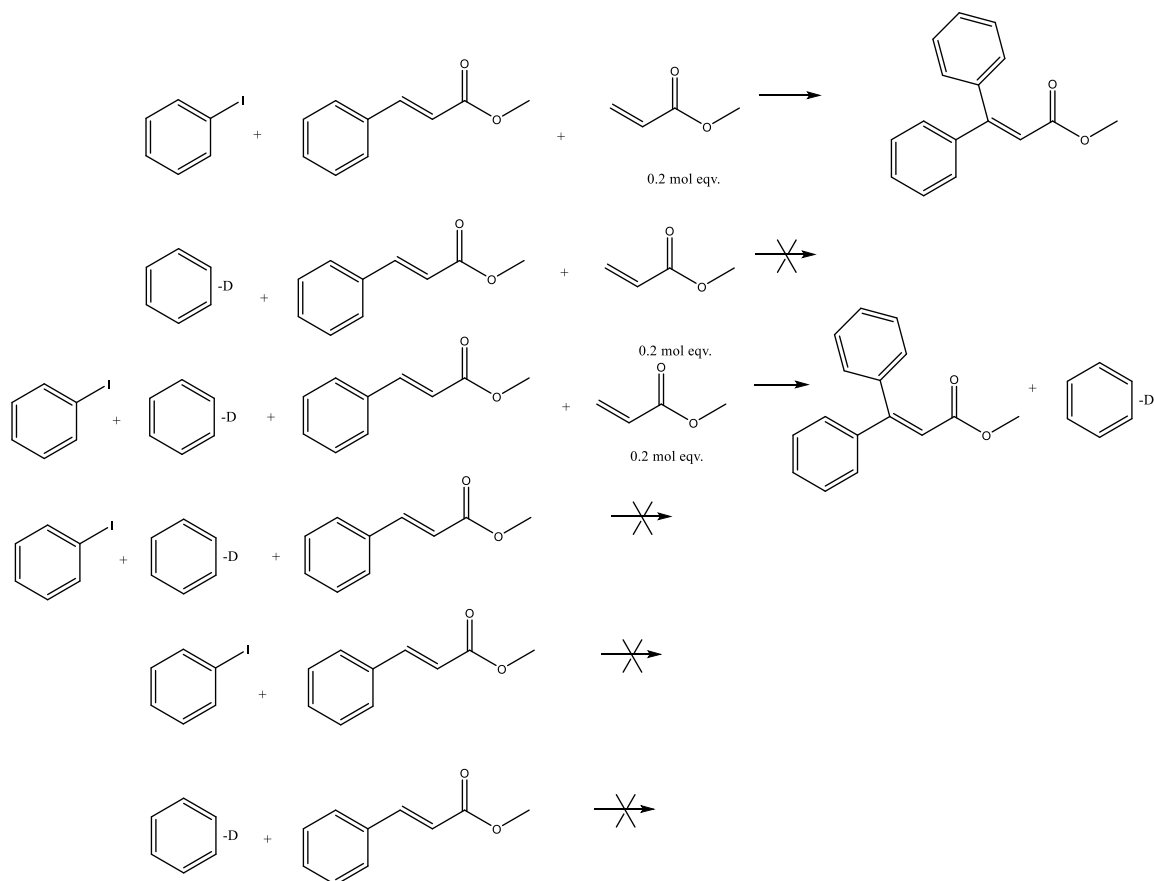
Figure 4.23 Possible reactions of forming methyl 3,3-diphenylacrylate

In summary, it could be confirmed that the side product appearing during the Heck reaction is identified to be methyl 3,3-diphenylacrylate. By comparison among the yield of the side product produced with reusing catalyst shown in Table 4.6, only the first run could produce this side product significantly. This could be explained by the fact that the palladium leached off in the first use of catalyst, subsquently producing methyl 3,3-diphenylacrylate. In the further use of catalyst, limited amount of palladium was released from the catalyst, thus there is not high proportion of side product as in the first run. Moreover, when another portion of starting materials was added to the post-reaction solution, the proportion of the side product also increased, suggesting that the leached palladium in the solution still had a positive effect on forming methyl 3,3-diphenylacrylate.

Table 4.6 Production of side product by using Pd-CSC catalyst in the propylene carbonate

Run number	Estimated yield of side product %
1	15.5 ±1.0
2	1.6 ±0.6
3	1.4 ±0.4
4	1.0 ±0.5
5	0.4 ±0.3
6	1.8 ±0.6
7	1.1 ±0.3

The yield of the reaction as a function of reaction time was monitored by GC. The yield of the desired product is achieved up to 61% after 24 hour reaction, which is in correlation to the result in Table 4.2. According to the discussion above, this is due to the production of side product methyl 3, 3-diphenylacrylate, leading to a relatively low yield of desired product, but high conversion (> 80%). Although the result indicated a good yield of 75% in the beginning of the reaction, there was a significant drop after 7 hour reaction. This phenomenon could be explained by the generation of methyl 3, 3-diphenylacrylate. The mechanism for the generation of this side product has been discussed above in detail. The desired product methyl cinnamate proceeds *via* a further addition with iodobenzene and another Heck reaction was initiated. As such, the content of methyl cinnamate increased dramatically and then decreased during the reaction. Besides, the decreased production of methyl cinnamate is consistent with the theory of the generation of side product.
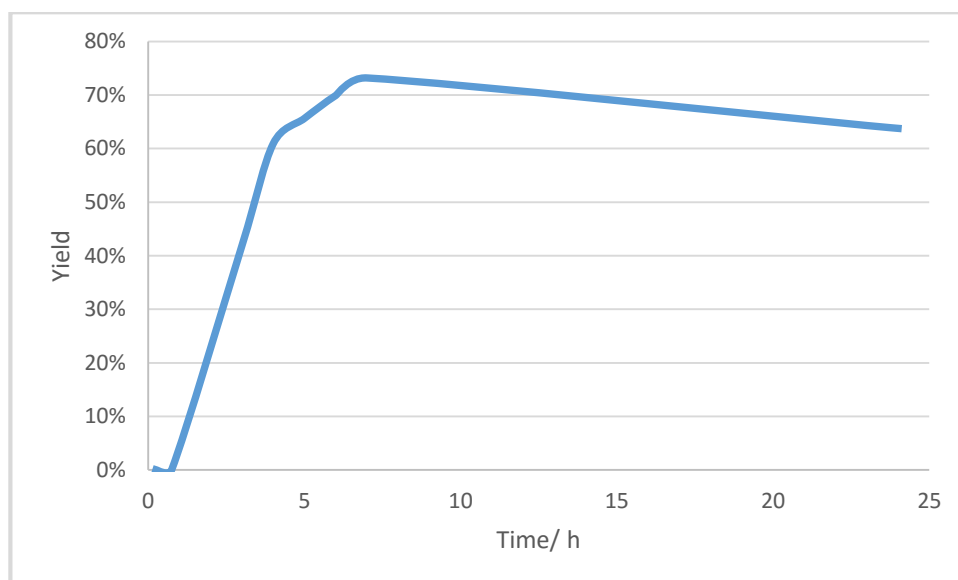
Figure 4.24 Yield of desired product monitored over time by GC analysis

4.4.2 Catalytic activity of pre-washed Pd-CSC catalyst using propylene carbonate as solvent

As mentioned above, the Pd leaching test by ICP analysis from liquid phase has been done for all the runs, which suggested that there was massive Pd loss of 26% in the initial use of the catalyst, while its concentration changed very little during the subsequent recycle runs. This is probably due to the isolation of the palladium nanoparticles which were not polymerized with carbonaceous layer during the preparation process. Sheldon's hot filtration test is well-known as a test for leaching and was utilized in order to see if there is any palladium leached into the liquid phase.[297] This process involves the filtration of the Pd-CSC catalyst part way through a reaction, followed by continuation of the reaction in the absence of the catalyst. After 24 hour reaction, results showed that a high conversion (91%) of methyl acrylate has achieved, proving the fact that the palladium was leached into the liquid phase.
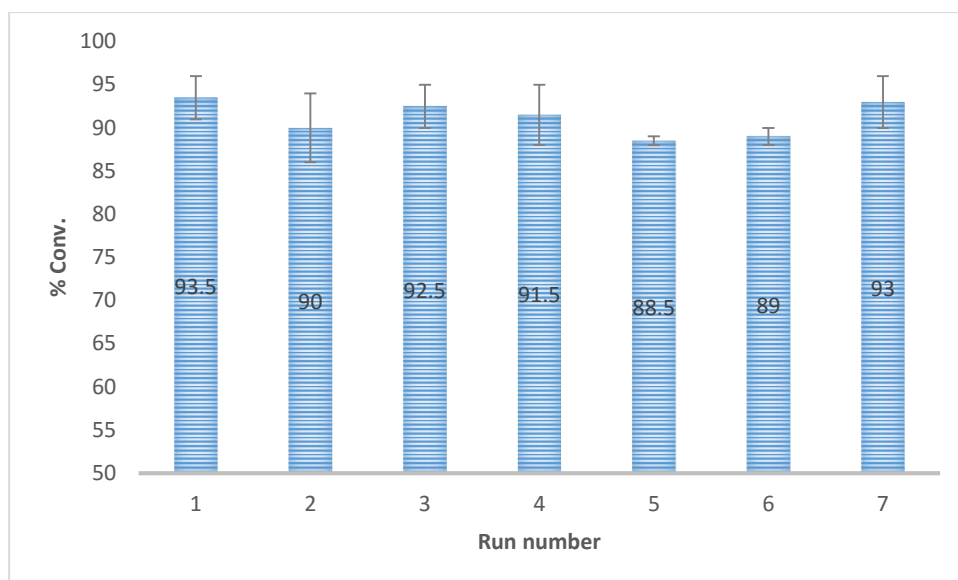
Figure 4.25 Conversion of Heck reaction using Pd-CSC material in propylene carbonate with pre-washed Pd-CSC

Therefore, in order to minimise the palladium leaching, the catalyst should be pre-washed before use to remove any loosely physisorbed complexes. The fresh catalyst was impregnated with propylene carbonate at 100 °C for 24 hours prior to use. ICP analysis of the liquid phase for the washing demonstrates 19.2% Pd loss into the solution. This value is close to the one detected from the solution of the 1st run with fresh catalyst (26%).

Table 4.7 Pd loss percentage and the selectivity of each run using pre-washed Pd-CSC catalyst

Runs	Pd loss %	Selectivity %	Runs	Pd loss %	Selectivity %
1	1.2	96	5	0.4	98
2	0.3	95	6	0.4	97
3	0.4	87	7	0.9	98
4	0.5	89			

The conversion of the first run by using the washed catalyst is 91% and it could be reused at least 7 times with a high conversion shown in Figure 4.25. Importantly, the ICP results shown in Table 4.7 depicts a much lower palladium loss (average 0.58%) for the reactions

by using washed catalysts compared to unwashed catalyst. This implies the CSC substrate could strongly stabilize the metallic palladium and have an impressive recoverability. It is important to note that as a result of pre washing step, the selectivities of these reactions including the 1st run are all over 85% (Table 4.7), indicating most of the starting materials were converted to the desired product instead of the side product. This could be explained by the lower amounts of palladium leached into the liquid phase, preventing the generation of benzene, thus improving the yield of methyl cinnamate.

4.4.3 Catalytic activity of the Heck reaction at different amounts of Pd-CSC

Figure 4.26 demonstrates the catalytic activity of the Heck reaction at different amounts of catalyst. Theoretically, the lower amount of palladium is added, the lower the conversion the reaction will achieve. The observed result is consistent with this common proposal. The Pd-CSC has a high catalytic activity until the quantity is decreased to as low as 0.04 mol%. This is due to the good dispersion of Pd nanoparticles on the surface of CSC support, allowing the metal to catalyse the reaction more efficiently.
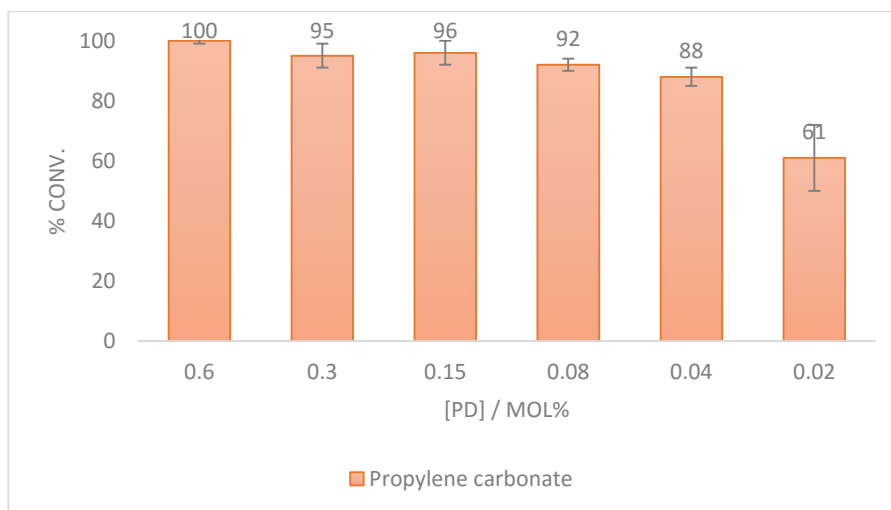
Figure 4.26 Conversion of the Heck reaction using different amounts of Pd-CSCs

The conversion started to drop by using NMP when the Pd loading was 0.04 mol%, while the catalyst in propylene carbonate still exhibited a high activity. This implies that propylene carbonate has an effective performance for the Heck reaction in comparison with NMP. As discussed above, the deactivation of the catalyst in NMP is caused by the

adsorption of Et₃NHI. This probably suggests that propylene carbonate is better at preventing the Et₃NHI to block the pores.

4.4.4 Catalytic activity of Pd-CSC-300, Pd-CSC-400 and Pd-CSC-500

As discussed in Chapter 3, the CSC materials not only exhibit well-ordered mesoporous structures with high specific BET surface area, uniform pore sizes, but also have the feature that their properties could be easily tuned by adjusting the carbonization temperature. This is considered as a dominant advantage compared to other materials. The continuum functionalities of the surface range from polar hydroxyl groups to aromatics when the temperature changes from 300 °C to 800 °C. Hence, CSC-300, CSC-400 and CSC-500 materials were utilized as solid supports to deposit the palladium nanoparticles. The resultant Pd-CSC-300, Pd-CSC-400 and Pd-CSC-500 catalysts were then used for the Heck reaction to detect the catalytic activity and recoverability.
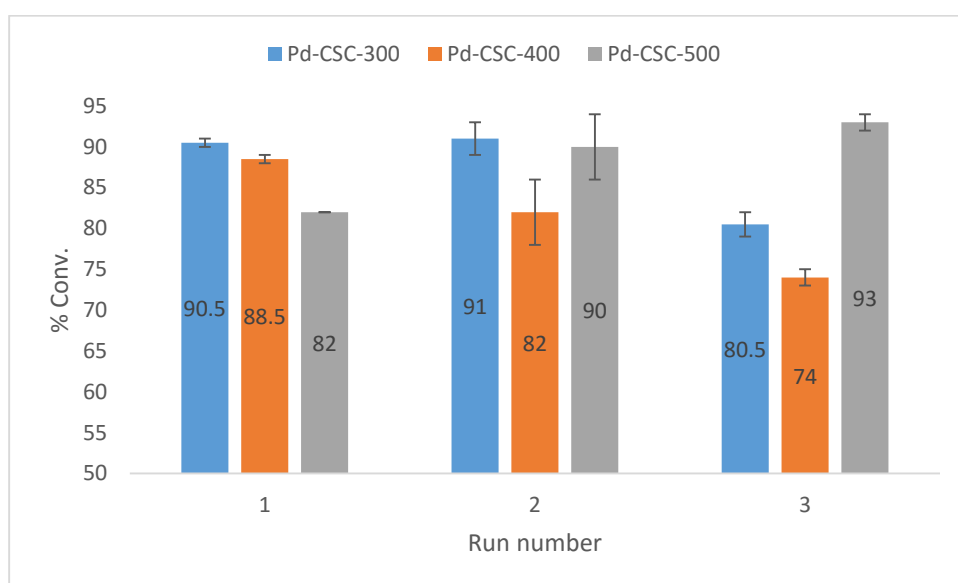
Figure 4.27 Conversion of Heck reaction by using Pd-CSC-300, Pd-CSC-400 and Pd-CSC-500 as catalyst

Figure 4.27 exhibited the conversions of the Heck reaction by using Pd-CSC catalyst which were prepared at 300 °C, 400 °C and 500 °C, respectively. The previous study in Chapter 3 summarised that CSC-300 material was non-porous and had a low BET specific surface area, which implied CSC-300 could not become an appropriate solid support for depositing palladium nanoparticles. Surprisingly, 90% of the conversion rate indicated

214

that the catalytic activity of Pd-CSC-300 was as high as that of Pd-CSC-400 and Pd-CSC-500, which is presumably because more palladium come off as more palladium are on the surface of the solid support and are less well stabilised. Further work is needed to explore the ratio of stabilised palladium to loose palladium on the CSC catalysts. Although the Pd-CSC-300 and Pd-CSC-400 could catalyse the reaction well, the catalytic activity began to decrease after two uses, and the conversion decreased below 80% in the 3rd runs. This is likely to be due to the deposition of Pd nanoparticles into the polymerised carbonaceous layer rather than just stabilized by porous silica framework. Hence, such palladium nanoparticles were easily leached and removed during the reaction process. Whereas the Pd-CSC-500 one performed an increased catalytic activity when it is recycled and reused. Resulting from the discussions above, it could be concluded that the continuum functionality ranging from polar hydroxyl groups to aromatic surfaces of the CSC supports gives little difference in the Heck reaction in terms of the catalytic efficiency and the recoverability, but this unique feature could potentially be applied in other applications specifically for column chromatography and the separation. Further investigation is needed to seek out other applications of this CSC material.

A control experiment of using CSC and SBA-15 without loading palladium as catalyst to carry out Heck reaction has also been done. The final results indicated that neither CSC materials nor SBA-15 silicas could catalyse this reaction.

4.4.5 Catalytic performances on different Pd-modified catalysts

In Section 4.2.1, Pd-CSC, Pd-AC and Pd-SBA-15 catalysts were characterized and compared with each other. The results demonstrated that due to the high dispersion of palladium nanoparticles and well-ordered mesoporous structure, Pd-CSC catalyst could have a better catalytic activity and recoverability by using the hybrid carbon silica material as support.
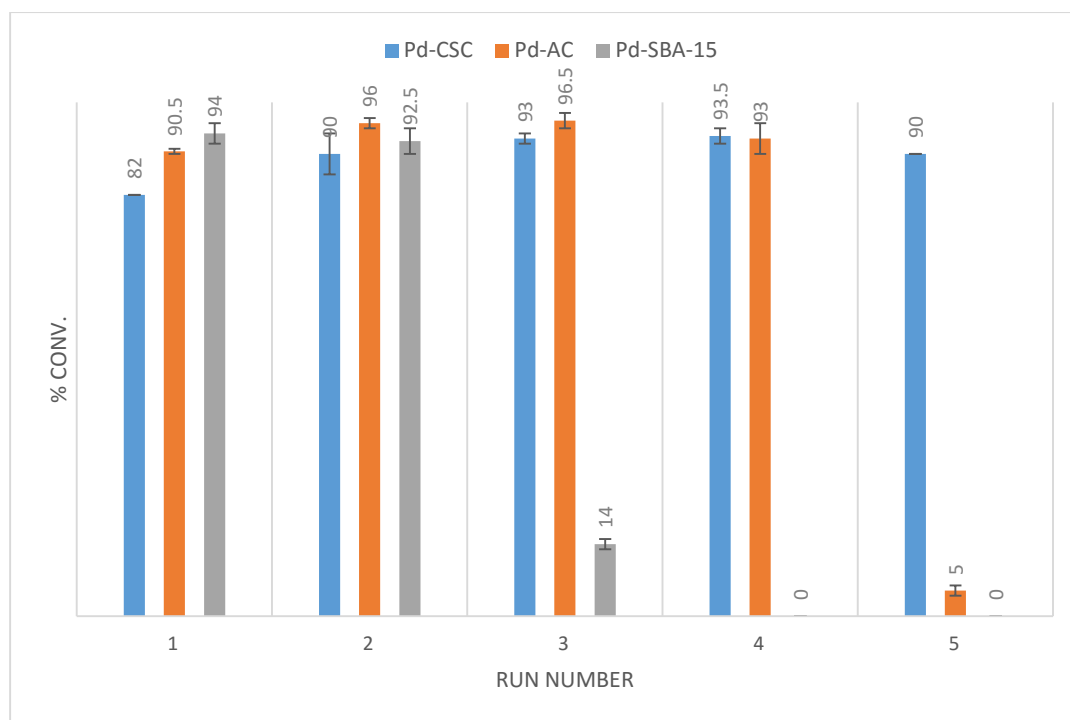
Figure 4.28 Conversion of Heck reaction by using different Pd-modified catalysts

Figure 4.28 demonstrates that the catalytic properties of Pd-CSC, Pd-AC and Pd-SBA-15 and their recoverability. All of the catalysts exhibit an excellent catalytic activity in their first run, achieving a high yield over 90%, showing either the carbon or silica supports would not affect the catalytic activity significantly. After two runs of catalysis, the conversion of the reaction with Pd-SBA-15 has decreased by about 80% and the catalysts could not retain high catalytic activity for the Heck reaction. In terms of commercial Pd-AC catalyst, it worked well and could be reused for 3 times. As discussed above, the Pd-CSC catalyst could be reused at least 7 times, showing a better recyclability compared to other catalyst.

A reactivation step of both Pd-SBA-15 and Pd-AC has been done *via* the heating process at 500 °C under nitrogen flow, followed by the reuse of these reactivated catalysts. The data indicated that there was 7% of conversion after 24-hour run, resulting from the deactivation of the catalyst.

4.4.6 Substituted aryl halides utilized for Heck reaction

The three catalysts have also been utilized in the Heck reaction using a range of different substituted aryl halides as starting materials in order to investigate any changes that could arise due to the use of different catalysts.

Table 4.8 Conversion of Heck reaction with a range of substituted aryl halides
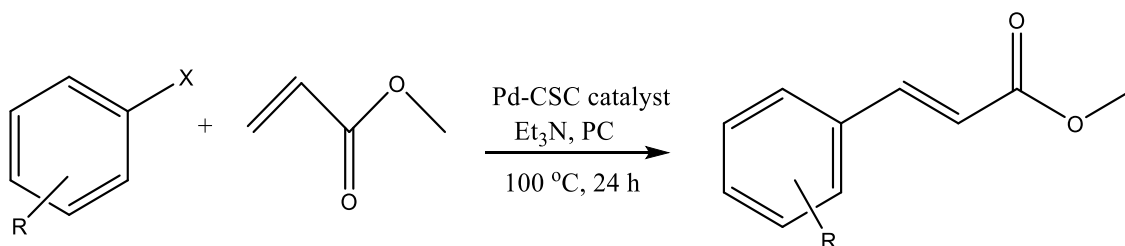
Entry	X	R	% Conversion		
			Pd-CSC	Pd-AC	Pd-SBA-15
1	Cl	H	7 ±1	9 ±1	14 ±2
2	Cl	4-CN	6 ±1	4 ±1	10 ±1
3	Br	H	14 ±4	8 ±1	12 ±1
4	Br	2-CH$_3$	16 ±2	11 ±2	10 ±2
5	Br	4-COCH$_3$	25 ±1	9 ±1	14 ±2
6	Br	4-NO$_2$	97 ±2	92 ±2	90 ±4
7	Br	2-NO$_2$	94 ±3	99 ±1	93 ±6
8	Br	2-CN	90 ±3	67 ±3	99 ±1
9	I	3-NO$_2$	83 ±5	80 ±6	83 ±1

Various substituted aryl halides were tested in order to determine any changes that could be occurred due to the use of different catalysts. Results shown in Table 4.8 indicated that comparable or superior conversions of the reaction were achieved when using Pd-CSC catalyst. It is well documented that the Heck reactions involving chlorobenzene as starting materials were regarded as difficult ones to initiate, which is due to the rate of oxidative addition to Pd(0).[298, 299] Primarily, because the bond strength of C-Cl is stronger than C-Br and C-I, the rate of oxidation addition C-Cl to Pd(0) is slower.

Thus all of these three catalysts gave very low conversions when using aryl chlorides under the reaction conditions tested (Entry 1, 2). When the aryl bromides with electron withdrawing groups such as NO_2 and CN groups were used as reagents, the corresponding conversion was high (Entry 6, 7, 8). On the contrary, there is a poor conversion when using the aryl bromides with electron donating groups (Entry 3, 4, 5). Further work is needed to improve the catalytic performance of the catalysts for these low-conversion reactions through the development of heterogeneous catalysts.

4.5 <u>Conclusion</u>

In conclusion, Pd-CSC catalyst has been fully characterized and compared with different mesoporous carriers by N_2 porosimetry, microscopy and XRD, showing this heterogeneous palladium nanoparticles have been supported in a well dispersed manner on ordered mesoporous carbon-silica composites, exhibiting a uniform pore structure and comparable surface area and pore size to the parent materials.

Initially the Pd-CSC catalyst was used for conventional Heck reaction in NMP to test the catalytic activity. The novel Pd-CSC catalyst performed a good catalytic ability in > 80% conversion and could be reused for four times at 100 ^oC, showing an excellent recyclability. The Heck reaction was also carried out in the alternative solvent propylene carbonate at a high conversion over 80%. The Pd catalyst is stable when using propylene carbonate, proving a negligible metal leaching after the first run and can be used at least seven times. Surprisingly, during the reaction by using this catalyst, not only the desired product methyl cinnamate, but also a side product methyl 3, 3-diphenylacrylate generated. This compound was identified by using GC-MS, GC and ^1H NMR. The deuterated hydrogen track test indicated that the production of this side product is attributed to the double addition of iodobenezene.

In order to improve the selectivity of the reaction and eliminate the palladium leaching during the reaction so that making the Heck reaction more elemental sustainable, a pre washing step was carried out to remove the detached palladium nanoparticles. The pre washed catalyst was then used for the Heck reaction. The ICP results indicated that the detached palladium was dissolved into the liquid phase during the washing step. The

recyclability of the catalyst is as good as unwashed catalyst and could be used at least seven times without the decrease of catalytic activity. It is important to note that by using the washed Pd-CSC catalyst, the production of side product has been eliminated drastically due to the prevention of Pd leaching in the 1st run, so that the overall selectivity of this reaction is increased compared to those of the reactions using unwashed catalyst.

A range of catalysts supported with different mesoporous carriers have been used for catalysing the Heck reaction. The results indicated that the catalytic activity of Pd-CSC-300 and Pd-CSC-400 tended to decrease from the third run, while Pd-CSC-500 sample could be used for at least seven times with a high conversion of the reaction. This is due to a better surface feature with higher specific BET surface area and larger pore size of Pd-CSC-500, which was demonstrated in 4.2.1. Other types of mesoporous carriers including activated carbon and SBA-15 were also tested for the Heck reaction. The result indicated that these two catalysts could only be reused for at most four times, while Pd-CSC catalyst has a better recoverability and could be recycled at least seven times.

Chapter 5   Carbonaceous materials etching from CSCs

5.1 Background on synthesis of ordered mesporous carbons (OMCs) by hard templating approach

Porous carbonaceous materials have played an important role in many fields of modern science and technology, such as separation processes, electronics, energy storage, biomedical devices and more.[221, 222] Generally, the synthetic routes to porous carbon materials can be divided into four types: [300] 1) Chemical activation, physical activation, and a combination of the physical and chemical activation processes, 2) Carbonization of a polymer aerogel precursor, 3) Carbonization of polymer blends composed of a carbonizable polymer and a pyrolyzable polymer (soft templating), 4) Using porous inorganic templates (hard templating). Hard template routes to carbonaceous materials are well studied because the resultant material possesses the same pore structure and morphology as the template. The general hard templating method for porous carbon includes the impregnation / infiltration of the carbon precursor into inorganic template, followed by the carbonization at specific temperature and the removal of the inorganic template. This synthesis route was developed by Knox and Ross on the production of porous carbons from silica gel.[301]

Although numerous research have been done on the synthesis of porous carbon materials, ordered porous carbons with uniform pore structure are still difficult to prepare.[300] Ryoo first reported the use of a mesoporous structured MCM-48 silica material as the hard template for the synthesis of ordered mesoporous carbons designated as CMK-1 in 1999.[223, 224] The standard preparation procedure of this material involves the infiltration of mesoporous silica pores with mono- and di-saccharides, followed by their carbonization and silica removal. One of the advantages of this carbonization technique is that the resultant carbon materials could replicate the inverse mesostructural order after removing the silica templates with HF or NaOH solution. Further studies were carried out on the modification of CMK with crosslinked polymers or metals to form chemically enhanced carbon materials.[225-227] Since then, a variety of mesoporous silica templates with different structures such as SBA series, MCM series and MSU series were applied in the fabrication of OMCs.

Table 5.1 examples of carbon materials synthesized by hard templating approach

Ordered mesoporous carbon	Silica template	Carbon precursor	Reference	
CMK-1	MCM-48	Sucrose	Ryoo[302] Joo[303]	Reverse replica
CMK-2	SBA-1	Sucrose	Ryoo[222]	
CMK-3	SBA-15	Sucrose	Jun[223]	
CMK-4	Partially disordered MCM-48	Acetylene	Joo[304]	
Porous carbon	Monolithic meso-macroporous silica	Resorcinol formaldehyde	Kim[305]	
Mesoporous carbons	Acid functionalized silica	Furufryl alcohol	Seo[306]	
Hierarchical porous carbon	Porous silica monolith	Mesophase pitch	Adelhelm[307]	
Mesoporous carbon materials	SBA-15	Resorcinol formaldehyde	Babic[308]	
Mesoporous structured carbon	MSU-H silica	sucrose	Kim[309]	
Ruthenium doped carbon	SBA-15	Methylated β-cyclodextrin	Gokilakrishnan[310]	
Mesoporous carbons	SBA-15, FDU-1 Silica gel	polyacrylonitrile	Kruk[311]	
Hierarchical nanostructured carbon	Hierarchical nanostructured silica	Divinylbenzene furfuryl alcohol	Fang[312]	
Polymer derived CMK-3	SBA-15	Furfuryl alcohol	Niebrzydowska[313]	
CMK-5	SBA-15	Furfuryl alcohol	Che[314]	replica
Tubelike carbon	Large pore mesoporous silica	Furfuryl alcohol	Che[315]	
Carbon films	Silica nanoparticle	Glucose	Tian[316]	
Ordered mesoporous carbon with hexagonal arrays of tubes	SBA-15	Furfuryl alcohol	Lu[317, 318]	
Carbon material	SBA-15, MCM-41, KIT-6, MMSBA	Bio-oil	Our work	Reverse replica and replica

Studies on carbon materials prepared by hard templating approach are listed in Table 5.1. In the earlier stage, the morphologies of most OMCs are the reverse replica of their parent silicas. During the preparation, the silica pores are fully filled with organic compounds by the repeat infiltration of carbon precursors. Thus the removal of silica substrates gave rise to the rod-like carbon material and the so-called pores (shown in Figure 5.1 Pathway 1).[222, 223, 302-313] In order to prevent external carbon deposition when carbon precursor was used excessively and achieve a highly faithful carbon replica, Seo *et al.* developed a modified method using phosphoric acid-impregnated SBA-15 as a template, thus forming phosphate ester groups on the mesopore walls of SBA-15, resulting in the slow polymerization of carbon precursor.[306] Ryoo and co-workers successfully synthesised ordered mesoporous carbons with controllable pore size ranging from 2.2 nm to 3.3 nm by using mesoporous silicas with a range of different wall thicknesses.[303]

Although the reverse carbon replica had achieved great success as this approach allows the synthesis of ordered mesoporous carbon material replication from silica substrate, the pore size of this carbon materials is difficult to be controlled or tuned, because the mesoporous structure of the OMC only lies in the thickness of the silica walls, which has described above. Under this circumstance, a novel carbon replica with tuneable pore size was developed by some researchers, referred as tubular-like carbon material (Pathway 2 in Figure 5.1). Terasaki *et al.* developed this carbon material designated as CMK-5 by the partial wetting of furfuryl alcohol onto the SBA-15 silica.[314] The ordered mesoporous carbon with pore diameter ranging from 3.0 nm to 8.2 nm was interconnected by the carbon formed in the disordered complementary micropores.[314]
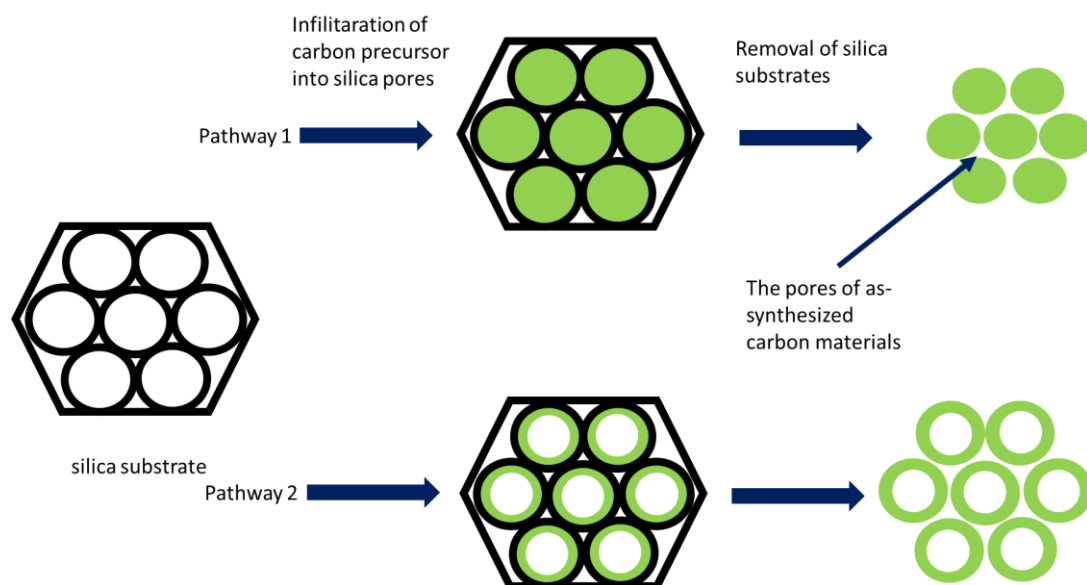
Figure 5.1 Synthetic schemes of carbon replicas

It should be noted that as listed in Table 5.1, many types of organic compounds were conventionally chosen to be carbon sources. However, the polymerization process of these compounds is frequently difficult to control.[318] In case of furfuryl alcohol, the acidic sites resulting from tetrahedral aluminium are needed to catalyse the polymerization process, which makes the whole synthesis route complicated. Later, a modified process using oxalic acid as homogeneous catalyst instead of heterogeneous alumina catalyst was published by Lu *et al.*,[318] thus being considered as a time-saving process. Mesophase pitches are excellent carbon precursors as they consist of carbon-rich, condensed, polyaromatic moieties that transform into a well-defined and ordered graphene structure.[307] However, pitches are difficult to use in hard templating approach as their melt is relatively viscous and their solubility is poor.

Hence, a systematic study of carbonaceous material continuously ranging from rod-like carbon to tubular-like carbon has been developed in this chapter. Bio-oil, as an environmentally sustainable and economically viable carbon source, is used for fabrication of ordered mesoporous carbons. Through the adjustment of the ratio of bio-oil to silica support, the resultant carbon materials could be controlled to either rod-like or tubular-like. The thickness of the tubular carbon is also controllable by simply changing the bio-oil amount.

5.2 <u>Tuneable thickness of carbonaceous layer in CSCs</u>

Through adjusting the ratio of bio-oil / silica, the silica pores are controlled to be fully or partially filled with bio-oils, thus fabricating a range of CSC materials with continuous thickness of carbonaceous layer from 0.26 nm to 4 nm, estimated from the porosimetry data below.

Table 5.2 shows the textural properties of the CSC materials prepared with different ratio of bio-oil/SBA at 500 $^{\circ}$C. It is clearly observed that all the textural properties including specific BET surface areas, pore volume, and pore diameter decreased as the increase of the bio-oil/SBA ratio. When the ratio reaches to 8, the CSC material has merely 28 m^2/g of specific BET surface area, which indicated that the silica pores have been fully filled with bio-oil. The estimated thickness of carbonaceous layer was calculated by the pore diameter of parent SBA-15 and corresponding CSC. When more and more amounts of bio-oil added into the silica pore, the thickness of the carbonaceous layer turns to be thicker and thicker.

Table 5.2 Textural properties of CSCs prepared with different amounts of bio-oil

	Ratio of bio-oil/SBA	BET surface area (m^2/g)	Pore volume (cm^3/g)	Pore diameter (nm)	Estimated thickness of carbonaceous layer (nm)	C Parameter
SBA-15	/	795	0.80	4.04	/	356
25 mg	0.25	672	0.68	4.02	0.02	743
50 mg	0.5	656	0.62	3.78	0.26	-1323
100 mg	1	608	0.51	3.33	0.71	-608
200 mg	2	517	0.37	2.85	1.19	-590
400 mg	4	475	0.30	2.50	1.54	-271
800 mg	8	28	/	/	4.04	-37

Interestingly, it should be noted that C parameter has a correlation with the bio-oil/SBA ratio. Sing mentioned, "According to the BET theory, C is related exponentially to the enthalpy (heat) of adsorption in the first adsorbed layer. It is now generally recognized,

however, that although the value of C may be used to characterize the shape of the isotherm in the BET range it does not provide a quantitative measure of enthalpy of adsorption but merely gives an indication of the magnitude of the adsorbent-adsorbate interaction energy. Thus, in reporting BET data it is recommended that C values are stated, but not converted to enthalpies of adsorption."[119] This implies that the sample with a high C parameter such as parent SBA-15 and 25 mg CSC sample has a strong interaction with nitrogen, while the interaction energy decrease with the decrease of C parameter. In other words, the silica species have a strong interaction with liquid nitrogen compared to carbon species.
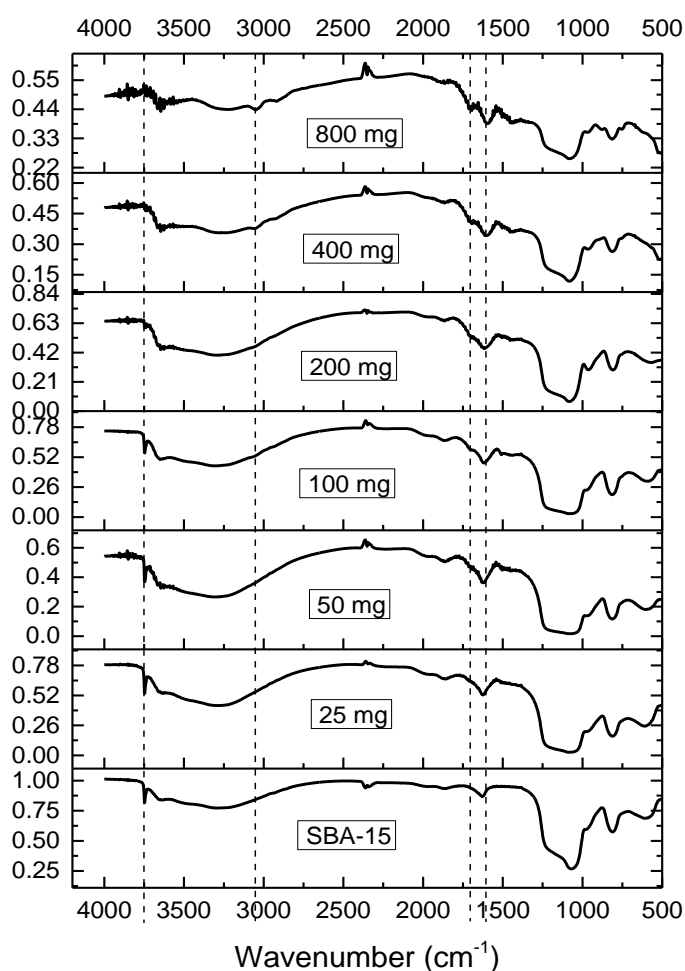
Figure 5.2 IR spectra of the CSCs prepared with different amounts of the bio-oil

Figure 5.2 exhibits the DRIFT spectra of CSC materials prepared with a range of bio-oil/SBA ratios. The spectra of all the CSC materials contain the characteristic peaks of SBA-15, indicating the existence of SBA-15 in the CSCs. Compared to SBA-15, there are

several weak peaks between 3000 cm^{-1} and 2700 cm^{-1} appeared in 400 mg and 800 mg samples. They were assigned to the -CH stretching vibrations, however these peaks could not be observed in the spectrum of other CSCs. This implies that not all the –CH groups have been removed in 400 mg and 800 mg sample, further indicating the functionality of the CSCs could be tuned by the adjustment of the bio-oil/silica ratio.

As mentioned before, three characteristic peaks shown at 3700 cm^{-1}, 1060 cm^{-1} and 800 cm^{-1} were ascribed to the vibrations in silica materials.[254] it is evident that more bio-oil added in the synthesis of CSCs could weaken the relative intensities of these peaks. Besides, a sharp peak appeared at ~3750 cm^{-1}, which is assigned to the separated Si-OH group vibrations, could also disappear due to the combination of separated Si-OH groups with organic matters or could shift a long way due to H-bonding to adsorbed organics.
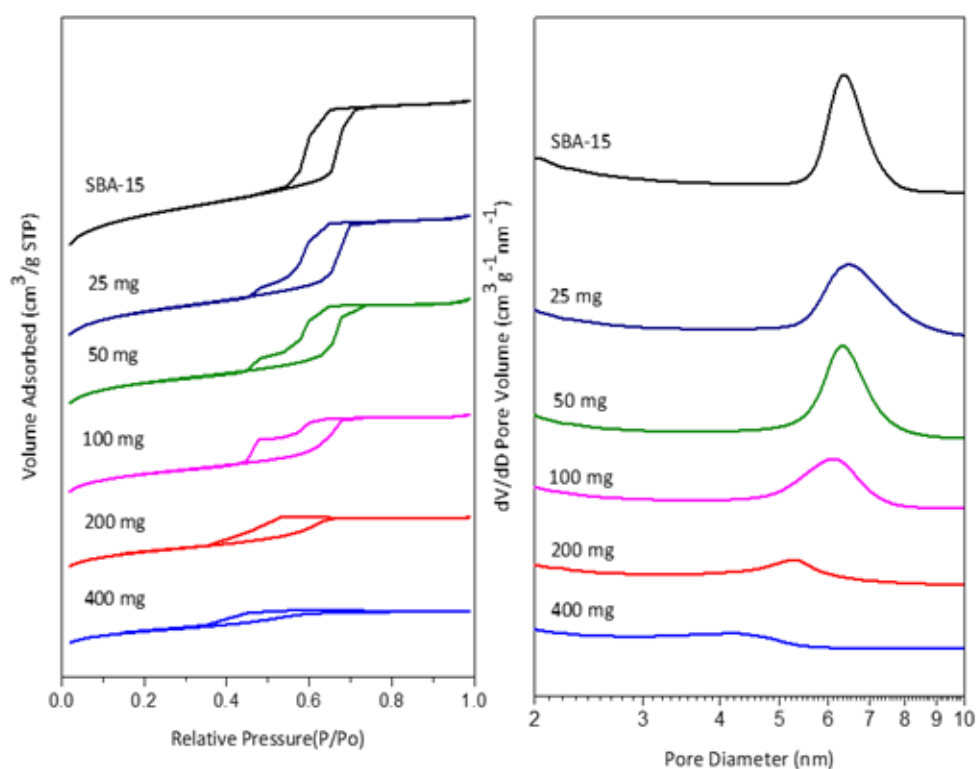
Figure 5.3 Nitrogen adsorption/desorption isotherm plots of different amounts of the bio-oil (left)

Figure 5.4 Pore size distributions of different amounts of the bio-oil (right)

Figure 5.3 and Figure 5.4 depicts the isotherm plots and pore size distributions of different amount of the bio-oil, respectively. For comparison, the corresponding curves of parent SBA-15 are also presented. The CSC-800 mg sample has an incomplete hysteresis loop (not shown) and the BET specific surface area is extremely low at 28 m^2/g supporting that the silica pores have been fully filled with the bio-oil. The shape of the isotherm plot of the CSC sample tends to be more like that of SBA-15 sample when decreasing the amount of the bio-oil added. A high ratio of bio-oil/silica also leads to a narrow hysteresis loop as the pore diameter and the pore volume has decreased to 2.5 nm and 0.3 cm^3/g, respectively. This is due to the filling of organic matters into pores of silica substrates.

It is clearly observed from Figure 5.4 that the pore size of the CSCs decreased with more bio-oil added in the CSC synthesis, which is consistent with the results in Table 5.2. All the peaks of the CSCs except for CSC-400mg sample are sharp, suggesting that the organic matters were well dispersed in the silica materials and the pore sizes of the resultant CSCs are uniform. Besides, the decreased intensity of the peak in the pore size distribution curve is due to the decrease of the pore volume of the CSC material, which is assigned to the addition of the bio-oil.
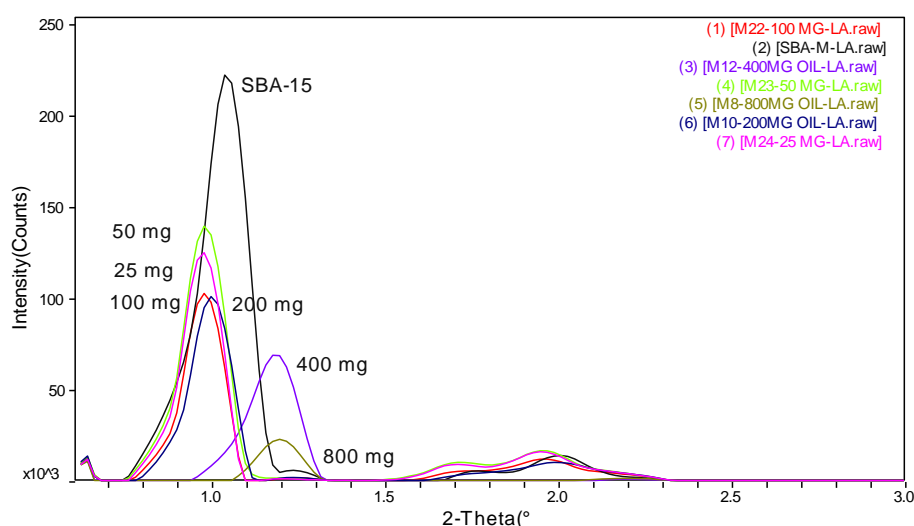
Figure 5.5 Small angle XRD patterns of the CSCs prepared with different amounts of the bio-oil

XRD analysis is a useful technique for obtaining the information of structural ordering of the materials. Figure 5.5 demonstrates the small angle XRD patterns of the silicas and the CSCs prepared with different amounts of the bio-oil. According to the Bragg equation, the positon of the characteristic peak tends to shift to large angle as more bio-oil added into silicas, resulting in a smaller interplanar distance d_{100} and thus a smaller corresponding unit cell. As mentioned in Chapter 3, this is due to the acids and water from bio-oils accelerating the crosslink effect of silanol groups, thus resulting in a shrinkage of silica. Instead of peak position, the intensity of the peak has also decreased as more bio-oil added into silicas, indicating that the degree of the structural ordering of the CSC has decreased. It is concluded that the excess of the oil has a negative effect on the mesoporous structure of the CSC material.

The TEM images demonstrate that the mesopore structure is difficult to observe from the 800 mg sample, which is due to the extensive filling of bio-oil in the silica pores. The average pore size of 400 mg sample, 200 mg sample, 100 mg sample, 50 mg sample and 25 mg sample measured from TEM image is 1.34 nm, 3.47 nm, 3.93 nm, 4.88 nm and 4.84 nm, respectively, suggesting that the pore diameter of the material is increasing as the decrease of the ratio of bio-oil to silica. This is in good correlation to the porosimetry result. It is worthwhile to note that with the incorporation of bio-oil into silica framework, the linear pore arrangement of the silica pore is still retained, which could be observed from the TEM images of the samples except for 800 mg one.
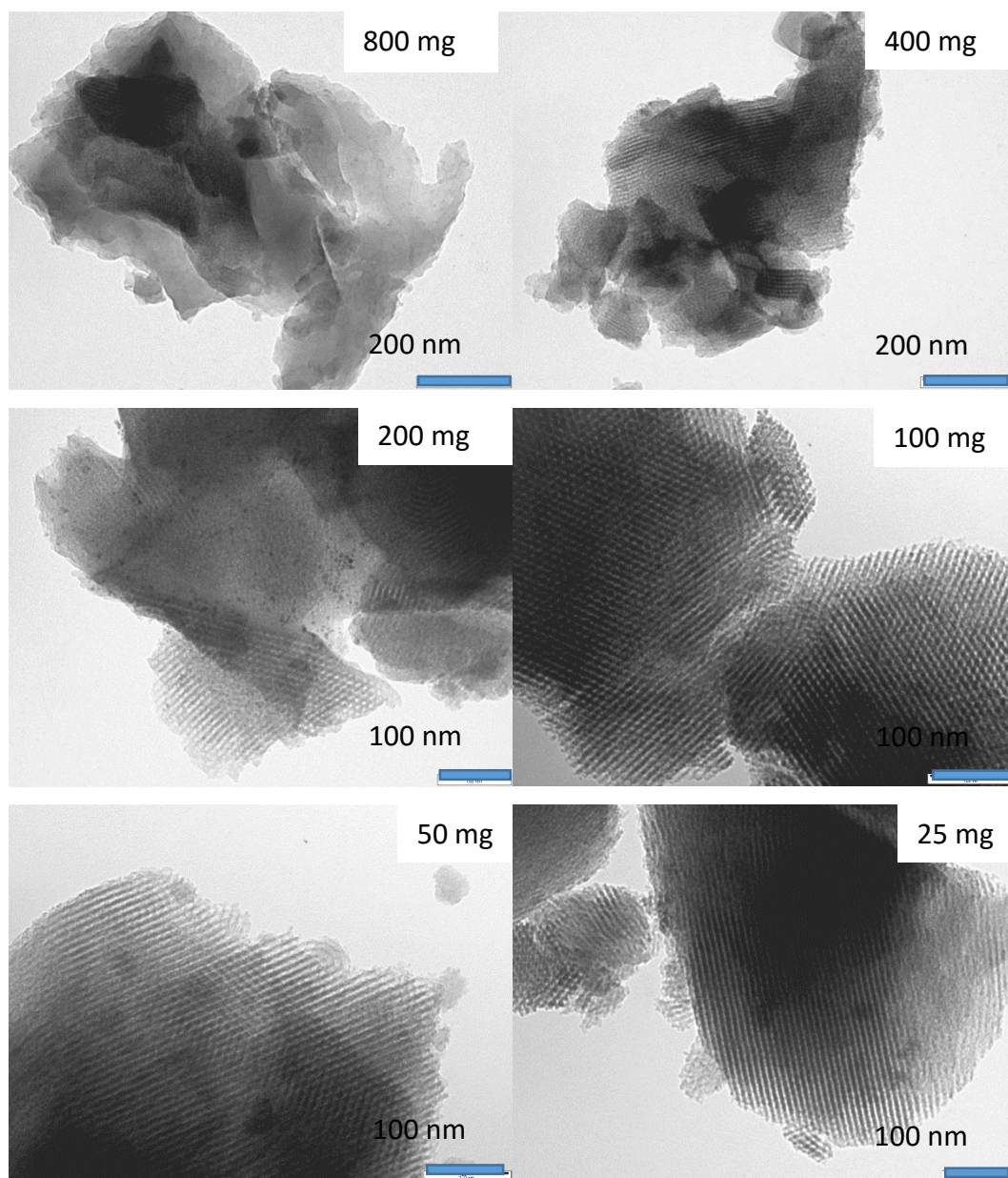
Figure 5.6 TEM images of CSC materials prepared with different amount of bio-oil

5.3   Carbonaceous materials etching from CSCs

All the results above demonstrated that the pores of silica substrates were partially or completely filled with bio-oil by adjusting the bio-oil amount. The pore size and the carbon thickness of resultant CSC material could be easily controlled by adjusting the amounts of bio-oil. Thus it could be predicated that after the removal of parent silica species, the obtained carbonaceous layer may perform as either rod-like or tubular-like (shown in Figure 5.7).
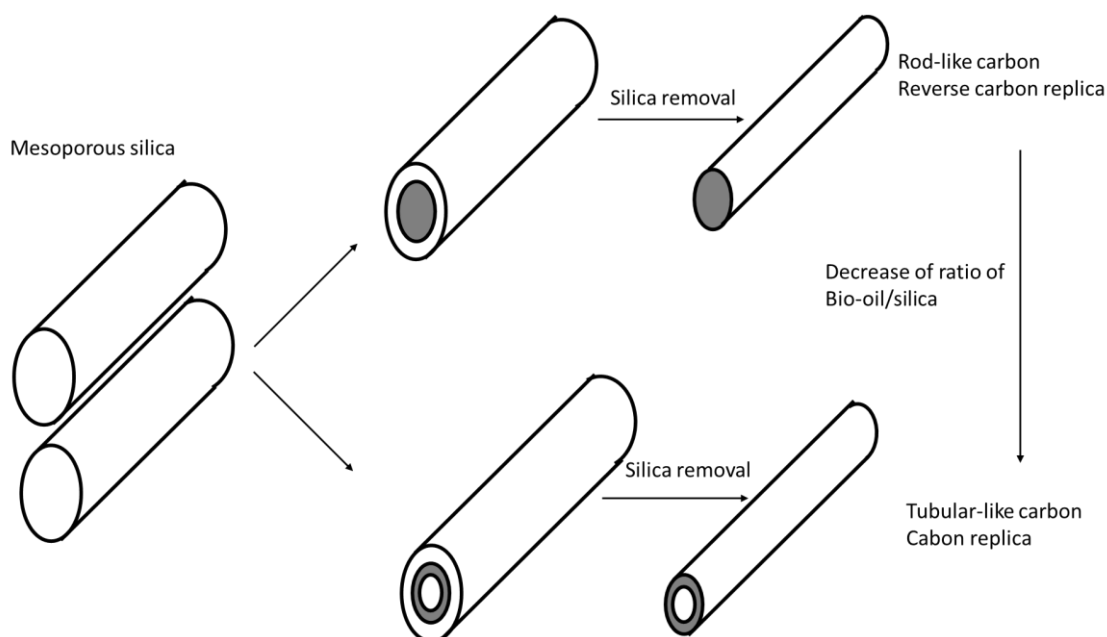
Figure 5.7 Synthetic process of rod-like carbon and tubular-like carbon

According to Terasaki's procedure,[223] the carbonaceous sample was prepared by dissolving the silica species of CSC materials into concentrated sodium hydroxide. They claimed that there was almost no silica content in the product after washing twice. The detailed experiment was described in Chapter 6. The carbonaceous samples were named according to the bio-oils added into the CSC materials.

Table 5.3 Textural properties of C100, C200, C400, C600 and C800 sample

	Ratio of bio-oil/SBA	BET surface area (m²/g)	t-plot micropore area (m²/g)	Pore volume (cm³/g)	Pore diameter (nm)
C100	1	103	19	0.04	3.3
C200	2	189	77	0.09	4.0
C400	4	67	25	0.04	4.3
C600	6	3	-	<0.01	1.2
C800	8	-	-	-	-

Table 5.3 shows the textural properties of C100, C200, C400, C600 and C800 samples. According to the values of the textural properties, these samples could be divided in to

two groups: C100, C200, C400 and C600, C800. This may be attributed to the partial or complete filling of pore with bio-oi. The partial filling happened in C100, C200 and C400 sample so that the surface areas of these samples are higher. Resulting from the high ratio of bio-oil to silica, a thicker carbon layer on the walls and smaller pore sizes were obtained, ultimately leading to a structure full of carbon. In the case when the ratio was 8:1, complete blocking of the pore structure was achieved and thus no specific surface area was observed. The pore size of the resulting carbonaceous materials is difficult to calculate because the pores of such materials could occupy two parts: 1) the pores created by carbon layer, and 2) the residual spaces after the silica removal (shown in Figure 5.1). It should be noted that for C600 and C800 sample, the organics not only blocked the pores of silica, but also covered its external surface. TGA result shows that there are still a large quantities of silica residues after the calcination at 625 °C under air. Thus indicating that the etching process could not completely remove the silica portion, leading to the poor surface area and pore volume. Thereby, further work is needed to investigate other method for etching away the silica which is covered by carbon species.
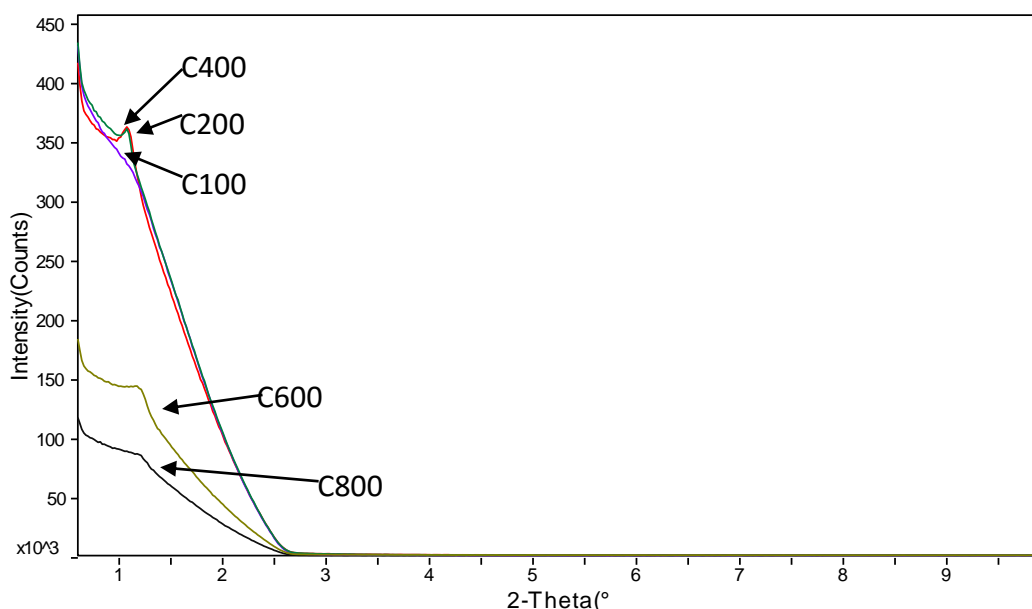
Figure 5.8 Small angle XRD patterns of C100, C200, C400, C600 and C800 samples

Small angle XRD patterns of C100, C200, C400, C600 and C800 samples are shown in Figure 5.8. No peak is observed from the pattern of C100 sample, indicating the pore

structure of this carbonaceous material is not well-ordered. This maybe due to insufficient amounts of bio-oil to form a stable uniform carbon layer on the silica substrate resulting in a thin carbon layer that leads to collapse during the etching process. However, further work would be needed to determine if this postulated reasoning is ture. C200 and C400 sampls exhibit the simliar pattern and the peaks are located at the same position.It should be noted that ther is a minor peak on the pattern of C600 and C800 sample, which is possibly attributed to the residual SBA-15 silica. It is straightforward to observe the long channel mesoporous structure (green circle in Figure 5.9) on the TEM image of C200 sample, which is similar to that on the image of SBA-15 sample, further proving the successful preparation of mesoporous carbonaceous layer.
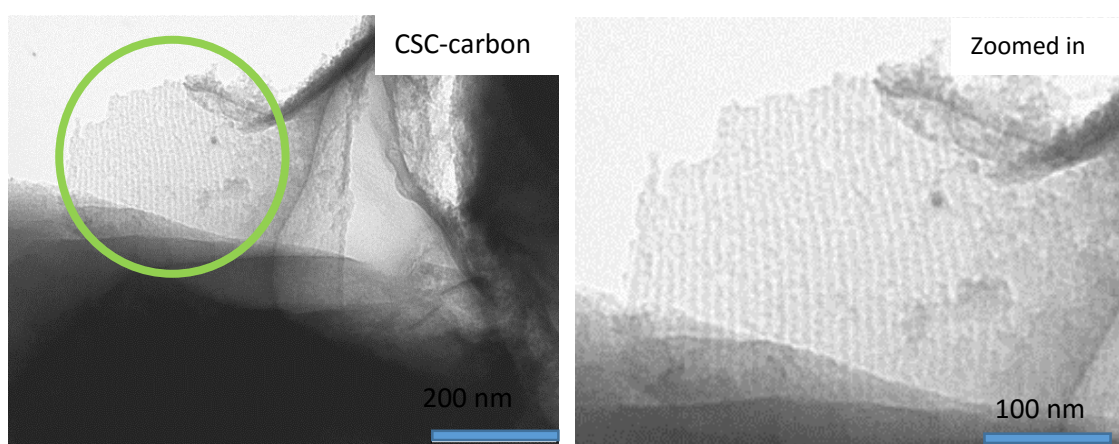
Figure 5.9 TEM images of C200 sample

5.4 Conclusion

Through adjusting the ratio of bio-oil/silica, the thickness of carbonaceous layer in the CSC material could be simply controlled up to 4 nm, which is concluded from porosimetry data. However, there is a negative effect on the structural ordering of the CSC material by increasing the bio-oil loading, which is reflected from small angle XRD analysis, as the incorporation of excess organic matter may block the silica pores.

After the etching process, a mesoporous carbonaceous material with morphology ranging from rod-like to tubular-like could be synthesized. Porosimetry data indicated that C100, C200 and C400 sample exhibited the tubular-like structure, and C600 and C800 one gave the rod-like structure. Further work would investigate the SEM analysis

of these contrasting materials to provide further evidence for the production of tubes and rods. XRD results showed that the well-ordered structures existed in C200 and C400 sample. Further investigation is needed to improve the even distribution and deposition of the bio-oil onto the silica surface in order to make high quality carbonaceous layer, and potentially this could be achieved through pre-treatment of the silica substrate or further investigation of the solvent based impregnation system. The method presented in this work represents an innovative and potentially cost effective method for the synthesis of mesoporous carbon materials ranging from tubes and rods.

Chapter 6   Materials and methodology

6.1 <u>Chemicals and reagents</u>

All chemicals were purchased from Sigma-Aldrich and Fisher Scientific and were used without any further purification. De-ionised water was used as supplied by the chemistry stores. Supercritical grade carbon dioxide (99.95% purity) was supplied by the BOC Group Plc. and used without purification. Analytical grade solvents including ethanol, acetone, and hexane were purchased from Fisher Scientific. Deuterated solvents such as chloroform-D were used for NMR analysis and they were purchased from Sigma Aldrich.

6.2 <u>Silica synthesis for Chapter 2</u>

6.2.1 Conventional SBA-15 synthesis

The SBA-15 preparation route was followed by the work done by Stucky *et al.* published in 1998.[14] In a typical silica preparation, a desired amount of P123 was dissolved in the mixture solution of water and acid with stirring at 35 $^{\circ}$C until the surfactant was fully dissolved. Then the precursor TEOS was added into that solution with stirring at 35 $^{\circ}$C for 20 hours. The mixture was aged at 80 $^{\circ}$C overnight without stirring. The solid product was recovered, washed by distilled water and air-dried at RT. Calcination was carried out in air by slowly increasing temperature from room temperature to 500 $^{\circ}$C at a rate of 1 $^{\circ}$C / min and holding at 500 $^{\circ}$C for 2 hours. The modest mass ratio of P123 : TEOS : H_2O is 1 : 2.1 : 37.5.

6.2.2 SCF phase silica preparation

6.2.2.1 Isolated preparation process in SCF

The required amount of P123 as a template was accurately weighed, and loaded into a sample vial. If ethanol or water was taken as the starting material, the template should be dissolved into it by shaking and stirring for around 20 minutes, followed by the addition of the certain amount of TFA into the previous vial. The TEOS was added slightly using a pipette to the bottom of the 100 mL view cell high pressure reactor. The prepared vial was then placed in the centre of the chamber (Figure 6.1a). The vial and the liquid level were observed clearly through the window, which is shown in Figure 6.1b. Then the internal volume of the reactor was filled with CO_2 without stirring at desired pressure

and temperature with the pressuring rate of 40 g/min. As soon as the pressure was achieved to the required value, closing the inlet valve and outlet valve immediately in order to keep the system sealed. Figure 6.1c indicated an opaque state was observed through the window, proving carbon dioxide was not transparent during the reaction owing to the dissolution of the starting material into the supercritical fluid and the particles obtained in the reactor were large enough for eye watching. After a reaction time of 24 hours with the stirring, the experimental pressure was reduced to atmospheric with the rate of 30 s / bar. A white precipitate appeared on the internal surface of the reactor (Figure 6.1d). Then the solid was obtained and calcined as the water phase preparation.
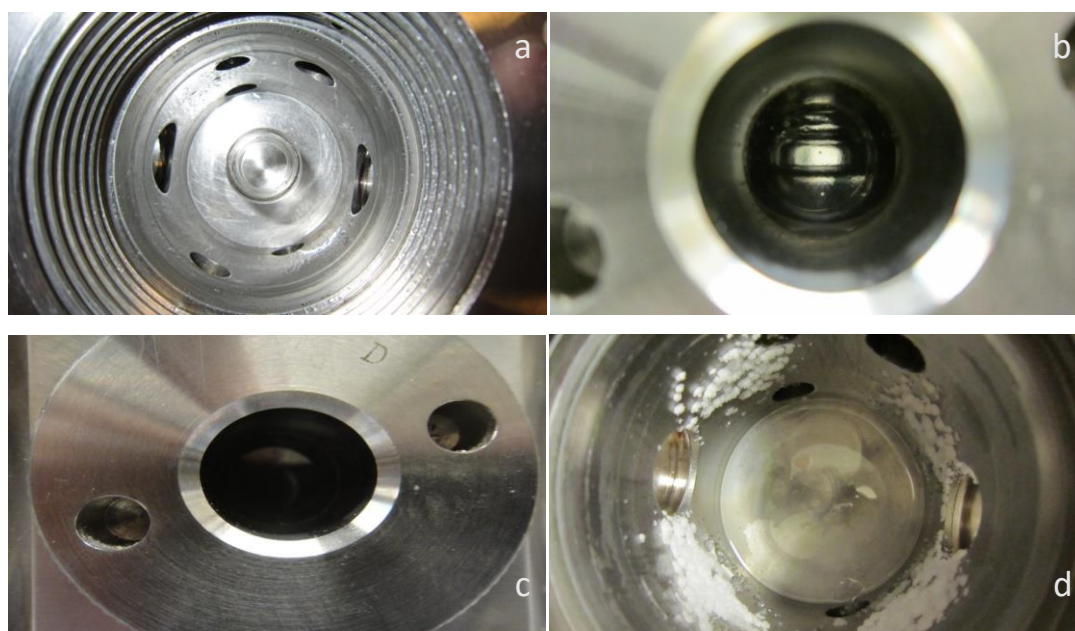
Figure 6.1 Isolated synthesis of silica using SCF as alternative solvent

6.2.2.2 Mixed preparation process in SCF (microemulsion reaction)

In a mixed preparation experiment, the required amount of P123 as a template was accurately weighed and dissolved in water by stirring. The acid was then added into the previous solution and the mixture stirred vigorously again for 10 minutes. This mixed solution was then loaded into the 104 mL view cell reactor, followed by the slow addition of the silica source TEOS. The adjustments of temperature and pressure were taken by the same means as in 6.2.2.1 during the reaction. Finally the solid was also recovered and calcined as the water phase preparation. In terms of static reaction process, the only

difference from above procedure was that the reaction took place without stirring in the view cell reactor.
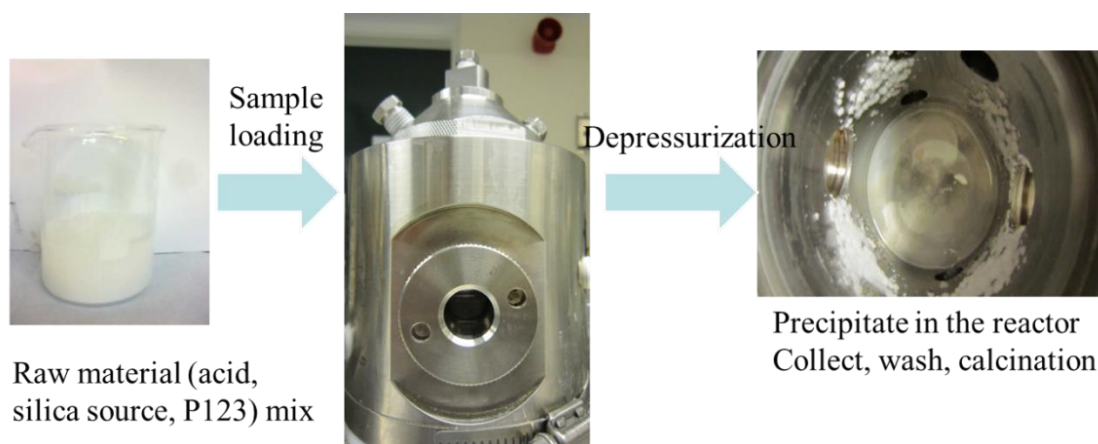
Figure 6.2 Mixed synthesis of silica using SCF as alternative solvent

6.3   Oil modification on silicas for Chapter 3

6.3.1 SBA-15 synthesis

The parent SBA-15 was synthesized according to the method published in 1998 by Stucky *et al.*.[14] In a typical synthesis, amphiphilic triblock copolymer, poly(ethylene glycol)-block-poly(propylene glycol)-block-poly(ethylene glycol) (Pluronic P123), was dissolved in HCl solution, followed by the addition with stirring of tetraethylorthosilicate (TEOS) to the homogeneous solution. The gel mixture was stirred overnight and aged at 100 °C for another 24 hours. The solid product was then filtered, washed with deionized water, dried and finally calcined in air flow. The resultant white powder was used as the substrate for the further modification.

6.3.2 MCM-41 synthesis

The procedure followed the green synthesis method developed by Macquarrie.[260] All steps were carried out at atmospheric pressure. K120 was mixed with CTAB and distilled water at 85 °C. Ethyl acetate, the hydrolysing agent, was added to this mixture which was rapidly stirred for 10 minutes. The solution was left to cool to room temperature. An aliquot of the reaction mixture was then adjusted to pH = 10 with concentrated H_2SO_4

or concentrated NaOH and left to age at room temperature for 24 hours. The ensuing precipitate was filtrated, washed with water, dried and calcined at 500 °C for 2 hours.

6.3.3 Bio-oil preparation

A Milestone ROTO SYNTH Rotative Solid Phase Microwave Reactor (Milestone Srl., Italy) fitted with a vacuum pump (see Figure 6.3) was utilized for the preparation of bio-oil. Waste paper was weighed and placed into the microwave vessel. The sample was heated from 40 °C to 200 °C under vacuum with the power of 1200 W. Volatile components were collected after condensation.
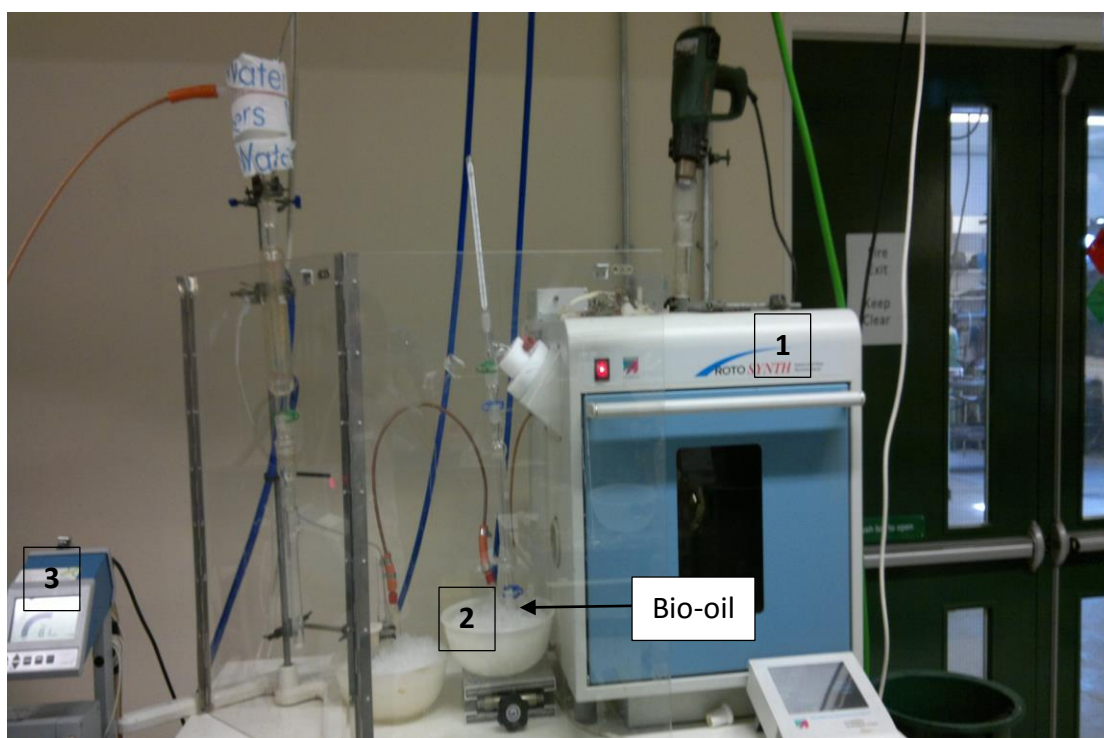
Figure 6.3 Set-up for microwave pyrolysis. (1) Microwave reactor, (2) round bottom flash for collection of bio-oil, (3) vacuum pump

6.3.4 Carbon-silica composite preparation

Carbon groups were modified onto porous silica surfaces by wet impregnation process. A solution was prepared by dissolving different amounts of bio-oil into the desired amount of acetone, followed by the addition of silica powder. After stirring overnight,

the solution was then carbonized at different temperatures under nitrogen flow to carbonize bio-oil, and finally the carbon-silica composites were obtained.

6.4 Catalysis for Chapter 4

6.4.1 Catalyst preparation

The SBA-15 support was synthesized according to the sol-gel method published in 1998 by Stucky *el al.*.[14] Bio-oils and palladium acetate were loaded into SBA-15 supports by wet impregnation process. A solution was prepared by dissolving bio-oil and palladium acetate into acetone, followed by the addition of SBA-15 powder. After stirring overnight, the solution was then carbonized at 500 $^{\circ}$C with a heating rate of 1 $^{\circ}$C/min under the nitrogen flow, and finally the carbon-silica composites were obtained with grinding. For comparison, Pd-SBA-15 catalyst was also prepared by the same synthesis route of Pd-CSC except for the use of SBA-15 as solid support. The Pd-AC catalyst (10 wt.% Pd loading on matrix activated carbon support) was directly purchased from Sigma-Aldrich.

6.4.2 Catalyst testing

In a typical experiment, the following reagents were weighed: iodobenzene or aryl halides (5 mmol), methyl acrylate (1.2 mol eqv.) and trimethylamine (1.2 mol eqv.). 2 mL of solvent was then added into the mixture. When heating to 100 $^{\circ}$C, the catalysts was added and started to stir. The reaction was allowed to proceed for 24 hours. The reaction conversion was determined by ^{1}H NMR spectroscopy. The experiment of catalytic activity over time and the yield of the product was monitored by GC-MS.

6.5 Etch out test for Chapter 5

The silica etching test was followed by the procedure published by Ryoo and co-workers.[223] The resultant carbon silica composite was washed with 1 M NaOH solution (50 vol % EtOH – 50 vol % H_2O) twice at 100 $^{\circ}$C for 5 minutes. The carbon product was then washed with ethanol and dried at 100 $^{\circ}$C.

6.6 Analysis techniques

6.6.1 GC analysis

GC analysis of the sample was conducted using an Agilent 6890 N gas chromatograph with a flame ionisation detector (GC - FID). This was fitted with a DB5HT capillary column (30m x 250 μm x 0.25 μm nominal) at constant pressure of 21.54 psi. The carrier gas used was helium and flow rate was set at 2.2 ml min^{-1} in constant flow mode. The split ratio used was 40:1. The initial oven temperature was maintained at 323 K for 4 minutes. The temperature was then ramped at a rate of 10 K min^{-1} to 573 K and held for 10 minutes. The injector was set at 563 K and the FID was maintained at 613 K. 0.5 mL of diethyl succinate was added into the liquid phase and used as internal standard. Quantification of yield was determined by peak area comparison between product and diethyl succinate standard, and the standard curve is shown in Figure 6.4.
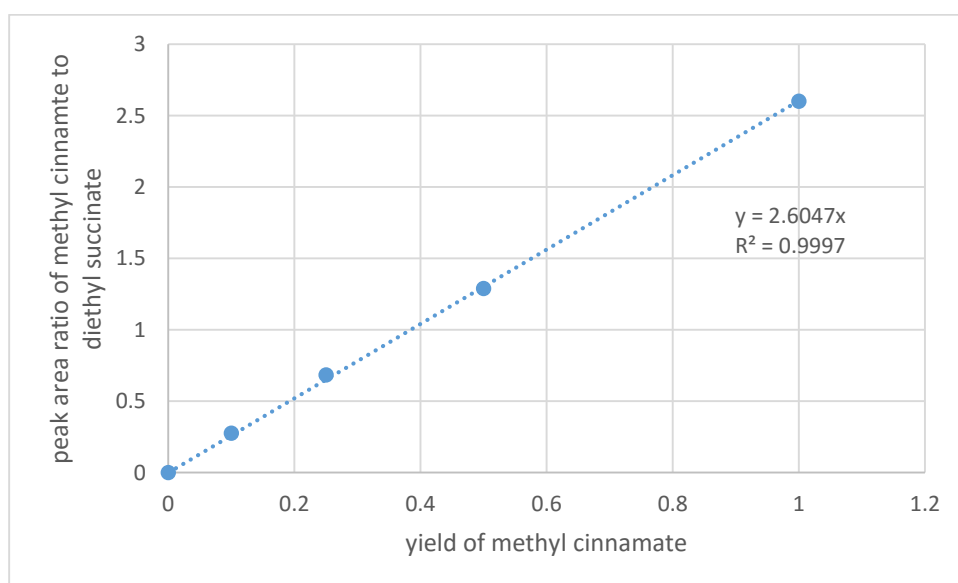
Figure 6.4 standard curve of methyl cinnamate

6.6.2 GC-MS analysis

The sample was dissolved in EtOH and analysed using a capillary column DB-5HT, 30 m x 0.25 mm I.D. x 0.25 μm film thickness. The oven was held at 60 °C for 1 minute, then temperature programmed to 300 °C at 8 °C / min and held for 10 minutes. The temperature of the injector was 290 °C. A Perkin Elmer Clarus 500 Gas chromatograph

with an auto sampler was coupled to a Perkin Elmer Clarus 560s mass spectrometer. The mass spectrometer was operated in electron impact mode (EI) at 70 eV.

6.6.3 ICP-MS analysis

Inductively coupled plasma mass spectrometry (ICP-MS) analysis was performed by the departmental service using Agilent 7700x. Sample & skimmer cones was Ni and analysis was run in He mode.

6.6.4 CHN analysis

Elemental analysis based on carbon, hydrogen and nitrogen content was carried out using an Exeter analytical CE440 elemental analyser, calibrated against acetanilide with an S-benzyl-thiouronium chloride internal standard.

6.6.5 Thermogravimetric analysis

Thermogravimetric analysis was performed on a PL Thermal Sciences STA 625. A small amount (5 mg) of sample was accurately weighed into an aluminium TGA pan and heated under the nitrogen flow to avoid oxidation of the sample. The programmed temperature was started at room temperature, and then increased up to 625 ^{o}C at the rate of 10 ^{o}C / min.

6.6.6 Microscopy

SEM and TEM micrographs were carried out with the assistance of Dr Meg Stark at the Department of Biology, University of York. SEM images were recorded using a JEOL JSM-6490LV scanning electron microscope, and TEM images were viewed on an FEI Tecnai 12 G2 transmission electron microscope.

6.6.7 Infrared spectroscopy

Infrared absorption spectra were obtained either on Bruker Vertex 70 FTIR spectrometer or Perkin Elmer Spectrum 400. Solid samples were finely ground and placed on the crystal surface with a sapphire anvil clamping. Spectra were taken from 4000 cm^{-1} to 650

cm^{-1} at 64 scans with a spectral resolution of 4 cm^{-1} with blank window for the background.

6.6.8 N_2 adsorption/desorption analysis

Nitrogen adsorption/desorption analyses were carried out at 77 K using a Micromeritics Tristar volumetric adsorption analyser. Before analysis, finely ground samples (100 mg) were degassed at 180 °C for 4 hours under the nitrogen flow. Specific surface areas were calculated using the Brunauer, Emmett and Teller (BET) method and the total pore volume was determined from the amount of nitrogen adsorbed at P/P_o ~0.99.[121] All pore size distribution curves were determined from the desorption branch based on Barrett, Joyner and Halenda (BJH) method.

6.6.9 Powder X-Ray Diffraction (XRD)

A Bruker-AXS B8 Advance diffractometer with a Kristalloflex 760 X-ray generator which produces monochromatic Kα X-rays from a copper source was employed. A finely ground powder was placed and levelled within a small round hole bevelled out of an aluminium sample holder. Scans were taken across the range 0.6 – 10 2θ with a 40 kV voltage and 40 mA current.

6.6.10 X-ray photoelectron spectroscopy

XPS measurements were performed on a Kratos Axis HSi spectrometer equipped with a monochromatic A1 Kα X-ray source and charge neutraliser. This is done by Dr Mark Isaacs at EBRI of Aston University.

6.6.11 NMR

6.6.11.1 Solution NMR

Both ^1H and ^{13}C NMR spectra were recorded. All spectra were acquired on a JEOL JNM-ECS400 MHz spectrometer using chloroform-D as solvent at 298 K.

6.6.11.2   Solid state NMR

All the solid state NMR analysis were carried out by Dr David Apperley (EPSRC Solid State NMR service, Durham University). Solid-state ^{13}C and ^{29}Si NMR (nuclear magnetic resonance) experiments were performed on a Varian VNMRS spectrometer. Spectral referencing was with respect to neat, external tetramethylsilane. ^{29}Si NMR spectra were measured at 79.4 MHz with 30 s recycle delay, and ^{13}C NMR spectra were measured at 100.5 MHz with a 1 s recycle delay.

Chapter 7   Conclusion and further work

7.1   <u>Conclusion</u>

The objectives of this thesis were to develop a novel route of synthesising silica and silica-based materials using green techniques and investigate the applications in a range of fields.

Owing to the properties of supercritical fluids, it has become an alternative solvent in material chemistry. The physical properties of SCFs could be simply tuned to more liquid or more gas like thus providing an enhanced selectivity of the solubility. Thereby, SCFs was employed as for the synthesis of porous silicas. Prior to that, a study of acid effect on the conventional synthesis of mesoporous silica SBA-15 was carried out. The results indicated that well-ordered hexagonal mesoporous silica was synthesised using inorganic acids such as HCl, H_2SO_4 and H_3PO_4, while there was a vesicle matrix with an average particle diameter of 40 -60 nm observed from the sample prepared by TFA accompanied with the BET surface area of 768 m^2/g and pore volume of 1.01 cm^3/g. It should be noted that disordered silica was formed at higher (3.06 mol/L) TFA acid concentration. Due to the strongly corrosive nature of hydrochloric acid to the reactor, TFA was applied as a substitution of HCl for hydrolysing the silica precursor in SCF system. Various conditions such as temperature, pressure, water amount, TEOS location, reaction time and kinetics were then investigated in supercritical fluid in order to synthesise spherical structure silica. The resultant samples were characterized by a range of analytical tools including porosimetry, XRD, SEM and TEM, which indicated that the hollow spherical silica with high textural properties was successfully synthesised by using TFA as acid in the supercritical fluid without stirring. The best pressure and temperature for forming this silica structure is 80 – 150 bar and 40 – 60 °C, respectively, which is very close to the supercritical point of carbon dioxide. The BET surface area, pore volume and the pore size of the resultant hollow spherical silica materials cover the ranges from 346 - 761 m^2/g, 0.23 - 0.48 cm^3/g, 2.1 - 2.7 nm, respectively.

A novel synthetic approach of carbon-silica composite has been developed by using bio-oil as carbon precursor. The bio-oil, which is generated from microwave pyrolysis of waste office paper, was characterized and its composition was identified *via* GC-MS, NMR, FT-IR and TG. The GC-MS, NMR and IR results demonstrated that the composition

of the bio-oil is complex. The bio-oil was classified into three groups, which were carbohydrate and its derivatives, furanic compounds and phenolic compounds. The resultant CSC possesses not only high specific BET surface area ranging from 39 to 636 m^2/g, narrow pore size distribution and ordered mesoporous structure, but also tuneable surface properties by adjusting the carbonization temperature ranging from 300 to 800 ^{o}C. TG analysis was monitored over the production and the results showed that 45% of the weight lost when the sample was heated to 400 ^{o}C, which could be attributed to the decomposition of aliphatics and carbonyl groups. The heating rate test indicated that a quick heating rate led to the shrinkage of the silica support in the CSC materials. In order to enlarge the application of this synthetic approach, other porous silica substrates including MCM-41, MMSBA, KIT-6 and the silicas prepared in Chapter 2 were also applied for the synthesis of CSCs.

The novel CSC was subsequently used as solid support for the deposition of palladium nanoparticles to catalyse the Heck reaction. This catalyst has been characterized and compared with different carriers by nitrogen porosimetry, microscopy and XRD, showing highly dispersived palladium nanoparticles were deposited onto the CSC supports. Also it exhibits a uniform pore structure and high surface area and pore volume as comparison to other types of catalysts. This CSC catalyst performed a high catalytic activity for the Heck reaction by using conventional solvent NMP and could be reused for four times without losing the catalytic power (82% - 93%). According to the previous literature, propylene carbonate was considered as a green alternative solvent for the Heck reaction instead of NMP. As such, the catalytic performance of CSC catalyst was tested in the presence of propylene carbonate. The results showed an excellent catalytic activity (82% - 99.5%) and recoverability of the CSC catalyst (at least 7 times). It should be noted that a side product produced methyl 3, 3-diphenylacrylate produced during the reaction by using CSC catalyst in the propylene carbonate. It was found that the generation of this side product was attributed to the further addition of iodobenzene and methyl cinnamate. As there was the significant Pd leaching in the 1st run, a pre-washing step of the CSC catalyst was carried out prior to running the Heck reaction. The conversion of the methyl acrylate indicated that the catalytic activity (89% - 93%) and the recoverability of the washed catalyst (at least 7 times) did not decrease. It is

important that the production of the side product was eliminated by using the washed CSC catalyst. A range of catalysts such as Pd-CSC-300, Pd-CSC-400, Pd-SBA-15 and Pd-AC were also tested, indicating excellent catalytic performance at the 1st use (90.5%, 88.5%, 82%, respectively). However, the results showed that Pd-CSC-300 and Pd-CSC-400 catalysts could only be reused for three or four times as these catalysts had poor pore accessibility compared to the Pd-CSC-500 one. In case of comparing Pd-CSC catalyst with Pd-AC and Pd-SBA-15 catalyst, the Pd-AC catalyst showed a comparable or superior catalytic performance when utilizing iodobenzene or other aryl halides as starting materials.

The ratio of silica and bio-oil amount is playing an important role in tailoring the thickness of carbonaceous layer of the resultant CSC material. By adjusting the ratio of bio-oil/silica, the thickness of carbonaceous layer in CSC materials could be controlled up to 4 nm and the BET surface area and pore volume range from 28 to 672 m^2/g and 0.30 to 0.68 cm^3/g, respectively. XRD and TEM results indicated that the resulting materials still possessed a regular linear pore arrangement as parent SBA-15 silica. After silica removal by the etching process, a mesoporous carbonaceous material with the morphology ranging from rod-like to tubular-like could be synthesised. Porosimetry data suggested that in the case of when the ratio was up to 4:1, the sample had a relatively high surface area from 103 to 189 m^2/g, thus exhibiting tubular-like structure. When the ratio was 6:1 and 8:1 the results showed that complete blocking of the pore structure was achieved, indicating the rod-like carbon structure was synthesised.

7.2   <u>Further work</u>

The work in this thesis has demonstrated the investigation of novel mesoporous silica and carbon materials involving the green techniques. However, some further work is still needed.

- The vesicular silica was successfully synthesised using P123 as template. Other surfactants are also worth trying as templates in further work in order to design mesoporous silicas with different morphologies.

- The critical opalescence state is extremely impressive, which could potentially utilized to make structured silica and silica based materials due to the formation of large molecular CO_2 clusters. However, this state has not been extensively studied. Such clusters could possibly be used as a novel template for synthesising ordered mesoporous silicas, in which the supercritical carbon dioxide is regarded both as solvent and template. Thereby, further work is needed to synthesise the structured silica under critical opalescence state.

- Silica modification using bio-oil as carbon source is an innovative and potentially cost effective method for the production of carbon-silica composite. In this work, it is demonstrated that there is no interactions between silica species and carbon species. Thus, further work will explore the possibility of silicon-carbide formation at higher temperatures.

- It is well demonstrated that the ratio of silica and bio-oil amount is extremely important in controlling the thickness of carbonaceous layer and pore size of the resultant composite. Hence, it is worthwhile to investigate the correlation between this ratio and the textural properties of the composite.

- Although some of the mesoporous silica substrates were applied in the synthesis of carbon silica composites, it is worth introducing other mesoporous materials with specific morphology to get novel carbon-modified composites.

- The catalysis test indicated the comparable catalytic activity of Pd-CSC catalyst. It is important to further investigate the formation of the side product methyl 3,3-diphenylacrylate, which was hardly reported in previous literature. Further work is needed to develop the catalytic activity of the catalyst for the Heck reaction involving chlorobenzene as starting material, which still gave low conversion and poor yield.

- Although tubular and rod carbon materials were successfully obtained by using sodium hydroxide to etch out the silica species from CSCs, it is worthwhile to further develop the process of removing silica substrate when synthesising carbonaceous materials in order to protect the thin carbon layers from collapsing.

Abbreviations

The following abbreviations are used in the thesis:

AOT	Sodium bis(2-ethylhexyl sulfosuccinate)
BET	Brunauer, Emmett and Teller
BJH	Barrett, Joyner and Halenda
$C_{15}AS$	Perfluoropolyether ammonium carboxylate
CFD	Chemical fluid deposition
CMC	Critical micelle concentration
CSC	Carbon silica composite
CTAB	Cetyltrimethylammonium bromide
Et_3NHI	triethylamine hydroiodide
EtOH	Ethanol
FTIR	Fourier Transform Infrared spectroscopy
H_2SO_4	Sulfuric acid
H_3PO_4	Phosphoric acid
HCl	Hydrochloric acid
N-EtFOSA	*N*-Ethyl perfluorooctylsulfonamide
P123	Pluronic P123
PAA	Poly (acrylic acid)
PCS	Polycarbosilane
PEG	Polyethylene glycol
$PFPECOONH_4$	Ammonium carboxylate perfluoropolyether
$PFPE-NH_4$	*F*-Pentanol or ammonium perfluoropolyether
$PFPE-PO_4$	Perfluoropolyether-phosphate
PHS	Poly (4-hydroxystrene)
PS	Polystyrene
p-TSA	*p*-Toluenesulfonic acid
PVAc-PFOA	Polyvinylacetate-polyfluorinated octyl acrylate
RESS	Rapid expansion of supercritical solutions

SANS	Small angle neutron scattering
SAS	Supercritical antisolvent precipitation
$SCCO_2$	Supercritical carbon dioxide
SCF	Supercritical fluid
SEM	Scanning Electron Microscopy
TEM	Transmission Electron Microscopy
TEOS	Tetraethyl orthosilicate
TFA	Trifluoroacetic acid
TGA	Thermogravimetric analysis
TON	Turnover number
TTIP	Titanium tetraisopropoxide
VOC	Volatile organic compound
XPS	X-Ray photoelectron spectroscopy
XRD	Powder X-Ray Diffraction

References

1. P. T. Anastas and J. C. Warner, *Green chemistry: theory and practice*, Oxford University Press, 0198502346, 2000.

2. R. E. Morris and S. J. Weigel, *Chem. Soc. Rev.*, 1997, **26**, 309-317.

3. F. M. Kerton and R. Marriott, *Alternative solvents for green chemistry*, Royal Society of chemistry, Cambridge, 1849735956, 2013.

4. I. Smallwood, *Handbook of organic solvent properties*, Butterworth-Heinemann, 0080523781, 2012.

5. P. Anastas and N. Eghbali, *Chem. Soc. Rev.*, 2010, **39**, 301-312.

6. B. Naik and N. N. Ghosh, *Recent Pat. Nanotechnol.*, 2009, **3**, 213-224.

7. D. Mravec, J. Hudec and I. Janotka, *Chem. Pap.*, 2005, **59**, 62-69.

8. X. S. Zhao, G. Q. Lu and G. J. Millar, *Ind, Eng. Chem. Res.*, 1996, **35**, 2075-2090.

9. J. Nagy, *Synthesis, characterization and use of zeolitic microporous materials*, DecaGen, 9630497506, 1998.

10. D. W. Bruce, D. O'Hare and R. I. Walton, *Porous materials*, Wiley, Chichester, 2010.

11. C. T. Kresge, M. E. Leonowicz, W. J. Roth, J. C. Vartuli and J. S. Beck, *Nature*, 1992, **359**, 710-712.

12. Y. Wan and D. Zhao, *Chem. Rev.*, 2007, **107**, 2821-2860.

13. J. C. Vartuli, K. D. Schmitt, C. T. Kresge, W. J. Roth, M. E. Leonowicz, S. B. McCullen, S. D. Hellring, J. S. Beck and J. L. Schlenker, *Chem. Mater.*, 1994, **6**, 2317-2326.

14. D. Zhao, Q. Huo, J. Feng, B. F. Chmelka and G. D. Stucky, *J. Am. Chem. Soc.*, 1998, **120**, 6024-6036.

15. R. Huirache-Acuña, R. Nava, C. L. Peza-Ledesma, J. Lara-Romero, G. Alonso-Núez, B. Pawelec and E. M. Rivera-Muñoz, *Materials*, 2013, **6**, 4139-4167.

16. D. Zhao, J. Feng, Q. Huo, N. Melosh, G. H. Fredrickson, B. F. Chmelka and G. D. Stucky, *Science*, 1998, **279**, 548-552.

17. D. Zhao, J. Sun, Q. Li and G. D. Stucky, *Chem. Mater.*, 2000, **12**, 275-279.

18. J. S. Yun and S. K. Ihm, *J. Phys. Chem. Solids*, 2008, **69**, 1133-1135.

19. J. Dhainaut, J. P. Dacquin, A. F. Lee and K. Wilson, *Green Chem.*, 2010, **12**, 296-303.

20.   E. F. Vansant, P. Van Der Voort and K. C. Vrancken, *Characterization and chemical modification of the silica surface*, Elsevier Science, Amsterdam, 0080528953, 1995.

21.   Q. Jiang, Z. Y. Wu, Y. M. Wang, Y. Cao, C. F. Zhou and J. H. Zhu, *J. Mater. Chem.*, 2006, **16**, 1536-1542.

22.   C. Gu, P. A. Chia and X. S. Zhao, *Appl. Surf. Sci.*, 2004, **237**, 387-392.

23.   P. Wu, T. Tatsumi, T. Komatsu and T. Yashima, *Chem. Mater.*, 2002, **14**, 1657-1664.

24.   P. Shah, A. V. Ramaswamy, K. Lazar and V. Ramaswamy, *Microporous Mesoporous Mater.*, 2007, **100**, 210-226.

25.   A. Y. Khodakov, R. Bechara and A. Griboval-Constant, *Appl. Catal., A: Gen.*, 2003, **254**, 273-288.

26.   Y. Park, T. Kang, J. Lee, P. Kim, H. Kim and J. Yi, *Catalysis Today*, 2004, **97**, 195-203.

27.   C. M. Yang, M. Kalwei, F. Schüth and K. J. Chao, *Appl. Catal., A: Gen.*, 2003, **254**, 289-296.

28.   P. Han, X. Wang, X. Qiu, X. Ji and L. Gao, *J. Mol. Catal. A: Chem.*, 2007, **272**, 136-141.

29.   A. J. Hunt, V. L. Budarin, J. W. Comerford, H. L. Parker, V. K. Lazarov, S. W. Breeden, D. J. Macquarrie and J. H. Clark, *Mater. Lett.*, 2014, **116**, 408-411.

30.   G. Ertl, H. Knözinger and J. Weitkamp, *Preparation of solid catalysts*, Wiley-Vch, 3527620680, 2008.

31.   X. S. Zhao, F. Su, Q. Yan, W. Guo, X. Y. Bao, L. Lv and Z. Zhou, *J. Mater. Chem.*, 2006, **16**, 637-648.

32.   Y. Fukushima and H. Wakayama, *J. Phys. Chem. B*, 1999, **103**, 3062-3064.

33.   H. Wakayama and Y. Fukushima, *Chem. Mater.*, 2000, **12**, 756-761.

34.   H. Wakayama and Y. Fukushima, *Ind. Eng. Chem. Res.*, 2000, **39**, 4641-4645.

35.   H. Wakayama and Y. Fukushima, *Ind. Eng. Chem. Res.*, 2006, **45**, 3328-3331.

36.   Y. F. Shi, Y. Meng, D. H. Chen, S. J. Cheng, P. Chen, H. F. Yang, Y. Wan and D. Y. Zhao, *Adv. Funct. Mater.*, 2006, **16**, 561-567.

37.   Q. Xu, H. Fan, Y. Guo and Y. Cao, *Mater. Sci. Eng., A*, 2006, **435-436**, 158-162.

38.   J. Cabana, T. Valdés Solís, M. R. Palacín, J. Oró Solé, A. Fuertes, G. Marbán and A. B. Fuertes, *J. Power Sources*, 2007, **166**, 492-498.

39.   W. Guo, F. Su and X. Zhao, *Carbon*, 2005, **43**, 2423-2426.

40. W. Guo and G. X. S. Zhao, in *Stud. Surf. Sci. Catal.*, eds. S. Abdelhamid and J. Mietek, Elsevier, 2005.

41. R. Aiello and R. Barrer, *Journal of the Chemical Society A: Inorganic, Physical, Theoretical*, 1970, 1470-1475.

42. Y. Shi, Y. Wan and D. Zhao, *Chem. Soc. Rev.*, 2011, **40**, 3854-3878.

43. E. M. Johansson, Controlling the pore size and morphology of mesoporous silica, 2010

44. C. Yu, J. Fan, B. Tian, G. D. Stucky and D. Zhao, *J. Phys. Chem. B*, 2003, **107**, 13368-13375.

45. J. Fan, C. Yu, L. Wang, B. Tu, D. Zhao, Y. Sakamoto and O. Terasaki, *J. Am. Chem. Soc.*, 2001, **123**, 12113-12114.

46. Z. Liu, O. Terasaki, T. Ohsuna, K. Hiraga, H. J. Shin and R. Ryoo, *Chem. Phys. Chem.*, 2001, **2**, 229-231.

47. M. Impéror-Clerc, P. Davidson and A. Davidson, *J. Am. Chem. Soc.*, 2000, **122**, 11925-11933.

48. T. Tsoncheva, J. Rosenholm, M. Linden, L. Ivanova and C. Minchev, *Appl. Catal., A*, 2007, **318**, 234-243.

49. J. Wang, Y. Xia, W. Wang, R. Mokaya and M. Poliakoff, *Chem. Commun.*, 2005, **2**, 210-212.

50. J. Wang, Y. Xia, W. Wang, M. Poliakoff and R. Mokaya, *J. Mater. Chem.*, 2006, **16**, 1751-1756.

51. X. Li, T. Fan, Z. Liu, J. Ding, Q. Guo and D. Zhang, *J. Eur. Ceram. Soc.*, 2006, **26**, 3657-3664.

52. J. Jiao, Q. Xu and L. Li, *J. Colloid Interface Sci.*, 2007, **316**, 596-603.

53. R. A. Pai, R. Humayun, M. T. Schulberg, A. Sengupta, J. N. Sun and J. J. Watkins, *Science*, 2004, **303**, 507-510.

54. H. Wakayama, S. Inagaki and Y. Fukushima, *J. Am. Ceram. Soc.*, 2002, **85**, 161-164.

55. H. Wakayama, H. Itahara, N. Tatsuda, S. Inagaki and Y. Fukushima, *Chem. Mater.*, 2001, **13**, 2392-2396.

56. B. S. Chun, P. Pendleton, A. Badalyan and S. Y. Park, *Korean J. Chem. Eng.*, 2010, **27**, 983-990.

57. S. Kawi and M. W. Lai, *Chem. Commun.*, 1998, 1407-1408.

58.   R. V. Grieken, G. Calleja, G. D. Stucky, J. A. Melero, R. A. Garcia and J. Iglesias, *Langmuir*, 2003, **19**, 3966-3973.

59.   B. Tian, X. Liu, C. Yu, F. Gao, Q. Luo, S. Xie, B. Tu and D. Zhao, *Chem. Commun.*, 2002, **11**, 1186-1187.

60.   F. Bérubé and S. Kaliaguine, *Microporous Mesoporous Mater.*, 2008, **115**, 469-479.

61.   S. Kawi and M. W. Lai, *AlChE J.*, 2002, **48**, 1572-1580.

62.   J. Eastoe, M. J. Hollamby and L. Hudson, *Adv. Colloid Interface Sci.*, 2006, **128-130**, 5-15.

63.   W. Leitner, *Nature*, 2000, **405**, 129-130.

64.   J. M. Dobbs, J. M. Wong, R. J. Lahiere and K. P. Johnston, *Ind. Eng. Chem. Res.*, 1987, **26**, 56-65.

65.   F. J. Senorans and E. Ibanez, *Anal. Chim. Acta*, 2002, **465**, 131-144.

66.   A. Clifford and T. Clifford, *Fundamentals of supercritical fluids*, Oxford University Press, 0198501374, 1999.

67.   D. Matson, J. Fulton, R. Petersen and R. Smith, *Eng. Chem. Res*, 1987, **26**, 2298-2306.

68.   R. D. Smith, Method of making supercritical fluid molecular spray films, powder and fibers, Patent, US 4734227 A, 1988.

69.   X. Ye and C. M. Wai, *J. Chem. Educ.*, 2003, **80**, 198-204.

70.   Y. P. Sun, H. W. Rollins and R. Guduru, *Chem. Mater.*, 1998, **11**, 7-9.

71.   Y. P. Sun, R. Guduru, F. Lin and T. Whiteside, *Ind. Eng. Chem. Res.*, 2000, **39**, 4663-4669.

72.   Y. P. Sun and H. W. Rollins, *Chem. Phys. Lett.*, 1998, **288**, 585-588.

73.   D. E. Fremgen, E. S. Smotkin, R. E. Gerald, R. J. Klingler and J. W. Rathke, *J. Supercrit. Fluids*, 2001, **19**, 287-298.

74.   J. L. Dickson, B. P. Binks and K. P. Johnston, *Langmuir*, 2004, **20**, 7976-7983.

75.   J. P. Cason and C. B. Roberts, *J. Phys. Chem.*, 2000, **104**, 1217-1221.

76.   J. Liu, S. Cheng, J. Zhang, X. Feng, X. Fu and B. Han, *Angew. Chem. Int. Ed.*, 2007, **46**, 3313-3315.

77.   Z. Xue, J. Zhang, L. Peng, J. Li, T. Mu, B. Han and G. Yang, *Angew. Chem. Int. Ed.*, 2012, **51**, 12325-12329.

78. C. Zhang, J. Zhang, X. Zhang, X. Feng, J. Chen, B. Han and G. Yang, *J. Supercrit. Fluids*, 2007, **42**, 142-149.

79. K. T. Lim, H. S. Hwang, W. Ryoo and K. P. Johnston, *Langmuir*, 2004, **20**, 2466-2471.

80. J. L. Fulton and R. D. Smith, *J. Phys. Chem.*, 1988, **92**, 2903-2907.

81. R. M. Lemert, R. A. Fuller and K. P. Johnston, *J. Phys. Chem.*, 1990, **94**, 6021-6028.

82. D. W. Matson, J. L. Fulton and R. D. Smith, *Mater. Lett.*, 1987, **6**, 31-33.

83. P. W. Bell, M. Anand, X. Fan, R. M. Enick and C. B. Roberts, *Langmuir*, 2005, **21**, 11608-11613.

84. E. Reverchon, G. Della Porta and E. Torino, *J. Supercrit. Fluids*, 2010, **53**, 95-101.

85. J. Zhang, B. Han, W. Li, Y. Zhao and M. Hou, *Angew. Chem. Int. Ed.*, 2008, **47**, 10119-10123.

86. D. C. Martino, R. Triolo, J. B. McClain, J. R. Combes, D. E. Betts, D. A. Canelas, J. M. DeSimone, E. T. Samulski, H. D. Cochran, J. D. Londono and G. D. Wignall, *J. Mol. Struct.*, 1996, **383**, 3-10.

87. T. Hoefling, D. Stofesky, M. Reid, E. Beckman and R. M. Enick, *J. Supercrit. Fluids*, 1992, **5**, 237-241.

88. Z. Guan and J. M. DeSimone, *Macromolecules*, 1994, **27**, 5527-5532.

89. Z. Chen, S. Li, F. Xue, G. Sun, C. Luo, J. Chen and Q. Xu, *Colloids Surf., A*, 2010, **355**, 45-52.

90. G. Sun, Z. Chen, S. Wang, L. Li, J. Fu, J. Chen and Q. Xu, *Colloid. Polym. Sci.*, 2011, **289**, 1397-1406.

91. V. R. Tirumala, R. A. Pai, S. Agarwal, J. J. Testa, G. Bhatnagar, A. H. Romang, C. Chandler, B. P. Gorman, R. L. Jones, E. K. Lin and J. J. Watkins, *Chem. Mater.*, 2007, **19**, 5868-5874.

92. F. Triolo, A. Triolo, R. Triolo, D. E. Betts, J. B. McClain, J. M. D. Simone, D. C. Steytler, G. D. Wignall, B. Demé and R. K. Heenan, *J. Appl. Cryst.*, 2000, **33**, 641-644.

93. R. Triolo, A. Triolo, F. Triolo, D. C. Steytler, C. A. Lewis, R. K. Heenan, G. D. Wngnall and J. M. DeSimone, *Phys. Rev. E*, 2000, **61**, 4640-4643.

94. S. Salaniwal, S. T. Cui, P. T. Cummings and H. D. Cochran, *Langmuir*, 1999, **15**, 5188-5192.

95. A. I. Cooper, *Adv. Mater.* , 2003, **15**, 1049-1059.

96.   A. S. O'Neil, R. Mokaya and M. Poliakoff, *J. Am. Chem. Soc.*, 2002, **124**, 10636-10637.

97.   J. Morère, M. J. Tenorio, M. J. Torralvo, C. Pando, J. A. R. Renuncio and A. Cabañas, *J. Supercrit. Fluids*, 2011, **56**, 213-222.

98.   E. T. Thostenson and T. W. Chou, *Composites: Part A*, 1999, **30**, 1055–1071.

99.   D. Jones, T. Lelyveld, S. Mavrofidis, S. Kingman and N. Miles, *Resour. Conserv. Recy.*, 2002, **34**, 75-90.

100.   D. Mohan, C. U. Pittman and P. H. Steele, *Energy Fuels*, 2006, **20**, 848-889.

101.   N. M. Mokhtar, R. Omar and A. Idris, *Energy Sources, Part A*, 2012, **34**, 2104-2122.

102.   C. Wu, V. L. Budarin, M. J. Gronnow, M. De Bruyn, J. A. Onwudili, J. H. Clark and P. T. Williams, *J. Anal. Appl. Pyrolysis*, 2014, **107**, 276-283.

103.   Q. Lu, W. Z. Li and X. F. Zhu, *Energy Convers. Manage.*, 2009, **50**, 1376-1383.

104.   A. Oasmaa and P. Koponen, *Physical characterisation of biomass-based pyrolysis liquids*, Espoo, 951385051X, 1997.

105.   S. Czernik and A. Bridgwater, *Energy Fuels*, 2004, **18**, 590-598.

106.   T. Ba, A. Chaala, M. Garcia-Perez and C. Roy, *Energy Fuels*, 2004, **18**, 188-201.

107.   T. Ba, A. Chaala, M. Garcia-Perez, D. Rodrigue and C. Roy, *Energy Fuels*, 2004, **18**, 704-712.

108.   J. N. Murwanashyaka, H. Pakdel and C. Roy, *J. Anal. Appl. Pyrolysis*, 2001, **60**, 219-231.

109.   R. Lu, G. P. Sheng, Y. Y. Hu, P. Zheng, H. Jiang, Y. Tang and H. Q. Yu, *Biomass Bioenergy*, 2011, **35**, 671-678.

110.   F. Zeng, W. Liu, H. Jiang, H. Q. Yu, R. J. Zeng and Q. Guo, *Bioresource technology*, 2011, **102**, 1982-1987.

111.   K. Sipilä, E. Kuoppala, L. Fagernäs and A. Oasmaa, *Biomass Bioenergy*, 1998, **14**, 103-113.

112.   Z. Zhang, D. J. Macquarrie, M. De bruyn, V. L. Budarin, A. J. Hunt, M. J. Gronnow, J. Fan, P. S. Shuttleworth, J. H. Clark and A. S. Matharu, *Green Chem.*, 2015, **17**, 260-270.

113.   A. Oasmaa, E. Kuoppala, S. Gust and Y. Solantausta, *Energy Fuels*, 2003, **17**, 1-12.

114.   A. Oasmaa, E. Kuoppala and Y. Solantausta, *Energy Fuels*, 2003, **17**, 433-443.

115.   A. Oasmaa and E. Kuoppala, *Energy Fuels*, 2003, **17**, 1075-1084.

116.   Q. H. Song, J. Q. Nie, M. G. Ren and Q. X. Guo, *Energy Fuels*, 2009, **23**, 3307–3312.

117.   S. Wang, Y. Gu, Q. Liu, Y. Yao, Z. Guo, Z. Luo and K. Cen, *Fuel Process. Technol.*, 2009, **90**, 738-745.

118.   S. Westermarck, *Use of mercury porosimetry and nitrogen adsorption in characterisation of the pore structure of mannitol and microcrystalline cellulose powders, granules and tablets*, University of Helsinki Helsinki, Finland, 9529125364, 2000.

119.   K. S. Sing, *Pure Appl. Chem.*, 1985, **57**, 603-619.

120.   M. Thommes, *Chem. Ing. Tech*, 2010, **82**, 1059-1073.

121.   S. Brunauer, P. H. Emmett and E. Teller, *J. Am. Chem. Soc.*, 1938, **60**, 309-319.

122.   I. Langumuir, *J. Am. Chem. Soc.*, 1916, **38**, 2221-2295.

123.   R. K. Iler, *The chemistry of silica: solubility, polymerization, colloid and surface pro perties, and biochemistry*, Wiley, 047102404X, 1979.

124.   P. Barrett and L. Joyner, *J. Am. Chem. Soc*, 1951, **73**, 373-380.

125.   G. Blázquez, M. Calero, F. Hernáinz, G. Tenorio and M. A. Martín-Lara, *Chem. Eng. J.*, 2010, **160**, 615-622.

126.   R. E. Dinnebier and S. J. Billinge, *Powder diffraction: theory and practice*, Royal society of chemistry, 0854042318, 2008.

127.   P. Atkins and J. de Paula, *Atkins' Physical Chemistry*, OUP Oxford, 9780199697403, 2014.

128.   C. C. Chusuei and D. W. Goodman, *X-Ray Photoelectron Spectros-copy. In: Meyers RA, editor. Encyclopedia of Physical Scienceand Technology, 3rd ed.*, Academic Press, NY, 2002.

129.   T. G. Rochow and P. A. Tucker, *Introduction to microscopy by means of light, electrons, X-rays, or acoustics*, Springer Science & Business Media, 0306446847, 1994.

130.   J. Akitt, *NMR and chemistry: an introduction to modern NMR spectroscopy. 3*, 1992.

131.   PerkinElmer, Thermogravimetric Analysis: a beginner's guide, http://www.perkinelmer.co.uk/CMSResources/Images/44-74556GDE_TGABeginnersGuide.pdf, 2015.

132. F. Zheng, D. N. Tran, B. J. Busche, G. E. Fryxell, R. S. Addleman, T. S. Zemanian and C. L. Aardahl, *Ind, Eng. Chem. Res.*, 2005, **44**, 3099-3105.

133. N. Hiyoshi, K. Yogo and T. Yashima, *Microporous Mesoporous Mater.*, 2005, **84**, 357-365.

134. X. Yan, L. Zhang, Y. Zhang, G. Yang and Z. Yan, *Ind, Eng. Chem. Res.*, 2011, **50**, 3220-3226.

135. Y. Wan, Y. Shi and D. Zhao, *Chem. Commun.*, 2007, 897-926.

136. D. G. Choi and S. M. Yang, *J. Colloid Interface Sci.*, 2003, **261**, 127-132.

137. C. Yu, B. Tian, J. Fan, G. D. Stucky and D. Zhao, *Chem. Commun.*, 2001, 2726-2727.

138. K. Flodström, C. V. Teixeira, H. Amenitsch, V. Alfredsson and M. Lindén, *Langmuir*, 2004, **20**, 4885-4891.

139. A. Katiyar, S. Yadav, P. G. Smirniotis and N. G. Pinto, *J. Chromatogr. A*, 2006, **1122**, 13-20.

140. K. De Witte, A. M. Busuioc, V. Meynen, M. Mertens, N. Bilba, G. Van Tendeloo, P. Cool and E. F. Vansant, *Microporous Mesoporous Mater.*, 2008, **110**, 100-110.

141. K. P. Johnston and P. S. Shah, *Science*, 2004, **303**, 482-483.

142. A. I. Cooper, *Adv. Mater.*, 2001, **14**, 1111-1114.

143. X. Cui, W. C. Zin, W. J. Cho and C. S. Ha, *Mater. Lett.*, 2005, **59**, 2257-2261.

144. J. Li, Q. Hu, H. Tian, C. Ma, L. Li, J. Cheng, Z. Hao and S. Qiao, *J. Colloid Interface Sci.*, 2009, **339**, 160-167.

145. P. W. Bell, A. J. Thote, Y. Park, R. B. Gupta and C. B. Roberts, *Ind, Eng. Chem. Res.*, 2003, **42**, 6280-6289.

146. X. Li and B. D. Vogt, *Chem. Mater.*, 2008, **20**, 3229-3238.

147. Bordwell pKa Table, http://www.chem.wisc.edu/areas/reich/pkatable/index.htm, 2015.

148. Y. Lu, H. Fan, A. Stump, T. L. Ward, T. Rieker and C. J. Brinker, 1999, **398**, 223-226.

149. G. Zhou, Y. Chen, J. Yang and S. Yang, *J. Mater. Chem.*, 2007, **17**, 2839-2844.

150. L. Lecren, T. Toupance and R. Backov, *Mater. Lett.*, 2005, **59**, 817-820.

151. Q. Sun, P. J. Kooyman, J. G. Grossmann, P. H. H. Bomans, P. M. Frederik, P. C. M. M. Magusin, T. P. M. Beelen, R. A. Van-Santen and N. A. J. M. Sommerdijk, *Adv. Mater.*, 2003, **15**, 1097-1100.

152. Z. Li, T. Shi and L. Guo, *J. Serb. Chem. Soc.*, 2010, **75**, 385-394.

153. D. C. Thomas and S. M. Benson, *Carbon Dioxide Capture for Storage in Deep Geologic Formations*, Elsevier Science, 9780080457482, 2005.

154. M. Cocero and L. Calvo, *J. Am. Oil. Chem. Soc.*, 1996, **73**, 1573-1578.

155. Isothermal Properties for Carbon dioxide, http://webbook.nist.gov/cgi/fluid.cgi?Action=Load&ID=C124389&Type=IsoTherm&Digits=5&PLow=150&PHigh=350&PInc=10&T=60&RefState=DEF&TUnit=C&PUnit=bar&DUnit=g%2Fml&HUnit=kJ%2Fmol&WUnit=m%2Fs&VisUnit=uPa*s&STUnit=N%2Fm, 2015.

156. H. Wakayama, Y. Goto and Y. Fukushima, *Phy. Chem. Chem. Phys.*, 2003, **5**, 3784-3788.

157. M. McHugh and V. Krukonis, *Supercritical fluid extraction: principles and practice*, Elsevier, 0080518176, 2013.

158. P. F. Fulvio, S. Pikus and M. Jaroniec, *J. Mater. Chem.*, 2005, **15**, 5049-5053.

159. Isobaric Properties for Carbon dioxide, http://webbook.nist.gov/cgi/fluid.cgi?Action=Load&ID=C124389&Type=IsoBar&Digits=5&P=250&THigh=85&TLow=40&TInc=5&RefState=DEF&TUnit=C&PUnit=bar&DUnit=g%2Fml&HUnit=kJ%2Fmol&WUnit=m%2Fs&VisUnit=uPa*s&STUnit=N%2Fm, 2015.

160. J. L. Lopez-Fontan, A. Gonzalez-Perez, J. Costa, J. M. Ruso, G. Prieto, P. C. Schulz and F. Sarmiento, *J. Colloid Interface Sci.*, 2006, **297**, 10-21.

161. J. M. Ruso, E. Blanco and P. V. Messina, *J. Porous Mater.*, 2012, **20**, 95-105.

162. T. Fukuda, T. Maekawa, T. Hasumura, N. Rantonen, K. Ishii, Y. Nakajima, T. Hanajiri, Y. Yoshida, R. Whitby and S. Mikhalovsky, *New Journal of Physics*, 2007, **9**, 321-321.

163. T. Fukuda, N. Watabe, R. Whitby and T. Maekawa, *Nanotechnology*, 2007, **18**, 4156041-4156046.

164. J. White and B. Maccabee, *Physical Review Letters*, 1971, **26**, 1468-1471.

165. J. Zipfel, J. Berghausen, G. Schmidt, P. Lindner, P. Alexandridis and W. Richtering, *Macromolecules*, 2002, **35**, 4064-4074.

166. A. J. Karkamkar, S. S. Kim, S. D. Mahanti and T. J. Pinnavaia, *Adv. Funct. Mater.*, 2004, **14**, 507-512.

167. S. S. Kim, Y. Liu and T. J. Pinnavaia, *Microporous Mesoporous Mater.*, 2001, **44–45**, 489-498.

168. S. S. Kim, W. Zhang and T. J. Pinnavaia, *Science*, 1998, **282**, 1302-1305.

169. J. Zhang and B. Han, *Acc. Chem. Res.*, 2013, **46**, 425-433.

170. S. R. P. D. Rocha, K. L. Harrison and K. P. Johnston, *Langmuir*, 1999, **15**, 419-428.

171. R. A. Pai and J. J. Watkins, *Adv. Mater.*, 2006, **18**, 241-245.

172. Confederation of paper industries, Manufacture of paper, http://www.recycledpaper.org.uk/information/school_resources/paper_manufacture.pdf, 2015.

173. B. Lu, A. Xu and J. Wang, *Green Chem.*, 2014, **16**, 1326-1335.

174. T. Foyle, L. Jennings and P. Mulcahy, *Bioresour. Technol.*, 2007, **98**, 3026-3036.

175. *Technologies for reducing dioxin in the manufacture of bleached wood pulp*, DIANE Publishing, 9781428922372.

176. European Recovered Paper Council, Paper recycling monitoring report, http://www.paperforrecycling.eu/uploads/Modules/Publications/WEB_lowres_Monitoring%20report%202012.pdf, 2015.

177. H. Merrild, A. Damgaard and T. H. Christensen, *Resour. Conserv. Recy.*, 2008, **52**, 1391-1398.

178. CEPI's key statistics, European pulp and paper industry, http://www.paper.org.uk/members/statistics/papermaking/eukey/CEPI_KeyStatistics_2013.pdf, 2015.

179. E. Y. Park, P. N. Anh and N. Okuda, *Bioresour. Technol.*, 2004, **93**, 77-83.

180. Y. Ikeda, E. Y. Park and N. Okuda, *Bioresour. Technol.*, 2006, **97**, 1030-1035.

181. H. W. Yen and D. E. Brune, *Bioresour. Technol.*, 2007, **98**, 130-134.

182. M. Wayman, S. Chen and K. Doan, *Process Biochem.*, 1992, **27**, 239-245.

183. H. Ono, T. Yamada, Y. Hatano and K. Motohashi, *J. Adhes.*, 1996, **59**, 135-145.

184. G. C. Galletti, P. Bocchini, M. E. Guadalix, G. Almendros, S. Camarero and A. T. Martínez, *Bioresour. Technol.*, 1997, **60**, 51-58.

185. L. Li, H. Zhang and X. Zhuang, *Energy Sources*, 2005, **27**, 867-873.

186. M. I. Jahirul, M. G. Rasul, A. A. Chowdhury and N. Ashwath, *Energies*, 2012, **5**, 4952-5001.

187. S. S. Lam and H. A. Chase, *Energies*, 2012, **5**, 4209-4232.

188.   A. V. Bridgwater, *Biomass Bioenergy*, 2012, **38**, 68-94.

189.   M. F. Demirbas and M. Balat, *Energy Convers. Manage.*, 2006, **47**, 2371-2381.

190.   D. Vamvuka, *International Journal of Energy Research*, 2011, **35**, 835-862.

191.   Y. Zhang, D. Y. Chen, D. Zhang and X. F. Zhu, *J. Fuel Chem. Technol,*, 2012, **40**, 1194-1199.

192.   A. V. Bridgwater, *Chem. Eng. J.*, 2003, **91**, 87-102.

193.   E. Pretsch, P. Bühlmann and M. Badertscher, *Structure Determination of Organic Compounds: Tables of Spectral Data*, Springer Berlin Heidelberg, 9783540938101, 2009.

194.   C. Q. Jiao, S. F. Adams and A. Garscadden, *J. Appl. Phys.*, 2009, **106**, 0133061-0133064.

195.   G. Marques, A. Gutierrez and J. C. del Rio, *J. Agric. Food. Chem.*, 2007, **55**, 1327-1336.

196.   A. E. Crotti, T. Fonseca, H. Hong, J. Staunton, S. E. Galembeck, N. P. Lopes and P. J. Gates, *Int. J. Mass spectrom.*, 2004, **232**, 271-276.

197.   W. Pongsuwan, T. Bamba, T. Yonetani, A. Kobayashi and E. Fukusaki, *J. Agric. Food. Chem.*, 2008, **56**, 744-750.

198.   A. Stergiou, A. Bariotaki, D. Kalaitzakis and I. Smonou, *J. Org. Chem.*, 2013, **78**, 7268-7273.

199.   F. Shafizadeh and P. P. Chin, *Carbohydr. Res.*, 1976, **46**, 149-154.

200.   Y. Halpern, R. Riffer and A. Broido, *J. Org. Chem.*, 1973, **38**, 204-209.

201.   Y. Halpern and J. P. Hoppesch, *J. Org. Chem.*, 1985, **50**, 1556-1557.

202.   A. M. Sarotti, M. M. Zanardi, R. A. Spanevello and A. G. Suarez, *Curr. Org. Synth.*, 2012, **9**, 439-459.

203.   M. S. Miftakhov, F. A. Valeev and I. N. Gaisina, *Russ. Chem. Rev.*, 1994, **63**, 869-882.

204.   V. Bailliez, A. Olesker and J. Cleophax, *Tetrahedron*, 2004, **60**, 1079-1085.

205.   N. M. Bennett, S. S. Helle and S. J. B. Duff, *Bioresour. Technol.*, 2009, **100**, 6059-6063.

206.   M. R. Nimlos and R. J. Evans, *Fuel Chemistry Division Preprints*, 2002, **47**, 393-394.

207.   J. Schneider, F. Freutel, S. Zorn, Q. Chen, D. Farmer, J. Jimenez, S. Martin, P. Artaxo, A. Wiedensohler and S. Borrmann, *Atmos. Chem. Phys.*, 2011, **11**, 11415-11429.

208. D. Gardiner, *J. Chem. Soc. C*, 1966, 1473-1476.

209. X. F. Zhu and Q. Lu, *Production of chemicals from selective fast pyrolysis of biomass*, Sciyo, Croatia, 2010.

210. U. Moralı and S. Şensöz, *Fuel*, 2015, **150**, 672-678.

211. A. E. Pütün, E. Apaydın and E. Pütün, *Energy*, 2004, **29**, 2171-2180.

212. A. E. Pütün, A. Özcan and E. Pütün, *J. Anal. Appl. Pyrolysis*, 1999, **52**, 33-49.

213. İ. Demiral, A. Eryazıcı and S. Şensöz, *Biomass Bioenergy*, 2012, **36**, 43-49.

214. C. A. Mullen, G. D. Strahan and A. A. Boateng, *Energy Fuels*, 2009, **23**, 2707-2718.

215. B. Scholze, C. Hanser and D. Meier, *J. Anal. Appl. Pyrolysis*, 2001, **58–59**, 387-400.

216. P. Rutkowski, *Fuel Process. Technol.*, 2011, **92**, 517-522.

217. A. Prima, R. Zhbankov and R. Marupov, *J. Struct. Chem.*, 1965, **5**, 783-788.

218. Q. Lu, X. l. Yang and X. f. Zhu, *J. Anal. Appl. Pyrolysis*, 2008, **82**, 191-198.

219. A. Oasmaa and S. Czernik, *Energy Fuels*, 1999, **13**, 914-921.

220. S. Czernik, Storage of biomass pyrolysis oils, *Proceedings of Specialist Workshop on Biomass Pyrolysis Oil Properties and Combustion*, 1994

221. J. Wang, C. Xiang, Q. Liu, Y. Pan and J. Guo, *Adv. Funct. Mater.*, 2008, **18**, 2995-3002.

222. R. Ryoo, S. H. Joo, M. Kruk and a. M. Jaroniec, *Adv. Mater.*, 2001, **13**, 677-681.

223. S. Jun, S. H. Joo, R. Ryoo, M. Kruk, M. Jaroniec, Z. Liu, T. Ohsuna and O. Terasaki, *J. Am. Chem. Soc.*, 2000, **122**, 10712-10713.

224. S. H. Joo, S. Jun and R. Ryoo, *Microporous Mesoporous Mater.*, 2001, **44-45**, 153-158.

225. A. H. Lu, W. Schmidt, N. Matoussevitch, H. Bönnemann, B. Spliethoff, B. Tesche, E. Bill, W. Kiefer and F. Schüth, *Angew. Chem. Int. Ed.*, 2004, **43**, 4303-4306.

226. G. Liu, S. Zheng, D. Yin, Z. Xu, J. Fan and F. Jiang, *J. Colloid Interface Sci.*, 2006, **302**, 47-53.

227. M. Choi and R. Ryoo, *Nat. Mater.*, 2003, **2**, 473-476.

228. S. H. Joo, S. J. Choi, I. Oh, J. Kwak, Z. Liu, O. Terasaki and R. Ryoo, *Nature*, 2001, **412**, 169-172.

229. J. Lee, S. Han and T. Hyeon, *J. Mater. Chem.*, 2004, **14**, 478-486.

230. J. Lee, J. Kim and T. Hyeon, *Adv. Mater.*, 2006, **18**, 2073-2094.

231. G. Du, Y. Zhou and B. Xu, *Mater. Charact.*, 2010, **61**, 427-432.

232. Y. Y. Tsai, J. S. Su, C. Y. Su and W. H. He, *J. Mater. Process. Technol.*, 2009, **209**, 4413-4416.

233. J. Prasek, J. Drbohlavova, J. Chomoucka, J. Hubalek, O. Jasek, V. Adam and R. Kizek, *J. Mater. Chem.*, 2011, **21**, 15872-15884.

234. M. Si, D. Feng, L. Qiu, D. Jia, A. A. Elzatahry, G. Zheng and D. Zhao, *J. Mater. Chem. A*, 2013, **1**, 13490-13495.

235. L. Song, D. Feng, C. G. Campbell, D. Gu, A. M. Forster, K. G. Yager, N. Fredin, H. J. Lee, R. L. Jones, D. Zhao and B. D. Vogt, *J. Mater. Chem.*, 2010, **20**, 1691-1701.

236. R. Liu, Y. Shi, Y. Wan, Y. Meng, F. Zhang, D. Gu, Z. Chen, B. Tu and D. Zhao, *J. Am. Chem. Soc.*, 2006, **128**, 11652-11662.

237. M. Sevilla, C. Falco, M. M. Titirici and A. B. Fuertes, *RSC Adv.*, 2012, **2**, 12792-12797.

238. M. M. Titirici, R. J. White, C. Falco and M. Sevilla, *Energ. Environ. Sci.*, 2012, **5**, 6796-6822.

239. E. Thompson, A. Danks, L. Bourgeois and Z. Schnepp, *Green Chem.*, 2015, **17**, 551-556.

240. M. E. Miller and R. Wool, Carbon Fibers from Chicken Feather Keratin, *APS Meeting Abstracts*, 2006

241. T. G. Glover, K. I. Dunne, R. J. Davis and M. D. LeVan, *Microporous Mesoporous Mater.*, 2008, **111**, 1-11.

242. F. de Clippel, A. Harkiolakis, X. Ke, T. Vosch, G. Van Tendeloo, G. V. Baron, P. A. Jacobs, J. F. Denayer and B. F. Sels, *Chem. Commun.*, 2010, **46**, 928-930.

243. B. Charmas, R. Leboda, S. Pikus, A. Jezierski and E. Kobylas, *Colloids and Surfaces A: Physicochem. Eng. Aspects*, 2002, **208**, 93-102.

244. J. Shen, M. Wang, Y. Wu and F. Li, *RSC Adv.*, 2014, **4**, 21089-21092.

245. Y. Pan, M. Ju, C. Wang, L. Zhang and N. Xu, *Chem. Commun.*, 2010, **46**, 3732-3734.

246. H. Wang and J. Yao, *Ind. Eng. Chem. Res.*, 2006, **45**, 6393-6404.

247. A. Demirbas, *Energy Sources, Part A*, 2007, **29**, 753-760.

248. B. Boote, H. Subramanian and K. T. Ranjit, *Chem. Commun.*, 2007, 4543-4545.

249. C. Xue, B. Tu and D. Zhao, *Adv. Funct. Mater.*, 2008, **18**, 3914-3921.

250. Z. Luan, J. A. Fournier, J. B. Wooten and D. E. Miser, *Microporous Mesoporous Mater.*, 2005, **83**, 150-158.

References

251. P. Shah and V. Ramaswamy, *Microporous Mesoporous Mater.*, 2008, **114**, 270-280.

252. Y. Usami, T. Hongo and A. Yamazaki, *J. Porous Mater.*, 2011, **19**, 897-902.

253. Y. Li, Y. Chen, L. Li, J. Gu, W. Zhao, L. Li and J. Shi, *Appl. Catal., A*, 2009, **366**, 57-64.

254. A. S. M. Chong and X. S. Zhao, *J. Phys. Chem. B*, 2003, **107**, 12650-12657.

255. K. S. Novoselov, A. K. Geim, S. V. Morozov, D. Jiang, Y. Zhang, S. V. Dubonos, I. V. Grigorieva and A. A. Firsov, *Science*, 2004, **306**, 666-669.

256. Z. M. Wang, K. Hoshinoo, K. Shishibori, H. Kanoh and K. Ooi, *Chem. Mater.*, 2003, **15**, 2926-2935.

257. V. L. Budarin, J. H. Clark and S. J. Tavener, *Chem. Commun.*, 2004, 524-525.

258. A. Avila, I. Montero, L. Galán, J. M. Ripalda and R. Levy, *J. Appl. Phys.*, 2001, **89**, 212-216.

259. N. W. Smith and M. B. Evans, *Chromatographia*, 1995, **41**, 197-203.

260. J. R. Dodson, E. C. Cooper, A. J. Hunt, A. Matharu, J. Cole, A. Minihan, J. H. Clark and D. J. Macquarrie, *Green Chem.*, 2013, **15**, 1203-1210.

261. C. Y. Chen, H. X. Li and M. E. Davis, *Microporous Mater.*, 1993, **2**, 17-26.

262. J. P. Dacquin, J. Dhainaut, D. Duprez, S. Royer, A. F. Lee and K. Wilson, *J. Am. Chem. Soc.*, 2009, **131**, 12896-12897.

263. F. Kleitz, S. Hei Choi and R. Ryoo, *Chem. Commun.*, 2003, 2136-2137.

264. C. Pirez, J. M. Caderon, J. P. Dacquin, A. F. Lee and K. Wilson, *ACS Catalysis*, 2012, **2**, 1607-1614.

265. P. Y. Bruice, *Organic chemistry*, Prentice Hall, 9780321663139, 2010.

266. C. C. Johansson Seechurn, M. O. Kitching, T. J. Colacot and V. Snieckus, *Angew. Chem. Int. Ed.*, 2012, **51**, 5062-5085.

267. P. Taladriz-Blanco, P. Hervés and J. Pérez Juste, *Top. Catal.*, 2013, **56**, 1154-1170.

268. J. Guerra and M. A. Herrero, *Nanoscale*, 2010, **2**, 1390-1400.

269. Y. Wan, H. Wang, Q. Zhao, M. Klingstedt, O. Terasaki and D. Zhao, *J. Am. Chem. Soc.*, 2009, **131**, 4541–4550.

270. P. Wang and X. Zheng, *Powder Technol.*, 2011, **210**, 115-121.

271. J. Demel, J. Čejka and P. Štěpnička, *J. Mol. Catal. A: Chem.*, 2010, **329**, 13-20.

272. C. P. Mehnert, D. W. Weaver and J. Y. Ying, *J. Am. Chem. Soc.*, 1998, **120**, 12289-12296.

273. A. S. Singh, U. B. Patil and J. M. Nagarkar, *Catal. Commun.*, 2013, **35**, 11-16.

274. C. Jiménez González, A. Curzons, D. C. Constable and V. Cunningham, *Int J LCA*, 2004, **9**, 114-121.

275. S. Liu and J. Xiao, *J. Mol. Catal. A: Chem.*, 2007, **270**, 1-43.

276. H. L. Parker, J. Sherwood, A. J. Hunt and J. H. Clark, *ACS Sustain. Chem. Eng.*, 2014, **2**, 1739-1742.

277. J. H. Clark, D. J. Macquarrie and E. B. Mubofu, *Green Chem.*, 2000, **2**, 53-56.

278. G. V. Ambulgekar, B. M. Bhanage and S. D. Samant, *Tetrahedron Lett.*, 2005, **46**, 2483-2485.

279. K. Köhler, R. G. Heidenreich, J. G. E. Krauter and J. Pietsch, *Chem. Eur. J.*, 2002, **8**, 622-631.

280. J. Sun, S. i. Fujita and M. Arai, *J. Organomet. Chem.*, 2005, **690**, 3490-3497.

281. M. O. Ramin, Heterogeneously catalyzed synthesis of propylene carbonate using carbon dioxide, 2006

282. N. Eghbali and C. J. Li, *Green Chem.*, 2007, **9**, 213-215.

283. B. Schäffner, F. Schäffner, S. P. Verevkin and A. Börner, *Chem. Rev.*, 2010, **110**, 4554-4581.

284. B. Schaffner, J. Holz, S. P. Verevkin and A. Borner, *ChemSusChem*, 2008, **1**, 249-253.

285. J. Bayardon, J. Holz, B. Schäffner, V. Andrushko, S. Verevkin, A. Preetz and A. Börner, *Angew. Chem. Int. Ed.*, 2007, **46**, 5971-5974.

286. P. Lenden, P. M. Ylioja, C. Gonzalez-Rodriguez, D. A. Entwistle and M. C. Willis, *Green Chem.*, 2011, **13**, 1980-1982.

287. A. A. Kelkar, *Tetrahedron Lett.*, 1996, **37**, 8917-8920.

288. B. Schaldach and H. F. Grützmacher, *Org. Mass Spectrom.*, 1980, **15**, 175-181.

289. A. N. Miller, C. S. Walsh and J. D. Cohen, *Plant Physiol.*, 1987, **84**, 491-494.

290. J. Kiviaho, T. Hanaoka, Y. Kubota and Y. Sugi, *J. Mol. Catal. A: Chem.*, 1995, **101**, 25-31.

291. F. Zhao, B. M. Bhanage, M. Shirai and M. Arai, *Chem. Eur. J.*, 2000, 6, No. 5, **6** 843-848.

292. Z. She, Y. Shi, Y. Huang, Y. Cheng, F. Song and J. You, *Chem. Commun.*, 2014, **50**, 13914-13916.

293. R. C. Jones, M. Galezowski and D. F. O'Shea, *J. Org. Chem.*, 2013, **78**, 8044-8053.

294. C. H. Ying, S. B. Yan and W. L. Duan, *Org. Lett.*, 2014, **16**, 500-503.

295. N. A. Cortese, C. B. Ziegler-Jr., B. J. Hrnjez and R. F. Heck, *J. Org. Chem.*, 1978, **43**, 2952–2958.

296. X. Xie, J. Lu, B. Chen, J. Han, X. She and X. Pan, *Tetrahedron Lett.*, 2004, **45**, 809-811.

297. H. E. B. Lempers and R. A. Sheldon, *J. Catal.*, 1998, **175**, 62-69.

298. A. F. Schmidt, V. V. Smirnov and A. Al-Halaiga, *Kinet. Catal.*, 2007, **48**, 390-397.

299. R. F. Heck and J. P. Nolley, *J. Org. Chem.*, 1972, **37**, 2320-2322.

300. R. J. White, V. Budarin, R. Luque, J. H. Clark and D. J. Macquarrie, *Chem. Soc. Rev.*, 2009, **38**, 3401-3418.

301. P. Ross and J. H. Knox, *Adv. Chromatogr.*, 1997, **37**, 121-162.

302. R. Ryoo, S. H. Joo and S. Jun, *J. Phys. Chem. B*, 1999, **103**, 7743-7746.

303. J. S. Lee, S. H. Joo and R. Ryoo, *J. Am. Chem. Soc.*, 2002, **124**, 1156-1157.

304. M. Kaneda, T. Tsubakiyama, A. Carlsson, Y. Sakamoto, T. Ohsuna, O. Terasaki, S. H. Joo and R. Ryoo, *J. Phys. Chem. B*, 2002, **106**, 1256-1266.

305. A. Kim, R. Black, Y. J. Hyun, L. F. Nazar and E. Prouzet, *Chem. Commun.*, 2012, **48**, 4335-4337.

306. Y. Seo, K. Kim, Y. Jung and R. Ryoo, *Microporous Mesoporous Mater.*, 2015, **207**, 156-162.

307. P. Adelhelm, K. Cabrera and B. M. Smarsly, *Sci. Tech. Adv. Mater.*, 2012, **13**, 0150101-0150108.

308. B. Babić, M. Kokunešoski, M. Miljković, B. Matović, J. Gulicovski, M. Stojmenović and D. Bučevac, *Ceram. Int.*, 2013, **39**, 4035-4043.

309. S. S. Kim and T. J. Pinnavaia, *Chem. Commun.*, 2001, 2418-2419.

310. N. Gokulakrishnan, G. Peru, S. Rio, J. F. Blach, B. Leger, D. Grosso, E. Monflier and A. Ponchel, *J. Mater. Chem. A*, 2014, **2**, 6641-6648.

311. M. Kruk, B. Dufour, E. B. Celer, T. Kowalewski, M. Jaroniec and K. Matyjaszewski, *J. Phys. Chem. B*, 2005, **109**, 9216-9225.

312. B. Fang, J. H. Kim, M. S. Kim and J. S. Yu, *Acc. Chem. Res.*, 2013, **46**, 1397-1406.

313. P. Niebrzydowska, R. Janus, P. Kuśtrowski, S. Jarczewski, A. Wach, A. M. Silvestre-Albero and F. Rodríguez-Reinoso, *Carbon*, 2013, **64**, 252-261.

314.   S. Che, K. Lund, T. Tatsumi, S. Iijima, S. H. Joo, R. Ryoo and O. Terasaki, *Angew. Chem. Int. Ed.*, 2003, **42**, 2182-2185.

315.   S. Che, A. E. Garcia-Bennett, X. Liu, R. P. Hodgkins, P. A. Wright, D. Zhao, O. Terasaki and T. Tatsumi, *Angew. Chem. Int. Ed.*, 2003, **42**, 3930-3934.

316.   Z. Tian and M. A. Snyder, *Langmuir*, 2014, **30**, 12411-12420.

317.   A. H. Lu, W. Schmidt, B. Spliethoff and F. Schüth, *Adv. Mater.*, 2003, **15**, 1602-1606.

318.   A. H. Lu, W. C. Li, W. Schmidt, W. Kiefer and F. Schüth, *Carbon*, 2004, **42**, 2939-2948.